Seniority as a tool for truncating configuration interaction wave functions, and constructing pair Hamiltonians

Het gebruik van senioriteit om configuratie interactie golffuncties te beknotten, en paarHamiltonianen te construeren

Mario Van Raemdonck

Supervisors: Prof. Dr. P. Bultinck, Prof. Dr. D. Van Neck,
Dr. S. De Baerdemacker, Prof. Dr. F. De Proft
Dissertation submitted in fulfillment of the requirements for the
degree of Doctor (Ph.D.) in Science: Chemistry

Department of Inorganic and Physical Chemistry
Faculty of Sciences
Ghent University
Academic year 2016-2017

UNIVERSITEIT
GENT

Members of the examination committee

Chair

Prof. Dr. Ir. Zeger Hens (Universiteit Gent)

Jury Members
Prof. Dr. Paul W. Ayers (McMaster University)
Prof. Dr. Jeremy Harvey (Katholieke Universiteit Leuven)
Prof. Dr. Ir. An Ghysels (Universiteit Gent)
Prof. Dr. Ir. Toon Verstraelen (Universiteit Gent)
Dr. Sofie Van Damme (Universiteit Gent)

Supervisors
Prof. Dr. Patrick Bultinck (Universiteit Gent, *promotor*)
Prof. Dr. Dimitri Van Neck (Universiteit Gent, *copromotor*)
Dr. Stijn De Baerdemacker (Universiteit Gent, *copromotor*)
Prof. Dr. Frank De Proft (Vrije Universiteit Brussel, *copromotor*)

Acknowledgement

In the first place, I would like to thank my promotor Prof. Dr. Patrick Bultinck and my three co-promotors Prof. Dr. Dimitri Van Neck, Dr. Stijn De Baerdemacker and Prof. Dr. Frank De Proft. Without them, this thesis would not have been possible. Furthermore, I gratefully acknowledge all my fantastic colleagues at the Center for Molecular Modelling, the Ghent Quantum Chemistry Group and the theoretical chemistry group of McMaster University, for making me laugh during numerous occasions and making my four year journey a pleasant trip. Special thanks go to Dr. Stijn De Baerdemacker for introducing me to exactly solvable models and all the patience he had during this process. Many thanks also go to Prof. Dr. Diego Alcoba for the fruitful collaboration and all the guidance he provided during my research visit in Buenos Aires. And last but not least I have to thank my wonderful family and girlfriend for all the support, love and understanding they provided, especially during the last pressing months, when I was not able to give them the time they deserved.

Mario Van Raemdonck
Gent, 12 september 2016

Contents

Samenvatting

De kwantumchemie is het deelgebied van de natuurkunde en de theoretische scheikunde dat tracht chemische verschijnselen zoals chemische binding en katalyse te beschrijven met behulp van de kwantummechanica. Een van de meest fundamentele inzichten dat uiteindelijk zal leiden tot de moderne kwantumchemie zoals we die nu kennen, is het feit dat alle materie is opgebouwd uit gelijkaardige bouwstenen genaamd atomen. Over dit feit werd al gefilosofeerd in de oudheid door de oude Griekse wijsgeren, en vanaf het begin van de 19$^{\text{de}}$ eeuw werd het als wetenschappelijke theorie geïntroduceerd door het werk van Dalton. Een volgende grote doorbraak kwam er in 1869 met de introductie van de periodieke tabel van Mendeljev, die periodieke trends aantoonde van de toen bekende elementen en gebaseerd op deze trends kon Mendeljev eigenschappen voorspellen van toen nog onbekende elementen, waarvan hij verwachtte dat deze gaten in de tabel zouden vullen. Hierna volgden experimentele resultaten van Thomson en Rutherford die duidelijk maakten dat atomen niet ondeelbaar waren en er onderscheid gemaakt kan worden tussen de elektronenwolk en de kern. Vooral de elektronen die zich verder van de kern bevinden bepalen de chemische eigenschappen van de atomen. Het bleek echter zeer lastig om het gedrag van deze elektronenwolk correct te beschrijven, wat nodig is om correcte voorspellingen over chemische reacties en evenwichtstoestanden te doen.

Het was wachten tot de ontwikkeling van de kwantummechanica, die het eerste alomvattende kader creëerde voor de chemische beschrijving van atomen en moleculen. De wereld beschreven op het niveau van de kwantummechanica is compleet anders dan wat we gewoon zijn in onze macroscopische wereld. Er zijn enkel nog waarschijnlijkheden en er is de deeltje-golf dualiteit. Een van de belangrijkste vergelijkingen van de kwantummechanica is de Schrödingervergelijking, die een niet-relativistisch kwantummechanisch systeem beschrijft. Oplossingen van deze vergelijking noemt men golffuncties. Deze golffuncties bieden zeer goede beschrijvingen voor het gedrag van onder andere elektronenwolken. Voor het waterstofatoom kan men deze vergelijking nog exact oplossen, maar voor alle zwaardere atomen moet men grijpen naar numerieke hulpmiddelen en/of benaderende theoretische beschrijvingen. Een ander probleem met de huidige theorie is dat de meeste atomen en moleculen vele elektronen bevatten en de complexiteit van het kwantummechanische probleem exponentieel schaalt met

een toenemend aantal deeltjes vanwege de onderlinge interacties.

In deze thesis, die uit twee delen bestaat, wordt in het eerste deel senioriteit geïntroduceerd als een hulpmiddel om nieuwe golffuncties te genereren. Het senioriteitskwantumgetal werd voordien hoofdzakelijk gebruikt in de kernfysica en is minder bekend in de chemische wereld. Daarna wordt onderzocht wat de eigenschappen zijn van de verschillende senioriteitsblokken in de exacte golffunctie voor een eindige basis set. Dit in tegenstelling met de gebruikelijke excitatie gebaseerde onderverdeling van de golffunctie. Na het bestuderen van de verschillende blokken in de exacte golffunctie kijken we naar wat er gebeurt als we enkel subblokken gebruiken als benaderende beter schalende golffunctie. De laagste in rang van deze hierarchie is de bekende doubly occupied configuration interaction (DOCI) golffunctie. Deze golffunctie bestaat enkel uit determinanten met senioriteit nul, wat wil zeggen dat alle elektronen in paren voorkomen. We bespreken welke soorten correlaties ze adequaat beschrijven in vergelijking met de excitatie gebaseerde reductie technieken. We onderzoeken ook of de senioriteitshierarchie sneller naar de exacte limiet convergeert dan de excitatie gebaseerde hierarchie. De kracht van de senioriteits gebaseerde hierarchie komt voort uit het feit dat deze niet van een referentie determinant afhangt en een globale onderverdeling veronderstelt, waardoor ze zeer geschikt is om statische correlatie correct te beschrijven. Verder zijn deze senioriteits gebaseerde golffuncties afhankelijk van een unitaire transformatie van de één-deeltjes basis. Daarom onderzoeken we ook het effect van deze transformaties op hun eigenschappen. De ideale basis voor senioriteits gebaseerde golffuncties zal de basis blijken te zijn die de senioriteit van de exacte golffunctie minimaliseert. Het berekenen van deze basis gaat relatief vlot door het bestaan van iteratieve algoritmen. Ook senioriteit geminimaliseerde basissen van gerestricteerde golffuncties doen het zeer goed. Verder blijkt dat deze basis een zeer lage Shannon entropie heeft voor de coefficienten van de exacte golffunctie, wat een indicatie geeft van de hoge mate van ordening die deze basis heeft voor de afzonderlijke Slater determinanten. Daarna worden de voordelen en tekortkomingen van de DOCI golffunctie uitgebreider besproken en wordt er geprobeerd om de tekortkomingen één voor één te elimineren. Dit wordt gedaan door dynamische correlatie toe te voegen via extra één deeltjes excitaties, en het maximale aantal paarexcitaties te beperken zodat de schaling reduceert naar polynomiaal. Als uiteindelijk resultaat bekomen we een golffunctie opgebouwd uit enkel en dubbel geëxciteerde Slater determinanten gecombineerd met hogere paar excitaties die maar een fractie van de computationele capaciteit nodig heeft van de exacte golffunctie, en toch bijna exact de dissociatie van uitdagende molecules zoals BeH_2 kan beschrijven. Van alle geteste benaderende methoden gaf deze veruit de beste resultaten over een volledig dissociatie proces. Verder zal ook blijken dat DOCI als één van de weinige benaderende golffuncties in staat is om exotische eigenschappen van atomen op oneindige afstand correct te voorspellen zoals fractionele ladingen, sterke densiteitsveranderingen na infinitesimale veranderingen van de Hamiltoniaan en het stapsgewijs lineair gedrag van de energie in functie van de lading op één van de atomen.

In het tweede deel van deze thesis wordt een andere manier om benaderende golffuncties te bekomen beschouwd, namelijk het vereenvoudigen van de Hamiltoniaan tot de meest eenvoudige Hamiltoniaan die in staat is om de essentiële fysische of chemische eigenschappen van het systeem te genereren. Specifiek focussen we ons op paarHamiltonianen. PaarHamiltonianen worden vooral in de vaste-stof fysica gebruikt omdat ze een degelijke beschrijving van supergeleiding bieden. Een bijkomend voordeel van een veelvoorkomende klasse van paarHamiltonianen is dat ze integreerbaar zijn, wat wil zeggen dat er evenveel commuterende variabelen bestaan als vrijheidsgraden van het systeem. Deze integreerbaarheid is ook bruikbaar voor het bekomen van oplossingen voor de Hamiltoniaan, zoals Richardson en Gaudin onafhankelijk aantoonden. Het grote voordeel van de Richardson-Gaudin methode is dat ze lineair schaalt met het aantal deeltjes en toch de exacte oplossingen levert in tegenstelling tot de conventionele exacte diagonalisatie procedures die tegen een exponentiële muur aanlopen. Nadeel is dat er sterke singulariteiten opduiken bij het oplossen van de resulterende Richardson-Gaudin vergelijkingen. Recent is er veel onderzoek gedaan naar het oplossen van dit probleem. In deze thesis maken we vooral gebruik van resultaten die gegenereerd zijn door de singulariteiten te ontwijken door naar het complexe vlak te gaan of de quasi-spin algebra te veranderen. Na het afleiden van de algemene theorie passen we het formalisme toe op twee specifieke Hamiltonianen gegenereerd met respectievelijk de zogenaamde XXX en de XXZ variant. Voor de XXX variant die onder andere de gereduceerde BCS Hamiltoniaan genereert, onderzoeken we de effecten van perturbaties van de geometrie op de supergeleidende toestand van nano-korrels. De XXZ variant genereert een Hamiltoniaan die paring op een tweedimensionaal rooster met een $p_x + ip_y$ symmetrie beschrijft. Het fase diagram van deze Hamiltoniaan is zeer interessant door de Read-Green and Moore-Read punten. Er worden enkele relaties afgeleid tussen deze punten van het fasediagram en de Tamm Dancoff benaderingen (TDA) die naar de juiste toestanden leiden.

Onderzoek dat volgt op deze thesis kan nagaan in hoeverre mate de resulterende golffuncties van het XXX model de DOCI golffunctie kan benaderen. Verder kunnen de effecten van het aanpassen van de één-deeltjes niveaus, de paringsparameter en het effect van basistransformaties onderzocht worden. Echter met de ervaring die gedurende het creëeren van deze thesis bekomen is, kunnen al enkele zaken geconcludeerd worden. Voor twee elektron systemen is het mogelijk om de exacte resultaten te reproduceren, want ook DOCI is exact voor het twee elektron probleem. Verder is het benodigde RAM-geheugen sterk gereduceerd, maar de computationele tijd niet door de huidige trage implementatie van het multidimensionale optimalisatie probleem om de beste één-deeltjes niveaus en paringsparameter van de gereduceerde BCS Hamiltoniaan te bepalen voor niet-relativistische kwantumchemische Hamiltonianen. Verder kan men verbanden onderzoeken tussen de optimale distributie van de één-deeltjes niveaus en koppelingsconstante bij verschillende posities op de potentiaal energie curve zoals bij evenwicht en bij de dissociatie limiet waar de statische correlatie belangrijker wordt. Voor grote systemen is DOCI nauw-

keurigheid niet praktisch werkbaar door de multidimensionale optimalisatie. Dit valt te omzeilen door enkel de paringsparameter te optimaliseren en de Hartree-Fock gemiddeld-veld basis te gebruiken. In dat geval is men zeker dat men in het slechtste geval terug de Hartree-Fock energie bekomt, namelijk in de limiet waar de paringsparameter wegvalt, en wanneer deze in kleine stapjes oploopt dan bekomt men een gecorreleerde golffunctie met DOCI dimensie en significant betere energieën dan HF. Deze golffunctie levert voor middelgrote moleculen een sterk verbeterde beschrijving voor dissociatieprocessen op. Bij het nog beter onder de knie krijgen van de singulariteiten die optreden bij het oplossen van de Richardson-Gaudin vergelijkingen en mits meer ervaring bij het kiezen van de optimale parameters van de Richardson-Gaudin Hamiltonianen om de kwantumchemische Hamiltoniaan te benaderen, kan deze methode in de toekomst gebruikt worden om processen te beschrijven waar zeer grote moleculen een rol spelen, door de lineaire schaling van de oplossingsmethode met betere resultaten dan conventionele gemiddeld veld methodes zoals Hartree-Fock (HF) en densiteits functionaal theorie (DFT).

Abstract

Nothing is as simple as it seems at first.
Or as hopeless as it seems in the middle.
Or as finished as it seems in the end.

Quantum chemistry lies at the interface between physics and theoretical chemistry. The main goal is to describe chemical bonding and catalysis with the framework provided by quantum mechanics. One of the most fundamental facts which eventually led to modern quantum chemistry is that all matter is built from similar building blocks, called atoms. This was already conjectured by the old Greek philosophers and at the start of the 19$^{\text{the}}$ century it became a scientific theory through the work of Dalton. The next breakthrough occurred in 1869 with the introduction of the periodic system by Mendeljev. It showed periodic trends of the known elements and based on those trends it was possible to predict properties of still unknown elements, which were expected to fill blanks in the table. Experimentally it was shown by Thomson and Rutherford that atoms are constituted of a negatively charged cloud consisting of electrons and a positive nucleus. Of particular importance for the chemical properties of the atoms are the electrons that are farther from the nuclei. It was and still is a huge challenge to correctly describe the behaviour of the electron cloud, which is necessary to predict chemical reactions and equilibrium geometries. One had to wait till the advent of quantum mechanics, which provided the first consistent and complete theoretical framework for the description of atoms and molecules. One of the most important equations of quantum mechanics is the Schrödinger equation, which describes a non-relativistic quantum mechanical system. Solutions of this equation are called wave functions. For the hydrogen atom it is possible to solve the Schrödinger equation exactly, but for all heavier atoms one has to use numerical tools and approximative descriptions. One of the main challenges of quantum chemistry is that most atoms and molecules consist of many electrons and the complexity of the problem scales exponentially with the system size, due to the mutual interactions.

In the first part of this two part thesis, the seniority number is introduced as a tool to generate new wave functions in quantum chemistry. Previously, the seniority quantum number was mainly used in nuclear physics and was

less known in quantum chemistry, which is dominated by an excitation based approach for the construction of wave functions. The properties of the different seniority blocks of the exact wave function are analysed for finite basis sets. After the study of the different wave function blocks we take a look at what happens when those parts are used as isolated wave functions. Furthermore we test if the seniority based hierarchy converges faster than the excitation based hierarchy to the exact limit. The seniority hierarchy starts with the doubly occupied configuration interaction (DOCI) wave function. This wave function consists only of seniority zero determinants, meaning that all electrons form pairs. We discuss which sorts of correlation are adequately described by seniority approaches in comparison with the excitation based ones. One of the strong points of the seniority based hierarchy is that it does not depend on a reference determinant, which makes it especially suitable for the description of static correlation. These seniority based wave functions depend on a unitary transformation of the single particle orbitals. Therefore it is investigated which effect these transformations have on the properties of the seniority based wave functions. It is concluded that the ideal basis for wave functions with a low seniority is the seniority minimized basis of the exact wave function. The calculation of this basis goes relatively smooth and fast because of the existence of some iterative algorithms. If it is not possible to calculate the exact wave function for the system one can resort to the seniority minimization of restricted wave functions, which also works particularly well. Another property of the seniority minimized basis is that it has a remarkably low Shannon entropy for the coefficients of the exact wave function, which indicates the high order it introduces to the different Slater determinants. Finally we discuss more extensively the properties and shortcomings of the DOCI wave function. It is checked if it is possible to alleviate the shortcomings one by one. Low seniority wave functions typically have problems with dynamic correlation and still scale exponentially. Those two problems can be solved by truncating the higher pair excitations from a reference determinant and adding extra seniority broken determinants. In essence we study methods that combine the configuration interaction method with single and double excitations (CISD) with higher pair excitations in seniority minimised bases of the CISD wave function. This wave function describes almost exactly the dissociation of challenging molecules such as BeH_2, and gives the best results compared to all other approximative methods we have tested. Furthermore we show that the DOCI wave function correctly describes several exotic properties of atoms separated by large distances such as fractional charges, strong changes in the density upon infinitesimal changes in the Hamiltonian, and the piece-wise linear behaviour of the energy in function of the charge on one of the atoms.

In the second part of this thesis we discuss another way to generate approximate wave functions by simplifying the Hamiltonian that needs to be solved. A typical approximation mostly done in physics consists of stripping away all the non-essential information of the Hamiltonian, and keeping only the simplest possible form of the Hamiltonian that generates the desired physical properties.

This thesis specifically focusses on pair Hamiltonians for which the seniority number is an exact quantum number. Pair Hamiltonians are mainly used in condensed matter physics because they give a suitable description for superconductivity. An extra advantage of the pair Hamiltonians is that they can be integrable, meaning that there are as many commuting variables as there are degrees of freedom of the system. This exact integrability is exploitable for the generation of solutions for those Hamiltonians, as is shown by Richardson and Gaudin independently. The main advantage of the Richardson-Gaudin method is that it scales linearly with the number of particles in the system and still generates the exact solution. This is in big contrast with the conventional exact diagonalisation methods that scale exponentially with the number of particles in the system. This seems too good to be true and in fact it is, because additional caveats show up in the Richardson-Gaudin scheme in the form of strong singularities, when one tries to solve the complex system of non-linear equations that generate the solutions. However, recently many breakthroughs occurred that help to deal with those singularities. In this work we mainly solved this problem by generalizing the interaction constant to the complex plane or the adaptation of the quasi-spin algebra. After the derivation of the general theory, the formalism is applied to two specific Hamiltonians that are derivable respectively from the so-called XXX and XXZ variants of the Richardson-Gaudin models. For the reduced BCS Hamiltonian generated from the XXX variant we studied the effects of perturbations of the geometry on the superconducting state in nano-grains. For the $p_x + ip_y$ Hamiltonian, generated from the XXZ model, which describes pairing with $p_x + ip_y$ symmetry on a two dimensional grid, is the phase diagram studied. This phase diagram consists of many interesting points such as the Read-Green and Moore-Read points, which are connected to particular combinations of solutions of the Tamm-Dancoff approximation (TDA) by a pseudo-deformation of the quasi spin algebra. This keeps them more easily tractable for big systems.

Future work based on this thesis can attempt to approximate DOCI wave functions with resulting wave functions of the XXX model. Furthermore the effects of changing the single-particle levels, and the pairing parameter can be investigated together with the effect of basis transformations. However with the experience obtained during the creation of this thesis some conclusions can be made already. One of those conclusions is that for small systems Richardson-Gaudin wave functions are able to reproduce DOCI energies, and for two electron systems even exact results (because DOCI is exact for the two electron problem). This with a strongly reduced use of memory, but unfortunately not reduced computational time, due to the complexity of the multi-dimensional optimization problem for the parameters of the reduced BCS Hamiltonian, it is our aim to strongly reduce this time in future implementations. One can also search for patterns between the optimal distribution of the single-particle levels and interaction constant at different positions on the potential energy surface, such as near equilibrium and at the dissociation limit where static correlation is more important. Currently it is not possible to reproduce DOCI accuracy

for big systems. But it is possible to improve significantly on the Hartree-Fock (HF) energies even for very large systems. This is done by using the Hartree-Fock single-particle bases for the expression of the Richardson-Gaudin wave function. From this it follows that the Hartree-Fock wave function and energy are reproduced in the absence of a pairing interaction. When the interaction constant is increased until a minimal energy of the quantum chemical Hamiltonian is obtained, then a significant improvement of the Hartree-Fock energy and wave function is obtained, with a correlated wave function that has the same dimension as the DOCI wave function and linear scaling. Even with very rudimentary guesses for the single-particle levels dissociation curves are correctly reproduced for some molecules. These results are promising for the future and with an improved ability to deal with the singularities and improved experience for the selection of the optimal parameters of the Richardson-Gaudin models, this method could be used to describe correlated processes of large molecules more accurately than one can with Hartree-Fock and density functional theory (DFT) methods.

List of Figures

List of Tables

Part I

A seniority number based view of configuration interaction theory

Chapter 1

Introduction and theoretical background

In this first chapter the research program is framed in a broader context, and the terminology necessary for the next chapters is introduced along with the theoretical background.

1.1 Framing of the performed research

One of the most fundamental facts, which leads to modern chemistry, is that all matter is built from similar building blocks, called atoms. Although this was already conjectured in ancient Greece, it became a scientific theory at the start of the 19^{the} century by the work of Dalton. Another great breakthrough occurred in 1869 with the introduction of the periodic system of Mendeljev. This periodic system revealed periodic trends of the physical and chemical properties of the known elements and based on those trends it was possible to predict properties of unknown elements, which were expected to fill blanks in the table. Experimentally, Thomson and Rutherford showed that atoms are constituted of a negatively charged cloud consisting of electrons and a positive nucleus. Particularly important for the chemical properties of the atoms are the electrons that are the most distant from the nuclei, the so-called valence electrons. It was and still is a huge challenge to correctly describe the behaviour of this electron cloud, which is necessary to predict chemical reactions and equilibrium geometries.

With the advent of computers in the last decades, numerical methods started to play an increasingly prominent role in chemistry; it even led to a new part of chemistry called computational chemistry. One can think of computational chemistry as chemistry performed using computers rather than chemicals. Powerful molecular modelling tools have been developed, which are capable of

accurately predicting structures, energetics, reactivities and other properties of molecules. These developments have come about largely due to the dramatic increase in computer speed and the design of efficient quantum chemical algorithms. There are many advantages involved with the use of computers: simulations are easy to perform, whereas experiments are often difficult. Furthermore calculations are becoming less costly each year, whereas experiments are becoming more expensive on average. Calculations can be performed on any system, even those that are currently impossible in the lab, whereas many experiments are limited to relatively stable molecules. Calculations are safe, whereas many experiments have an intrinsic danger associated with them. One of the main disadvantages is that calculations can be very expensive in terms of the amount of time required. Furthermore it should be emphasized that computational chemistry is not a replacement for experimental studies, but plays an important role in enabling chemists to explain and rationalise known chemistry or to explore new and unknown chemistry.

Computational chemistry can be further subdivided in a range of disciplines such as statistical mechanics, molecular mechanics, semi-empirical frameworks, and ab initio quantum chemistry. All the previous frameworks except the last one rely on empirical input information such as experimental parameters, energy levels, ... This thesis focusses only on ab initio quantum chemistry. Ab initio means "from the beginning" or "from first principles". This means that it is based only on established laws of nature such as quantum mechanics. The theory of quantum mechanics provided the first consistent and complete theoretical framework to describe the electronic behaviour of atoms and molecules. One of the most important equations of quantum mechanics is the Schrödinger equation. This equation describes a non-relativistic quantum mechanical system and its solutions are called wave functions. For the hydrogen atom, it is possible to solve the Schrödinger equation exactly, but for all heavier atoms one has to use numerical tools and approximative descriptions. One of the main challenges of quantum chemistry is that most atoms and molecules contain many electrons and the complexity of this quantum many-body problem scales exponentially with the system size, due to the mutual interactions. Therefore approximations are necessary. Among ab initio methods, wave function methods play a key role. These explicitly construct wave functions for the systems under consideration, this in contrast with density based methods such as density functional theory (DFT) which rely primarily on the functional dependence of the energy on the electron density. This thesis focuses on wave function based methods. The first part of this thesis discusses the introduction of seniority as a new quantum number to partition and build wave functions in quantum chemistry. The second part discusses the performance of some model Hamiltonians that have seniority as an exact quantum number for the description of condensed matter systems, and the variational approximation of the non-relativistic quantum chemical Hamiltonian.

In the next section the starting-point of all quantum chemistry is discussed,

that is the Schrödinger equation for a general molecular system. After that, a short introduction is given about wave function based quantum chemistry and configuration interaction theory in particular. The aim is to summarize important results that will be used in subsequent chapters of this thesis and to introduce the necessary terminology.

1.2 The non-relativistic quantum chemical Hamiltonian

As already mentioned in the previous section, quantum mechanics is centered around the solution of the Schrödinger equation. This equation is given by:

$$i\hbar\frac{\partial\Psi}{\partial t} = \hat{H}\Psi. \tag{1.1}$$

The operator $\hat{H}$ is the Hamiltonian and the expectation value of the wave function Ψ with respect to $\hat{H}$ is the energy of the system under consideration. When the Hamiltonian does not depend on time, it is convenient to do a separation of variables, which leads to the stationary Schrödinger equation:

$$\hat{H}\Psi = E\Psi \tag{1.2}$$

The state with the lowest energy is called the ground state, and the other solutions are called excited states. If there are states with the same energy, they are called degenerate states. Any linear combination of degenerate states is also an eigenstate of the Hamiltonian with the same energy, and one needs other quantum numbers to distinguish between them. This can be done if operators exist that commute with the Hamiltonian but have different eigenvalues for the degenerate states, as elementary quantum mechanics teaches us that mutually commuting operators can be diagonalized with a common eigenbasis[1].

If this wave function is obtained somehow, all the observable properties can be calculated as the expectation value of that observable with respect to the wave function. Furthermore many chemical properties can be obtained from derivatives of the energy with respect to some parameter, an example of this will be discussed in the last chapter of the first part of this thesis (see Ch. 4). Some examples of those external parameters are geometric parameters such as bond lengths, angles, ..., external electric fields from solvents or other molecules, external magnetic fields (Nuclear Magnetic Resonance experiments). First and second order derivatives of the energy are readily available, higher derivatives are much more complicated and expensive to compute as they require higher order density matrices. Some molecular properties that can be computed, when the wave function is known, are bond energies, reaction energies, structures of ground-, excited- and transition-states, atomic charges and electrostatic potentials, vibrational frequencies (Infrared and Raman spectroscopy), transition energies, intensities for Ultraviolet and Infrared spectra, Nuclear Magnetic

Resonance chemical shifts, dipole moments, polarisabilities and hyperpolarisabilities, reaction pathways and mechanisms. The Hamiltonian in eq.(1.2) can be written for molecules with N electrons at positions $\mathbf{r}_i$, and M nuclei at positions $\mathbf{R}_A$ as:

$$\begin{aligned}\hat{H} = &-\frac{1}{2}\sum_{i}^{N}\hat{\nabla}_i^2 - \frac{1}{2}\sum_{A}^{M}\frac{\hat{\nabla}_A^2}{M_A} - \sum_{A}^{M}\sum_{i}^{N}\frac{Z_A}{|\mathbf{r}_i - \mathbf{R}_A|} \\ &+ \frac{1}{2}\sum_{ij,i\neq j}^{N}\frac{1}{|\mathbf{r}_i - \mathbf{r}_j|} + \frac{1}{2}\sum_{AB,A\neq B}^{M}\frac{Z_A Z_B}{|\mathbf{R}_A - \mathbf{R}_B|}\end{aligned} \tag{1.3}$$

Atomic units are used in the above equation, this means that the elementary charge e, the reduced Planck constant $\hbar$, the electron mass m_e, and $4\pi\epsilon_0$ are all set identically to one. The individual electrons are labelled with small latin indices starting from i, and the nuclei with capital latin indices starting from A. Eq.(1.2) provides such a challenging problem for molecules that many previous theses and also this thesis consist only out of the design and testing of approximative solutions to eq.(1.2). This observation made Dirac write already in 1930 that [2]:

> "The underlying physical laws necessary for the mathematical theory of a large part of physics and the whole of chemistry are thus completely known, and the difficulty is only that the exact application of these laws leads to equations much too complicated to be soluble."

A need for good approximations thus arises. One of the most important and frequently used approximations to simplify the above Hamiltonian is the Born-Oppenheimer approximation[3]. It makes use of the fact that nuclei are much heavier than that of electrons (the mass of a proton is three orders of magnitude bigger than electrons), and therefore nuclei move much slower than electrons. From this one can assume that electrons instantaneously adapt their configuration, upon a change in the nuclear coordinates, and that the derivative of the electronic wave function with respect to the nuclear coordinates is approximately zero. These assumptions allow us to factorise the wave function in a part that only depends on the nuclear coordinates, and a part that depends on the electron coordinates, where the nuclear coordinates are treated as parameters, and for all sets of those parameters (geometries of the molecule) the resulting electron cloud can be calculated. This means that it is possible to have good approximations of the electron cloud at a given nuclear geometry, when the nuclear coordinates are kept fixed. From this it follows that the last term of the above Hamiltonian reduces to an easily computable constant, and the kinetic energy of the nuclei can be ignored until it is reintroduced in the Schrödinger equation for the nuclear motion, leading to rotational and vibrational contributions. The Born-Oppenheimer approximation carries the essence of the validity of potential energy surfaces (PES). This means that

solving eq.(1.2) reduces to the search for the dependency of the many body wave function Ψ on the $4N$ electron coordinates. The coordinates of one electron are the spatial coordinates $\mathbf{r} = (x, y, z)$ and an extra spin coordinate s that can have the values α and β (sometimes also denoted as up and down). The resulting wave function depends thus on $4N$ correlated coordinates, and eq.(1.2) simplifies to finding the eigenstates, and eigenvalues of

$$\left(-\frac{1}{2}\sum_{i}^{N}\hat{\nabla}_i^2 - \sum_{A}^{M}\sum_{i}^{N}\frac{Z_A}{|\mathbf{r}_i - \mathbf{R}_A|} + \frac{1}{2}\sum_{ij,i\neq j}^{N}\frac{1}{|\mathbf{r}_i - \mathbf{r}_j|}\right)\Psi(\mathbf{r}_1, s_1, \ldots, \mathbf{r}_N, s_N) = E\Psi(\mathbf{r}_1, s_1, \ldots, \mathbf{r}_N, s_N), \tag{1.4}$$

where E is the electronic energy. Another approximation is to use finite basis sets to expand the wave function in order to make practical calculations possible. It is then assumed that the basis set is big enough to produce relevant results. A test for the quality of the basis set is comparing the results with those obtained from larger basis sets. A basis set is a set of functions that can span orthogonal molecular orbitals ($\chi(\mathbf{x})$). Basis functions are mostly (approximate) atomic orbitals centered on atoms, but theoretically they can be any function. For example plane waves are frequently used in condensed matter calculations, and sometimes grids in real space are also used to express the wave function. For a concise introduction to basis set theory see Helgaker et.al. [4].

The Pauli principle states that all physical wave functions need to change sign upon interchange of any two fermions. From this principle it follows that the most straightforward N electron many-body wave function that can be generated is an anti-symmetrized direct product of N one-electron wave functions (orbitals), also called Slater determinants. Slater determinants can be thought of as determinants where the column indices change the single-particle orbitals and the rows are associated to the electron-index, thus imposing the necessary anti-symmetry rules. One can generate all N electron Slater determinants supported by a given finite basis set by acting with a unitary transformation on a starting determinant generated from the finite basis set. The full space that the finite basis set describes is spanned by all possible Slater determinants created by distributing the N electrons over all K orbitals. The dimension of the Hilbert space of a finite basis set is thus equal to the binomial coefficient $\binom{K}{N}$. By using Stirlings formula one sees that this dimension scales exponentially with the number of electrons and single-particle orbitals, at half-filling $\binom{K}{\frac{K}{2}} \approx e^{K\ln(2)}$. This makes it only feasible to calculate the exact solution for small molecules and basis sets. A powerful formalism to reason and derive expressions for many-body systems is the formalism of second quantization [5] (see also appendix A). This formalism makes it possible to leave all explicit spatial dependencies over to the basis set by projecting all many-body operators under consideration onto this basis set. The operators depend in second quantization on the chosen spin-orbital basis, as they are

projected operators. This is in contrast with the first quantized case where operators are independent of the spin-orbital basis, but depend explicitly on the number of electrons. The Hamiltonian of eq. (1.3) can be written in second quantization after projecting it on a given finite basis set. This projection is done by integrating out the spatial and spin dependencies. The obtained integrals that incorporate all the spatial and spin dependencies become:

$$h_{pq} = \int \chi_p^*(\mathbf{x}) \left(-\frac{1}{2}\hat{\nabla}^2 - \sum_A \frac{Z_A}{|\mathbf{x} - \mathbf{R}_A|} \right) \chi_q(\mathbf{x}) \mathrm{d}\mathbf{x} \tag{1.5}$$

$$g_{pqrs} = \int\int \frac{\chi_p^*(\mathbf{x}_1)\chi_r^*(\mathbf{x}_2)\chi_q(\mathbf{x}_1)\chi_s(\mathbf{x}_2)}{|\mathbf{x}_1 - \mathbf{x}_2|} \mathrm{d}\mathbf{x}_1 \mathrm{d}\mathbf{x}_2 \tag{1.6}$$

$$h_{nuc} = \frac{1}{2} \sum_{A \neq B} \frac{Z_A Z_B}{|\mathbf{R}_A - \mathbf{R}_B|} \tag{1.7}$$

Chemical notation is used for the two body integrals. Thus the Hamiltonian of eq.(1.3) in second quantization becomes:

$$\hat{H} = \sum_{pq} h_{pq} a_p^\dagger a_q + \frac{1}{2} \sum_{pqrs} g_{pqrs} a_p^\dagger a_r^\dagger a_s a_q + h_{nuc}, \tag{1.8}$$

where $a_p^\dagger$ creates an electron in single-particle spin orbital p and a_p annihilates a particle in single-particle spin orbital p (see also appendix A). They fulfill the fermion anti-commutation relations[6]:

$$a_i^\dagger a_j + a_j a_i^\dagger = \delta_{ij} \tag{1.9}$$

$$a_i^\dagger a_j^\dagger + a_j^\dagger a_i^\dagger = 0 \tag{1.10}$$

$$a_i a_j + a_j a_i = 0. \tag{1.11}$$

The non-relativistic Hamiltonian does not mix states with different spin and spin-projection, therefore one can express the Hamiltonian in block-diagonal form when expanded in configuration state functions that have a good spin and spin-projection or in determinants which have only a definite spin-projection. The advantage of using configuration state functions (CSF's) is that less memory is needed to construct the Hamiltonian, the disadvantage is that they are more difficult to construct and more difficult to handle than determinants resulting in a speed deficit. Furthermore Slater determinants can be efficiently, stored in a computer program as integers, and generating excitations is efficiently done by bit operations and built-in functions on any platform. Such an implementation increases the speed considerably. The number of Slater determinants with a correct spin-projection (ignoring spatial point-group symmetry) can be calculated as:

$$\mathrm{Dim}(K, N_\alpha, N_\beta) = \binom{K}{N_\alpha} \binom{K}{N_\beta}, \tag{1.12}$$

with K as before the number of single-particle orbitals and N_α the number of particles with spin up, and N_β the number of particles with spin down.

For configuration state functions this dimension can be calculated with Weyl's dimension formula, with S the total spin, K the number of orbitals, and N the number of electrons, the dimension of the CI-space in CSF's is [7–9]:

$$\mathrm{Dim}(S,K,N) = \frac{2S+1}{K+1}\binom{K+1}{\frac{N}{2}-S}\binom{K+1}{\frac{N}{2}+S+1} \tag{1.13}$$

From Slater determinants it is a small step to the next topic configuration interaction theory.

1.3 Introduction to configuration interaction theory

In this section a short introduction to configuration interaction (CI) theory and the conventional single-particle based truncation methods is given . Of all ab-initio methods, configuration interaction theory is one of the most accurate and easiest to understand conceptually, but one of the most difficult to implement efficiently on a computer. A more elaborate introduction can be found in the excellent book of Helgaker, Jorgensen and Olsen [4], and the online introduction of D. Sherrill [10]. In essence, CI-theory is a projection of the Hamiltonian (eq. 1.8) on a finite basis of Slater determinants, after which a diagonalization follows to generate the optimal coefficients of the linear expansion. Below the variational optimization problem is discussed together with the standard excitation based truncation methods, the amount of correlation they are able to account for and their scaling. The traditional scope of CI theory is to improve the Hartree-Fock (HF) solution by increasing the space for the variational optimization of all possible many-electron wave functions from a single Slater determinant to a larger set of Slater determinants constructed from a given basis set. For this basis set, the wave function can be expanded in a basis of N-electron Slater determinants.

$$|\Psi\rangle = \sum_i |\phi_i\rangle \langle\phi_i|\Psi\rangle = \sum_i C_i |\phi_i\rangle \tag{1.14}$$

For HF-theory this summation reduces to a single element, the Slater determinant made from the occupied HF one-electron orbitals [6]. In general, an arbitrary N-electron wave function can be expressed as a linear combination of all possible N-electron Slater determinants formed from a complete set of spin orbitals $\chi_i(\mathbf{x})$. If the matrix mechanics problem of eq.(1.4) is solved in a complete basis of N-electron functions, all electronic eigenstates of the system are obtained. Therefore all eigenstates can be expressed as:

$$|\Psi^j\rangle = \sum_i C_i^j |\phi_i\rangle . \tag{1.15}$$

Here the upper index j indicates the order of the eigenstate. If there are M N-electron Slater determinants, the matrix $\mathbf{H}$ is constructed so that

$$H_{ij} = \langle \phi_i | \hat{H} | \phi_j \rangle \tag{1.16}$$

for $i, j = 1, 2, \ldots, M$. These matrix elements are constructed from the one- and two-electron integrals according to the Slater-Condon rules[6]. It is possible to write the N-electron basis functions ϕ_i as substitutions or excitations from the Hartree-Fock reference determinant ($|\phi_0\rangle$).

$$\begin{aligned} |\Psi\rangle = c_0 |\phi_0\rangle + \sum_{ar} c_a^r |\phi_a^r\rangle + \sum_{a<b, r<s} c_{ab}^{rs} |\phi_{ab}^{rs}\rangle \\ + \sum_{r<s<t, a<b<c} c_{abc}^{rst} |\phi_{abc}^{rst}\rangle + \ldots \end{aligned} \tag{1.17}$$

$|\phi_a^r\rangle$ stands for the Slater determinant where the a-th occupied spin-orbital is replaced by the empty spin-orbital r. Every N-electron Slater determinant can be described by the set of N occupied spin-orbitals from which it is formed. A graphical representation of different determinants together with their excitation based labelling is given by Fig. 2.1. The Hamiltonian matrix is a Hermitian matrix and expanded in a Slater determinant basis ordered by blocks corresponding to the different excitation levels of (eq. 1.17) the sparsity is revealed.

$$\mathbf{H} = \begin{bmatrix} \langle \phi_0 | \hat{H} | \phi_0 \rangle & 0 & \langle \phi_0 | \hat{H} | D \rangle & 0 & \ldots \\ 0 & \langle S | \hat{H} | S \rangle & \langle S | \hat{H} | D \rangle & \langle S | \hat{H} | T \rangle & \ldots \\ \langle D | \hat{H} | \phi_0 \rangle & \langle D | \hat{H} | S \rangle & \langle D | \hat{H} | D \rangle & \langle D | \hat{H} | T \rangle & \ldots \\ 0 & \langle T | \hat{H} | S \rangle & \langle T | \hat{H} | D \rangle & \langle T | \hat{H} | T \rangle & \ldots \\ \vdots & \vdots & \vdots & \vdots & \vdots \end{bmatrix} \tag{1.18}$$

Where the S, D and T stand respectively for all single, double and triple excited determinants. This sparsity can be exploited by using sparse matrix classes to construct the Hamiltonian matrix, which significantly reduces the necessary RAM-memory.

Another way of viewing the configuration interaction method is as the matrix mechanics solution of the time independent Schrödinger equation. One typically variationally optimizes the coefficients of eq. (1.17) to minimize the total energy:

$$E = \frac{\langle \Psi | \hat{H} | \Psi \rangle}{\langle \Psi | \Psi \rangle} \tag{1.19}$$

If the energy is variationally optimized in a basis of all possible Slater determinants for a given single-particle basis set, the procedure is called full-CI (FCI). When the basis set is complete, the method is called complete-CI. In practice however, complete-CI calculations are virtually never possible. A big advantage of CI methods is their generality, they can be applied to open-shell systems, to

systems far from their equilibrium geometries, and for excited states. This is in big contrast with traditional single-reference perturbation theory and coupled-cluster approaches [4] that generally assume that the reference configuration is dominant, and they fail considerably when this is not the case. However, FCI is intractable for all but the smallest systems, as the scaling is exponential (see eq. 1.12). For larger systems it becomes necessary to reduce the FCI space somehow, while retaining a desired accuracy. One of the most common approaches is the CISD method that includes only those determinants that can be mapped onto a reference determinant by single or double excitations. This reference determinant is mostly the Hartree-Fock determinant. This is a good approximation around equilibrium geometries because the dominant reference determinant includes already most of the dynamics of the total wave function, and through the Hamiltonian it can only interact with singly and doubly excited determinants, so including these determinants already accounts for the bulk of the correlation energy (typically around 95 %). The correlation energy is defined as the energy difference between the HF-wave function and the FCI wave function [11]

$$E_{FCI} - E_{HF} = E_{corr}, \tag{1.20}$$

for a complete basis set. HF treats the electron repulsion in an averaged way as it is essentially a mean-field method. The correlation energy is further divided in two parts, a part coming from the electron repulsion (the electrons trying to avoid each other) the so-called dynamic correlation, and a part that reflects the inadequacy of a single reference determinant when degeneracies arise, or rearrangements in partially filled shells called static correlation. When a bond is dissociated, the correlation energy typically increases gradually due to the fact that the static correlation increases faster than the dynamic correlation decreases. One can also truncate the wave function in (eq. 1.17) at higher excitation level. This creates the CISDT, CISDTQ, ... wave functions. Another approximation that is often used is to excite only from the valence electrons (frozen core CI), and/or excite only to the energetically lowest virtual orbitals.

1.3.1 Calculation of properties

It is of chemical interest to efficiently calculate observables and response properties from wave functions. This can be done easily for CI wave functions. All properties that can be represented as linear combinations of creation and annihilation operators that maximally change two electrons after acting on a Slater determinant, can be calculated by taking the trace with the two electron reduced density matrix (2RDM). The one and two electron reduced density matrices are compact representations of a wave function, which contain all the information necessary to calculate respectively the one and two electron properties of this wave function. They can be constructed from a wave function

by applying the following formulas.

$$\begin{aligned} \rho_{pq} &= \langle\Psi|\hat{E}_{pq}|\Psi\rangle & (1.21)\\ \Gamma_{pqrs} &= \langle\Psi|\hat{E}_{pq}\hat{E}_{rs} - \delta_{rq}\hat{E}_{ps}|\Psi\rangle = \langle\Psi|\hat{e}_{pqrs}|\Psi\rangle \\ &= \sum_{\sigma\tau}\langle\Psi|a^\dagger_{p\sigma}a^\dagger_{r\tau}a_{s\tau}a_{q\sigma}|\Psi\rangle, & (1.22)\end{aligned}$$

where the $\hat{E}_{pq} = a^\dagger_{p\alpha}a_{q\alpha} + a^\dagger_{p\beta}a_{q\beta}$ is the singlet excitation operator. The density matrices obey many permutational symmetries. An observable consisting of a constant, a one electron piece and a two electron piece (such as the Hamiltonian) can always be written as:

$$\hat{\Omega} = \sum_{pq}\Omega_{pq}\hat{E}_{pq} + \frac{1}{2}\sum_{pqrs}\Omega_{pqrs}\hat{e}_{pqrs} + \Omega_0 \tag{1.23}$$

The expectation value under the normalized wave function Ψ thus becomes:

$$\langle\Psi|\hat{\Omega}|\Psi\rangle = \sum_{pq}\Omega_{pq}\rho_{pq} + \frac{1}{2}\sum_{pqrs}\Omega_{pqrs}\Gamma_{pqrs} + \Omega_0 \tag{1.24}$$

The quantities $\omega_p = \rho_{pp}$ can be interpreted as the occupation number of a single orbital p, and the $\omega_{pq} = \Gamma_{ppqq}$ are interpreted as the simultaneous (pair) occupations of two orbitals. Those orbital occupation numbers are restricted to the following intervals:

$$\begin{aligned} 0 &\leq \omega_p \leq 2 & (1.25)\\ 0 &\leq \omega_{pq} \leq 2(2-\delta_{pq}) & (1.26)\end{aligned}$$

Furthermore the sum of the diagonal elements of the first order reduced density matrix is equal to the total number of electrons in the system under consideration, and the sum of the diagonal elements of the second order reduced density matrix is equal to the number of pairs $\frac{N(N-1)}{2}$. A particularly useful set of occupation numbers is obtained by diagonalizing the one-electron density matrix with a unitary matrix:

$$\rho = \mathbf{U}\eta\mathbf{U}^\dagger \tag{1.27}$$

The eigenvalues η_p are the so-called natural-orbital occupation numbers and the eigenvectors of ρ (columns of $\mathbf{U}$) are the natural orbitals of the system. The eigenvalues of the density matrices have straightforward interpretations as orbital occupation numbers.

1.3.2 The size extensivity problem

The size extensivity of a quantum chemical method guarantees that the calculated energy scales linearly with the system size. The term “size consistency

error“ is used for the differences that arise for a system consisting of isolated parts and the sum of the treatments of the parts. This happens when subsystems are separated to a large distance (e.g. for bond breaking[12]). A physical wave function Ψ_{ab} that consists of two isolated fragments a and b can be written as a direct product of the wave functions of the fragments.

$$|\Psi_{ab}\rangle = |\Psi_a\rangle \otimes |\Psi_b\rangle \tag{1.28}$$

The Hamiltonian $\hat{H}_{ab} = \hat{H}_a + \hat{H}_b$ is the sum of those fragments because all coupling terms are zero due to the fact that there is no interaction between the fragments. Acting with the above product wave function on the Hamiltonian gives $E_{ab} = E_a + E_b$. Size consistency implies the correct description of the dissociation products. For example restricted HF is size extensive but not size consistent. Most truncated CI methods are not size extensive, which leads to large errors for dissociation problems and chemical reactions. This is one of the main reasons CISD became less popular after the discovery of this error by Pople in 1973 [13], as its accuracy degrades with increasing system size. The deficiencies of truncated excitation based CI can be linked to product terms in the CI projection equations that correspond to unlinked diagrams in the diagrammatic expansion of the theory. In contrast, coupled-cluster methods are always size extensive because their excitation operator is an exponential operator[4], but coupled cluster methods have the disadvantage that they are not variational, and they are less straightforwardly adapted to multi-reference problems[4]. There even exists a contested conjecture that states that there are no tractable approximate methods that are both variational and size-consistent [14]. However, the size-extensivity error decreases rapidly with increasing size of the CI expansion. Another way of reducing the size-extensivity error is using multiple reference determinants to excite from, leading to multi-reference CI [4]. A third way of reducing the size-extensivity error consists of adding correction terms. The best known correction term is the Langhoff-Davidson correction [15], which accounts for the correlation effects of unlinked quadruple excitations, which is a major part of the size-extensivity error of CID, and CISD. The correction term is given by:

$$\Delta E_{LD} = (E_{CISD} - E_{HF})\,(1 - c_0^2), \tag{1.29}$$

where c_0 is the coefficient of the HF determinant in the expansion. Another interesting view to the size extensivity problem is the one from Duch and Diercksen [16]. They pointed out that quantum mechanics is a holistic theory and therefore fails to provide a well-defined way of describing subsystems. Taking this into account, they stated that size consistency is not the most important property of a quantum chemical method. Methods can be valuable as long as one properly accounts for the size-consistency error, and the dissociation process is correctly described. Another key issue of approximate CI methods is their convergence to the FCI-limit upon which will be expanded in the next section.

1.3.3 Convergence rates

The orbitals occupied in the reference Slater determinant are called internal orbitals. Those that substitute the internal orbitals in the CI expansion are called external orbitals[12]. The HF canonical orbitals, natural orbitals, Brueckner orbitals, localized orbitals are typically used as internal orbitals. The external orbitals are mostly the virtual orbitals of a HF calculation or any type of improved virtual orbitals [12]. In 1955, Löwdin introduced the natural orbitals (NO's) [17] which helped to analyze and understand the wave function of a CI calculation. NO's are obtained by diagonalizing the one-electron density matrix of the CI wave function, as explained in section 1.3.1. Löwdin showed that using the NO's led to the most rapid convergence of the CI expansion by effectively reducing the number of configurations to obtain the FCI energy. The problem is that one needs first the FCI wave function to calculate the first order reduced density matrix, so this is not practically useful. Bender and Davidson [18] solved this problem by introducing in 1966 the iterative natural orbital (INO) method. They were able to exploit the advantageous properties of the natural orbitals without constructing the first order reduced density matrix of the FCI wave function. This was done by first calculating an approximative truncated CI wave function of which the occupation numbers were analyzed to reduce the number of unimportant configurations, and adding new more important configurations. This procedure was repeated until convergence, which arose when the CI expansion did not change anymore (mostly four or five cycles). In this way they were able to obtain 89 % of the correlation energy of LiH with only 45 configurations. The NO approach made an important contribution to the development of more efficient CI methods. However, it became clear that using NO's only pays off for a relatively small amount of configurations. For more configurations, in the order of millions, they became less useful. In modern quantum chemistry packages they are used indirectly to setup basis sets for CI calculations, because they improve the convergence to the basis set limit. This is done by calculating generally contracted Gaussian basis sets from the atomic natural orbitals extracted from CISD calculations on atoms [19].

In the next chapter a global convergence approach to the FCI wave function that does not depend on a reference determinant is discussed. This convergence criterion is based on the seniority number. Here seniority means the number of spatial single-particle orbitals occupied by a single electron. Truncating CI expansions based on the seniority number converges faster to the FCI energy than the excitation based hierarchy in NO when static correlation is prevalent. Furthermore the generation and effects are discussed of the recently introduced [20–23] seniority minimizing single-particle basis. This basis exploits maximally the rapid convergence of the seniority number hierarchy for systems with a considerable amount of static correlation.

Chapter 2

Seniority hierarchy

From a historical point of view, configuration interaction theory is mostly thought of as sequentially adding more and more one-electron excitations, based on a reference determinant or on a set of reference determinants (MRCI) [4] (see chapter: 1). FCI aside, this implies an explicit distinction between occupied and virtual spaces. However, for strongly correlated systems, and systems where no dominant determinant exists, a significant amount of correlation is missed when this distinction is made. The need for a global criterion thus arises. In most physical systems electrons tend to pair. This makes it physically interesting to answer the question: "What happens when we group the determinants according to the number of paired electrons?". In this chapter we try to answer this question for configuration interaction theory, by means of a partitioning of the FCI wave function using the seniority quantum number, which is a measure of the number of unpaired electrons. This will lead to a sequential approach to the FCI wave function based on a global criterion, the seniority number. Furthermore, it will be shown that, for some cases, the seniority hierarchy converges quicker to the FCI limit then a hierarchy based on natural orbitals. The weight of the rapidly converging Hilbert subspaces diminishes quickly for higher seniority blocks, and only retaining the lowest seniority blocks provides already a good approximation to the static correlation present in the FCI wave function[20–22, 24].

It is well known that only the FCI wave function is invariant under any unitary transformation of the single-particle orbitals. To avoid any confusion in the following chapters, the used non-orthogonal basis functions such as STO-3G, 6-31G, ... will be referred to as the used basis set and the orthonormal orbitals used to generate the wave function such as molecular orbitals coming from a restricted Hartree-Fock calculation (MO), the natural orbitals of the FCI wave function (FNO), seniority minimizing orbitals of the FCI wave function (Mmin), ... are refered to as the used basis. This basis dependency of truncated CI methods is a serious extra complication for wave functions constructed

based on the seniority hierarchy. For one electron excitation based methods very good single-particle bases are already available such as the Hartree-Fock single-particle basis or the natural orbitals of a multi-determinant calculation. Another issue that will be shown to play an important role for the seniority based hierarchy is spatial point-group symmetry (see chapter 3). Breaking the spatial point-group symmetry of the orbitals will have a big impact on the energy and the convergence of the seniority hierarchy [24]. Another important point is that any wave function based method can take advantage of the seniority concept introduced in this chapter. In fact, other ab initio approaches also benefited recently from the seniority number approach such as the projected Schrödinger equation approach [25–27] and the coupled cluster approach[28, 29]. Furthermore the seniority number concept is closely related to the one of particle pairing, which has deep roots in condensed matter and nuclear physics, where it is used for the description of superconductivity, superfluidity, pairing of nucleons and other exotic quantum phenomena that depend on strong electron correlation. In the second part of this thesis some of these techniques are discussed and applied to selected problems.

2.1 The seniority number

The seniority number operator $\hat{\Omega}$ is defined as:

$$\hat{\Omega} = \sum_{i,\sigma} a^\dagger_{i\sigma} a_{i\sigma} - \sum_{i\sigma_1\sigma_2} a^\dagger_{i\sigma_1} a^\dagger_{i\sigma_2} a_{i\sigma_2} a_{i\sigma_1} \tag{2.1}$$

Expressed in a spin-free formulation this becomes:

$$\hat{\Omega} = \sum_{i} \hat{E}_{ii} - \hat{e}_{iiii}, \tag{2.2}$$

where $\hat{E}_{ii}$ the usual singlet excitation operator (see section 1.3.1) and $\hat{e}_{pqrs} = \hat{E}_{pq}\hat{E}_{rs} - \delta_{rq}\hat{E}_{ps}$ is the second-order replacement operator. If a chosen orbital contains one and only one electron, it contributes one to the seniority expectation value, otherwise it contributes zero. The total seniority for a single Slater determinant can be calculated as the sum of the seniorities of the single-particle orbitals. Seniority can therefore be seen as a representation of an SU(2) algebra and is often thought of as quasi-spin[30]. The expectation value of the seniority operator of a Slater determinant is thus equal to the difference of the number of electrons N with the number of electrons in doubly occupied orbitals in that determinant, which is equal to the number of unpaired electrons in the Slater determinant. Fig. 2.1 illustrates the seniority number concept for a number of Slater determinants with 3 up and 3 down electrons in 6 orbitals. The number of particle hole excitations, necessary to generate the Slater determinants from the reference determinant, is also given to compare the seniority number labeling with the excitation based one. The reference determinant is the one with the three energetically lowest single-particle orbitals doubly occupied. The

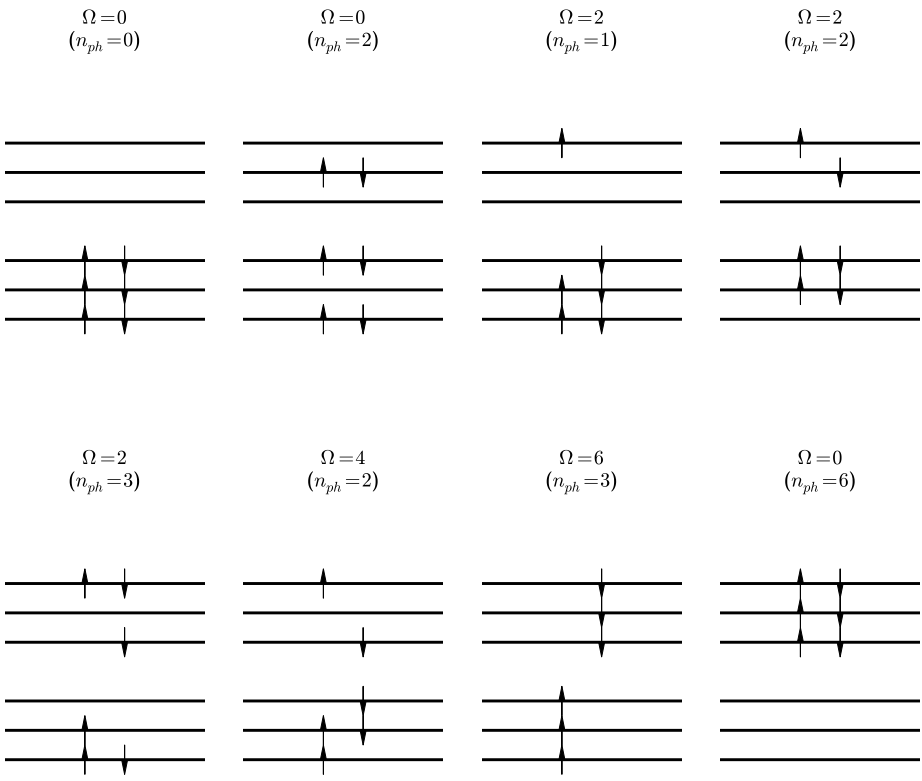

Figure 2.1: Examples of Slater determinants with 3 up and 3 down electrons in 6 single-particle levels that belong to different parts of the excitation and seniority partitioning of the wave function. Ω stands for the seniority number of the determinant and n_{ph} stands for the number of particle hole excitations with respect to the RHF reference determinant.

extension to general multiconfigurational wave functions is straightforward as the weighted sum of the seniority number of all determinants in the expansion of the wave function,

$$\begin{aligned} \Omega = \langle \hat{\Omega} \rangle_\Psi &= \langle \Psi | \hat{\Omega} | \Psi \rangle \\ &= \sum_i \rho_{ii} - 2 \sum_i \Gamma_{iiii} \\ &= N - 2 \sum_i \Gamma_{iiii}. \end{aligned} \tag{2.3}$$

Here, the ρ_{ii}, and Γ_{iiii} are elements of the spin-free first and second order reduced density matrices (see eq. (1.21) and (1.22)), corresponding to Ψ. N is the number of electrons in the wave function. It can be straightforwardly checked that the seniority number operator does not commute with the electronic Hamiltonian eq.(1.8). The seniority number is thus not a good quantum number for electronic wave functions. This is mainly due to the second term in eq. (2.3) as the particle number operator commutes with the electronic Hamiltonian, and is a constant for a given wave function, independent of the single-particle basis used. The second term $2\sum_i \Gamma_{iiii}$ does not commute with $\hat{H}$ and depends on the used single-particle basis, a basis transformation changes its value. Therefore the seniority number also depends on the used single-particle basis. Maximizing the second term in eq.(2.3) by an appropriate unitary transformation will minimize the seniority number of the wave function. This will be exploited in section 2.4, where some algorithms are discussed to minimize the seniority number.

Fortunately there are operators that do commute with the seniority number operator, and also with the electronic Hamiltonian such as the $\hat{S}^2$ (spin-squared operator), and $\hat{S}_z$ (projected spin-operator)[4].

$$\hat{S}_+ = \sum_p a^\dagger_{p\alpha} a_{p\beta} \tag{2.4}$$

$$\hat{S}_- = \sum_p a^\dagger_{p\beta} a_{p\alpha} \tag{2.5}$$

$$\hat{S}_z = \frac{1}{2}\sum_p (a^\dagger_{p\alpha} a_{p\alpha} - a^\dagger_{p\beta} a_{p\beta}) \tag{2.6}$$

$$\hat{S}^2 = \hat{S}_-\hat{S}_+ + \hat{S}_z(\hat{S}_z + 1) \tag{2.7}$$

Their quantum numbers can be used to label the exact eigenstates of the electronic Hamiltonian. Furthermore, linear combination of degenerate spin eigenstates can be used to construct states with distinct seniority numbers. Alternatively, one can also create linear combinations of states corresponding to the same seniority eigenvalues to generate distinct eigenstates of the $\hat{S}^2$ and $\hat{S}_z$ operator. This can be easily seen by noting that the seniority operator can be expressed in a spin-free formulation eq.(2.2), and recalling the fact that singlet-operators commute with both spin-operators.

$$\left[\hat{S}^2, \hat{\Omega}\right] = 0, \tag{2.8}$$

$$\left[\hat{S}_z, \hat{\Omega}\right] = 0. \tag{2.9}$$

Unfortunately the electronic Hamiltonian does not commute with the seniority number, but many model Hamiltonians exist that have seniority as an exact quantum number. Those Hamiltonians are mainly used in condensed matter and nuclear physics. An example is the Reduced BCS Hamiltonian (also known

as the picket-fence Hamiltonian):

$$\hat{H} = \sum_{j\sigma} \epsilon_j a^\dagger_{j\sigma} a_{j\sigma} + g \sum_{ij} a^\dagger_{i\alpha} a^\dagger_{i\beta} a_{j\beta} a_{j\alpha} \tag{2.10}$$

This Hamiltonian captures the essential physics of singlet pairing between fermions. It is also a member of an entire class of exactly solvable models, and exact solution methods that scale linearly with the system size are available for it using Bethe ansatz techniques (see Part II, Chapter: 6). Although this Hamiltonian is a drastic approximation to the electronic structure Hamiltonian, in the 2nd part of this thesis results are presented of approximations to the full electronic Hamiltonian by wave functions that are variational solutions of the picket-fence model.

By selecting all determinants corresponding to a given seniority number or a set of seniority numbers, it is possible to build new wave functions based on the seniority quantum number. As an example all seniority zero determinants describe the $\Omega = 0$ sector of the Hilbert space which incorporates all paired excitations, and is equal to the doubly occupied configuration interaction (DOCI) wave function[31]. DOCI wave functions are already extensively studied and their value for chemical purposes lies in its connections with Geminal-based theories for chemical bonding[32]. From a FCI point of view, DOCI is a singlet wave function that is able to describe any possible pairing structure of the chemical bond. As a matter of fact, recent calculations[24] have established that DOCI wave functions are perfectly suited to capture the static correlation associated to chemical bonds. Furthermore, DOCI wave functions are size consistent. The DOCI wave function can also be written as:

$$|\Psi_{\text{DOCI}}\rangle = \sum_{j=1}^{\binom{K}{\frac{N}{2}}} c_j \prod_{i=1}^{\frac{N}{2}} S^\dagger_{\mathbf{j}(i)} |\theta\rangle \tag{2.11}$$

where $|\theta\rangle$ is the pair vacuum, and $S^\dagger_i = a^\dagger_{i\alpha} a^\dagger_{i\beta}$ is the pair creation operator of the i-th orbital. $\mathbf{j}$ is a vector that maps the $\frac{N}{2}$ pairs to a selected set of occupied orbitals of the K spatial single-particle orbitals. Recently a seniority zero based perturbation theory was introduced [33], by means of pair-orbital energies, which are analogous to the known orbital energies (eigenvalues of the Fock matrix) [6].

$$\epsilon_i = f_i + f_{\bar{i}} - V_{i\bar{i}i\bar{i}} \tag{2.12}$$

$$\epsilon_a = f_a + f_{\bar{a}} + V_{a\bar{a}a\bar{a}}. \tag{2.13}$$

The i index stands for occupied orbitals of a reference determinant, and a for a virtual orbital. The f_i are the diagonal elements of the Fock matrix. They can also be seen in the context of double ionization potentials (ϵ_i) or double electron affinities (ϵ_a). This approach suffers less from intruder states, through the extra V terms in comparison with conventional Møller-Plesset or Epstein-Nesbet perturbation theory[6].

The seniority two determinants span the $\Omega = 2$ sector. This sector represents all paired excitations plus one broken pair. The seniority four determinants span the $\Omega = 4$ sector, which represents all paired excitations plus two broken pairs and so on for the seniority 6, 8, ... sectors. Besides constructing wave functions based only on one seniority sector one can also combine them. This generates wave functions consisting of all $\Omega = 0, 2$, $\Omega = 0, 2, 4, \ldots$ determinants. When all seniority sectors are used one has the entire full CI Hilbert space. This makes it possible to investigate the convergence of the seniority hierarchy to the full CI solution in a given basis set. The minimum seniority value for a sector of the electronic Hilbert space with spin-projected value $\langle \hat{S}_Z \rangle = s_z$ is $\Omega_{min} = 2s_z$, and the maximum value depends on whether the number of orbitals K is larger than the total amount of electrons N. If this is the case then $\Omega_{max} = N$ otherwise $\Omega_{max} = 2K - N$. Potential energy curves of wave functions constructed by selecting determinants according to their seniority number, together with a study of the convergence rate is given in section 2.5. But first the special case of the two electron problem is discussed in the next section.

2.2 Two electron problem

For all two-electron problems the DOCI wave function with optimized orbitals is equal to the exact singlet wave function. This implies that the minimal seniority of the exact singlet wave function is zero, and the seniority minimized orbitals (see section 2.4) are equal to the orbitals that minimize the energy of the DOCI wave function. This can be seen by expanding the exact two electron wave function in a Slater determinant basis:

$$\Psi = \sum_{i,j} c_{i,j} a^\dagger_{i\alpha} a^\dagger_{j\beta} |\theta\rangle \tag{2.14}$$

It is now possible to diagonalize the symmetric matrix $C = UDU^\dagger$ and express the exact wave function in this basis as:

$$\Psi = \sum_{i} d_i b^\dagger_{i\alpha} b^\dagger_{i\beta} |\theta\rangle \tag{2.15}$$

Where the new creation operators are expressed as linear combinations of the old according to the columns of the unitary transformation U that diagonalize the coefficient matrix of the exact wave function: $b^\dagger_{i\alpha} = \sum a^\dagger_{j\alpha} U_{ji}$. This boils down to the fact that one can rotate the orbitals in such a way that the seniority two determinants no longer contribute to the exact wave function, which implies that the DOCI wave function is invariant to the addition of single excitations from all the DOCI determinants. It is important to emphasize the fact that the subspace spanned by determinants of a given seniority depends strongly on orbital rotations. In the next section formulas for the dimensions of the seniority spaces are derived.

2.3 Dimensions of the seniority spaces

In this section formulas are derived for the sizes of the seniority Hilbert spaces from which the full CI Hilbert space can be built [24]. As previously mentioned, the size of the FCI space is: $\mathrm{Dim}(K,\ N_\alpha\ ,\ N_\beta) = \binom{K}{N_\alpha}\ \binom{K}{N_\beta}$ for a system with K spatial single-particle orbitals, and N_α up- and N_β down-electrons. It is assumed in the following that $N_\alpha = N_\beta = \frac{N}{2} = M$. The dimension corresponding to a space with seniority $\Omega = 2z$, with z equal to the number of unpaired α electrons, can be calculated by constructing determinants with seniority $2z$ stepwise, adding first the α electrons and then the β electrons. One can generate $\binom{K}{M}$ determinants with M α electrons spread over K orbitals. To add the β electrons one should take into account the desired seniority of $2z$ which can be created by selecting z unpaired α electrons. This can be done in $\binom{M}{z}$ ways for each of the α determinants. Now the position of $(M-z)$ β electrons is already fixed as they need to form pairs with the $(M-z)$ paired α electrons. What is left is to put the remaining z unpaired β electrons in the remaining $(K-M)$ orbitals. This can be done in $\binom{K-M}{z}$ ways. The total number of determinants corresponding to a sector with seniority $2z$ is thus:

$$\mathrm{Dim}_{(\Omega=2z)} = \binom{K}{M}\binom{M}{z}\binom{K-M}{z} \tag{2.16}$$

The above formula can be generalized for the case that N_α is not equal to N_β. The number of α electrons is then equal to $N_\alpha = M + s_z$ and the number of β electrons is equal to $N_\beta = M - s_z$. The above formula thus generalizes to:

$$\mathrm{Dim}_{(\Omega=2(z-s_z))} = \binom{K}{M+s_z}\binom{M+s_z}{z+s_z}\binom{K-(M+s_z)}{z-s_z} \tag{2.17}$$

To obtain the dimension that all combined seniority spaces span, one must sum over z.

$$\mathrm{Dim}_{(All\ \Omega)} = \sum_{z=0}^{M}\binom{K}{M}\binom{M}{z}\binom{K-M}{z} \tag{2.18}$$

This can be simplified by Vandermonde's identity:

$$\sum_{z=0}^{r}\binom{K-M}{z}\binom{M}{r-z} = \binom{K}{r}, \tag{2.19}$$

where r can be any number positive integer larger than 0. If we use the special case $r = M$ and the identity $\binom{M}{M-z} = \binom{M}{z}$, one sees that $\mathrm{Dim}_{(All\ \Omega)} = \binom{K}{M}\binom{K}{M} = \mathrm{Dim}_{(FCI)}$.

2.4 Minimization of the seniority number

Truncated configuration interaction wave functions based on the expectation value of the seniority number operator depend strongly on the single-particle

basis used. This makes it of great interest to find a single-particle basis that gives maximal weight to low seniority determinants. A good candidate for this is the seniority minimized basis of a well chosen wave function that contains determinants with higher seniorities. Ideally, this is the FCI wave function, but this wave function can only be used for proof of principle calculations and benchmarking. Therefore it is also of interest to determine how the seniority minimized basis of wave functions such as the CISD wave function behave for DOCI and other low seniority wave functions. The algorithm used revolves around the lemma[34] that given an invertible matrix $\mathbf{R}$ the function $\mathrm{f}(\mathbf{U}) = \mathrm{Tr}(\mathbf{RU})$ has exactly one local (and global) maximum if $\mathbf{U}$ is special orthogonal ($\mathbf{UU^T} = 1$ and $\det(\mathbf{U}) = 1$), with the global maximum given by

$$\mathbf{U} = \mathbf{R}(\mathbf{R}^\dagger\mathbf{R})^{-\frac{1}{2}}. \tag{2.20}$$

The second part of eq.(2.20) is guaranteed to be unitary because of the polar decomposition of a square complex matrix[35]. As the first term in the definition of the seniority number operator (eq. (2.1)) is independent of a unitary transformation of the single-particle basis, it is possible to minimize the seniority of a wave function by maximizing the second part,

$$\xi(\phi_1, \ldots, \phi_M) = \sum_i^M \Gamma_{iiii}. \tag{2.21}$$

Here, the diagonal elements of the second order reduced density matrix explicitly depend on the used single-particle orbitals. A favorable point for the seniority minimization scheme is that a fast iterative procedure exists for this minimization [34]. This can be further accelerated by applying a direct inversion of the iterative subspace (DIIS) accelerator. If a start basis of m orthonormal occupied molecular orbitals is denoted as $\{\phi_i^0\}_{i=1}^m$, which are most often orbitals coming from a restricted Hartree-Fock calculation or Löwdin orthonormalized atomic orbitals, the orbital dependent part of the seniority can be written as a function of an orthogonal matrix:

$$\xi(\mathbf{U}) = \sum_{ijklr} U_{ji}U_{ki}U_{li}U_{ri}\Gamma^0_{jklr}, \tag{2.22}$$

where the second order reduced density matrix is expressed in the start orthonormal basis $\{\phi_i^0\}_{i=1}^m$. The seniority of the wave function is now minimized, when the $\mathbf{U} \in SO(m)$ is found that maximizes eq.(2.22). The seniority minimizing orbitals are then given by:

$$\phi_i^* = \sum_j \phi_j^0 U_{ji}^{max} \tag{2.23}$$

To do this we parametrize the $SO(K)$ group by its antisymmetric generators Δ.

$$\mathbf{U} = e^{\Delta}. \tag{2.24}$$

Differentiating eq.(2.22) with respect to Δ_{ab} we find.

$$\frac{\partial \xi}{\partial \Delta_{ab}}|_{\Delta=0} = \sum_{ijklr} 4(\delta_{ja}\delta_{ib} - \delta_{jb}\delta_{ia})\delta_{ik}\delta_{li}\delta_{ri}\Gamma_{jklr} \tag{2.25}$$

$$= 4(\Gamma_{abbb} - \Gamma_{baaa}) \tag{2.26}$$

The stationary points of ξ thus correspond to those orthonormal orbitals for which the matrix $R_{ij} = \Gamma_{ijjj}$ is symmetric.

Unfortunately it is not possible to analytically maximize eq.(2.22). This can be circumvented by introducing an alternative function with the same first order derivatives.

$$\eta(\mathbf{U}) = \sum_{ij} U_{ji}\Gamma_{jiii} = \sum_{ij} R_{ji}U_{ji} = \mathrm{Tr}(\mathbf{R}^T\mathbf{U}) \tag{2.27}$$

The above mentioned lemma (see eq.(2.20)) now guarantees that eq.(2.27) has a unique global maximum at $\mathbf{U} = \mathbf{R}(\mathbf{R}^\dagger\mathbf{R})^{\frac{-1}{2}}$. Both functions have the same stationary points, but the loss of control over the higher derivatives makes it impossible to guarantee a maximization instead of a minimization. However by making use of the proportionality of both equations one can deduce that:

$$\xi(\mathbf{U}) = \xi(\mathbf{Id} + \mathbf{\Delta}) \tag{2.28}$$

$$= \xi(\mathbf{Id}) + \sum_{i<j} \frac{\partial \xi}{\partial \Delta_{ij}}|_{\Delta=0} \cdot \Delta_{ij} \tag{2.29}$$

$$= \xi(\mathbf{Id}) + \sum_{i<j} 4\frac{\partial \eta}{\partial \Delta_{ij}}|_{\Delta=0} \cdot \Delta_{ij} \tag{2.30}$$

$$\approx \xi(\mathbf{Id}) + 4\delta\eta \tag{2.31}$$

In each step $\delta\eta > 0$, which implies that if the starting orbitals are chosen close enough to the seniority minimizing orbitals such that the step sizes are small ξ increases with each step. However, one has to be cautious because ξ and η have different second and higher derivatives. Thus it can occur that when the iterative steps are to large that ξ decreases.

A summary of the iterative scheme thus boils down to the following steps:

1. Start with a set of orthonormal orbitals, e.g. the RHF molecular orbitals.
2. For $k \geq 0$ (k indicates the number of cycles) determine the 2-RDM (Γ) for which we want to minimise the seniority number.
3. Construct the matrix $R^{(k)}_{ji} = \Gamma^{(k)}_{ji,ii}$
4. Construct the unitary transformation $U^{(k+1)} = R^{(k)}\left[\left(R^{(k)}\right)^\dagger R^{(k)}\right]^{-\frac{1}{2}}$.
5. Transform the current orbitals to the new basis with the unitary matrix $U^{(k+1)}$.

6. Set $k = k+1$, repeat steps 2-6 until $R^{(k)}$ is sufficiently close to a symmetric matrix and the process has converged.

The total transformation from the start orbitals to the final seniority minimizing orbitals is thus given by:

$$\mathbf{D}^{(k+1)} = \mathbf{D}^{(k)} \cdot \mathbf{U}^{(k+1)} = \mathbf{U}^{(1)} \cdot \mathbf{U}^{(2)} \dots \mathbf{U}^{(k)} \cdot \mathbf{U}^{(k+1)} \tag{2.32}$$

When the iteration converges we must have:

$$\lim_{k\to\infty} U^{(k)} = \lim_{k\to\infty} \mathbf{R}^{(k)} (\mathbf{R}^{\dagger(k)} \mathbf{R}^{(k)})^{\frac{-1}{2}} = \mathbf{Id} \tag{2.33}$$

which implies that $\mathbf{R} = \mathbf{R}^{\dagger}$. In the remainder of this thesis, the orbitals produced by minimizing the seniority number of a FCI wave function are denoted by the labels Mmin and Mmin-c1, depending respectively on whether only rotations between orbitals of the same irreducible representation of the spatial point-group are considered or symmetry breaking is allowed. If the seniority number is minimized using a wave function other than FCI, a subscript is added to denote the wave function used (e.g. $\text{Mmin}_{\text{CISD}}$).

2.4.1 Acceleration with the direct inverse of the iterative subspace (DIIS)

It is possible to speed up the algorithm above by introducing a direct inverse of the iterative subspace (DIIS) method [36, 37]. These algorithms are prevalent in SCF theory[4]. In this case it is our goal to search for orthogonal MxM matrices ($\mathbf{D}$) for which the corresponding $\mathbf{R}$ matrices are symmetric.

The error matrix for this problem is defined as the lack of symmetry of $\mathbf{R}(\mathbf{D})$.

$$E_{ij}(\mathbf{D}) = R_{ij}(\mathbf{D}) - R_{ji}(\mathbf{D}) \tag{2.34}$$

The assumption of DIIS-algorithms is that for small changes in $\mathbf{D}$, the changes in the error matrix are linear. The algorithm boils down to the following iterative cycle.

1. Start with a set of orthonormal orbitals, e.g. the RHF molecular orbitals.

2. For $k \geq 0$ (k indicates the number of cycles) determine the 2-RDM (Γ), calculate $R_{ij}^{(k)}$ and the error matrix $E_{ij}^{(k)} = R_{ij}^{(k)} - R_{ji}^{(k)}$.

3. Construct the DIIS $\mathbf{B}$-matrix for $1 \leq i, j \leq k$: $B_{ij} = \langle E^{(i)} | E^{(j)} \rangle = \sum_{r,s} = E_{rs}^{(i)} E_{rs}^{(j)}$

4. Set up the standard DIIS equations and solve for the coefficients c_i:

$$\begin{pmatrix} B_{11} & B_{12} & \dots & B_{1k} & -1 \\ B_{21} & B_{22} & \dots & B_{2k} & -1 \\ \vdots & \vdots & \ddots & \vdots & -1 \\ B_{k1} & B_{k2} & \dots & B_{kk} & -1 \\ -1 & -1 & \dots & -1 & 0 \end{pmatrix} \begin{pmatrix} c_1 \\ c_2 \\ \dots \\ c_k \\ \lambda \end{pmatrix} = \begin{pmatrix} 0 \\ 0 \\ \dots \\ 0 \\ -1 \end{pmatrix} \tag{2.35}$$

   The Lagrange multiplier λ makes sure that the coefficients c_i add to one.

5. Construct the extrapolated matrix $\mathbf{C}^{(k+1)} = \sum_{a=1}^{k} c_a \mathbf{D}^{(a)}$.

6. At the extrapolated $\mathbf{C}^{(k+1)}$ construct an extrapolated $\mathbf{R}$, by noting that to first order around the identity:

$$\tilde{R}_{ij}^{(k+1)} = \sum_{a=1}^{k} c_a R_{ji}^{(a)} \tag{2.36}$$

7. Perform a generalized η step that rotates the non-orthogonal orbitals back to orthogonal orbitals while minimizing the seniority. More precisely, construct:

$$\tilde{\mathbf{V}}^{(k+1)} = (\tilde{\mathbf{S}}^{(k+1)})^{-1} \tilde{\mathbf{R}}^{(k+1)} ((\tilde{\mathbf{R}}^{(k+1)})^T (\tilde{\mathbf{S}}^{(k+1)})^{-1} \tilde{\mathbf{R}}^{(k+1)})^{\frac{-1}{2}}. \tag{2.37}$$

   Then $\mathbf{D}^{(k+1)} = \mathbf{C}^{(k+1)} \tilde{\mathbf{V}}^{(k+1)}$, with the new improved orbitals $\phi_i^{(k+1)} = \sum_j \phi_j^{(0)} D_{ji}^{(k+1)}$.

8. Set $k = k+1$, repeat steps 2-7 until $R^{(k)}$ is sufficiently close to a symmetric matrix and the error matrix is close to zero.

However by constructing the transformation $\mathbf{C}^{(k+1)}$ by extrapolation, an extra complication arises: the intermediate orbitals $\tilde{\phi}$ obtained by the transformation $\mathbf{C}^{(k+1)}$ are non-orthogonal. The generalized η step then minimizes the seniority while acknowledging the fact that the starting orbitals ($\tilde{\phi}$) are not orthonormal, but have overlap matrix $\tilde{\mathbf{S}}$. One can understand the generalized η step by the following arguments. Given the non-orthogonal set of orbitals $\tilde{\phi}_i$, the orthonormal orbitals $\phi_i = \sum_j \tilde{\phi}_j V_{ji}$ that maximize the η function:

$$\eta \mathbf{V} = \sum_i \tilde{\Gamma}_{iiii} = \sum_{ij} V_{ji} \tilde{\Gamma}_{jiii} \tag{2.38}$$

It is possible to enforce orthogonality by writing: $\mathbf{V} = \mathbf{S}^{\frac{-1}{2}} \mathbf{U}$ for $\mathbf{U}$ orthogonal. Therefore the above equation can be written as:

$$\eta(\mathbf{U}) = \sum_{ijk} S_{jk}^{\frac{-1}{2}} U_{ki} \tilde{\Gamma}_{jiii} = \mathrm{Tr}(\mathbf{R}^T \mathbf{S}^{\frac{-1}{2}} \mathbf{U}) \tag{2.39}$$

Application of lemma eq.(2.20) shows that η is maximized for $\mathbf{U} = \mathbf{S}^{\frac{-1}{2}}\mathbf{R}(\mathbf{R}^T\mathbf{S}^{-1}\mathbf{R})^{\frac{-1}{2}}$, which gives the total generalized η transformation: $\mathbf{V} = \mathbf{S}^{-1}\mathbf{R}(\mathbf{R}^T\mathbf{S}^{-1}\mathbf{R})^{\frac{-1}{2}}$.

The DIIS procedure is significantly faster than the previous procedure, but extra caution is required because a good guess is necessary before the DIIS can be used. This is because by constructing the $\tilde{\mathbf{R}}$ matrices an extra approximation is made. The implementation used to generate the results presented in this thesis, starts with a number of normal minimization steps and if a given accuracy is obtained the DIIS kicks in. This significantly speeds up the final iterations. This is important because experimentally it was observed that very small reductions of the seniority, could have an impact on the DOCI energy that is several orders of magnitude larger. Therefore very good convergence of the minimal seniority is required typically up to 1e-8.

In the following section the convergence of the seniority based hierarchy to the FCI limit is investigated for a number of different single-particle bases including the seniority minimized basis. Furthermore the contribution of different seniority blocks to the FCI wave function are compared. Potential energy surfaces of wave functions constructed by selecting different seniority parts of the Hilbert space of some selected molecules are also analyzed and depicted. Seniority minimized orbitals are also compared with the natural orbitals and the canonical molecular orbitals.

2.5 Results of convergence and energy properties

In this section, the results are represented of selected calculations on a test set consisting of atoms and small molecules. In some cases the seniority results are compared with those obtained with the standard excitation based hierarchy. All configuration interaction calculations presented in this thesis are done with CIFlow, a flexible and general configuration interaction solver developed at the UGent, see appendix B for more details. The one and two electron integrals are obtained from the Psi4 package [38], or by using an in house developed Obara-Saika integrator, and to read those integrals into memory the Hamiltonian class of CheMPS2 is used [39, 40].

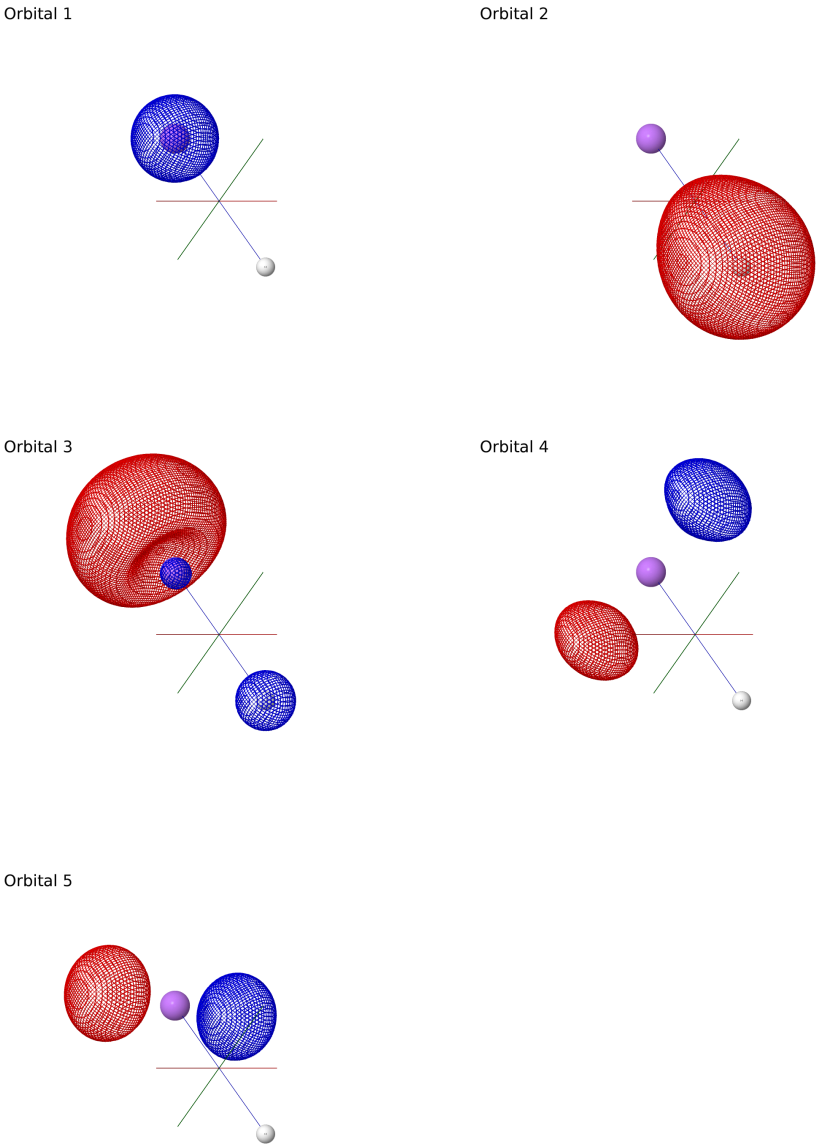

Figure 2.2: The first 5 MO orbitals according to a restricted Hartree-Fock calculation for the LiH(R_{st}) molecule with the 6-31G basis set, with R_{st} equal to two times the experimental geometry. The colors indicate the relative sign.

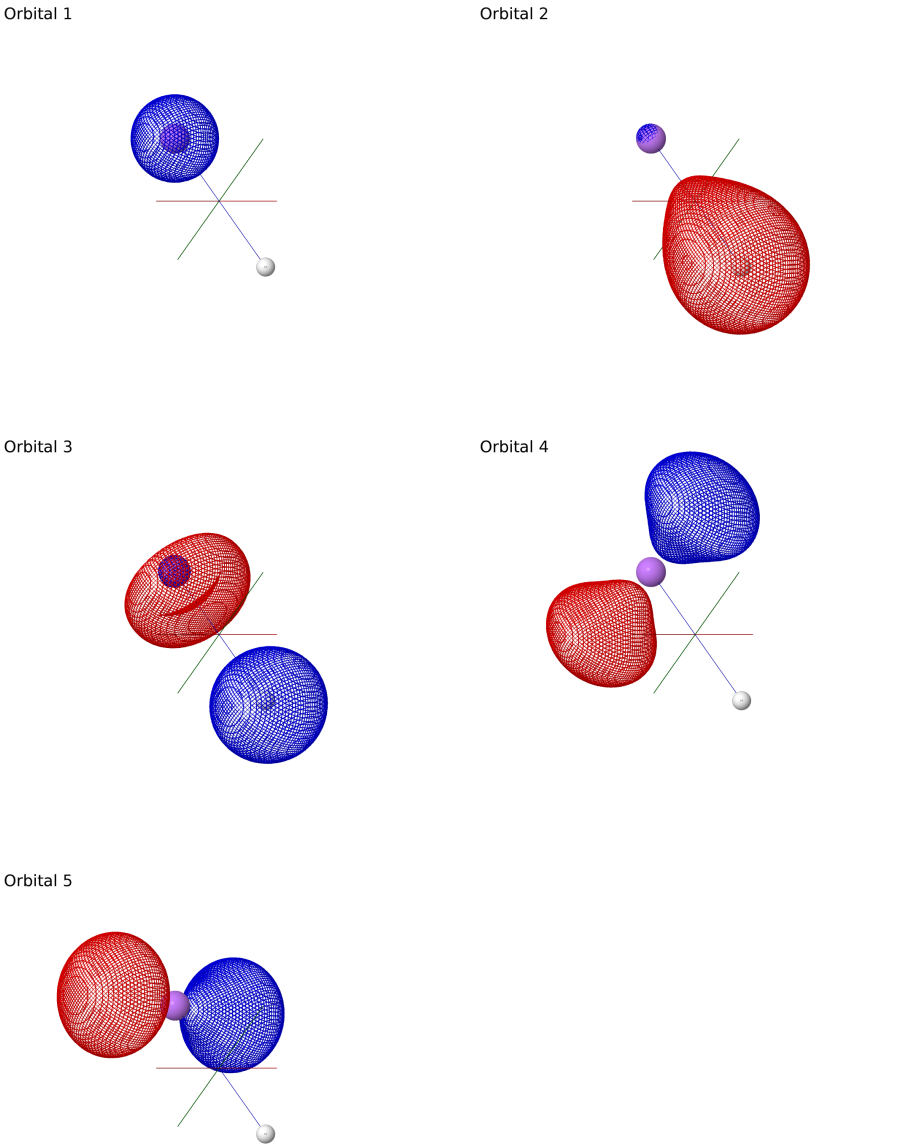

Figure 2.3: The first 5 Mmin orbitals according to a seniority minimization of the FCI wave function for the LiH(R_{st}) molecule with the 6-31G basis set, with R_{st} equal to two times the experimental geometry. The colors indicate the relative sign.

To test what the effect is of the single-particle orbital basis on the seniority number of the FCI wave function, table 2.1 depicts the seniority of the FCI wave function expanded in a basis coming from a restricted Hartree-Fock calculation (MO), seniority minimization procedure (MMin), or the natural orbital basis (FNO) all starting from the 6-31G basis set. A similar table is presented in [20] for the STO-3G basis set. The seniority number concept is important when static correlation is prevalent therefore results are depicted for comparison at experimental equilibrium distances and at stretched ones. Together with the Be atom, which is a prime example of static correlation[24], and for comparison the Ne atom is presented where dynamic correlation is the dominant factor. An aspect of table 2.1 that deserves to be highlighted is the effect of electron correlation on the expectation value of the seniority operator. Most molecules presented in table 2.1 have larger seniority values at equilibrium geometries than at stretched bond distances when the MO basis is used. This can be explained as increased importance of excited determinants with higher seniority in the wave function expansion. This also means that one needs less determinants with higher seniority to describe molecules at stretched distances. This is a result in contrast with [20], where it was stated that higher seniority values arise for stretched geometries when the MO basis is used, which is probably an artefact of using minimal basis sets such as STO-3G. For the seniority minimized and FNO bases the opposite is the case, but no real trend can be seen. Furthermore it is confirmed that the seniority minimized basis gives the lowest seniority values for the FCI wave functions. These seniority values are considerably lower than for the MO basis. The seniority values of the FNO basis come close except for the BH molecule at stretched distance and the BeH_2 molecule at equilibrium distance. These results were to be expected as the Mmin basis generated by maximizing the sum $\sum_i^M \Gamma_{iiii}$, maximises the importance of determinants with repeated indices leading to a lower total seniority and consequently a decrease of the importance of determinants with larger seniority values. A general point to note is that all the expectation values of the seniority number operator presented in table 2.1 are quite small. Consequently this means that the contribution of higher seniority determinants to the FCI wave function is also small. This validates the claim of fast converging expansions by truncating wave functions based on seniority number. Furthermore it shows that the seniority number operator as expressed by eq.(2.1) can be used as a measure for the compactness of the CI expansion in terms of Slater determinants.

To compare the MO with the MMin ones Fig. 2.2 and Fig. 2.3 show the first 5 orbitals of the $LiH(R_{st})$ molecule for respectively the MO basis and the MMin orthonormal single-particle bases. This is done with Jmol[41]. The isosurfaces $f(x, y, z) = 0.05$ are shown in red and the isosurfaces $f(x, y, z) = -0.05$ in blue. The shape of the 1s orbitals of Li is the same for both bases, but the main observation here is that for all other orbitals, the Mmin orbitals seem to have a similar shape as the MO ones though with a larger probability of being found close to the Li atom. It is concluded then that being found slightly closer

Table 2.1: The number of electrons N, spatial orbitals K, seniority of the FCI wave function ($\langle\psi_{FCI}|\hat{\Omega}|\psi_{FCI}\rangle$) for the MO, Mmin and FNO bases, for both experimental equilibrium distances (R_e) and symmetrically stretched ones (R_{st}). The stretched distances correspond to: $R_{st} = 2\ R_e$ for all molecules.

			$\langle\psi_{FCI}\|\hat{\Omega}\|\psi_{FCI}\rangle$		
system	N	K	MO	Mmin	FNO
Be	4	9	0.0369	0.0003	0.0003
Ne	10	9	0.0590	0.0546	0.0589
LiH(R_e)	4	11	0.3871	0.0002	0.0003
LiH(R_{st})	4	11	0.0364	0.0002	0.0002
BH(R_e)	6	11	0.1315	0.0112	0.0119
BH(R_{st})	6	11	0.0968	0.0210	0.0321
BeH_2(R_e)	6	13	0.0423	0.0143	0.0423
BeH_2(R_{st})	6	13	0.5030	0.2852	0.2873

to the Li atom enhances the probability to form a pair with another electron. Probably the second orbital of the Mmin set that is more prolonged over the H-Li axis plays a crucial role for the improvement of the pairing scheme if one changes from the MO orbitals to the MMin orbitals, because it makes it easier to pair electrons in a bond between the H and Li atoms.

Next the FCI wave function is scrutinized, by partitioning it by its seniority components.

2.5.1 Seniority weights in the FCI wave function

In this section, it is investigated how large the contributions of the different seniority blocks are to the FCI wave function and what their basis dependencies are. The contribution of each seniority sector is measured as the part of the total norm of the FCI wave function that can be attributed to it. Thus the weight of the seniority 0, 2, ... sectors can be calculated respectively as $w_0 = \sum_{i(0)} |c_i|^2$, $w_2 = \sum_{i(2)} |c_i|^2$, ... The c_i are the coefficients of the Slater determinants in the FCI wave function, and the summations run over all seniority zero ($i(0)$), seniority two ($i(2)$), ... determinants. Those weights can also be interpreted as probabilities that after measurement the system can be found in a seniority zero, two, ... state. Table 2.2 contains the probability that the system is found in a state associated to a particular seniority sector. The results shown are for the Be and Ne atoms, the LiH, BH, and BeH_2 molecules. For the molecules again results at equilibrium distance (R_e) and at stretched distance ($R_{st} = 2R_e$) are given. Three orthonormal single-particle bases are considered: the MO, Mmin, and FNO bases.

It can be concluded that for all three orthonormal bases and for all atoms and molecules the bulk of the norm is claimed by the seniority zero sector. However, for the MO basis the contributions of the seniority zero sector to the norm are significantly lower than the other two bases, and the MMin basis gives the largest contribution of the seniority zero sector to the norm of the

FCI wave function for all atoms and molecules, except for the Ne atom. For the special case of the Ne atom the contribution of the seniority zero sector is larger for the MO bases, but this is compensated by the decrease of the seniority four contributions of the Mmin basis. Resulting in the fact that when all contributions are added the seniority number of the FCI wave function in the Mmin basis is also for the Ne atom the lowest. The FNO basis also significantly enhances the contribution of the seniority zero sector as compared with the MO basis. Furthermore the FNO basis is cheaper to compute than the Mmin basis. However for some systems the seniority zero contribution to the norm of the FCI wave function of the FNO basis is significantly less than the MMin basis. If one wants to use the FNO basis as an approximation to the Mmin basis, one should be very cautious. For some systems it is possible to reduce the contributions of other sectors to values under 1e-4, when the MMin basis is used.

Table 2.2: Partitioning of the 6-31G FCI wave function in parts with different seniority number for the MO, Mmin and FNO bases. The contribution to the norm of the FCI wave function of all seniority zero, two and four determinants is denoted respectively by $\sum_{i(0)} |c_i|^2$, $\sum_{i(2)} |c_i|^2$ and $\sum_{i(4)} |c_i|^2$. For both experimental equilibrium distances (R_e) and symmetrically stretched ones (R_{st}). The stretched distances are given by: $R_{st} = 2\ R_e$ for all molecules.

	MO			Mmin			FNO		
system	$\sum_{i(0)} \lvert c_i\rvert^2$	$\sum_{i(2)} \lvert c_i\rvert^2$	$\sum_{i(4)} \lvert c_i\rvert^2$	$\sum_{i(0)} \lvert c_i\rvert^2$	$\sum_{i(2)} \lvert c_i\rvert^2$	$\sum_{i(4)} \lvert c_i\rvert^2$	$\sum_{i(0)} \lvert c_i\rvert^2$	$\sum_{i(2)} \lvert c_i\rvert^2$	$\sum_{i(4)} \lvert c_i\rvert^2$
Be	0.9816	0.0184	4.7886e-05	0.9999	3.4073e-05	5.6519e-05	0.9999	3.4031e-05	5.6589e-05
Ne	0.9851	0.0004	0.0144	0.9861	0.0007	0.0132	0.9835	0.0037	0.0127
LiH(R_e)	0.8065	0.1935	4.1148e-05	0.9999	4.3197e-05	3.3675e-05	0.9999	5.2936e-05	3.6659e-05
LiH(R_{st})	0.9818	0.0182	2.7470e-05	0.9999	3.3052e-05	2.8245e-05	0.9999	3.3973e-05	2.8094e-05
BH(R_e)	0.9374	0.0595	0.0031828	0.9964	0.0016	0.0020	0.9960	0.0021	0.0019
BH(R_{st})	0.9554	0.0408	0.0038	0.9925	0.0046	0.0020	0.9881	0.0077	0.0042
BeH_2(R_e)	0.9832	0.0064	0.0104	0.9941	0.0047	0.0012	0.9891	0.0005	0.0103
BeH_2(R_{st})	0.8308	0.0870	0.0823	0.9233	0.0108	0.0660	0.9223	0.0118	0.0660

Fig. 2.4 shows the contribution to the 6-31G FCI wave function of the BeH_2 molecule for the three lowest seniority sectors. The orthonormal bases compared are the canonical molecular orbitals (MO), the seniority minimized CISD basis ($\text{Mmin}_{\text{CISD}}$), the natural orbitals (FNO) and the seniority minimized basis of the FCI wave function (Mmin). The seniority minimized CISD basis ($\text{Mmin}_{\text{CISD}}$) is the orthonormal basis that minimizes the seniority of the CISD wave function, in contrast with the MMin basis that minimizes the seniority of the FCI wave function. The advantage of using the seniority minimized CISD basis is that during the iterative minimization procedure only CISD calculations are required which are computationally less expensive than FCI calculations.

At short bond distances the FCI wave function is clearly dominated by the seniority zero sector of the Hilbert space. This is mainly due to the dominance of the Hartree-Fock determinant in this regime. However, when the bond is stretched, the contribution of the seniority zero sector decreases in favor of the seniority four sector and to a lesser extent the seniority two sector. At even

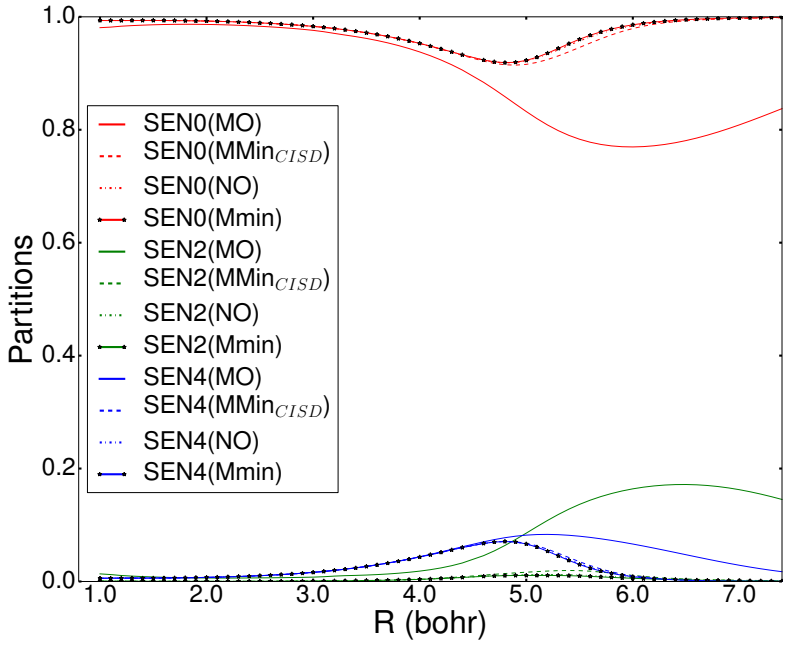

Figure 2.4: Partitioning of the norm of the 6-31G FCI wave function over the 3 lowest seniority sectors, for the linear BeH_2 molecule versus the Be-H distance. This for four different orthonormal bases namely the MO, FNO, $\text{Mmin}_{\text{CISD}}$ and Mmin bases.

larger distances the contribution of the seniority zero sector to the FCI wave function starts to increase again and grows slowly towards one. If the different orthonormal bases are compared, it can be seen that the contribution of the seniority zero sector to the FCI wave function in the MO basis is much lower than the FNO, Mmin_{CISD}, and Mmin bases at stretched distances.

For intermediate distances this decrease is mainly due to an increase of the importance of the seniority four sector, and for longer distances the seniority two sector quickly gains importance for the MO basis. The basis with the largest contributions of the seniority zero sector is the Mmin basis and consequently this basis has the lowest contributions of the seniority two and four sectors, as can be expected because the basis was generated by seniority minimizing the FCI wave function. The Mmin basis is also the most expensive basis to compute as many FCI calculations are needed to generate it, and as can be seen by Fig. 2.4 the improvements to the FNO and $\text{Mmin}_{\text{CISD}}$ bases are minimal for the symmetric stretch of the BeH_2 molecule. The contributions of the FNO and $\text{Mmin}_{\text{CISD}}$ bases are very similar with slightly larger contributions to the

seniority zero sector of the FNO basis. This is a remarkable fact because the generation of the FNO basis needs a FCI calculation while the generation of the $\text{Mmin}_{\text{CISD}}$ basis only needs CISD calculations. So the construction of the $\text{Mmin}_{\text{CISD}}$ requires much less effort for a similar exploitation of the seniority number hierarchy.

In general the seniority zero sector dominates the FCI wave function for all bases under consideration for both short and long distances. Only between 4 and 5 bohr there is a small decrease of the contribution of the seniority zero sector in favor of the seniority four sector. But beyond 5 bohr the seniority four sector goes very fast to zero. The seniority two sector is negligible during the entire bond dissociation of the BeH_2 molecule for the FNO, $\text{Mmin}_{\text{CISD}}$ and Mmin bases. This is also the biggest difference with the MO basis as for this basis beyond 4 bohr the seniority two sector gains a lot of importance and its contribution passes even the one from the seniority four sector. Another difference is that the contribution of the seniority four sector for the MO basis decreases much slower beyond 5 bohr than those from the FNO, $\text{Mmin}_{\text{CISD}}$ and Mmin bases. The biggest difference between the MO basis and the better performing bases is that when static correlation becomes important at stretched distances the FCI wave function in the MO basis receives a large contribution from pair broken terms, while the other two bases are optimized such that those pair broken terms remain negligible. To conclude, the above results show that the seniority number together with the seniority minimized bases can be used for the formulation of rapidly converging CI expansions with a minimal cost.

2.5.2 Energy properties of the seniority hierarchy

In the following subsections, energies obtained from seniority number truncating configuration interaction wave functions are presented. The results are generated for a number of different orthonormal single-particle bases, such as the natural orbitals (FNO), canonical orbitals coming from a previous restricted Hartree-Fock calculation (MO), seniority minimized orbitals (Mmin) coming from minimizing the seniority of the FCI wave function or the seniority of the CISD wave function, and orbitals coming from a local optimization of the DOCI wave function (LOCAL) through minimizing the gradient by subsequent Jacobi rotations of the single-particle orbitals as presented in [42] and discussed in section 5.3. Specifically it is aimed to answer the question if the seniority based scheme converges faster to the FCI limit than the excitation based one and for which cases it can be an efficient method for truncating configuration interaction wave functions. Furthermore in chapter 3 the effects of spatial symmetry breaking on the behaviour of seniority based wave functions is studied. Below a similar presentation of results will be given as in [21, 24] extended with some new results. Mostly the 6-31G basis set will be used and for some cases also the CC-PVDZ basis set. Furthermore to denote the seniority based wave functions: DOCI stands as usual for the seniority 0 case, SEN(0,2) for

the combination of the seniority zero and two sectors of the Hilbert space, SEN(0,2,4) for the seniority zero, two and four sectors combined, and so on for higher steps of the seniority hierarchy....

I. The Be and Ne atoms

Studying the beryllium and neon atom is of importance because they are two simple systems with very different behaviour. The beryllium atom is a prime example of a system where static correlation is prevalent. It has near-degeneracies of the 2s, $2p_x$, $2p_y$, and $2p_z$ orbitals. The CI active space to describe 2 electrons in 4 orbitals is sufficient to describe the strong correlation. In contrast the neon atom is an example where all orbitals are doubly occupied. The neon atom has no problems with near-degeneracies and therefore the correlation involved is mainly dynamic. Hence, the RHF determinant is a very good approximation for the neon atom, this means that for the neon atom the excitation based hierarchy will outperform the seniority based hierarchy. This is confirmed by table 2.3. This table shows the energy values of the MO, FNO, Mmin, Mmin$_{CISD}$, and LOCAL bases for the excitation and seniority based hierarchies. It is clear that for the Ne atom the excitation based hierarchy outperforms the seniority based hierarchy. With much fewer determinants a significantly better energy is obtained. In contrast, for the Be atom it can be seen that the low seniority wave functions provide energies that are comparable to the energies coming from the excitation based ones provided a suitable basis is choosen. Furthermore it is remarkable that those energies are obtained with much less determinants for the low seniority wave functions. Another observation that can be made is that the energies of all methods for the Ne atom have almost no dependence on the used orthonormal bases. For the Be atom the improvement of using the FNO or Mmin basis is significant for the seniority zero sector.

Table 2.3: The energies of the Be and Ne atoms in the CC-PVDZ (14 basis functions) basis for the excitation and seniority based partitions of the Hilbert space together with the number of determinants contained in their expansion. The RHF energy for the Be atom is -14.5723 hartree, and for the Ne atom: -128.48878 hartree. The 1s orbital of the Ne atom is kept frozen during the calculations. The compared bases are the MO, FNO, Mmin, Mmin$_{CISD}$, and LOCAL bases.

	Be				Ne			
partitioning	# determinants	MO	FNO	Mmin	# determinants	MO	LOCAL	Mmin$_{\text{CISD}}$
n_{ph} = 1,2	757	-14.61736	-14.61735	-14.61735	1801	-128.67362	-128.67365	-128.67343
n_{ph} = 1,2,3	3925	-14.61740	-14.61739	-14.61739	18025	-128.67458	-128.67465	-128.67461
n_{ph} = 1,2,3,4	8281	-14.61741	-14.61741	-14.61741	89125	-128.67891	-128.67897	-128.67890
Ω = 0	91	-14.60056	-14.61706	-14.61707	715	-128.55055	-128.55080	-128.55061
Ω = 0,2	2275	-14.61723	-14.61720	-14.61720	26455	-128.55360	-128.55362	-128.55368
Ω = 0,2,4	8281	-14.61741	-14.61741	-14.61741	180895	-128.67773	-128.67776	-128.67762

II. The BeH_2 molecule

The dissociation of the BeH_2 molecule is another prime example of the introduction of a significant amount of static correlation by dissociating the bond. For this reason it is an interesting molecule to include in this study.

Table 2.4 reports the number of determinants together with the percentage of the total number of FCI determinants used by the wave function for the BeH_2 molecule in the 6-31G atomic basis set when the 1s orbitals are always kept doubly occupied. It can be seen that for this case the number of DOCI determinants is significantly smaller than the number of CISD determinants. This indicates that the cost of generating the DOCI wave function is smaller than the CISD wave function for the BeH_2 molecule. This trend is the same for the next step of both hierarchies as the number of CISDT determinants is almost twice as high as the number of SEN(0,2) determinants.

Table 2.4: Number of determinants, N_{det}, for a selection of discussed methods for the BeH_2, CO and H_6 molecules in the 6-31G atomic basis set, and the corresponding fraction of the FCI Hilbert space expanded by those determinants. The 1s orbitals are kept doubly occupied for BeH_2 and CO.

	BeH_2		CO		H_6	
Methods	N_{det}	$\frac{N_{det}}{N_{det}(\text{FCI})}100$	N_{det}	$\frac{N_{det}}{N_{det}(\text{FCI})}100$	N_{det}	$\frac{N_{det}}{N_{det}(\text{FCI})}100$
CISD	531	12	4236	0.02	1000	2
CISDT	2331	54	68036	0.36	7000	14
CISDTQ	4356	100	555336	3	23200	48
DOCI	66	2	4368	0.02	220	0.45
SEN(0,2)	1386	32	244608	1	6160	13
SEN(0,4)	3036	70	2406768	13	23980	50
SEN(0,2,4)	4356	100	2647008	14	29920	62
FCI	4356	100	19079424	100	48400	100

Fig. 2.5(a) depicts the first two steps in the excitation based hierarchy together with the first three steps in the seniority based hierarchy in the MO basis. One can see that near the equilibrium distance the excitation hierarchy performs much better, but near the dissociation limit the SEN(0,2) wave function gains importance due to the increased importance of static correlation when the bond is stretched. The energy of the SEN(0,2) wave function crosses the one of the CISD wave function and comes close to the energy of the CISDT wave function. Furthermore the energy of the DOCI wave function approaches the FCI limit slowly at larger bond distances. These are interesting results as the seniority based hierarchy gives good results at bond dissociation even when the MO basis is used, although this is an orthonormal basis optimized for the excitation based hierarchy. The second plot of the seniority hierarchy of the bond dissociation of the BeH_2 molecule using the 6-31G basis set shows the impact of different orthonormal bases. The orthonormal bases under consideration are the LOCAL, FNO, and $\text{Mmin}_{\text{CISD}}$ bases. As can be seen the impact on the

energy of the DOCI wave function is quite big. Again in correspondence with results obtained by Bytautas, et. al. [24] and Alcoba et. al. [21]. The FNO basis is already a considerable improvement over the MO basis for the DOCI wave function and during dissociation the energy of the DOCI wave function goes rapidly towards the FCI limit when the FNO basis is used. But during the intermediate dynamic correlation regime the DOCI energy in the FNO basis has still a small bump above all the other energies. Only the DOCI energy in the MO basis is still higher. The LOCAL and $\text{Mmin}_{\text{CISD}}$ bases give the lowest energy values for the DOCI wave function and are indistinguishable on the curve, so only one of them is depicted. The energy values are even lower than the SEN(0,2) wave function in the MO basis during the entire dissociation process.

The effect of using these bases for the SEN(0,2) wave function is lower than for the DOCI wave function but the same relative order of the orthonormal bases remains with the FNO basis giving a sizeable improvement over the MO one and the LOCAL and $\text{Mmin}_{\text{CISD}}$ bases giving further improvements. It is remarkable that the DOCI wave function in a good basis can become lower in energy than the SEN(0,2) wave function in the MO basis as the MO basis is not the worst basis and the SEN(0,2) sector contains thirty times more determinants. However when also a suitable basis for the SEN(0,2) sector is chosen the energy of the SEN(0,2) wave function remains below all DOCI energies, but with a relatively small difference. This hints to the fact that optimizing the DOCI wave function means in essence decoupling the seniority zero and two blocks from each other such that the effects of pair breaking become negligible. If the SEN(0,2) wave function is then expanded in those optimized DOCI bases, one can see that the contribution and added value of the seniority two sector on top of the seniority zero sector becomes negligible, especially if one takes into consideration the extra cost of adding the one pair broken determinants. This is also revealed by looking at the relative energies of the DOCI and SEN(0,2) wave function. This is in accordance with the results of Fig. 2.4, which showed the partitions of contributions of the different seniority sectors to the FCI wave function. From this it can be seen that the seniority four sector has significantly larger contributions to the FCI wave function than the seniority two sector for the optimized bases, giving further evidence for the fact that optimizing the DOCI wave function mainly consists of minimizing the contribution of the seniority two sector. In fact one can use the SEN(0,2) energies in the MO basis as good guesses for the energies of the DOCI wave function in orbital optimized bases. As always this reveals a trade-off between memory and speed; the SEN(0,2) wave function needs more memory as more determinants are needed to expand the Hamiltonian in, but the orbital optimized DOCI wave functions needs more calculations to generate the optimized orbitals. To conclude: FCI accuracy is reached at the dissociation limit for all seniority based wave function if a proper orthonormal basis is used, again supporting the validity to use seniority based wave functions when static correlation becomes important.

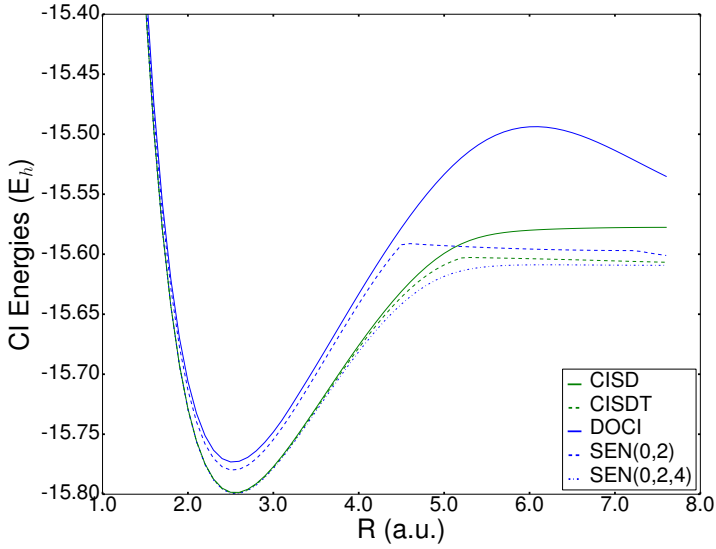

(a)

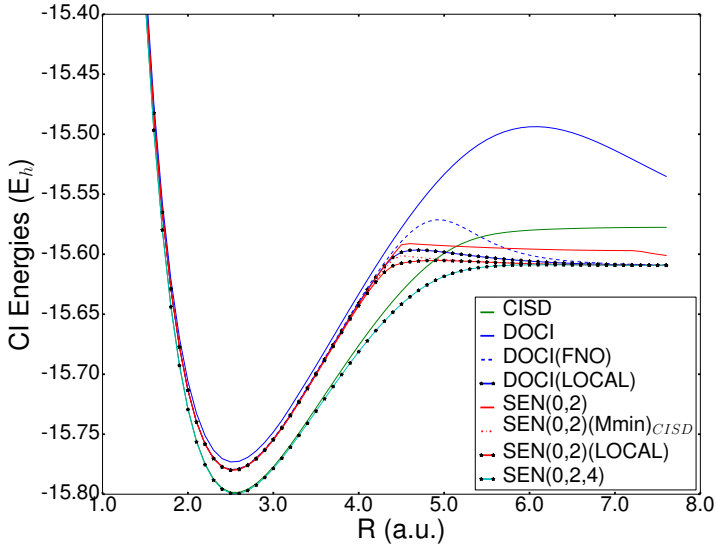

(b)

Figure 2.5: Comparison of excitation based energies with seniority based energies for the linear BeH_2 molecule as a function of the Be-H distance. In a) all results use the MO basis, and for b) the results are depicted for four different orthonormal bases namely the MO, FNO, $\text{Mmin}_{\text{CISD}}$ and LOCAL bases. The used single-particle basis set is 6-31G The 1s orbitals are kept doubly occupied.

III. The CO molecule

The results for the CO molecule in the 6-31 single-particle basis set are depicted in Fig. 2.6. The dissociation of the CO molecule is an interesting example because it consists of breaking a triple bond. Therefore it is of interest to know how the seniority based hierarchy performs in comparison with the excitation based hierarchy for this problem. In general the energetic dependence of the DOCI wave functions is not very smooth. This is probably due to convergence issues or changes in the underlying single-particle bases (MO) in combination with the big dependence of the energy values of the DOCI wave function upon the used single-particle bases. The interesting point to note is the big improvement of the SEN(0,2) energies when the $\text{MMin}_{\text{CISD}}$ is used. Furthermore when the bond is stretched the effect of minimizing the seniority of the CISD wave function is the highest. The SEN(0,2) wave function has no jumps and goes slightly towards lower energies near the dissociation limit. The SEN(0,2,4) wave function is already very smooth and the best wave function over the entire dissociation process, even if the MO basis is used. This is in agreement with the fact that when a larger percentage of the FCI Hilbert space is spanned by the Slater determinants, orbital optimizations become less important. For small molecular systems as studied in this thesis orbital optimizations are only necessary for the lowest steps in the seniority hierarchy such as the DOCI and SEN(0,2) wave functions. Comparing the excitation based wave functions with the seniority based ones for the CO molecule, it can be concluded that the excitation based hierarchy performs better for this molecule than the seniority based hierarchy. One needs the SEN(0,2,4) wave function to improve slightly on the CISDT wave function, and as table 2.4 shows the SEN(0,2,4) wave function contains almost three million Slater determinants in comparison with the seven thousand of the CISDT wave function.

IV. The H_6 linear chain

Another prime example of systems with a lot of static correlation are stretched hydrogen chains. Many studies of those chains are already published in the literature, some of them even including studies of the effects of breaking the spatial point-group symmetry on the energy values and quality of seniority based wave functions for the H_8 chain[24, 42]. Those previous studies stated that considerable improvements of the wave function can be made by breaking the spatial point-group symmetry. Below results are presented for the H_6 chain using the 6-31G basis set (see Fig. 2.7). Interesting points to observe from this figure are the fact that the energy values of the DOCI wave function in the FNO basis are worse then if one had used the MO basis. So one should be cautious with using FNO orbitals, they are able to give good guesses for the optimized DOCI orbitals, but there is no guarantee for it. Another interesting fact that becomes clear from the figure is the dependence on the starting orbitals for generating the LOCAL orbitals [42]. E.g., a sudden jump in energy around 2.5

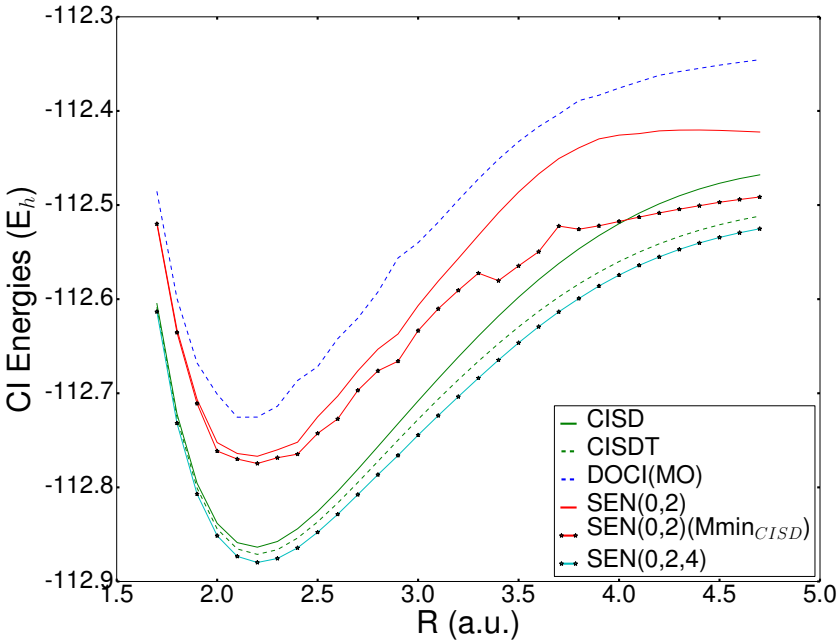

Figure 2.6: Comparison of excitation based and seniority based frozen core energies for the CO molecule as a function of the C-O distance. The results are depicted for different orthonormal bases namely the MO and Mmin$_{\mathrm{CISD}}$ bases.

bohr is found. This follows from the fact that the starting orbitals, from which the LOCAL optimization starts, change dramatically around 2.5 bohr from delocalized molecular orbitals to localized orbitals. The restricted Hartee-Fock routine that is used to obtain the starting orbitals for the LOCAL procedure is responsible for this. The applied Hartree-Fock routine makes use of the Generalized Wolfsberg-Helmholtz (GWH) guess implemented in psi4 [38]. The GWH guess is a simple Huckel-Theory-like method based on the overlap and core Hamiltonian matrices. It can be useful for open-shell systems and makes the psi4 restricted Hartree-Fock calculations converge in the dissociation limit. This guess makes the Hartree-Fock orbitals change from delocalized to localized ones when the 2.5 bohr point is crossed. Starting from the localized HF orbitals gives big improvements for the energy of the DOCI(LOCAL) wave function, at stretched bonds. Another interesting observation is the fact that the energy of the SEN(0,2) wave function in the MO basis goes below the energy coming from a CISD calculation although the CISD wave function contains more determinants. Furthermore the SEN(0,2,4) wave function has energy values that are almost indistinguishable from the FCI values, and it is the

best approximative wave function tested. As a last observation, it is remarked that the SEN(0,4) wave function is higher in energy than the CISDT wave function around equilibrium, but when the bounds are stretched the situation is reversed.

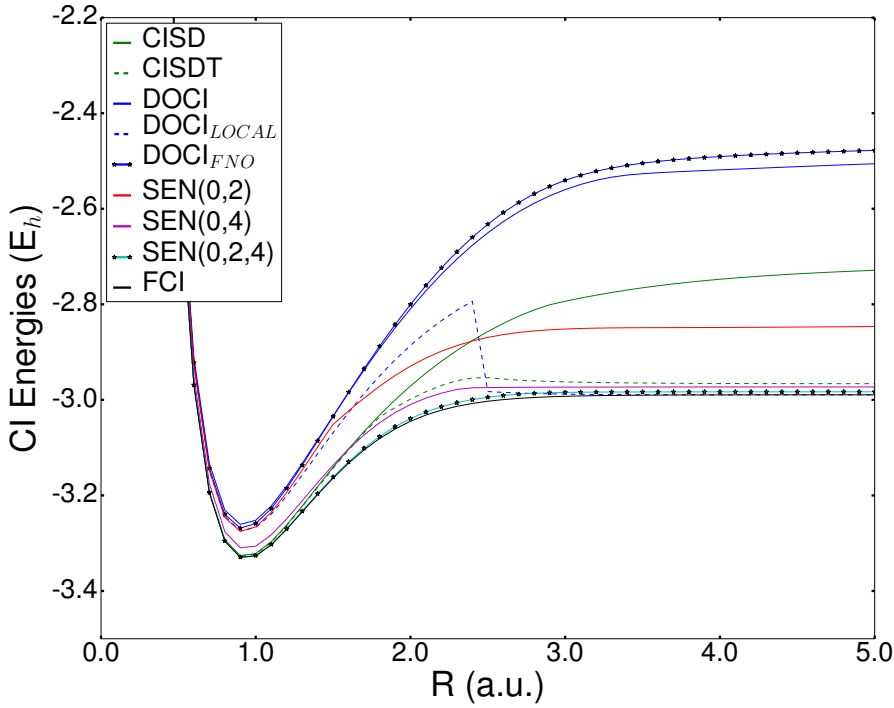

Figure 2.7: Comparison of excitation based energies with seniority based energies over the 3 lowest seniority sectors, for the linear H_6 molecule as a function of the H-H distance. The results are depicted for three different orthonormal bases namely the MO, FNO and LOCAL bases. The used atomic basis set is 6-31G.

V. The benzene molecule

Pierrefixe et. al. [43] derived a molecular orbital model of aromaticity. From this model it can be deduced that the π-electron system does not favour a symmetric, delocalized ring in benzene, confirming previous results obtained by Hiberty, Shaik, et. al. [44][45]. Furthermore it was stated that the regular symmetric structure of benzene has the same cause as that of planar cyclohexane, namely the σ-electron system. However, the π-system dictates if

de-localization occurs through qualitatively different dependency of the overlap of the deformed π-system on the geometry.

The deformation of the benzene molecule from a D_{6h} system to a D_{3h} system as described in [43] constitutes an interesting test for seniority truncated CI methods. The transformation groups the C atoms two by two and the angle between the two C atoms in a group is decreased from 60 degrees to 55 degrees while the distance to the center is kept fixed. This effectively reduces the D_{6h} symmetry to a D_{3h} system. Further it is assumed that the H-atoms remain on the line connecting the centre of the molecule to it's corresponding C-atom on the same distance. Furthermore the bonds change from 1.398 Å to 1.338 Å for C-atoms in a group and 1.581 Å for neighbouring C-atoms belonging to a different group. Fig. 2.8 is a graphical representation of the above described transformation.

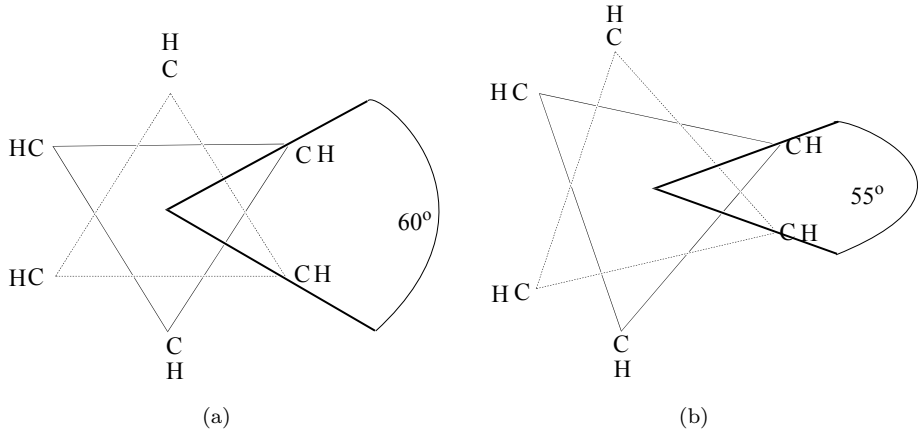

Figure 2.8: The symmetry breaking of the benzene molecule from a) D_{6h} to b) D_{3h}.

The π-system of benzene is easily isolated by using spatial symmetry. Psi4 [38] and the CI-solver developed for this thesis [46] make only use of Abelian symmetry groups for simplicity. The largest abelian supgroup of D_{6h} is D_{2h} and the largest abelian subgroup of D_{3h} is C_{2v}. The reducible representation of the π-system for the D_{2h} group of benzene can be decomposed to the following irreducible representations $\Gamma_{RV(D_{3h})} = B_{2g} + 2B_{3g} + A_u + 2B_{1u}$, and for the deformed benzene molecule with C_{2v} as its largest abelian point-group: $\Gamma_{RV(C_{2v})} = 3A_2 + 3B_1$. This makes it easy to perform active space calculations with the π-system of benzene, and the deformed benzene molecule, as the π-system can be selected by selecting all the orbitals corresponding to the irreducible representations of the spatial point-group that transform the same as the π-orbitals. Fig. 2.9 depicts the energies of the HF, CISD, DOCI(MO), DOCI(OO) and FCI wavefunctions as a function of the angle (in

radians) between two carbon atoms in a group. For the CI-wave functions an active space of 6 electrons in 12 orbitals is used corresponding to the π-system of benzene in the 6-31G basis set. An interesting observation is that DOCI(OO) is the only wave function for which the benzene molecule is not energetically stable when the π-system is chosen as active space. The OO basis is a global optimization procedure coming from a simulated annealing procedure as described in chapter: 3. It is remarkable that the energy for orbital optimized DOCI wave functions in a CAS(12,6) of π orbitals leads to a lower energy for the D_{3h} system. While the benzene molecule is energetically stable for the DOCI wave function that uses canonical molecular orbitals coming from a previous restricted Hartree-Fock calculation. Pointing out that the best orthonormal bases for the seniority based wave functions are not always the bases for which the energy of the DOCI wave function is the lowest. This result is also interesting as it shows the destabilizing character of the π-orbitals for a complex orbital optimized CI calculation such as DOCI(OO), confirming the results of the molecular orbital model by Pierrefixe et. al. It should be emphasized that those characteristics of the benzene molecule are only visible for seniority based wave functions (DOCI(OO)) and not for the excitation based ones as represented by the CISD(MO) wave function. Those characteristics are also not visible for the FCI wave function.

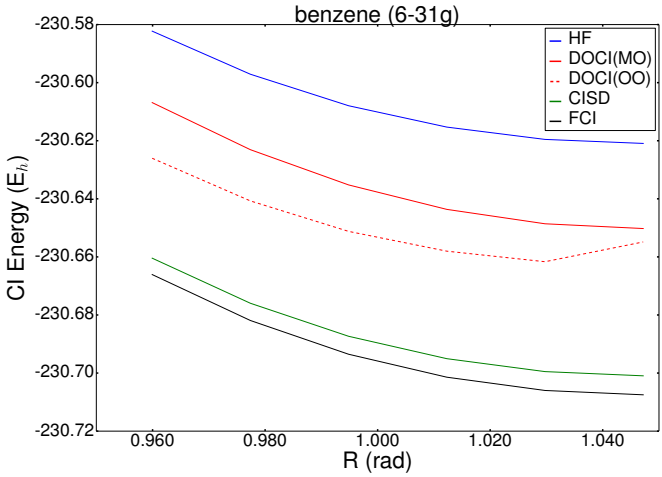

Figure 2.9: The HF, CISD, DOCI(MO), DOCI(OO), and FCI energies of the benzene deformation from D_{6h} symmetry to D_{3h} symmetry as a function of the smallest angle between two neighbouring carbon atoms in radians. The benzene molecule corresponds to 1.05 rad = 60^o. For the CI wave functions the π-system is used as an active space corresponding to 6 electrons in 12 orbitals or equivalently a CAS(6,12).

2.6 Entropy

A wave function is more compact when fewer determinants have coefficients significantly different from zero. The concept of compactness has high relevance in quantum chemistry, as it has long been recognized that much of the FCI space consists of unimportant determinants (so called dead-wood). This observation inspired work to find optimally sparse wave functions [47, 48]. A measure of the compactness of a wave function is the informational content (I_c) index which is defined as:

$$I_c = -\sum_{i}^{dim_H} |c_i|^2 \log_2(|c_i|^2). \tag{2.40}$$

Where the c_i are the coefficients of a wave function that is expanded in Slater determinants like: $\Psi = \sum_i c_i \phi_i$. It is derived in the context of Shannon's information entropy theory [49]. The Shannon entropy has the properties that the contribution from a Slater determinant gives 0 for $c_i = 0$ or 1 and $\frac{1}{2}$ for $c_i = \frac{1}{2}$. These indices have been used previously both for the excitation based case [50] and for the seniority based case [51]. In this section a basis is established in which the FCI wave function becomes as sparse as possible. The hypothesis that will be tested is: are bases that generate compact expansions of the FCI wave function a good starting point for truncated CI approaches by converging faster to the FCI limit for both the excitation based and seniority based approaches.

The basis that leads to the lowest I_c value for the FCI wave function can be obtained by a simulated annealing procedure. In short the simulated annealing procedure performs random Jacobi rotations on a starting orthonormal basis such as the MO, always accepting a rotation when the I_c value is decreased. When the I_c value increases, the Jacobi rotation is only accepted based on a criterion that depends on the absolute value of the I_c difference and the number of iterations already performed (it becomes less and less likely to accept Jacobi rotations that increase the I_c values). A detailed explanation of the simulated annealing procedure is given in section I. of chapter: 3. The I_c minimized basis obtained when only Jacobi rotations between orbitals with the same spatial-symmetry are considered is denoted as I_c(sym) and in the case symmetry breaking is allowed they are denoted as I_c(c1).

For two electron systems the FNO, MMin, OO, I_c bases are all equal and have consistently lower I_c values than the MO orbitals. This follows from section 2.2. Table 2.5 gives the Shannon I_c values for a number of different molecules and bases. The main conclusion is that the MMin basis is consistently more compact than the FNO and MO ones for the studied molecules. Another observation is that breaking the spatial symmetry can improve the compactness of the basis significantly. Furthermore the Mmin basis has Shannon indices that are almost equal to the Shannon index minimized basis when spatial symmetry breaking is allowed.

The possible relationship between the I_c value and truncated CI energies such as CIS, CISD, CISDT, ..., was computed starting from reference determinants

Table 2.5: Calculated I_c values for the FCI ground state wave functions in several orthonormal bases using the STO-3G basis set, for both equilibrium distances (R_e) and symmetrically stretched ones (R_{st}). The stretched distances are given by: R_{st} = 1.750 R_e (BH_3), R_{st} = 1.750 R_e (CH_4), R_{st} = 1.894 R_e (NH_3), R_{st} = 1.995 R_e (H_2O), R_{st} = 2.00 R_e (HF)

	$BH_3(R_e)$	$BH_3(R_{st})$	$CH_4(R_e)$	$CH_4(R_{st})$	$NH_3(R_e)$	$NH_3(R_{st})$	$H_2O(R_e)$	$H_2O(R_{st})$	$HF(R_e)$	$HF(R_{st})$
MO	0.358	2.803	0.495	3.850	0.462	4.788	0.281	2.442	0.132	0.860
FNO	0.357	2.792	0.515	3.822	0.443	4.142	0.261	2.362	0.117	0.829
Mmin	0.312	2.599	0.417	3.239	0.383	3.660	0.234	2.031	0.117	0.829
I_c(sym)	0.331	2.619	0.495	3.812	0.408	4.141	0.260	2.362	0.117	0.829
I_c(c1)	0.312	2.598	0.417	3.239	0.383	3.659	0.234	2.030	0.117	0.829

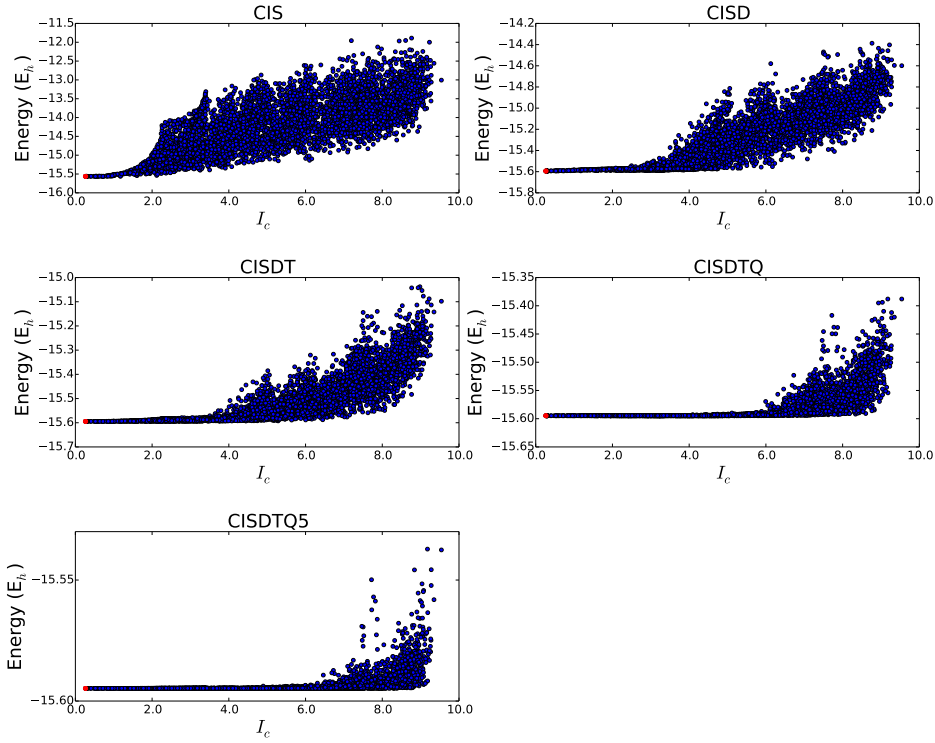

Figure 2.10: STO-3G excitation based truncated CI energies for different orthonormal bases versus their FCI I_c for BeH_2 at equilibrium distance. The red dots indicate the MO, FNO, Mmin and I_c bases, which are indistinguishable on the scale of the plot.

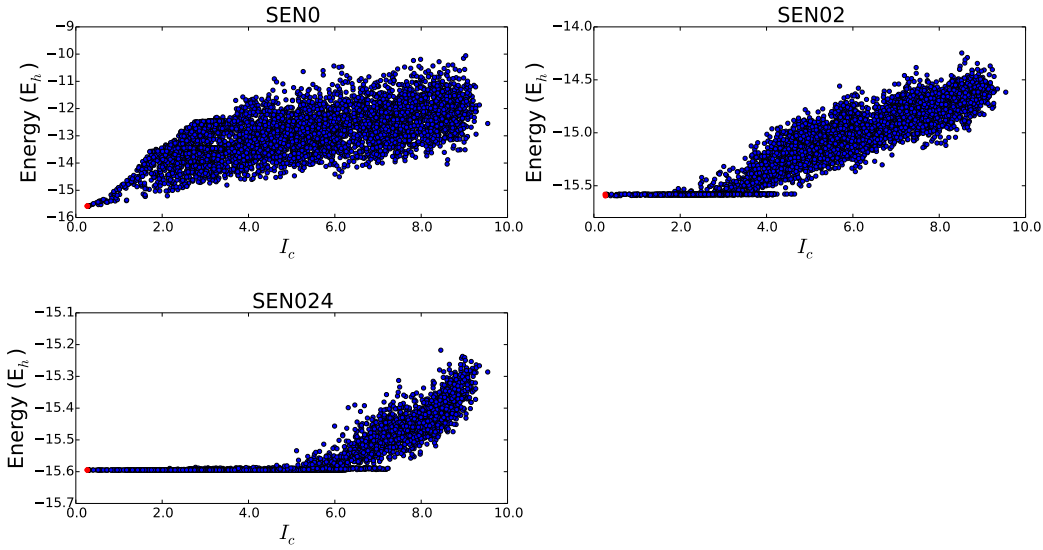

Figure 2.11: STO-3G seniority based CI energies for different orthonormal bases versus their FCI I_c for BeH_2 at equilibrium distance. The red dots indicate the MO, FNO, Mmin and I_c bases, which are indistinguishable on the scale of the plot.

obtained from MO's, FNO's, seniority minimizing, I_c minimizing orbitals and 1000 randomly chosen sets. The "special" MO, FNO, Mmin, and I_c bases are depicted by red dots, the random bases by blue dots. All special bases are situated at the same area in the scatter plot and are visually indistinguishable on the scale of the plot. The random bases are obtained by random Jacobi rotations starting from the MO orbitals. For each basis the FCI coefficients were computed, from which the I_c values followed. Fig. 2.10 shows the scatterplot for the truncated CI energies of BeH_2 versus the I_c values computed using the STO-3G basis set at equilibrium distance. There is no clear trend visible. This means that there is either no relationship between the I_c values and truncated CI energies or that some hidden ordering of the orbitals remains unknown or another reference determinant than the one with the highest coefficient should be taken to obtain rapid convergence. The original hypothesis is thus false and it is very difficult to improve upon the MO, FNO basis. Another interesting result is that the MMin basis is consistently more compact than the MO, and FNO basis with values that are indistinguishable from the I_c minimized bases.

To conclude it is stated that the study of entropy of truncated configuration interaction wave functions revealed that the MMin basis is very close to the entropy minimized basis for the systems under consideration. This means that the MMin basis generates very compact expansions of the FCI wave

function, indicating a fast convergence to the FCI limit. In the case of the MMin basis this can be exploited because the corresponding convergence to the FCI wave function is known, namely the seniority scheme. For random bases, however, there seems to be almost no correlation between the entropy and the convergence in either the excitation or seniority based schemes. This means that the hypothesis that a more compact FCI wave function would allow us to both extract a better single reference determinant to initiate a fast converging one electron excitation based truncated CI and an improved basis for the seniority scheme is shown to be false. This finalizes the overview of the seniority quantum number in configuration interaction theory.

In the next chapter a more thorough study of the zero'th order term of the seniority expansion, namely the DOCI wave function is presented. Special emphasis is made on the orbital optimization problem, and the lack of dynamic correlation. An attempt to solve the dynamic correlation problem is presented, adding extra seniority breaking determinants to the DOCI wave function by exciting from a reference determinant. Furthermore the effects of truncating the DOCI wave function are investigated for some small molecules and basis sets.

Chapter 3

Approximations and extensions to DOCI

[1] A class of polynomial scaling methods that approximate Doubly Occupied Configuration Interaction (DOCI) wave functions and improve the description of dynamic correlation is introduced. The accuracy of the resulting wave functions is analysed by comparing energies and studying the overlap between the newly developed methods and full configuration interaction (FCI) wave functions, showing that a low energy does not necessarily entail a good approximation of the exact wave function. Due to the dependence of DOCI wave functions on the single-particle basis chosen, several orbital optimisation algorithms are introduced. An energy-based algorithm using the simulated annealing (SA) method is used as a benchmark. As a computationally more affordable alternative, a seniority number minimising algorithm is developed and compared to the energy based one, revealing that the seniority minimising orbital set performs well. Given a well-chosen orbital basis, it is shown that the newly developed DOCI based wave functions are especially suitable for the computationally efficient description of static correlation and, to a lesser extent, dynamic correlation.

3.1 Introduction

The exact solution of the Schrödinger equation [4, 6] for an N-electron system is given, within any basis set, by the full configuration interaction (FCI) procedure. Unfortunately, the FCI method is usually intractable except for small

[1]Has been previously published as: M. Van Raemdonck, D. R. Alcoba, W. Poelmans, S. De Baerdemacker, A. Torre, L. Lain, G. E. Massaccesi, D. Van Neck, and P. Bultinck. *Polynomial scaling approximations and dynamic correlation corrections to doubly occupied configuration interaction wave functions* 2015: The Journal of Chemical Physics 143:10104106.

systems. Typically, the computational cost is reduced by incorporating only a selected set of N-electron Slater determinants in the configuration interaction (CI) wave functions, leading to the so-called truncated CI methods, for example CI with only single and double electron excitations (CISD). These excitations are defined with respect to a given reference, e.g. the restricted Hartree-Fock (RHF) determinant [4]. This kind of methods is typically well suited to account for dynamic correlation as they are closely related to performing perturbation theory around a good reference state.

A different way of reducing the FCI space is by projecting the wave function only on the determinants with a specified seniority number, where the seniority number equals the number of singly occupied orbitals in a determinant [30]. The seniority number operator may be formulated as:

$$\hat{\Omega} = \sum_{i,\sigma} a^\dagger_{i\sigma} a_{i\sigma} - \sum_{i,\sigma_1,\sigma_2} a^\dagger_{i\sigma_1} a^\dagger_{i\sigma_2} a_{i\sigma_2} a_{i\sigma_1}, \tag{3.1}$$

where $a^\dagger_{i\sigma}$ creates a particle in the i-th orbital of an orthonormal basis with spin σ (α or β type) and $a_{i\sigma}$ is the corresponding annihilation operator. In terms of reduced density matrices, the expectation value of the seniority number operator can be obtained as:

$$\begin{aligned} \left\langle \hat{\Omega} \right\rangle &= \langle \Psi | \hat{\Omega} | \Psi \rangle \\ &= \sum_i \rho_{ii} - 2 \sum \Gamma_{iiii} \end{aligned} \tag{3.2}$$

where $\sum_i \rho_{ii}$ is the trace over the first-order spin summed reduced density matrix ρ, which equals the number of electrons N, and $\sum_i \Gamma_{iiii}$ is the partial trace of the second order spin-summed reduced density matrix (2-RDM) Γ. The Doubly Occupied Configuration Interaction (DOCI) method is an example of this class of seniority number based methods, as it lies in the seniority zero sector of the FCI wave function[21, 24]. For a system with K orbitals, and $\frac{N}{2}$ electron pairs, the DOCI wave function is given by

$$|\Psi_{\mathrm{DOCI}}\rangle = \sum_{j=1}^{\binom{K}{\frac{N}{2}}} c_j \prod_{i=1}^{\frac{N}{2}} S^\dagger_{\mathbf{j}(i)} |\theta\rangle \tag{3.3}$$

where $|\theta\rangle$ is the pair vacuum, and $S^\dagger_i = a^\dagger_{i\alpha} a^\dagger_{i\beta}$ are the pair creation operators in the i-th orbital. Each j value corresponds to a vector $\mathbf{j}$ that refers to the string of doubly occupied orbitals for all $\frac{N}{2}$ pairs. The complexity of a DOCI wave function is much reduced compared to a FCI wave function and therefore comes with a lower computational cost. The interest in DOCI wave functions for chemical purposes lies in its connections with Geminal-based theories for chemical bonding[32]. From a FCI point of view, DOCI is a singlet wave function that is able to describe any possible pairing structure of the chemical bond. As a matter of fact, recent calculations[24] have established that DOCI

wave functions are perfectly suited to capture the static correlations associated with chemical bonds. Furthermore, DOCI wave functions are size extensive. Unfortunately, several problems remain with the DOCI method. Although the number of determinants expanding the DOCI wave function is strongly reduced compared to that of the FCI wave function, the factorial scaling persists. The first goal of this chapter is to examine whether truncated DOCI solutions give comparably good quality results at polynomial scaling computational cost. Reduced-cost DOCI solutions have previously been obtained either by a projected Schrödinger equation approach [25, 28], or by using exactly solvable models [52] or a variant of the variational 2-RDM method projected on the seniority zero sector of the Hilbert space [42].

DOCI performs well at accounting for static correlation but fails in describing dynamic correlation[24] whereas CISD wave functions perform rather well for the latter[4]. A second aim of this chapter is therefore to establish how methods based on the union of truncated DOCI and truncated one-electron excitations based CI spaces perform for both types of electron correlation at reduced computational cost. We report several DOCI variants and examine the quality of the corresponding wave functions by computing not only their corresponding energies but also their overlap with more advanced wave functions.

An important feature that is typical for non-FCI wave functions is that their quality depends on the single-particle basis chosen. FCI wave functions always lead to equivalent wave functions irrespective of the (orthonormal) basis chosen, be it e.g. natural orbitals, RHF molecular orbitals or any other orthonormal basis. This is no longer true for approximate wave functions such as DOCI and its variants. Hence the need to find the solution with the lowest energy obtainable through a unitary transformation of the orthonormal orbitals. Another aim of this chapter is therefore to develop an orbital optimisation algorithm well suited to escape from local energy minima. A good candidate for this purpose was found to be simulated annealing (SA)[53]. Although the SA procedure works very well for small systems, we found that it is not practically usable in those cases where the number of active orbitals or electrons is large ($N > 20$), so we also propose a new orbital basis suitable for DOCI and its variants. It was previously shown that the orbital basis that minimises the seniority number of a FCI wave function can be used to achieve a more compact determinantal expansion, where the determinants with zero seniority number are the dominant contributions to the FCI wave function[20] (see also chapter: 2). In practice, this means that this orbital basis can be used as a good approximation to the energy optimised DOCI orbitals. As FCI wave functions are hardly tractable for larger systems, we examine whether a seniority number minimising basis derived from a truncated CI wave function serves equally well.
The different wave functions corresponding to the methods reported in this chapter can be elegantly summarised using the Venn diagram in Fig. 3.1. In all cases, a bar ($^{\bar{}}$) notation means that each excitation involves two paired electrons. $\text{CI}\bar{\text{S}}$ for example, means that only excitations of a single electron

pair with respect to a closed-shell reference Slater determinant are considered, whereas CISD$\bar{\text{D}}$ means that all single and double electron excitations plus all double electron-pair excitations are taken into account. CI$\bar{\text{S}}$ is therefore a subset of CID, CISD$\bar{\text{D}}$ is a subset of CISDQ, etc.. In Fig. 3.1, the green circle

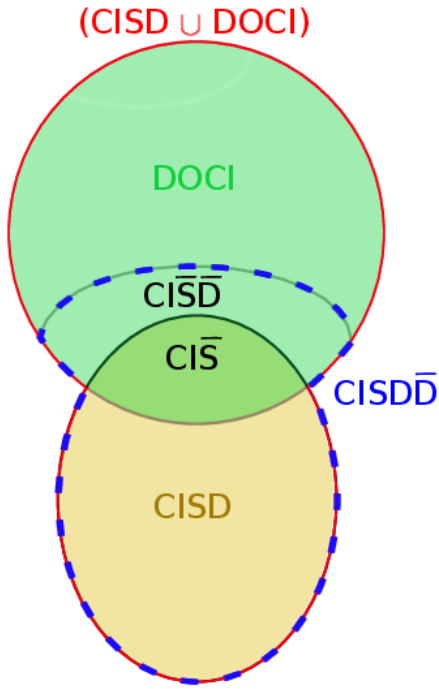

Figure 3.1: Overview of the wave functions used for approximations and extensions of the DOCI wave function.

stands for the DOCI space which comprises up to $\frac{\bar{N}}{2}$ electron-pair excitations, and the yellow ellipse underneath for the CISD space. The intersection of the DOCI and the CISD spaces is the CI$\bar{\text{S}}$ space. Furthermore we can distinguish within the DOCI space the double electron-pair excitations (with respect to the same reference as the CISD determinants). We will also discuss hybrid methods that consider the union of the DOCI and truncated CI spaces, such as CISD, which will be denoted as (CISD ∪ DOCI), and is contained in the red boundary, and the polynomial scaling approximate hybrid methods such as CISD$\bar{\text{D}}$, enclosed by a blue dotted line. All methods from Fig. 3.1 can be used with any choice of (orthonormal) orbitals. We choose for either molecular orbitals as obtained from a preceding Self Consistent Field (SCF) calculation, (globally) energy optimised orbitals by means of SA, or seniority number minimising orbitals.

3.2 Algorithms

3.2.1 Computational details and CI solver

In order to assess the accuracy of the methods reported in section 3.1, we consider the symmetric bond stretching of the BeH_2, H_2O and N_2 molecules, which are standard tests for methods that aim at describing strongly correlated systems. The used atomic basis sets range from minimal STO-3G to split valence cc-pVDZ. The use of minimal basis sets is considered appropriate here given the nature of the methods tested. All one- and two-particle integrals needed are generated by the PSI4 package [38]. For the interface with PSI4 we used the Hamiltonian class of CheMPS2[39, 40].

For all DOCI, truncated DOCI and hybrid DOCI calculations a general CI solver is used that takes as argument a list of Slater determinants. These Slater determinants, in turn, are built from an orthonormal set of orbitals that may correspond to molecular orbitals or some other orthonormal set. All determinants are encoded as binary strings in terms of this set and the Hamiltonian is represented in the Slater determinant basis. The variational problem of determining the Slater determinant coefficients is solved using an implicitly restarted Arnoldi algorithm [54] to locate the chosen number of low lying energy states. All potential energy curves reported below describe the ground state.

3.2.2 Orbital optimisation algorithms

DOCI and its variants depend on the chosen orthonormal orbital basis used in the Slater determinants entering the CI expansion. Limacher et al. [31] have shown that the basis-dependent DOCI energy surface has many local minima. To cope with those local minimum problems, we now introduce an orbital optimisation algorithm tailored at locating the global energy minimum. For this, the simulated annealing algorithm is chosen as an orbital optimiser. Such techniques have been used previously in quantum chemistry[55] albeit to limited extent, often because of their prohibitive computational cost. Here such calculations are nevertheless used whenever feasible because they give good benchmark results.

I. Energy based orbital optimisation through simulated annealing

SA is a probabilistic method introduced by Kirkpatrick et al. [53] for finding the global minimum of a cost function that may possess several local minima. It does so by emulating the physical process where a solid is gradually cooled and eventually freezes in a minimum energy configuration. This method performs particularly well when there are many local energy minima, as in the case of DOCI wave functions [31]. The work flow for the SA procedure pertaining

to the orbital optimisation of CI methods is depicted in Fig. 3.2. In our implementation, we perform a sequence of elementary Jacobi rotations [56] between randomly selected pairs of orbitals over a randomly chosen angle α. These rotations result in a new orthonormal basis that yields a new energy value. The new basis is then, depending on its energy, accepted or rejected with a certain probability depending on a "temperature" T. The rotation angles α are drawn from a normal distribution around zero, and are limited to the interval $[-\alpha_{\max}, \alpha_{\max}]$. Both the temperature T and the maximal angle $\alpha_{\max}$ decrease in the consecutive steps. The starting temperature T is chosen high enough to explore the entire energy surface. Based on our experience, a good choice is $T = 0.5$ E_h. The rate at which T decreases after each step is chosen as $\delta T = 0.99$. For $\alpha_{\max}$, an initial value $\alpha_{\max} = 1.4$ rad is chosen, and the rate of decrease of the maximum angle is set to $\delta\alpha_{\max} = 0.9999$ as we have found that it is convenient to decrease the maximum angle very slowly so that the flexibility to escape local minima remains. This process is repeated until convergence. For simplicity, we initialise the same T, α_{max}, δT , $\delta\alpha_{max}$ for all pairs of orbitals.

After the rotation of two orbitals, the energy is calculated (E_{new}) with the chosen level of theory and compared to the energy of the previous orbital configuration (E_{old}). If $E_{new} < E_{old}$, the change in the orbitals is always accepted. If $E_{new} \geq E_{old}$, a uniform random number $R_{0,1}$ between zero and one is drawn, and if

$$R_{0,1} < \frac{\exp^{\frac{E_{old}-E_{new}}{T}}}{\exp^{\frac{E_{old}-E_{new}}{T}}+1} \tag{3.4}$$

the change is also accepted. This means that the energy may occasionally increase which helps escaping local minima. When T has lowered sufficiently, the chances of such energy increases become negligibly small.

After each step i the temperature and maximum rotation angle are reduced for the next step $i + 1$:

$$T^{(i+1)} = T^{(i)}\delta T \tag{3.5}$$

$$\alpha_{max}^{(i+1)} = \alpha_{max}^{(i)}\delta\alpha_{max} \tag{3.6}$$

At the end of each cycle two convergence criteria are checked:

1. Has the maximum number of cycles been reached (here 20000)?
2. Has the maximum number of consecutive non-acceptance steps been reached (here 1000)?

If one of them is fulfilled, the simulated annealing loop is stopped. Otherwise the procedure is repeated.

In order to increase the chances of locating the global minimum, several separate SA calculations are performed and the optimal unitary matrix and energy

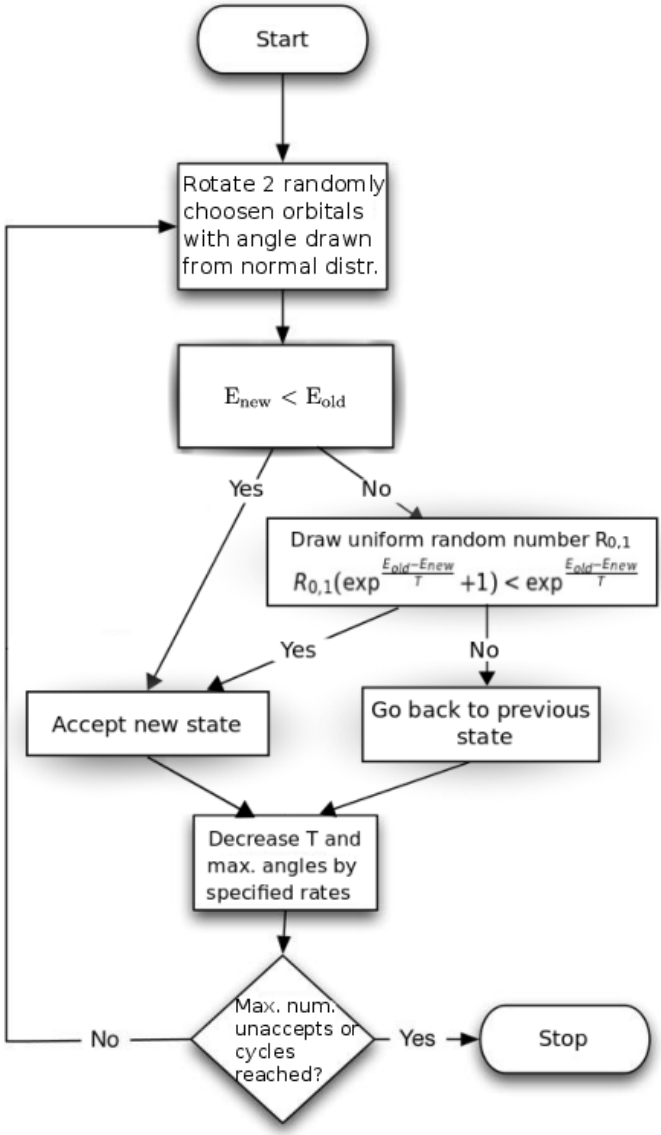

Figure 3.2: The work flow of the simulated annealing (SA) orbital optimisation procedure for CI methods as implemented for this thesis.

are selected. After this, an extra SA run is performed with very low T and very small maximum angle, in order to locally optimise the minimum further. Our calculations point out that the SA procedure is very effective, as it consistently produces lower energies than those obtained from methods using the orbital gradient and Hessian or the generalised Brillouin theorem [4, 57–59]. The SA results may therefore serve as a benchmark for other optimisation schemes.

In practice, we first perform all DOCI and related calculations using Hartree-Fock molecular orbitals and henceforth results obtained using this basis are labelled with the caption MO. Subsequently, the orbital basis is optimised. A first SA procedure allows only rotations among orbitals that belong to the same irreducible representation. Results using this optimised basis are denoted by OO. In a second procedure, rotations among all orbitals are allowed thereby permitting symmetry breaking. Results with this basis are denoted OO-c1.

II. Seniority based orbital optimisation

For large systems SA is no longer viable. It was previously shown[20] that a promising basis is the one that minimises the seniority number (Eq. (3.2)) of a FCI wave function. Unfortunately, the computational cost of a FCI calculation severely limits the applicability of this method. Here we propose to use an orbital basis that minimises the seniority number of a wave function that scales more favorably, e.g., CISD.

Our procedure to minimise the seniority number of a wave function is a very fast converging iterative process based on the algorithm of Subotnik et al.[34], originally introduced for the determination of localised molecular orbitals such as Edmiston-Ruedenberg orbitals [60]. It follows from Eq. (3.2) that if the partial trace of the spin summed second order reduced density matrix is maximised, the seniority number of the total wave function is minimised. Our adaptation of the procedure of Subotnik et al.[34] to minimise the seniority number proceeds as follows [20]:

1. Start with a set of orthonormal orbitals, e.g. the RHF molecular orbitals.
2. For $k \geq 0$ (k indicates the number of cycles) determine the 2-RDM for which we want to minimise the seniority number.
3. Construct the matrix $R^{(k)}_{ji} = \Gamma^{(k)}_{ji,ii}$
4. Construct the unitary transformation $U^{(k+1)} = R^{(k)} \left[\left(R^{(k)} \right)^{\dagger} R^{(k)} \right]^{-\frac{1}{2}}$.
5. Transform the current orbitals to the new basis with the unitary matrix $U^{(k+1)}$.
6. Set $k = k+1$, repeat steps 2-6 until $R^{(k)}$ is sufficiently close to a symmetric matrix and the process has converged.

The matrix U in step 4 is guaranteed to be unitary through the polar decomposition of a square complex matrix [35]. The orbitals produced by minimising the seniority number of a FCI wave function are denoted by the labels Mmin and Mmin-c1, depending respectively on whether only rotations between orbitals of the same irreducible representation are considered or symmetry breaking is allowed. If the seniority number is minimised using a wave function other than FCI, a subscript is added to denote the wave function used (e.g., $\text{Mmin}_{\text{CISD}}$ when the seniority of a CISD wave function is minimised without symmetry breaking).

3.3 Results and Discussion

In the following, both the orbital optimisation algorithms and newly described DOCI methods are tested for a set of small molecules with emphasis on their dissociation curves for the ground state. In the first section 3.3.1, the bond breaking curve of BeH_2 through linear symmetric stretching is examined with focus on the effect of different bases on the one hand (subsection I.) and the effect of extending DOCI with non-seniority conserving excitations on the other hand (subsection II.). As in both cases the OO basis is used, only a minimal basis set is considered. In the second section 3.3.2, we report on the performance of truncated DOCI methods (subsection I.) and truncated DOCI supplemented with non-seniority conserving excitations (subsection II.). Due to the fact that the truncation reduces the computational cost significantly while adding only limited non-seniority conserving excitations, we report results obtained using larger basis sets thereby allowing more insight in dynamic electron correlation effects.

3.3.1 Orbital optimisation and dynamic correlation in BeH_2

I. Basis dependence of DOCI wave functions and energies

We first describe the impact of the chosen orthonormal orbital basis on the DOCI energy in case of bond breaking in BeH_2 through linear symmetric stretching. This small molecule is computationally tractable for FCI methods and has significant multireference character at bond breaking, making it an ideal test for proof of principle calculations. Table 3.1 reports DOCI energies using the STO-3G atomic basis set for orbitals optimised with the SA approach (OO and OO-c1) and for the seniority number minimising ones (Mmin and Mmin-c1 derived from both FCI and CISD), along with the DOCI energy obtained using restricted Hartree-Fock (RHF) based molecular orbitals (MO). Although the STO-3G basis set has its shortcomings due to its size, it still captures the essence of the physics as the shape of the potential energy curve for BeH_2 remains similar for larger basis sets (see below). The lowest

energies, obtained using the OO-c1 basis arising from the energy driven global optimisation, can be considered reference values.

Figs. 3.3(a) and 3.3(b) show the DOCI potential energy curves in the selected bases with the RHF and FCI curves as references. Fig. 3.4 depicts DOCI energy differences for the different bases considered.

Table 3.1: STO-3G DOCI energy values and differences for the symmetric stretch of BeH_2 using different orthonormal bases. R is the length of the Be-H bonds.

	DOCI Energy/E_h								
R (Å)	MO	OO	Mmin	$\text{Mmin}_{\text{CISD}}$	$\text{Mmin}_{\text{CISD}}$ - OO	OO-c1	Mmin-c1	$\text{Mmin}_{\text{CISD}}$-c1	$\text{Mmin}_{\text{CISD}}$-c1 - OO-c1
0.86	-15.29597	-15.29648	-15.29647	-15.29647	0.00001	-15.29964	-15.29454	-15.29455	0.00509
1.02	-15.49048	-15.49092	-15.49091	-15.49091	0.00001	-15.49626	-15.48941	-15.48942	0.00684
1.34	-15.57800	-15.57846	-15.57844	-15.57842	0.00004	-15.59036	-15.59014	-15.59020	0.00016
1.66	-15.51072	-15.51152	-15.51141	-15.51134	0.00017	-15.53372	-15.53315	-15.53333	0.00039
1.98	-15.40203	-15.40454	-15.40378	-15.40351	0.00103	-15.44094	-15.43965	-15.43938	0.00156
2.13	-15.34717	-15.35387	-15.35079	-15.35021	0.00366	-15.39550	-15.39106	-15.39166	0.00384
2.29	-15.29703	-15.32807	-15.30690	-15.30555	0.02251	-15.35453	-15.34260	-15.34297	0.01156
2.45	-15.25516	-15.32598	-15.28808	-15.28297	0.04301	-15.32598	-15.28808	-15.28297	0.04301
2.61	-15.22536	-15.32812	-15.30732	-15.28890	0.03923	-15.32812	-15.30732	-15.28890	0.03923
2.77	-15.21072	-15.33064	-15.32517	-15.30703	0.02361	-15.33064	-15.32517	-15.30703	0.02361
3.09	-15.22627	-15.33419	-15.33378	-15.33096	0.00323	-15.33419	-15.33378	-15.33096	0.00323

Table 3.1 and Figs. 3.3 and 3.4 illustrate several important points. First, the MO basis is found to perform quite well for small interatomic distances compared to the computationally much more expensive OO basis. Beyond an internuclear distance of 1.66 Å the energies start to differ dramatically with differences going up to 120 mE_h at 2.77 Å(see Fig. 3.4(a)). Optimising the orbitals is therefore of utmost importance at longer bond distances although the differences decrease again at still longer distances. (see Fig. 3.4(a)). Fig. 3.4(b) shows that the energy obtained from the Mmin basis lies much closer to the OO energy over a larger range of interatomic distances, with differences up to only 38 mE_h near 2.45 Å. Moreover, the difference between energies obtained with the $\text{Mmin}_{\text{CISD}}$ and the Mmin bases is rather small as can be seen from Table 3.1. Fig. 3.3(c), which depicts the overlap of the DOCI wave function with the FCI wave function, illustrates the deficiencies of the DOCI wave function in the MO, OO and OO-c1 basis to approximate the FCI wave function around a bond distance of 2.45 Å.

Symmetry breaking has an effect at slightly shorter bond lengths than those where the highest deviations between the Mmin and OO based energies occur (see Fig. 3.4(c)). As expected for a variational method, symmetry-breaking may lower the energy. Note that the sharp angle in the DOCI(OO-c1) energy curve is not due to states crossing but due to a sudden change in the basis. A similar finding was reported previously by Bytautas et al.[24] for H_8. In the case of the OO-c1 versus OO basis, symmetry breaking leads to a maximum energy lowering of 42 mE_h at an internuclear distance of 2.13 Å. Such an effect does not necessarily occur for the Mmin and Mmin-c1 bases. Here symmetry breaking may result in higher energies especially at short bond lengths. Although counterintuitive, this is not in contradiction to the minimisation condition

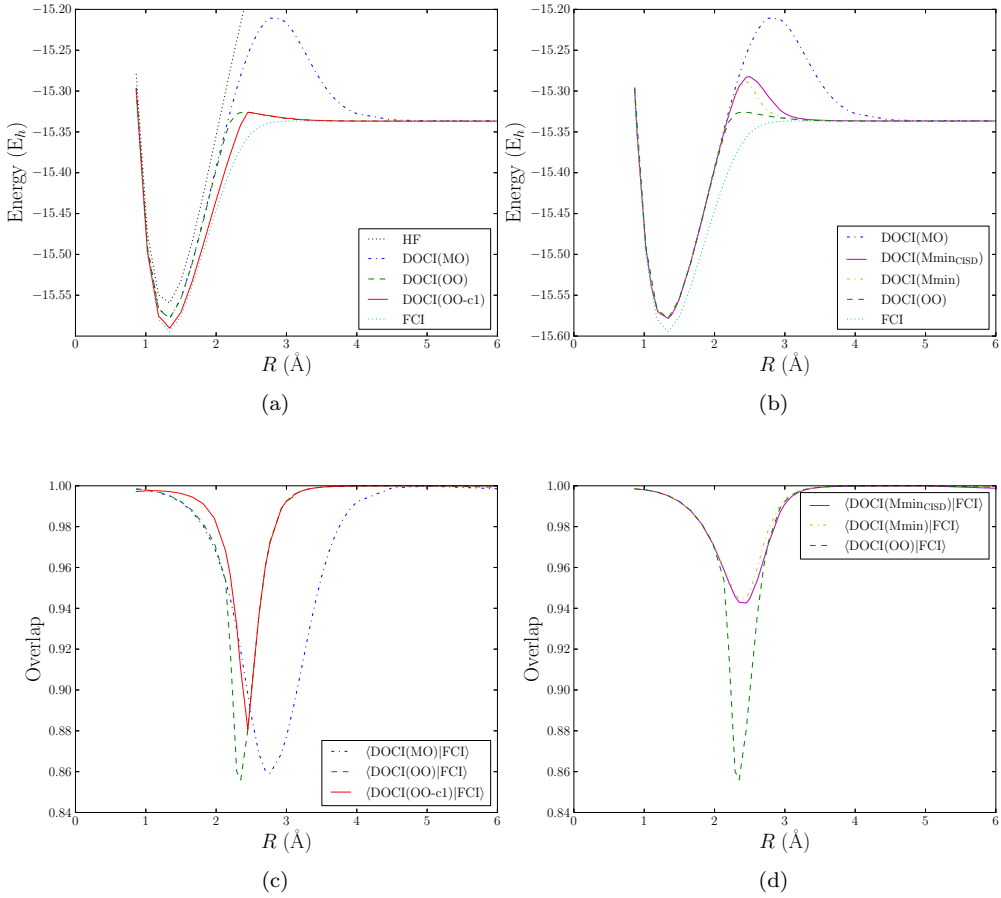

Figure 3.3: Symmetric stretch potential energy curves as a function of the Be-H distance (R) in BeH_2 for the (a) RHF, DOCI(MO), DOCI(OO), DOCI(OO-c1), and FCI wave functions, and (b) DOCI(MO), DOCI(Mmin$_{CISD}$), DOCI(Mmin), DOCI(OO), and FCI wave functions in the STO-3G atomic basis set. (c) overlap between the STO-3G DOCI and FCI wave functions in the MO, OO, and OO-c1 bases. (d) overlap of the STO-3G DOCI and FCI wave functions in the OO, Mmin, and Mmin$_{CISD}$ bases.

behind the Mmin procedure, as this procedure searches for a minimum in *seniority number*, rather than in *energy*. By breaking the symmetry, the method can better pair the electrons, irrespective of the energy. Still, the energy increase is marginal with a maximum of 2 mE$_h$ while for the vast majority of the energy curve symmetry breaking still lowers the energy.

As a whole, for most of the interatomic distances, the seniority-number minimising basis is a good alternative to the energy based optimised orbitals with

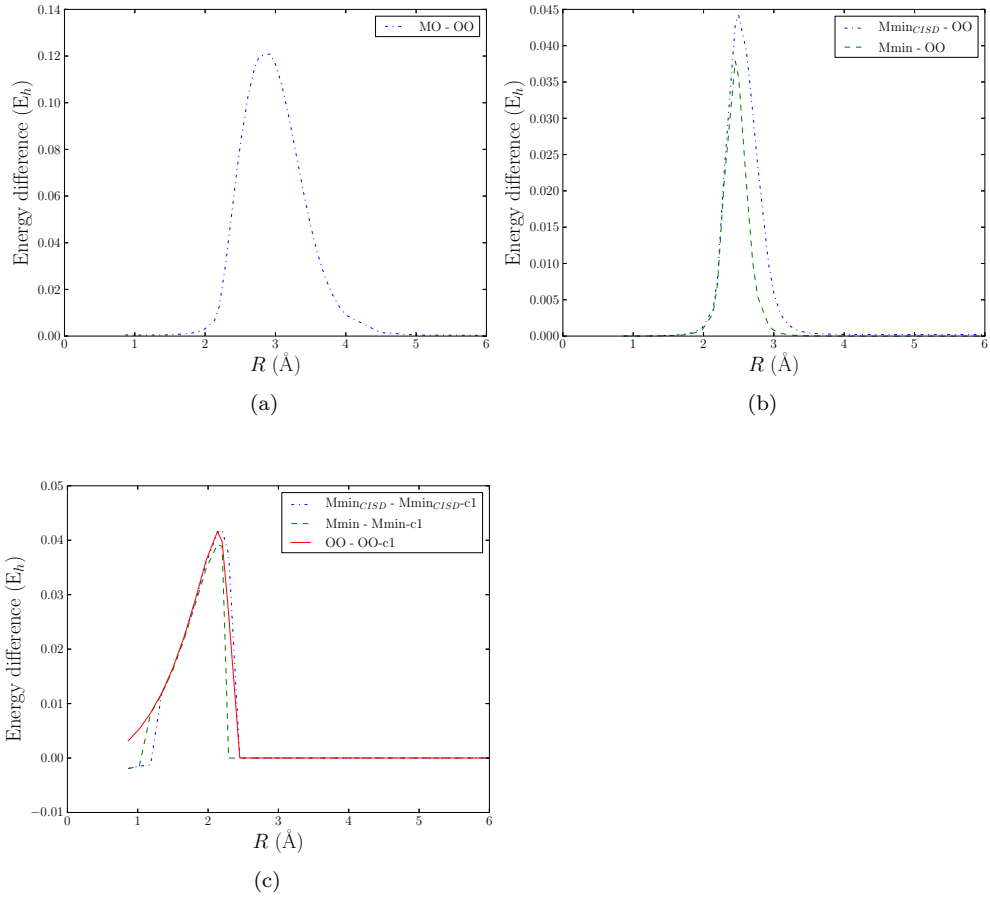

Figure 3.4: STO-3G DOCI energy differences between different bases as a function of the Be-H distance (R) in BeH_2. (a) effect of energy based orbital optimisation, (b) comparison between energies obtained with the energy optimised (OO) and Mmin and $\text{Mmin}_{\text{CISD}}$ seniority optimised orbitals, and (c) effect of symmetry breaking.

the computationally cheap $\text{Mmin}_{\text{CISD}}$ basis also performing rather well.

II. Dynamic correlation and hybrid DOCI wave functions.

It is clear from Table 3.1 and Figs. 3.3(a) and 3.3(b), that one can distinguish between three different regimes during bond breaking. At small bond distances Hartree-Fock theory yields a fairly good wave function. Indeed, near the equilibrium bond length the RHF determinant is the most important determinant in the FCI expansion. This regime extends well across the valley of the FCI

potential minimum. This is consistent with the observation that, in this regime, the FCI natural orbitals have occupations roughly zero or two (see Fig. 3.5).

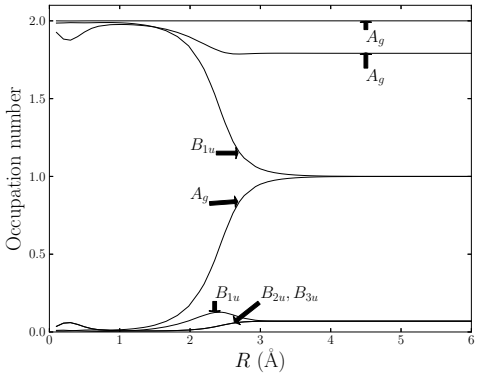

Figure 3.5: Occupation numbers of the STO-3G FCI natural orbitals as a function of the Be-H bond length (R) for the symmetric bond stretching of BeH_2. The symmetry labels used are based on the D_{2h} Abelian point group used in the calculations.

As soon as bond breaking starts, dynamic correlation becomes increasingly important, while farther towards dissociation static correlation gains importance. The interval where in BeH_2 dynamic correlation dominates corresponds approximately to [1.8 Å, 2.5 Å]. In this interval the occupation number of the natural orbitals closest to the Fermi level (between the highest occupied (HOMO) and lowest unoccupied molecular orbital (LUMO) levels from Hartree-Fock) start to differ from zero or two, although the complete smearing out of occupation numbers as in the strong correlation limit does not occur.

In the so-called static correlation regime it is no longer possible to find a good single reference approximation to the general wave function, e.g. the RHF energy deviates strongly from the FCI energy (see Fig. 3.3(a)). This is well reflected in the fact that many more natural orbitals have significant occupation numbers and hence, the distinction between occupied and virtual orbitals vanishes. The strong static correlation regime is characterised by degenerate strongly-occupied molecular orbitals. The particular structure of the DOCI wave function turns out to be very suitable to describe this, since the DOCI wave function is a complete CI expansion in terms of electron pairs[24].

As can be observed from Fig. 3.3(a), the peculiar hump in the DOCI(MO) potential energy curve within the dynamic correlation regime reflects the difficulties of the DOCI wave function to describe dynamic correlation properly in the MO basis. The hump itself is not an artefact of the minimal basis set as DOCI(MO) calculations using the 6-31G and cc-pVDZ basis set also show a similar feature (see below). Using the OO and OO-c1 bases reduces the extent of the problem but does not completely alleviate it. As the importance

of dynamic correlation increases, the FCI and DOCI energies differ more. Once static correlation becomes more important than dynamic correlation, the particular structure of the DOCI wave functions causes this difference to decrease. The problems of the DOCI wave function in the dynamic correlation regime can be solved by applying multi-reference perturbation theory [61, 62], or by adding extra determinants in its expansion[22].

To better understand the correspondence between the DOCI wave function in different bases and the FCI wave function, Fig. 3.3(c) shows the overlap between both wave functions in the MO, OO, and OO-c1 bases in the STO-3G basis set. This figure illustrates the failure of DOCI in the dynamic correlation regime. At shorter bond distances and near equilibrium, DOCI performs well as it basically acts as a correction for the dominant RHF ground-state. At large internuclear separation, in the strong correlation limit, we again find high overlap between DOCI and FCI wave functions. In the dynamic correlation regime the overlap is much lower with a minimum of about $|\langle \mathrm{DOCI(OO)}|\mathrm{FCI}\rangle|^2 = (0.86)^2 = 0.74$ around 1.7 Å, pointing out that the FCI wave function carries important contributions from configurations outside the DOCI space. Note that orbital optimisation from the MO to the OO basis does reduce the range of bond distances where these problems occur, but does not eliminate the effects of dynamic correlations completely. Also note that the poor overlap persists, however shifted towards shorter R. Remarkably, the overlap between the Mmin or $\mathrm{Mmin_{CISD}}$ based DOCI wave function and the FCI wave function is significantly better than the OO based one (see Fig. 3.3(d)) although the Mmin and $\mathrm{Mmin_{CISD}}$ based DOCI wave functions do not yield the lowest energies (see Fig. 3.3(b)). This is consistent with the previous reports [63, 64] that energy minimisation alone does not guarantee finding the wave function most similar to the FCI one. The OO basis is designed to lower the energy and will do so by focussing on those determinants that assist it maximally whereas the treatment of (incipient) static correlation is less important. The Mmin basis, on the other hand, capitalises maximally on zero seniority determinants typically important to properly treat static correlation. Breaking the symmetry as in the OO-c1 basis does improve the quality of the wave function in the dynamic correlation regime. Note that Fig. 3.3(c) shows that even the DOCI(MO) wave function has significantly higher overlap with the FCI wave function than the DOCI(OO) one for $2.1\text{Å} \leq R \leq 2.5\text{Å}$. To conclude, one should be cautious when performing energy optimisation, as this process may reduce the overlap with the exact wave function, even if a variational method is used (see Fig. 3.3(c)).

Although the Mmin and $\mathrm{Mmin_{CISD}}$ bases significantly improve the overlap of the DOCI wave function with the FCI wave function in the dynamic correlation regime compared with the OO, and even OO-c1 orbitals, there still remains a small discrepancy at intermediate bond distances (with a minimum of $|\langle \mathrm{DOCI(Mmin)}|\mathrm{FCI}\rangle|^2 = (0.94)^2 = 0.88$). In an attempt to improve the DOCI wave function, extra determinants from the CIS and CISD spaces are

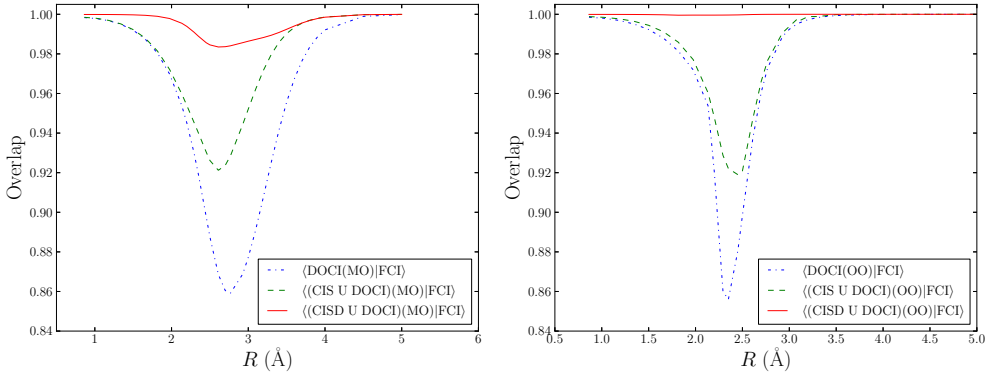

Figure 3.6: Overlap of the DOCI, (CIS ∪ DOCI), (CISD ∪ DOCI) wave function with the FCI wave function in the (a) MO and (b) OO bases for the BeH_2 molecule in the STO-3G atomic basis set. R is the distance of the stretched Be-H bonds.

now added to the Slater determinant expansion. This leads to the hybrid (CIS ∪ DOCI) and (CISD ∪ DOCI) wave functions, respectively. Fig. 3.6 shows the overlap between the DOCI, (CIS ∪ DOCI), and (CISD ∪ DOCI) wave functions and the FCI one, for the MO (Fig. 3.6(a)) and OO bases (Fig. 3.6(b)). These figures show that the overlap improves dramatically upon inclusion of broken pair excitations, again consistent with the described importance of dynamic correlation. This agrees with the fact that second order perturbation theory (MP2) improves on the description of dynamic correlation by including doubly excited determinants both inside and outside DOCI space. The advantage of methods that unite DOCI and truncated CI spaces is that, compared to FCI, the number of determinants remains smaller. For instance, in the case of BeH_2, the number of determinants required in the STO-3G (CISD ∪ DOCI) and FCI methods are 227 and 1225, respectively, while the overlap between the (CISD ∪ DOCI) and FCI wave functions remains consistently large over the entire bond-breaking curve (see Fig. 3.6(b)).

3.3.2 New approximate DOCI methods

I. Truncated DOCI

DOCI is a powerful method for the description of static correlation, but unfortunately still scales exponentially as it is a complete CI method albeit in electron-pair space. As in standard one-electron excitation based CI, it is therefore of interest to examine whether a truncated DOCI approach is viable. Henceforth,

truncated DOCI wave functions will be denoted by CI$\bar{\text{S}}$, CI$\bar{\text{S}}\bar{\text{D}}$, etc., for a single reference closed-shell determinant supplemented with either all single electron-*pair* excitations or all single and double electron-*pair* excitations respectively. DOCI then corresponds to CI$\bar{\text{S}}\bar{\text{D}}\bar{\text{T}}\bar{\text{Q}}\ldots\bar{K}$. To analyse how much information of the DOCI wave function remains in the truncated DOCI wave functions, the overlap between both is computed as well as the corresponding energies during the bond breaking of the N_2 molecule and the symmetric stretch of the BeH_2 molecule (see Figs. 3.7, 3.8, and 3.9). The MO basis obtained from a Hartree-Fock calculation with the 6-31G atomic basis set is used for all analyses in this subsection as the MO basis is the commonly used reference for one-electron excitation based CI.

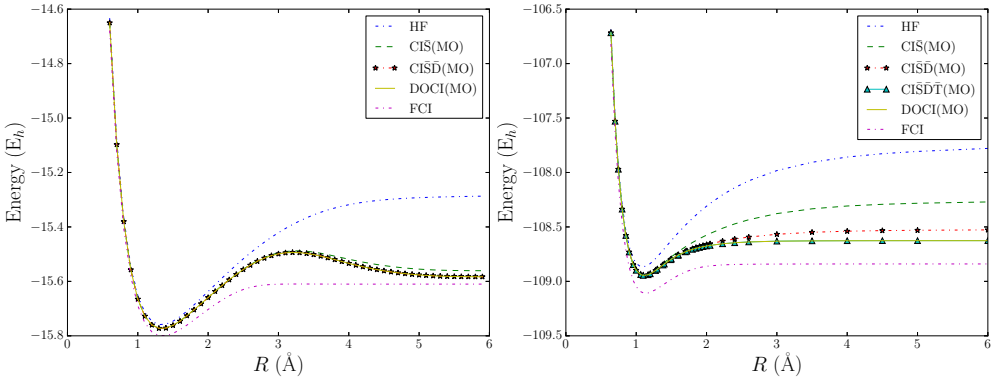

(a) BeH_2 (b) N_2

Figure 3.7: Potential energy curves for the symmetric stretch of (a) linear BeH_2 and (b) the N_2 molecule, at the RHF, CI$\bar{\text{S}}$, CI$\bar{\text{S}}\bar{\text{D}}$, DOCI and FCI levels of theory with 6-31G based MO orbitals. For N_2 the CI$\bar{\text{S}}\bar{\text{D}}\bar{\text{T}}$ method is also included. R is the length of the stretched bond.

Fig. 3.7 shows that the truncated DOCI methods yield energies fairly close to the DOCI result although the required level of truncation varies (N_2 requiring up to three electron-pair excitations whereas for the other molecule CI$\bar{\text{S}}\bar{\text{D}}$ largely suffices). Note that Fig. 3.7(a) shows a clear hump in the DOCI(MO) energy, reminiscent of what was found in Fig. 3.3(a) where a minimal basis set was used. The overlap of the truncated DOCI and DOCI wave functions is depicted in Fig. 3.8. It is clear that at small and intermediate bond distances single electron-pair excitations alone are able to describe the DOCI wave function with high accuracy. However, at larger bond distances single and double electron-pair excitations are needed for BeH_2, and even single, double and triple electron-pair excitations must be considered for N_2. There the overlap with DOCI is almost perfect over the entire range of distances. Finally, Fig. 3.9 shows the sum of the squares of the coefficients of the RHF

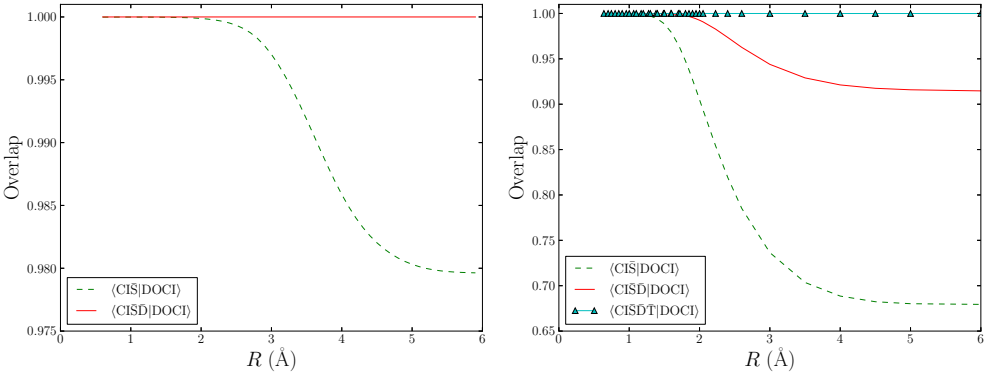

(a) BeH_2 (b) N_2

Figure 3.8: Overlap of the $\text{CI}\bar{\text{S}}$ and $\text{CI}\bar{\text{S}}\bar{\text{D}}$ wave function with the DOCI one using 6-31G based MO orbitals for the symmetric stretch of (a) linear BeH_2 and (b) the N_2 molecule. For N_2 the overlap with the $\text{CI}\bar{\text{S}}\bar{\text{D}}\bar{\text{T}}$ wave function is also included. R is the length of the stretched bond.

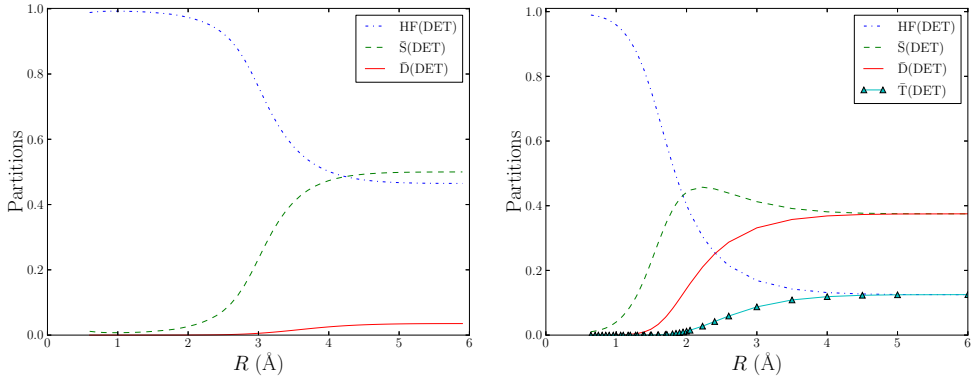

(a) BeH_2 (b) N_2

Figure 3.9: Sums of squared Slater determinant coefficients of different excitation levels in the DOCI wave function using 6-31G based MO orbitals for the symmetric stretch of (a) linear BeH_2 and (b) the N_2 molecule. R is the length of the stretched bond.

determinant (RHF(DET)), and all single ($\bar{\text{S}}$(DET)) and double ($\bar{\text{D}}$(DET)) electron-pair excited determinants of the DOCI wave function for the BeH_2 and N_2 molecules. For N_2, also the sum of the squares of the coefficients of triple electron-pair excited determinants ($\bar{\text{T}}$(DET)) are included. This reflects the amount of information of the DOCI wave function that is contained in its

parts. The figure confirms the trends expected from the earlier findings: RHF performs well at short bond distances and the contributions of higher excited determinants to the DOCI wave function become larger as the bond distance increases.

II. Approximate hybrid DOCI

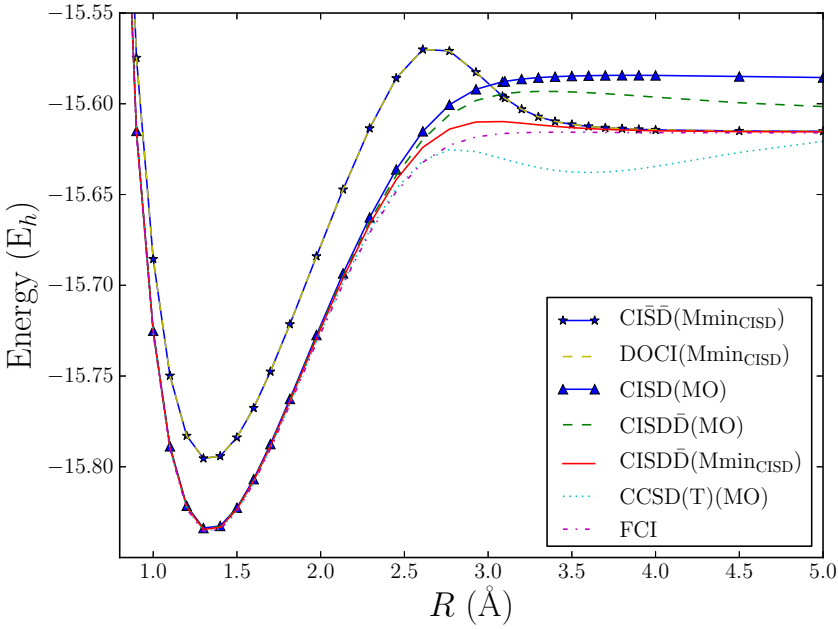

Figure 3.10: Potential energy curve for symmetric stretching of BeH_2 using the CIS$\bar{\text{D}}$, DOCI and CISD$\bar{\text{D}}$ methods in the seniority number minimising basis (Mmin$_{\text{CISD}}$) and CISD, CISD$\bar{\text{D}}$ and CCSD(T) methods in the MO basis with FCI as reference. All calculations were performed with the cc-pVDZ atomic basis set. R denotes the Be-H bond length.

On the one hand, hybrid methods based on the addition of disjoint determinant spaces to supplement the DOCI wave function, as described above in section II. and previously in [22], still scale in a less than desirable way with system size. On the other hand, fairly good approximations to DOCI are possible by truncating DOCI to lower excitation levels only, as put forward in section I.. Combining truncation of DOCI and extending it with electron-pair breaking determinants from standard one-electron excitation based CI, we come naturally to approximate methods that incorporate some lower *one-electron* excitations of a reference along with electron-*pair excited* determinants from DOCI. Examples

of such combinations are the CISD$\bar{\text{D}}$ and CISD$\bar{\text{D}}\bar{\text{T}}$ levels of theory, where CISD is augmented with two electron-*pair* excited determinants or two and three electron-*pair* excited determinants respectively. CISD$\bar{\text{D}}$ is therefore a subset of CISDQ where, among the quadruple excitations, only those determinants are included that correspond to excitations of two electron-*pairs*. In this way, it is possible to add many relevant higher excitations in a computationally feasible way. This can be combined with the seniority number minimising basis which is obtained through a fast iterative process and yet improves the description of the electronic structure in the static correlation regime (see Fig. 3.10). Seniority minimisation using a CISD wave function allows a further gain in speed compared to seniority number minimising directly in the approximate hybrid space as the CISD wave function contains fewer determinants compared to most approximate hybrid methods. The advantage of the present type of approximate hybrid methods is thus that the computational cost scales much more favourably with system size (in this case polynomial scaling, see Table 3.2) providing accurate energies at much smaller cost (e.g., CISD$\bar{\text{D}}$ for BeH_2 in the cc-pVDZ basis set contains 5986 Slater determinants compared to the 4096576 Slater determinants included in the FCI wave function).

Table 3.2: Number of determinants, N_{det}, for a selection of discussed methods for BeH_2 and N_2 in cc-pVDZ, together with the percentage of the FCI determinants contained.

	BeH_2		N_2	
Methods	N_{det}	$\frac{N_{det}}{N_{det}(\text{FCI})}100$	N_{det}	$\frac{N_{det}}{N_{det}(\text{FCI})}100$
CI$\bar{\text{S}}$	64	0.002	148	$1.100\ 10^{-8}$
CI$\bar{\text{S}}\bar{\text{D}}$	694	0.017	4558	$3.250\ 10^{-7}$
CI$\bar{\text{S}}\bar{\text{D}}\bar{\text{T}}$	2024	0.049	51108	$3.645\ 10^{-6}$
DOCI	2024	0.049	1184040	$8.446\ 10^{-5}$
CISD	5356	0.131	30724	$2.192\ 10^{-6}$
CISD$\bar{\text{D}}$	5986	0.146	35134	$2.506\ 10^{-6}$
CISD$\bar{\text{D}}\bar{\text{T}}$	7316	0.179	81684	$5.826\ 10^{-6}$
(CISD $\cup$ DOCI)	7316	0.179	1214616	$8.664\ 10^{-5}$
FCI	4096576	100	1401950721600	100

Fig. 3.10 shows the symmetric stretching potential energy curve for BeH_2 obtained using the CI$\bar{\text{S}}\bar{\text{D}}$(Mmin$_{\text{CISD}}$), DOCI(Mmin$_{\text{CISD}}$), CISD(MO), CISD$\bar{\text{D}}$(MO), CISD$\bar{\text{D}}$(Mmin$_{\text{CISD}}$) methods for the cc-pVDZ atomic basis set, and the FCI and coupled cluster CCSD(T) methods as references. It shows the improved description of the dissociation limit by adding extra pair excitations to the CISD wave function, and the enhancing effect of the Mmin$_{\text{CISD}}$ basis on those pair excitations. Both CISD$\bar{\text{D}}$ curves lie fairly close to the FCI one but with still a relevant improvement from using the seniority number minimising basis (Mmin$_{\text{CISD}}$). The remaining errors lie in the mE$_h$ scale. Note that CCSD(T) [65, 66] (in the MO basis) does not perform well when static correlation is important. The most significant deviation of the CISD$\bar{\text{D}}$(Mmin$_{\text{CISD}}$) energy from the FCI one is in the regime where dynamic correlation is dominant. This is most likely a remnant of the fact that the Mmin$_{\text{CISD}}$ basis does not yield very

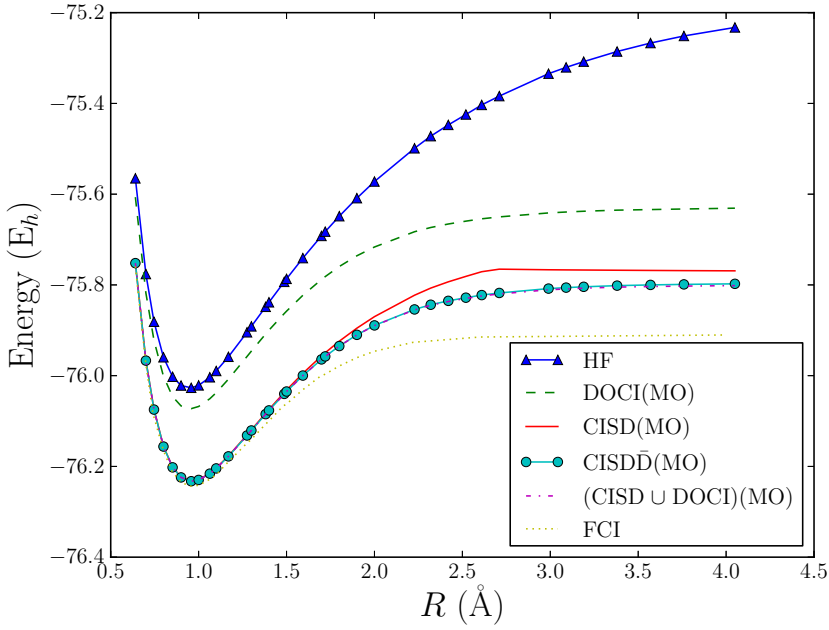

Figure 3.11: Potential energy curve for symmetric stretching of the H-O bonds in H_2O using the RHF, DOCI, CISD, (CISD ∪ DOCI), CISDD̄, and FCI methods using MO obtained from the cc-pVDZ atomic basis set. R denotes the H-O bond length.

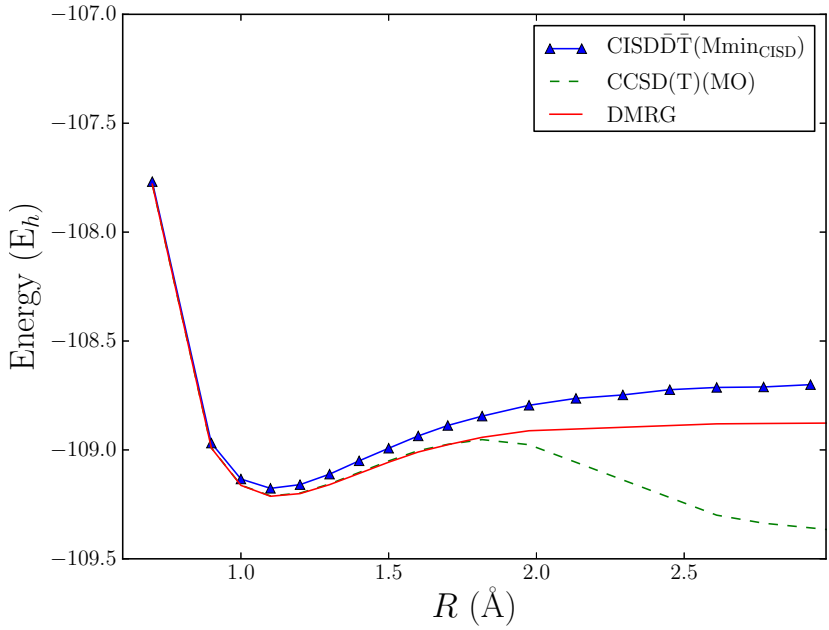

Figure 3.12: Potential energy curve for the N_2 dimer for CCSD(T) in the MO basis, CISDD̄T̄ (Mmin$_{\mathrm{CISD}}$, CAS(10,18)) and DMRG [39, 40] using the cc-pVDZ atomic basis set. R is the interatomic distance.

good energies in this regime. Note also that CISDD̄(MO) still results in a hump somewhat reminiscent of that observed earlier albeit now at larger distances and that it is much smaller. This is thanks to the inclusion of the one electron and unpaired two electron excitations that assist in properly accounting for dynamic correlation. The most important observation in Fig. 3.10 is that the CISDD̄(Mmin$_{\mathrm{CISD}}$) energies follow closely the CISD(MO) energy curve wherever the latter method lies close to FCI and that it lies very close to the DOCI(Mmin$_{\mathrm{CISD}}$) results towards dissociation. In the area between both regimes, the energy error with respect to FCI is the smallest among all methods tested.

Fig. 3.11 shows the potential energy curve of the symmetric stretching of the H_2O molecule at several levels of theory for the cc-pVDZ atomic basis set. It shows that the (CISD ∪ DOCI) and CISDD̄ potential energy curves are indistinguishable over the entire bond length range, and that both methods improve significantly on CISD in the static correlation regime. In general, for systems with not too many electrons, such as H_2O, the difference in energy between this approximate hybrid (CISDD̄) method and the hybrid method (CISD ∪ DOCI) is negligible.

Finally, Fig. 3.12 shows the potential energy surface for N_2 in the cc-pVDZ basis. The methods compared are CCSD(T) in the MO basis and the CISD$\bar{\text{D}}\bar{\text{T}}$ (Mmin$_{\text{CISD}}$, CAS(10,18)). Density matrix renormalisation group (DMRG)[39, 40] energies with FCI accuracy are added as a reference. CCSD(T) performs better at equilibrium and intermediate bond distances, but the approximate hybrid method outperforms CCSD(T) in the dissociation limit. The basic implementation of our routines made us resort to an active space of 10 electrons in 18 orbitals for N_2 in cc-pVDZ. This was probably the reason why CISD$\bar{\text{D}}\bar{\text{T}}$ (Mmin$_{\text{CISD}}$) is less accurate at equilibrium (see Fig. 3.12).

3.4 Conclusions

The orbital dependence of DOCI wave functions and energies has been scrutinised. This is done firstly by comparing the DOCI energies, obtained using different bases, among each other and with reference FCI energies, and secondly by studying wave function overlaps. The straightforward use of molecular orbitals often results in rather poor DOCI energies and wave functions. To ameliorate this, a technique based on simulated annealing (SA) is described to search for the optimal single-particle basis that globally minimises the energy. This approach is found to significantly reduce the energy difference between DOCI and the FCI wave function, especially in the dynamic correlation regime. The SA approach is computationally, however, too costly and it is shown that an orbital optimisation algorithm minimising the seniority of the CISD wave function, is an efficient alternative yielding nearly as good results, especially in the static correlation regime. Moreover, this basis often results in better overlap with the reference wave functions despite a slightly higher energy than that obtained with the SA optimised basis. This shows that better agreement in wave function and energy do not always coincide.

Next, a set of new methods related to DOCI has been introduced. The first type of methods are truncated DOCI methods where the level of pair excitations considered is reduced to e.g., only one pair, two pairs etc., much like in one electron excitation based CIS, CISD, ... The results obtained using this method show that static correlation, as present near bond dissociation, is already captured with a limited level of excitations. Dynamic correlation is not properly accounted for at this level. In order to properly describe dynamic correlation, in the second set of methods these truncated DOCI methods are supplemented with determinants obtained from unpaired electron excitations resulting in methods that combine e.g., one and two pair excitations from the determinants contained in DOCI with all unpaired one and two electron excitations. The resulting methods scale polynomially with system size, making them computationally attractive and affordable for larger systems.

In the next chapter we delve deeper into the realms of reaction mechanism, and charge transfer. This is done by constraining the configuration interaction

solutions to a fixed particle number on parts of the molecule. This allows a study of the charge transfer behavior of different methods during dissociation and at the dissociation limit. Interestingly enough, low seniority wave functions such as DOCI provide more accurate and better chemical predictions than CISD, for chemically relevant observables such as the chemical potential and hardness. DOCI also predicts the correct integer charges at the dissociation limit as opposed to most approximative methods, which fail to generate a derivative discontinuity at integer charges and consequently predict fractional charges at the dissociation limit.

Chapter 4

Constrained Configuration Interaction Theory

In this chapter, wave functions are constrained to a given Mulliken population on specific atoms in the molecule. This makes it possible to investigate the behaviour of approximative methods with respect to reaction mechanisms, charge transfer, the chemical potential and hardness. These are all concepts used, among others, in the context of conceptual density functional theory (DFT)[67, 68]. A method to extract them for multiconfigurational wave functions is discussed.

The Mulliken population constrained CI calculations are performed by adding a Lagrangian multiplier to the non-relativistic quantum chemical Hamiltonian. Results are shown for a set of constrained CI-calculations that impose different Mulliken populations on parts of the NO^+ molecule. Particularly interesting are the constrained full configuration interaction (FCI) calculations of strongly stretched molecules and atoms separated by an infinite distance. These calculations reveal derivative discontinuities and jumps of the chemical potential caused by the integer nature of electrons, those results provide also a direct computational proof of the piece-wise linear behavior of the energy for fractionally charged atoms without the use of ensembles as predicted by Perdew et. al. [69]. These results have deep implications for the electronegativity equalization method (EEM) [70, 71]. This method assumes a quadratic dependence of the energy on the charge, however Cioslowski et. al. [72] showed that for some molecules such as LiH this quadratic dependence is constrained to a very small region, leading to inaccurate predictions of the electronegativity equalization method. Furthermore, it is shown how infinitesimal perturbations of the Hamiltonian can cause very big changes in the electron density of the wave function. Improved understanding of those effects can lead to an extra criterion for the validation of new functionals for density functional theory (DFT), and other approximative methods. As an example different truncated

CI methods are compared with the FCI results. It is shown that configuration interaction with single and double excitations from a reference (CISD) fails completely for the description of charge transfer at large bond lengths. This is in contrast with the doubly occupied configuration interaction (DOCI) wave function, which provides a qualitatively correct description of charge transfer, and a chemical potential which is quantitatively closer to the exact one. This supports the claim that wave functions based on the seniority quantum number are better suited to describe dissociation processes than wave functions based on the excitation procedure (see chapter 2).

4.1 Introduction

The pioneering work of Perdew et. al. [69, 73] proved that the exact energy of fractionally charged systems should be piece-wise linear between subsequent integer electron values, and that derivative discontinuities occur with corresponding jumps of the chemical potential (related to the orbital energies). This work boosted interest in fractionally charged systems, which recently increased further after it was shown that many currently available approximative methods fail to describe dissociated systems [74–76]. Furthermore, problems arise for systems as small as infinitely stretched H_2 and $H_2{}^+$ in a minimal basis set due to static correlation, and self-interaction error respectively. This strongly reduces the faith one could have for applying those approximative methods to more challenging problems such as transition metal complexes, charge transfer in complex organic molecules, ... where no comparison with exact methods is available. Many approximate methods such as density functional theory (DFT), and variational 2rdm find a minimum of the potential energy curve somewhere between two integer populations because of the convex character of their potential energy curve [42, 77–79] instead of the piece-wise linear energy curve of the exact energy. Hartree-Fock (HF) obtains the minimal energy at the correct integer electron charge but for the wrong reasons, the potential energy curve as a function of the electron population is concave. A better understanding of the charge dependence of the molecular energy already led to new and improved functionals for DFT[80], and adaptations of the EEM to correctly predict integer charges for the dissociated parts of a molecule [81]. The fractional charge problem has also led to the concept of many electron self-interaction [82]. A reason for this is that approximative methods do not have the flexibility to describe the discontinuous behavior of the exchange-correlation functional in strongly correlated systems [83]. Furthermore recently exact conditions for the energy of systems with fractional populations were derived [74, 77, 84], and some theoretical extensions of many body theory and the approximate density functionals were made to fractional populations [85].

In this work, a method is proposed that gives access to the chemical potential of particular atoms in a molecule in the form of a set of Lagrange multipliers

associated with the constraints of particular populations on the atoms. Dissociating an atom from the rest of the molecule allows us to investigate the charge transfer process for a number of different wave functions for fractionally charged atoms and how they approach the dissociation limit. Essentially we use part of the molecule as a reservoir of electrons for the atom of interest, so the entire system remains integer charged but almost dissociated parts can be fractionally populated, and the charge on all parts is tunable with Lagrange multipliers. This makes it possible to perform calculations without using an ensemble to generate the exact energies and wave functions for fractionally charged atoms. The derivative discontinuities and piece-wise linear character show up, and the predicted gaps exhibited by the chemical potential when an integer number of electrons is crossed, is found. This improves the understanding of fractionally charged systems in a CI setting, and can boost further improvements of approximative methods such as the development of new functionals to adequately describe the features presented underneath. In the next section, the theory is introduced, starting with the formalism of Lagrange multipliers after which the constraints are derived to impose Mulliken populations on a predefined set of atoms. However one should be cautious because the absolute magnitude of the atomic Mulliken populations yielded by population analysis have little physical meaning, since they display a high degree of sensitivity to the atomic basis set with which they were calculated[86], but consideration of their relative values can yield useful information[87], provided a consistent basis set is used for their calculation. Furthermore when the overlap between the different orbital sets, upon which the constraint is imposed is low or zero as is the case for the dissociation limit, the Mulliken populations coincide unambiguously with the exact value of the electron population obtained from the electron number operator for the relative fragments. After the theory the results are discussed, they mainly focus on the dissociation of some selected dimers because many interesting things happen in the dissociation limit, while the fractional populations that occur naturally around equilibrium are restored to integer populations of electrons on all dissociated fragments. This formalism allows us to generate exact computational results of systems with a fractional electron number without using ensembles. The fractional charges shift gradually to integer charges when the bonds are dissociated towards the non-interacting limit. The more interaction between orbitals, the easier charge transfer can be forced as will be visible through the increasing slope of the chemical potential, upon dissociation. The exact results are compared with results from truncated CI wave functions with different properties such as the configuration interaction wave function based on single and double excitations from a reference (CISD) which is good for dynamic correlation but is not size extensive and fails for strongly correlated systems, and the doubly occupied configuration interaction wave function (DOCI) which is a better wave function for the description of static correlation [23]. It is shown that the DOCI wave functions describes much better the charge transfer process and the properties at infinite distance in comparison with excitation based wave functions such as CISD. Furthermore

it will be shown that infinitesimal changes in the Hamiltonian can cause huge changes in the density. This is similar to the big changes in the electronic structure that occur for fractionally charged nuclei[88]. From all this, it becomes more and more clear that there is a need for better scaling methods, that are able to describe significant changes in the density upon infinitesimal changes in the Hamiltonian.

4.2 Theory

It is possible to diagonalize a Hamiltonian under a given set of constraints for the resulting wave function. These constraints can always be expressed as the vanishing expectation value of an operator $\hat{f}_i$ for a given wave function ψ.

$$\langle\psi|\hat{f}_i|\psi\rangle = 0 \tag{4.1}$$

The constraints can be added to the original Hamiltonian and multiplied by a Lagrange multiplier (λ) which makes it possible to tune the importance of the constraints.

$$\hat{\mathcal{H}} = \hat{H} + \Sigma_i \lambda_i \hat{f}_i \tag{4.2}$$

The eigenstates and eigenvalues of the augmented Hamiltonian are explicitly dependent on the Lagrange multiplier.

$$\hat{\mathcal{H}}(\lambda)\,|\psi_n(\lambda)\rangle = \mathcal{E}_n(\lambda)\,|\psi_n(\lambda)\rangle \tag{4.3}$$

After deriving with respect to the Lagrange multipliers, it follows straightforwardly that the constraints are fulfilled at the local extrema of $\mathcal{E}_n(\lambda)$.

$$\frac{\partial \mathcal{E}_n(\lambda)}{\partial \lambda_i} = \frac{\partial \langle\psi_n(\lambda)|\hat{\mathcal{H}}(\lambda)|\psi_n(\lambda)\rangle}{\partial \lambda_i} = \langle\psi_n(\lambda)|\hat{f}_i|\psi_n(\lambda)\rangle = 0 \tag{4.4}$$

Where we made use of the Hellmann-Feynman theorem[4]. From this it also follows that the expectation value of the wave function with respect to the constrained Hamiltonian at these extremal values is equal to the one of the original Hamiltonian. A point to note is that different eigenstates $\psi_n(\lambda)$ have different solutions for the extremal Lagrange multipliers λ_n. However, one is mostly interested in the ground state. Another important point is that the Hamiltonian in eq.(4.2) for $\lambda = 0$ reduces to the original Hamiltonian from which it follows that $\mathcal{E}_n(0) = E_n$, with E_n the eigenvalues of the original Hamiltonian.

For this chapter, we are mainly interested in eigenstates of the non-relativistic quantum chemical Hamiltonian with constraints on the Mulliken populations of the different atoms in the molecule. This makes it possible to study the energy dependence of selected molecules on the electron population assigned to particular atoms in this molecule. A study of this can increase the understanding of reaction mechanisms, chemical bonding, and charge transfer. This chapter

focusses particularly on simulations that gradually dissociate the constrained atoms from the rest of the molecule. Results presented in the next section show the gradual transition of a quadratic to a linear dependence of the energy on the number of electrons. It is found that quadratic energy interpolation models[89] are ideally suited to describe the charge transfer between atoms in a molecule close to their equilibrium distances, while farther apart the ideal energy interpolation model becomes linear. In what follows Greek indices (μ, σ) will denote non-orthogonal atomic orbitals, and latin-indices will denote orthonormal orbitals.

The Mulliken operator is given by[90]:

$$\hat{w}_A^{mul} = \sum_{\sigma \in A, \mu} S^{-1}_{\sigma,\mu} \left|\sigma\right\rangle \left\langle\mu\right| \tag{4.5}$$

Where S^{-1} is the matrix inverse of the overlap of the atomic orbitals and $S^{-1}_{\sigma\mu}$ is a matrix element of S^{-1}. The summation over σ only goes over the atomic orbitals defined centered on A. This is nothing else than the projection operator onto the set of non-orthogonal orbitals defined by A [91]. This follows from the fact that for non-orthogonal bases the dual basis is represented by

$$\left|\mu^*\right\rangle = \Sigma_\sigma S^{-1}_{\sigma,\mu} \left|\sigma\right\rangle \tag{4.6}$$

The identity operator is thus:

$$\hat{\mathbf{I}} = \sum_\sigma \left|\sigma^*\right\rangle \left\langle\sigma\right| = \sum_{\sigma,\mu} S^{-1}_{\mu,\sigma} \left|\mu\right\rangle \left\langle\sigma\right|. \tag{4.7}$$

The projection operator on a set of orbitals A can be constructed from the above equation by limiting one of the summations to orbitals centered on A. If A in eq.(4.5) is equal to the entire set of orbitals, the expectation value of this operator is for any canonical wave function equal to the number of electrons N. The expectation value of the Mulliken operator after acting on it with a many-body wave function becomes:

$$\left\langle\psi\right|\hat{w}_A^{mul}\left|\psi\right\rangle = \sum_{\nu \in A} (PS)_{\nu\nu}. \tag{4.8}$$

Where $\bar{P}$ is the one body reduced density matrix in the atomic orbitals, and the trace is limited to indices corresponding to orbitals contained in A. For the diagonalisation of the Hamiltonian (see eq. (4.2)), one relies mostly on orthonormal single-particle bases such as those from Löwdin orthogonalized orbitals or the molecular orbitals. The basis transformation that transforms the atomic orbitals to an orthonormal set typically consists of an overlap dependent part and an extra unitary transformation.

$$\left|i\right\rangle = \Sigma_\mu C_{i,\mu} \left|\mu\right\rangle = \Sigma_{j',\mu} U_{i,j'} S^{-\frac{1}{2}}_{j',\mu} \left|\mu\right\rangle \tag{4.9}$$

Transforming the Mulliken operator to this basis we obtain:

$$\begin{aligned} \hat{w}_A^{mul} &= \Sigma_{i,j}\Sigma_{\sigma\in A,\mu} S^{-1}_{\sigma,\mu} |i\rangle \langle i|\sigma\rangle\langle\mu|j\rangle \langle j| \\ &= \Sigma_{i,j} |i\rangle \langle j| (\bar{C}\bar{S}\bar{D}_A\bar{C}^\dagger)_{i,j} \end{aligned} \tag{4.10}$$

Where the $^-$ bar denotes matrices and $\bar{D}_A$ is a diagonal matrix with ones when the orbital indices correspond to orbitals in the set A and otherwise only zeros. Using the above operator as a constraint in the Hamiltonian causes problems as this operator is not Hermitian. Therefore we construct our constraints based on the Hermitian operator:

$$\hat{w}_A^{mul,Herm} = \frac{\hat{w}_A^{mul} + \hat{w}_A^{mul\dagger}}{2} \tag{4.11}$$

The constrained Hamiltonian becomes thus:

$$\hat{\mathcal{H}}(\lambda) = \hat{H} + \Sigma_i \lambda_i (\hat{w}_i^{mul,Herm} - N_i) \tag{4.12}$$

Where N_i stands for the Mulliken population one wants to find on atom i. Note also that one should take care that always $\Sigma_i N_i = N$, from this it follows that for diatomic systems only one constraint is necessary as the population on the other atom is trivially $N - N_0$.

The energies obtained by diagonalizing the Hamiltonian in eq.(4.12) can be decomposed into atomic and interaction contributions[92][93]. If this is done when the constraints are exactly fulfilled, one can study the dependency of atomic energies as a function of fractional electron number. The total energy expressed as a function of the first and second order density matrices expressed in atomic orbitals using chemical notation and rearranged by atomic contributions becomes:

$$\begin{aligned} E^{tot} &= \sum_{A<B} \frac{Z_A Z_B}{R_{AB}} + \sum_{\mu\nu} \rho_{\mu\nu}\langle\nu|\hat{T}|\mu\rangle - \sum_A \sum_{\mu\nu} \rho_{\mu\nu}\langle\nu|\frac{Z_A}{r_A}|\mu\rangle \\ &+ \frac{1}{2}\sum_A \sum_B \sum_{\mu\in A} \sum_{\rho\in B} \sum_{\nu\sigma}^{all} \Gamma_{\mu\nu\rho\sigma}\langle\mu\nu|\rho\sigma\rangle. \end{aligned} \tag{4.13}$$

According to Mayer et. al. [92] the above energy can be decomposed in atomic and interaction contributions. Performing this decomposition the energy that can be assigned to a particular atom can be written as:

$$E_A = \sum_{\mu\in A\nu\in A} \rho_{\mu\nu}\langle\nu|\hat{T}|\mu\rangle - \sum_{\mu\in A\nu\in A} \rho_{\mu\nu}\langle\nu|\frac{Z_A}{r_A}|\mu\rangle + \frac{1}{2}\sum_{\mu\in A}\sum_{\rho\in A}\sum_{\nu\sigma}^{all} \Gamma_{\mu\nu\rho\sigma}\langle\mu\nu|\rho\sigma\rangle. \tag{4.14}$$

Accordingly the interaction energy of two atoms A and B can be written as:

$$\begin{aligned} E^{AB} &= \frac{Z_A Z_B}{R_{AB}} + 2\sum_{\mu\in A,\nu\in B} \rho_{\mu\nu}\langle\nu|\hat{T}|\mu\rangle - \sum_{\mu\in A,\nu} \rho_{\mu\nu}\langle\nu|\frac{Z_B}{r_B}|\mu\rangle \\ &- \sum_{\mu\in B,\nu} \rho_{\mu\nu}\langle\nu|\frac{Z_A}{r_A}|\mu\rangle + \sum_{\mu\in A}\sum_{\rho\in B}\sum_{\nu\sigma}^{all} \Gamma_{\mu\nu\rho\sigma}\langle\mu\nu|\rho\sigma\rangle. \end{aligned} \tag{4.15}$$

4.2.1 Computational details

In order to improve the understanding of charge transfer, charge distribution, derivative discontinuities, fractionally charged systems and strong changes in the density upon infinitesimal changes in the Hamiltonian (see eq. (4.12)), the bond stretching of the NO^+ molecule is considered. The used atomic basis set is minimal STO-3G. This is sufficient because the studied effects are similar in all basis sets. To check this we did some limited calculations in 6-31G that indicated the same effects. Another reason to use small basis sets that contain no diffuse functions is the use of the Mulliken operator as the operator that counts the number of electrons that can be contributed to a particular atom, as it is well known that problems arise when the Mulliken operator is used in combination with diffuse basis functions [94]. A further limitation of this approach is that when the number of electrons on a particular atom is increased above the threshold where the free electron energies start to mingle in the energy spectrum, the energy keeps increasing while it should become plateau-wise, fortunately for not too large electron numbers on a particular atom this effect plays no role. The energies shown are the energies of the total molecular system and of atomic energies obtained by the energy decomposition eq. (4.14) and eq. (4.15). However, one should be cautious as there is no unambiguous way to assign energies to the bath and system separately when a lot of interaction is present, as the energy of the system always depends on the properties of the electron bath when correlation is involved. Fortunately at stretched distances when the interaction is low the differences between different energy decomposition algorithms diminish quickly. All one- and two-particle integrals needed are generated by the PSI4 package [38]. For the interface with PSI4 we used the Hamiltonian class of CheMPS2[39, 40].

For all CI calculations a general CI solver is used that takes as argument a list of Slater determinants. These Slater determinants, in turn, are built from an orthonormal set of orbitals that may correspond to molecular orbitals or some other orthonormal set. All determinants are encoded as binary strings in terms of this set and the Hamiltonian is represented in the Slater determinant basis. After providing the Lagrange multipliers and the Mulliken populations that act as constraints, the extra terms of eq.(4.12) are added to the corresponding one-particle matrix elements that already incorporate the nuclear attraction and the kinetic energy. The variational problem of determining the Slater determinant coefficients is then solved using an implicitly restarted Arnoldi algorithm [54] to locate the chosen number of low lying energy states. For every set of populations that one wants to find on the atoms, it is necessary to scan the energy surface that depends on the set of Lagrange multipliers for those multipliers where the energy is extremal for all multipliers, At those points in the Lagrange multiplier parameter space all the constraints of the wave function are fulfilled and the expectation value of the Hamiltonian in eq.(4.12) will be equal to the expectation value of the non-relativistic quantum chemical Hamiltonian. To efficiently find those extremal values a golden section

search method or conjugate gradient method is used. In the next section we investigate the dependence of FCI energies and some truncated CI energies as a function of changes of the Mulliken populations of dimers with geometries ranging from equilibrium to the dissociation limit. In this limit one of the atoms will act as an electron basin for the other. This makes it possible to investigate fractionally charged atoms, derivative discontinuities, avoided level crossings and other interesting phenomena, which depend on the integer nature of the electron. In the next section the results that were obtained by solving eq.(4.12) are shown and discussed.

4.3 Results and Discussion

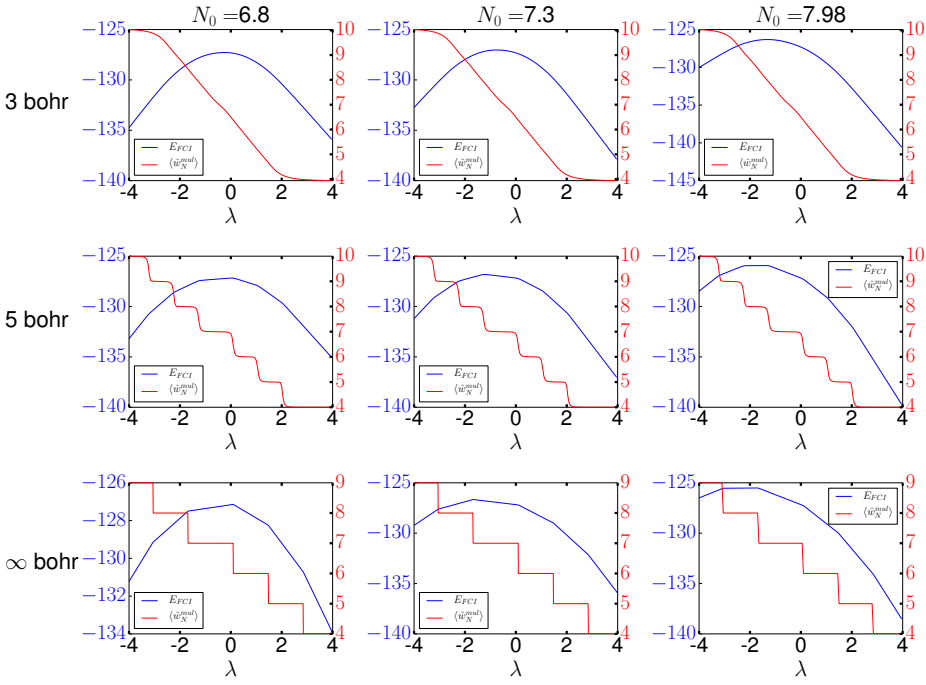

Figure 4.1: The dependency of the FCI energy and the Mulliken population on the Lagrangian multiplier λ is depicted for the NO^+ molecule, the rows of subplots correspond to internuclear distances of 3, 5 bohr and an infinite distance respectively, and the columns correspond to constrained populations on the nitrogen atom of $N_0 = 6.8$, 7.3 and 7.98 respectively.

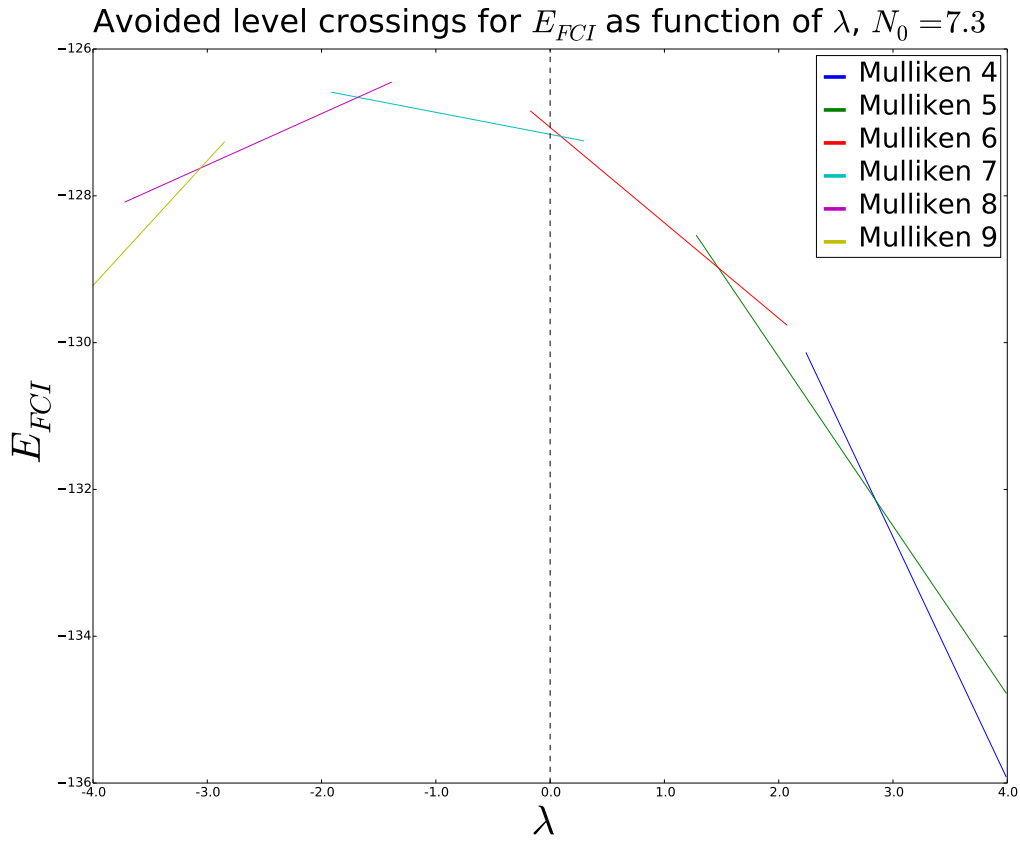

Figure 4.2: The dependency of the FCI energy on the Lagrangian multiplier λ is depicted, when $N_0 = 7.3$ for the lowest energies corresponding to different Mulliken populations in the forty lowest eigenvalues at an internuclear distance of ∞ bohr.

To obtain a first impression of the problem at hand, the λ dependence of the expectation value of eq.(4.12) is depicted in Fig. 4.1 for the NO^+ molecule at bond distances of 3, 5 bohr and at the limit of an infinite separation. This is nothing more than the energy of the constrained Hamiltonian as a function of λ. To construct the matrix elements for the infinite separation limit we have generated the matrix elements and overlaps for a N-atom and for a O-atom separately, and have combined them in one molecule by shifting the labelling of the oxygen matrix elements and overlap with the number of orbitals centered on the N-atom, this creates a molecule in which the orbitals corresponding to the O atom are not aware of the orbitals on the N atom

neither by the matrix elements nor in the overlap. This setup simulates exactly the infinitely separated NO^+ molecule when the number of electrons is set to 14. The calculations are performed for three different constrained Mulliken populations $N_0 =: 6.8$, 7.3 and 7.98. For all bond distances close enough to the equilibrium distance (1.225 Å), such as three bohr, this energy dependence will be parabolic with a unique well defined maximum, at this maximum the constrained Mulliken population is fulfilled for the resulting wave function, and the expectation value of the constrained Hamiltonian (eq. 4.12) is equal to the Hamiltonian without constraints. This maximum is linearly shifted as a function of the constraint N_0, when N_0 becomes larger it shifts to lower λ, when N_0 becomes lower it shifts to larger λ. This happens because the λ parameter is a measure for the energy shift of the single-particle levels on which the Mulliken operator of eq.(4.11) is assigned to act. Higher single-particle energy means less occupied and a lower contribution to the Mulliken population. If one looks at the behaviour of the Mulliken population as a function of λ, one also sees this linear behaviour, except for the two extrema of small and big Mulliken populations, which are in fact finite size effects because the used basis set only supports a maximum of 10 electrons on one atom, luckily the Mulliken populations of interest are between 6 and 8, this has no further effect on our results of interest. If one increases the bond distance to 5 bohr, the λ dependence of the Mulliken charge is still continuous, but a stepwise character becomes noticeable. At the infinite distance limit, one sees that the Mulliken charge as a function of λ has become a real step-wise function. This implies that the λ dependence of the Mulliken charge has become discontinuous, which is a remarkable result because it shows that infinitely small changes of the Hamiltonian (eq. 4.12), can cause very large changes in the electron density of the resulting wave function. This also goes for the original non-relativistic Hamiltonian as the results of $N_0 = 6.8$ show, the Mulliken charge on N for the dimer on an infinite distance is 7. We see that introducing a small perturbation of a positive λ will make the wave function jump to an electron distribution of 6 electrons on the N atom and 8 on the O atom. Introducing a small negative λ will not change the Mulliken charge and it remains at 7, until λ has become negative enough to conquer the threshold to jump to an electron distribution of 8 electrons. The behaviour of the energy at infinite distance as a function of λ is piece-wise linear between different integer Mulliken populations, and the extrema of the curve depend on the value of N_0 as it becomes the point where the value shifts from the Mulliken population defined by $\lfloor N_0 \rfloor$ to the Mulliken population defined by $\lceil N_0 \rceil$. The constraints also determine the slope of the piece-wise linear pieces neighbouring the extrema as they become more and more flat when an integer is approached (see the results of $N_0 = 7.98$ at infinite distance). This is because when N_0 passes through 8 the next maximum should occur at the λ value where the Mulliken population jumps from 8 to 9, and the slope of the piece between 8 and 9 has changed from positive to negative, while going through zero at the integer point. This makes it difficult to accurately determine maxima of the curve when the constraints approach

integer points.

The angles of the piece-wise linear parts of the λ dependency of the FCI energy on an infinite distance are created by avoided level crossings. This is clearly revealed by Fig. 4.2, which depicts all the lowest eigenvalues corresponding to eigenstates with a different Mulliken population in the 40 eigenstates with the lowest energy values for a constraint of $N_0 = 7.3$. The figure can be understood by remarking that changing λ has no influence on the relative position of states corresponding to the same Mulliken population they remain parallel for all values of λ, but states with different Mulliken populations have different slopes as a function of λ, and the absolute value of the slope increases the farther away the Mulliken population of the state is from the constraint N_O, with a positive slope for larger Mulliken populations and a negative slope for smaller Mulliken populations. From this it follows that the lowest energy corresponding to states with a higher Mulliken population grows faster for increasing λ than for those with a smaller Mulliken population. So states with a different Mulliken population grow to each other, intersect and switch their relative position. This dynamics generates the typical piece-wise linear behaviour of the ground-state energy. Another observation that one can make from Fig. 4.2 is that far from those intersection points all 40 energetically lowest states have the same Mulliken population, near the intersection points states with Mulliken populations that differ by one with the Mulliken population of the lowest eigenstate start to enter the window of the 40 energetically lowest eigenstates. The λ values where those events happen can be easily deduced from the figure. Finally for convenience we have added a dashed vertical line to the figure at $\lambda = 0$, to make it easier to see where the unperturbed Hamiltonian is situated for the NO^+ molecule at infinite distance. The ground state has Mulliken population seven (as expected), but states with Mulliken population six are not much higher in energy, and the intersection point of the states with Mulliken populations 6 and 7 lays very close to the unperturbed Hamiltonian. It can be concluded that a well behaved maximum value of the energy as a function of the Lagrange multiplier of the constrained Hamiltonian can almost always be found, except for the integer electron populations at infinite distance. This concludes the study of the λ dependency of the expectation value of the constrained Hamiltonian (see eq.(4.12)).

Next the energy dependence on some relevant chemical parameters such as the electron number and chemical potential is studied. Those results are generated from wave functions that are converged to one of the above described maxima. This means that the used wave functions have the same expectation values for the constrained and unconstrained non-relativistic quantum chemical Hamiltonian, and the constraints are exactly fulfilled (except for the infinite distance limit). Figs. 4.3, 4.4, 4.5 depict the behaviour of the constrained ground-state FCI wave function when the bonded NO^+ molecule is gradually dissociated to infinity. The dependency of the ground-state FCI energy on the Mulliken population and the Lagrange multiplier λ (chemical potential) that

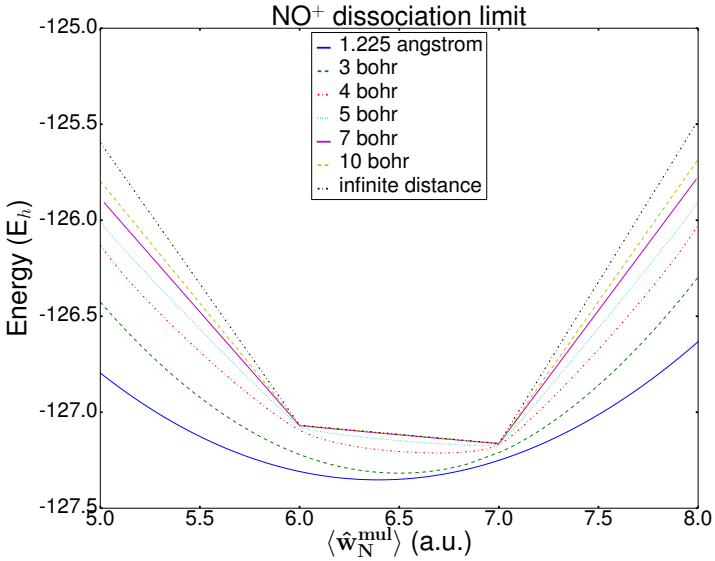

Figure 4.3: Depicts the FCI energy of the NO^+ molecule as a function of the Mulliken population on the N atom.

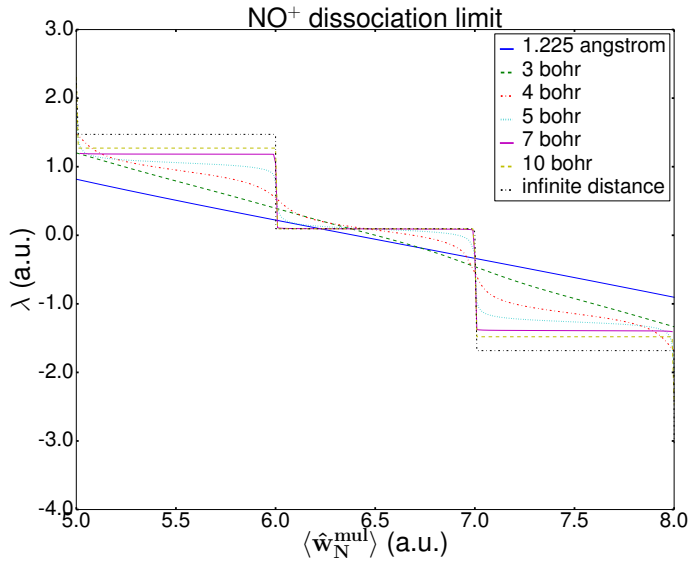

Figure 4.4: Fig. 4.4 depicts the relative chemical potential of the NO^+ molecule as a function of the Mulliken population on N.

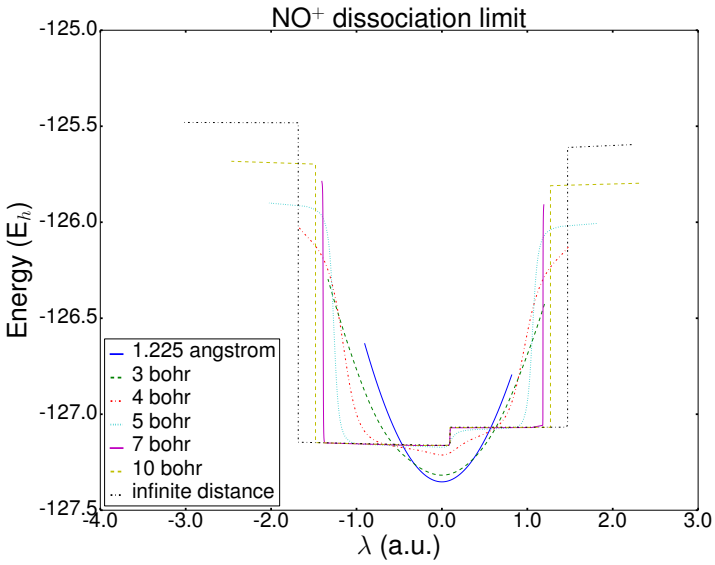

Figure 4.5: Fig. 4.5 depicts the FCI energy of the NO^+ molecule as a function of the chemical potential λ (in a.u.) at fulfilled constraints.

maximizes the energy for a given constrained (Mulliken population on the N atom) are depicted, together with the dependency of the chemical potential on the Mulliken population at fulfilled constraints. Fulfilled constraints means that every point represented in each of the graphs of Figs. 4.3, 4.4, 4.5 corresponds to a maximum of the energy as a function of λ for a given constraint. All constraints are fulfilled except in the case of infinitely separated atoms. For this case the Mulliken population of the wave function is always integer, and it is impossible to generate fractional populations due to the fact that the wave function will always collapse to one of the neighbouring integer populations. This happens due to computer limitations, which make it impossible to reach the desired accuracy to make states with neighbouring integer Mulliken populations exactly degenerate at an infinite distance. If this would be possible, all states with fractional populations between the two integer points can be constructed with the same energy, as linear combinations of the two integer states. But because of floating point round off errors the degeneracy is never exactly reachable and the wave function collapses to one of the neighbouring integer populations. However the energy remains continuous and therefore it is possible to assign the obtained energies to those that would arise if the necessary degeneracies could be obtained exactly to generate the fractional populations at infinity.

The dissociation limit is investigated by comparing the results from bond distances ranging from equilibrium to the infinite distance limit. Fig. 4.3

depicts the energy dependence as a function of the Mulliken charge on the atoms for the chosen bond distances for NO^+. At equilibrium distance this behaviour is a nice broad parabola with the minimum at fractional population. When the bond distance is gradually increased the minimum is gradually shifted to the integer value of 7 as expected. The curvature is also changing and becomes gradually piece-wise linear, with each piece having a different slope. There are no intersections of curves corresponding to different distances and it seems that for a given Mulliken charge the energy at higher distances starting from equilibrium is always higher because of the reduced possibilities to reduce the energy by charge transfer. The gap between the FCI energy at equilibrium distance and the one at an infinite distance is the lowest at Mulliken charge 7. This is logical because the equilibrium curve needs to move away from its minimal value to reach a Mulliken charge of 7 (so the energy increases), and for the system at an infinite distance it is the minimal value. Furthermore as remarked above, the relative ordering in energy is preserved and all other curves are sandwiched in this interval. Fig. 4.3 gives in fact a computational proof of the piece-wise linear character of the dependency of the FCI energy on the number of electrons (As there is no overlap between orbitals associated to the nitrogen atom with orbitals associated to the oxygen atom, the Mulliken population of the nitrogen atom corresponds exactly to the number operator on the nitrogen atom). We repeat the remark that all constraints are exactly fulfilled for all curves in Fig. 4.3 except for the system at infinite distance, but because the energy remains continuous upon infinitesimal changes of λ (only big changes of the Mulliken value occur) the energy depicted in Fig. 4.3 can be trusted as the real energy of the wave function with the fractional charge. Another view of observing this is by looking to the other curves that gradually approach the infinite distance limit and remarking that for all other curves the constraints are exactly satisfied.

Also of interest are the effects of dissociating a bond on the dependency of the chemical potential on the Mulliken distribution of the two atoms. Taking a look to Fig. 4.4 reveals that at small bond distances it is easier to transfer charges from one atom to the other, this is revealed in a linear dependence of the chemical potential on the Mulliken population with a small slope. When the bond distance is increased the slope of the chemical potential increases. This can be understood by noting that at a larger bond distance one needs to have a larger chemical potential to reduce the population at a given atom, or a stronger negative chemical potential to increase the population on the atom, because it becomes more and more difficult to generate the desired population transfer for larger bond distances. The slope of the chemical potential as a function of the Mulliken population can be seen as the difficulty for population transfer. The larger the more difficult population transfer will be. Remark that for bond distances around equilibrium geometry the willingness to transfer charges is equal for all Mulliken populations. At larger bond distances the λ dependency becomes wavy. In between integer values there is more willingness to transfer charges (smaller differences of the chemical potential are sufficient), because

the wave function starts to dislike more and more fractional populations. And there is also a very small willingness to transfer charges when the population is close to an integer value. In fact the slope of the chemical potential as a function of the Mulliken population for long bond distances can be seen as the chemical hardness [67, 95]. Because for large bond distances the Mulliken operator on an atom becomes equal to the number operator on this atom. This means that the slope corresponds in fact to the second derivative of the FCI energy with respect to the particle number on that atom, which is equal to the chemical hardness and that is a measure of the possibility of charge transport. At the infinite distance limit the willingness to transfer charges is zero at integer populations (slope of the chemical potential is ∞), and for fractional populations the charge transfer is instantaneous as the blockade to transfer charges is zero. This shows that fractional populations at an infinite distance are extremely unstable as the wave function will always collapse towards neighbouring integer populations and then remain there. All fractional populations are compressed to an infinitely small interval at the same chemical potential defined by the shift necessary to make the energies corresponding to neighbouring integer Mulliken populations degenerate.

Fig. 4.5 shows the dependence of the FCI energy on the chemical potential. A first remark is that at smaller bond distances the resulting curves have less width than for bigger distances. This means that at smaller distances one needs a smaller range of the chemical potential to cover the Mulliken populations from 5 till 8. Furthermore one sees that at smaller distances the curve is a well behaving parabola, but at larger distances it gets smeared out and the curve starts to make strange quirks. The curves with a lower minimum also cross all the curves with a higher minimum. This means that for smaller bond distances, increasing the chemical potential has a strong effect on the FCI energy. Also for larger distances the effect becomes less continuous and different regimes arise, one where small changes in the chemical potential can induce large shifts of the energy while there are also areas were changing the chemical potential has not much effect on the energy.

It is important to note that all energy values given in Fig. 4.3 are for the total NO^+ molecule. This is because the energy of the constrained system (N) always depend on the properties of the bath (ionization potential and electron affinity of the bath) when entanglement is present. It is only possible to disentangle them unambiguously when the system is separated from the environment/bath by an infinite distance. However at an infinite distance it is impossible to impose the constraints exactly. The bath acts in this approximation as a pure reservoir of electrons and the properties of the bath have no influence on the energy of the constrained system. However based on eq.(4.14) it is possible to calculate the energy that can be attributed to a particular atom. The results of this decomposition for a nitrogen atom separated from a oxygen atom with distances 2.32 bohr (experimental equilibrium geometry), 3 bohr, 4 bohr, 5 bohr, 8 bohr and the infinite distance limit is represented by Fig. 4.6. The corresponding

results for the oxygen atom are represented by Fig. 4.7. Finally the interaction energy between both atoms calculated with eq.(4.15) is depicted in Fig. 4.8. This figure gives a direct computational proof without the use of ensembles of the piece-wise linear dependency of the atomic energy on the number of electrons. Another interesting observation is that for stretched distances the interaction between the atoms is significantly lower for integer electron values that correspond to one neutral atom. This in correspondence with the above described results that indicated an increased stability of the integer electron values at stretched distances.

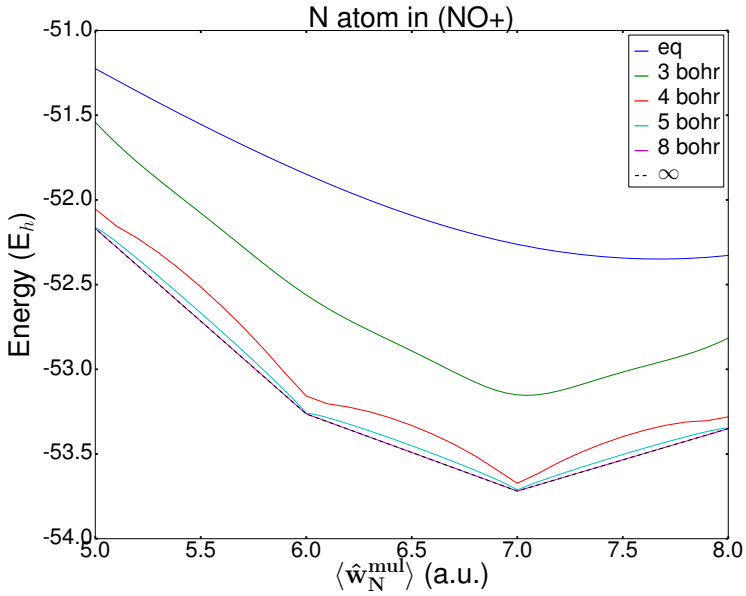

Figure 4.6: The contribution of the nitrogen atom to the FCI energy of the NO^+ molecule at 5 bohr as a function of the Mulliken population on the nitrogen atom. The dashed line is the linear interpolation of the atomic nitrogen energies with integer electron number in a basis set consisting of the STO-3G nitrogen basis functions together with the STO-3G oxygen basis functions at a distance of 5 bohr.

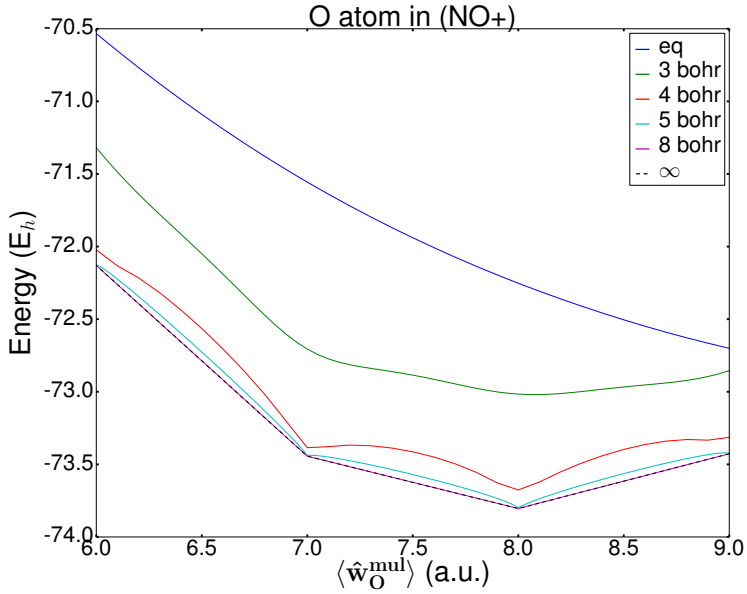

Figure 4.7: The contribution of the oxygen atom to the FCI energy of the NO^+ molecule at 5 bohr as a function of the Mulliken population on the oxygen atom. The dashed line is the linear interpolation of the atomic oxygen energies with integer electron number in a basis set consisting of the STO-3G oxygen basis functions together with the STO-3G nitrogen basis functions at a distance of 5 bohr.

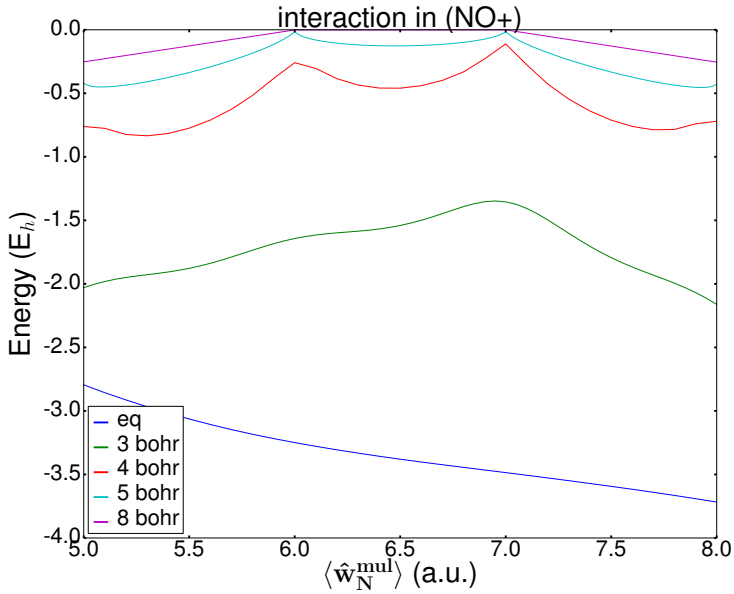

Figure 4.8: The interaction energy of the oxygen atom and the nitrogen atom of the NO^+ molecule at 5 bohr as a function of the Mulliken population on the nitrogen atom.

Table 4.1: Bond distances in Å and formation enthalpies in $kJmol^{-1}$ for NO^+, N_2, CN^- and CO.

	NO^+	N_2	CN^-	CO
H_f $(kJmol^{-1})$	198.22	0.	195.98	-110.53
Bond distance (Å)	1.066	1.098	1.177	1.128

Furthermore the derived chemical potential is relative with respect to the reservoir used. As an example Fig. 4.9 depict the E_{FCI} as a function of the Mulliken population and chemical potential, and the chemical potential as a function of the Mulliken population for constrained populations on the N atom for a O, C and N environment at 2, 3 and 4 bohr, together with the effect of constraining the Mulliken population on the C atom in a CO molecule. The interesting point to note is that the energy depends still quadratically on the Mulliken population for the NO^+ molecule at those distances but the CN^- molecule is already in the stepwise regime. This can be related to the fact that the bond of CN^- is weaker, and more easily broken. In fact one can see that the bond-distance where the linear dependence of the chemical potential on the population starts to shift to a stepwise character as the start of the bond breaking, and one can state that the bond is fully broken when the full stepwise

regime is reached. As a reference Table (4.1) depicts the bond distances and formation enthalpies of CN^-, N_2, NO^+, and CO.

Table 4.2: Energies and Mulliken populations (in a.u.) of truncated CI methods for the NO^+ molecule at 100 bohr in the STO-3G atomic basis-set. The used orthonormal basis is the one coming from a previous restricted Hartree-Fock calculation unless otherwise given.

	CISD	CISDD	SEN(0,2)	DOCI	DOCI(FNO)	DOCI(OO)	DOCI(MMIN)	FCI
E - E_{FCI} (mE_h)	115	115	177	273	272	133	134	0
Mul. pop. (N atom)	6.85	6.85	6.75	6.79	6.78	7.	7.	7.

To conclude this chapter the above derived machinery is used to compare some selected truncated CI methods. First table 4.2 compares the Mulliken populations and energy values of different truncated CI wave functions for the NO^+ molecule with a bond length of 100 bohr. As can be seen the DOCI wave function is the only truncated CI wave function that has the correct Mulliken population of 7 on each atom separately, provided the MMin and OO bases are used. This indicates again the importance of using appropriate single-particle bases for the DOCI wave function. Another interesting fact is that both DOCI(OO) and DOCI(MMIN) have higher energies than the CISD wave function but they have correct Mulliken populations while the CISD wave function has fractional charges. Secondly Fig. 4.10 compares DOCI(OO), and CISD to the FCI behaviour under the constrained of particular Mulliken populations. It is remarkable that CISD has lower energy (see Fig. 4.10(a)) but the chemical potential of DOCI(OO) is closer to the FCI value (see Fig. 4.10(b)). Furthermore, the λ dependency of the energy of the DOCI wave function is more similar to the FCI one. CISD predicts the minimum energy at a fractional Mulliken population of 6.018 while the FCI and DOCI wave function correctly predict a Mulliken population of 7. From the above and Fig. 4.10 one can conclude that DOCI performs better than CISD for this problem as the DOCI wave function gives much better estimates for important chemical descriptors such as the chemical potential, Mulliken population and the charge transfer process. As a final conclusion, it can be stated that it is more relevant to test an approximative method on the accuracy of chemical descriptors such as the chemical potential, charge transfer and distribution than absolute energy values as they do not provide any guarantee for the correctness of the wave function.

4.4 Conclusions

It is computationally proven that the energy of a system with fractional electron number is given by straight lines with different slopes connecting integer electron numbers. From this it follows that at the integers the energy has a derivative discontinuity and the density is discontinuous. It was also shown that

at the extremal values of the energy as a function of the Lagrange multiplier for two infinitely separated systems very small perturbations can produce very big changes in the density. The derived method allows also to investigate the willingness of charge transfer by capturing electrons from other atoms. An investigation of the dissociation limit revealed that around equilibrium distances this possibility is large. For intermediate bond distances this possibility lowers, and for the biggest bond distances an asymmetry arises between fractional and integer populations. Far from integer populations it becomes easier and easier to transport charges, but closer to integer populations it becomes increasingly difficult. This results in stable integer populations and unstable fractional populations. The method proposed in this chapter can also be used to improve the understanding of chemical bonds, how far they reach, when they are broken and when charge transfer is possible. The results of constraining the population on the N atom coupled to a selected number of different baths revealed that the charge transfer of CN^- becomes suboptimal at much shorter distances than for example N_2 and NO^+. It is remarkable that many approximative methods (such as CISD) predict ground-state wave functions with a fractional population for infinitely separated pieces while this behaviour is in denial of the dynamics of the exact wave function. It could be interesting to create more approximative methods that have the correct behaviour for this problem, as this is important for many chemical relevant observables such as charge transfer and reaction mechanics, instead of focussing blindly on lower energies. The comparison of the CISD, and the DOCI(OO) behaviour with the FCI wave function showed that the DOCI wave function predicts chemical potentials closer to the FCI one, and has a better description of the charge transfer process, with a correct value of 7 for the Mulliken population of the infinitely separated system. It is expected that this is due to the size consistency of the DOCI wave function. Finally it is concluded that fractional charge behaviour and transport over large bond distances is a challenging test for the accuracy of approximate methods.

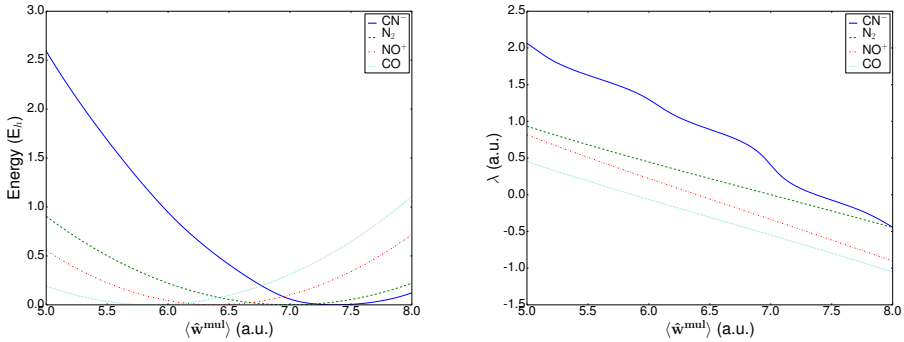

(a) 2 bohr

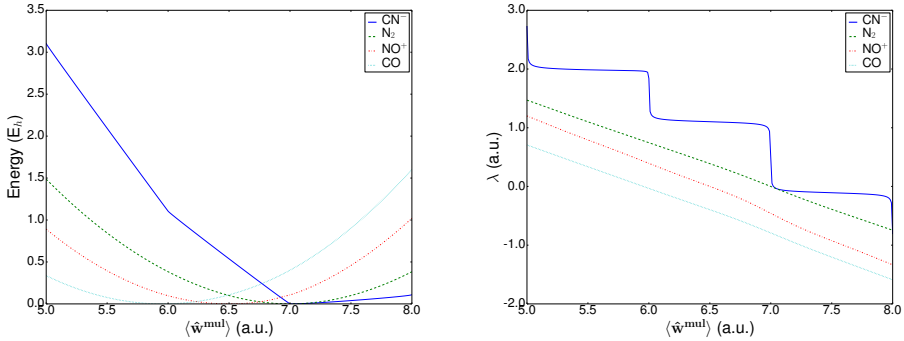

(b) 3 bohr

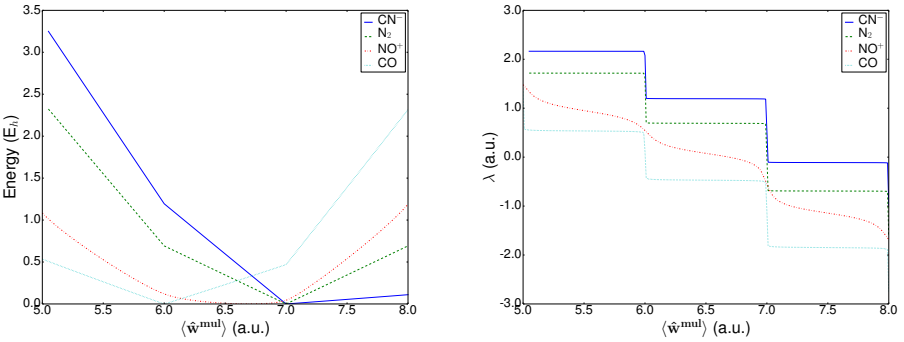

(c) 4 bohr

Figure 4.9: The first column of Fig. 4.9(a), 4.9(b) and 4.9(c) depicts the FCI energy with respect to the molecular ground-state energy as a function of the Mulliken population $\langle \hat{\mathbf{w}}^{\mathbf{mul}} \rangle$, the second column depicts the Lagrange multiplier λ at fulfilled constraints as a function of $\langle \hat{\mathbf{w}}^{\mathbf{mul}} \rangle$. The bond distances considered are 2, 3 and 4 bohr respectively for each row of plots. $\langle \hat{\mathbf{w}}^{\mathbf{mul}} \rangle$ corresponds to the Mulliken population on N (except for C in CO).

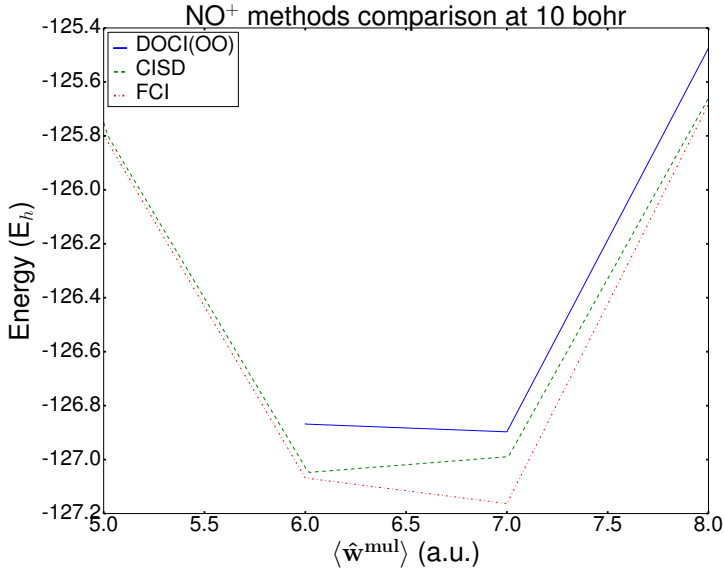

(a)

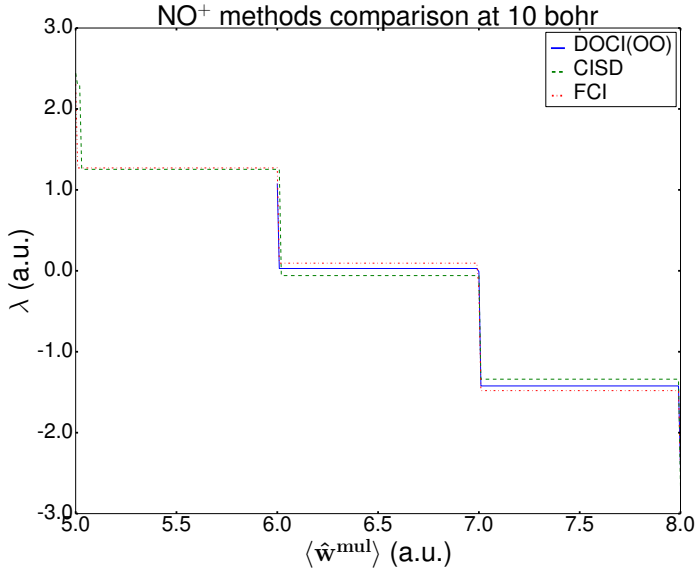

(b)

Figure 4.10: Fig. 4.10(a) depicts the DOCI(OO), CISD, and FCI energy as a function of the Mulliken population on the N atom at a distance of 10 bohr from the O atom, and Fig. 4.10(b) depicts the dependency of the chemical potential of the DOCI(OO), CISD and FCI wave function on the Mulliken population on N at a distance of 10 bohr from the O atom.

Chapter 5

Variational optimization of the second order density matrix corresponding to a seniority-zero configuration interaction wave function

[1] In this chapter, a different approach to the electronic structure problem is studied. A direct variational determination of the second order (two-particle) reduced density matrix is performed. The second order reduced density matrix corresponds to a many-electron system, under the restricted set of the two-index N-representability $\mathcal{P}$-, $\mathcal{Q}$-, and $\mathcal{G}$-conditions. In addition, a set of necessary constraints is imposed such that the two-particle density matrix must be derivable from a DOCI wave function, i.e. a singlet wave function for which the Slater determinant decomposition only contains determinants in which spatial orbitals are doubly occupied. We rederive the two-index N-representability conditions first found by Weinhold and Wilson and apply them to various benchmark systems (linear hydrogen chains, He, N_2 and CN^-). This work is motivated by the fact that a DOCI wave function captures in many cases the bulk of the static correlation. Compared to the general case, the structure of doubly-occupied two-particle density matrices causes the associated semidefinite program to have a very favorable scaling as K^3, where K is the number of spatial

[1] Has been previously published as: W. Poelmans, M. Van Raemdonck, B. Verstichel, S. De Baerdemacker, A. Torre, L. Lain, G. E. Massaccesi, D. R. Alcoba, P. Bultinck, and D. Van Neck. *Variational optimization of the second order density matrix corresponding to a seniority-zero configuration interaction wave function*, 2015: Journal of Chemical Theory and Computation, 11:4064-4076.

orbitals. Since the doubly-occupied Hilbert space depends on the choice of the orbitals, variational steps for the two-particle density matrix optimisation are interspersed with orbital-optimization steps (based on Jacobi rotations in the space of the spatial orbitals). We also point to the importance of symmetry breaking of the orbitals when performing calculations in a doubly-occupied framework.

5.1 Introduction

The main problem in many-body quantum mechanics, which comprises nuclear physics, quantum chemistry and condensed matter physics, is the exponential increase of the dimension of the Hilbert space with the number of particles. Of course, a complete diagonalization in many-electron space, Full Configuration Interaction (FullCI), will provide the exact answer, but is prohibitively expensive except for small systems[4]. The challenge has therefore been to develop approximate methods capturing the relevant degrees of freedom in the system without an excessive computational cost, i.e., with a polynomial increase.

Many approximate methods have been developed over the years[4, 6]. A standard approach is to start from a mean-field (Hartree-Fock) solution and improve on this by adding excitations of increasing complexity (Coupled Cluster Theory[96, 97], Perturbation Theory[97], etc.). These single-reference methods only work well when the wave function is dominated by a single Slater determinant. In bond-breaking processes, e.g., the Hartree-Fock (HF) approximation is qualitatively wrong and a multi-reference approximation is needed[98]. In Multiconfiguration Self-Consistent Field (MCSCF)[4, 99], one expands the wave function as a linear combination of Slater determinants (configurations), and the Configuration Interaction (CI) coefficients and the orbitals building the Slater determinants are optimized together.

In the last decades, new methods for strongly correlated systems were developed. Density Matrix Renormalization Group (DMRG)[100–103] can be made as accurate as FullCI while extending the computational limits far beyond what is possible with classical FullCI. Projected symmetry-broken Hartree-Fock[104–106] is a mean-field scaling method in which all symmetries are broken. While it is difficult to recover symmetries once they are lost, a self-consistent variation-after-projection technique can overcome these issues[107].

Another technique, which has received renewed interest, is Doubly-Occupied Configuration Interaction (DOCI)[24, 25, 28, 29, 52, 108]. In DOCI, all spatial orbitals are doubly occupied by two (spin-up/down) electrons. This is also called a seniority-zero wave function, where the seniority number equals the number of unpaired electrons[20, 24, 109]. FullDOCI is an exact diagonalization of the Hamiltonian (like FullCI), but in the Hilbert space restricted to Slater determinants where every spatial orbital is doubly occupied or empty. However, FullDOCI still suffers from factorial scaling. The interest in DOCI is motivated

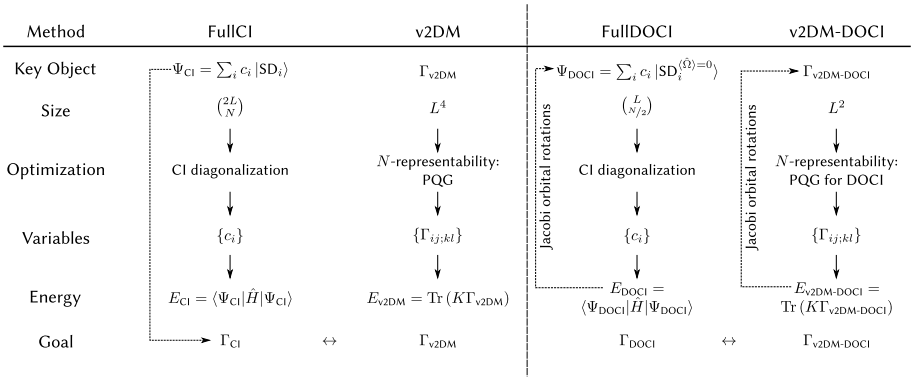

Figure 5.1: Overview of the methods used in this chapter. SD denotes a Slater determinant, Γ is the two-particle density matrix and K the associated reduced Hamiltonian. $\hat{\Omega}$ is the seniority-number operator.

by its ability to describe the static correlation[21, 24]. It was also realized that DOCI is the lowest rung on the ladder in a seniority hierarchy leading to FullCI[21, 110]: If one adds configurations of higher seniority (2, 4, ...) in the wave function expansion, one will eventually reach the FullCI limit[21, 24]. Furthermore, the chemical relevance of this approach is supported by the fact that General Valence Bond with perfect pairing is a special case of DOCI[25]. An efficient and low-scaling approximation to DOCI is available, the so-called AP1roG (antisymmetric product of 1-reference-orbital geminals)[25, 108, 111] or pair-Coupled Cluster Doubles[28, 29] (which are equivalent). However, like any truncated CI wave function, DOCI is orbital dependent[21, 24, 110] and approximations such as AP1roG need an orbital optimizer. This leads to a deterioration of the scaling.

In this chapter, the focus lies on an alternative way to approximate the ground state of an N-electron system, that concentrates on the two-particle reduced density matrix (2RDM)[112, 113]. The 2RDM contains all relevant information, such as all expectation values of two-particle operators, but its dimension only scales as K^4, with K the dimension of spatial orbital space. Unlike Density (Matrix) functional theory, the energy can be expressed as an exact yet simple linear function of the 2RDM and a variational optimization can be used to find the ground-state energy (v2RDM)[114] where the optimization should be constrained to the class of 2RDM's[115, 116] that can be derived from an antisymmetric wave function, the so-called N-representable 2RDM's. The wave function is not used in this method and we directly start from a 2RDM. The burden is shifted to the characterization of the N-representable class of 2RDM's. Since the complete characterization is known to be a QMA complete problem[117], one has to use a set of necessary but not (in general) sufficient conditions on the 2RDM. The role of the necessary N-representability

conditions is to enforce that the resulting 2RDM approximates a wave function derivable 2RDM as good as possible. Since the minimization of the energy is carried out over a too large set, one obtains lower bounds to the exact energy[116].

The most commonly used conditions are derived from positive semidefinite Hamiltonians and express the fact that their expectation value in any wave function should be positive. Examples are the standard $\mathcal{P}$, $\mathcal{Q}$ and $\mathcal{G}$ two-index conditions[116, 118] and the $\mathcal{T}_1$ and $\mathcal{T}_2$ three-index conditions[119]. Other kinds of conditions exist, such as subsystem constraints[120] or active-space constraints[121]. The resulting constrained optimization problem is known as a semidefinite program (SDP). This is a well-known class of convex optimization problems[122–124] for which a large collection of solvers exists[125]. We created a SDP solver tailored to v2RDM[126–134]: for the two-index conditions, basic matrix operations exhibit a scaling of $(2K)^6$ and for the three-index conditions, $(2K)^9$. Unfortunately, on the whole the v2RDM approach is not competitive with e.g. CCSD methods[135, 136].

In this chapter, it is aimed to study the 2RDM variational optimization restricted to DOCI space, henceforth called v2RDM-DOCI. In Figure 5.1, we give an overview of all relevant methods. We impose necessary conditions that the wave function from which the 2RDM was derived has the form of a DOCI wave function. This greatly simplifies the structure of the 2RDM[137, 138] and leads to a much better scaling. We need an orbital optimization scheme, which is far from trivial as the energy landscape contains a large number of local minima, many very close to or even degenerate with the ground-state energy[110]. The same problem is also encountered in MCSCF[139, 140] and Valence Bond Self-Consistent Field[141] where several solutions are at hand[139, 142, 143]. Most wave-function based methods[25, 28, 29, 52, 108] construct the 2RDM in order to perform the orbital optimization. In contrast, the v2RDM method works directly with the 2RDM, although the 2RDM is not completely N-representable. If a good starting point in the orbital space is available, a simple local minimizer can generate good results. In this chapter an algorithm utilizing Jacobi rotations[144] to avoid the full simultaneous four-index transformation of the two-electron integrals is utilized.

In section 5.2, we introduce the v2RDM framework and apply it to the case of a DOCI wave function, leading to v2RDM-DOCI. In section 5.3 the orbital optimization scheme is presented in detail, and in section 5.4 results are shown for several illustrative test cases, including situations where a multi-reference description is needed. A summary and discussion is presented in section 5.5.

5.2 Variational 2RDM

We use Greek letters $\alpha, \beta, \ldots$ to denote a general spinorbital ($2K$ in total), and Roman letters $a, b, \ldots$ to denote the spatial part of the orbital (K in total).

With the bar symbol, the pairing partner of a state is denoted: a and $\bar{a}$ form a pair of the same spatial orbital with opposite spin, e.g. $a \equiv a\uparrow$ and $\bar{a} \equiv a\downarrow$. All summations run over either the spinorbitals or the orbitals depending on whether Greek or Roman summation indices were used. We use the second-quantization formalism: $\hat{a}^\dagger_\alpha$ ($\hat{a}_\alpha$) denotes a creation (annihilation) operator for a fermion in the single particle state α. It is also assumed that the many-electron wave function is real.

5.2.1 General v2RDM

In second quantization a Hamiltonian with pairwise interactions can be written as[5]

$$\hat{H} = \sum_{\alpha\beta} \langle\alpha|\hat{T}|\beta\rangle\, \hat{a}^\dagger_\alpha \hat{a}_\beta + \frac{1}{4} \sum_{\alpha\beta\gamma\delta} \langle\alpha\beta|\hat{V}|\gamma\delta\rangle\, \hat{a}^\dagger_\alpha \hat{a}^\dagger_\beta \hat{a}_\delta \hat{a}_\gamma \ , \tag{5.1}$$

where $\hat{T}$ and $\hat{V}$ are the one- and two-particle operators. It should be noted that the formalism is completely general for Hamiltonians up to two-body interactions. However, all operators discussed concern field-free, non-relativistic electronic structure Hamiltonians, i.e. $\hat{T}$ is the sum of the electronic kinetic energy and the nuclei-electron attraction, whereas $\hat{V}$ represents the interelectronic Coulomb repulsion. The ground-state energy can be expressed solely in terms of the second order reduced density matrix (2RDM)[112] Γ,

$$E = \mathrm{Tr}\,(K\Gamma) = \frac{1}{4} \sum_{\alpha\beta\gamma\delta} K_{\alpha\beta;\gamma\delta} \Gamma_{\alpha\beta;\gamma\delta} \ , \tag{5.2}$$

where

$$\Gamma_{\alpha\beta;\gamma\delta} = \langle\psi|\hat{a}^\dagger_\alpha \hat{a}^\dagger_\beta \hat{a}_\delta \hat{a}_\gamma|\psi\rangle \ , \tag{5.3}$$

$$K_{\alpha\beta;\gamma\delta} = \frac{1}{N-1} \left(T_{\alpha\gamma}\delta_{\beta\delta} - T_{\beta\gamma}\delta_{\alpha\delta} - T_{\alpha\delta}\delta_{\beta\gamma} + T_{\beta\delta}\delta_{\alpha\gamma}\right) + V_{\alpha\beta\gamma\delta} \ , \tag{5.4}$$

with $|\psi\rangle$ the ground-state wave function for the Hamiltonian (5.1) with matrix elements $T_{\alpha\beta} = \langle\alpha|\hat{T}|\beta\rangle$ and $V_{\alpha\beta\gamma\delta} = \langle\alpha\beta|\hat{V}|\gamma\delta\rangle$. N is the number of particles, and (5.3) and (5.4) define matrix elements of the 2RDM and the reduced Hamiltonian $K_{\alpha\beta;\gamma\delta}$, respectively. Some elementary properties are easily derived,

$$\Gamma_{\alpha\beta;\gamma\delta} = -\Gamma_{\beta\alpha;\gamma\delta} = -\Gamma_{\alpha\beta;\delta\gamma} = \Gamma_{\beta\alpha;\delta\gamma} \ , \tag{5.5}$$

$$\Gamma_{\alpha\beta;\gamma\delta} = \Gamma_{\gamma\delta;\alpha\beta} \ , \tag{5.6}$$

$$\mathrm{Tr}\,(\Gamma) = \frac{1}{2} \sum_{\alpha\beta} \Gamma_{\alpha\beta;\alpha\beta} = \frac{N(N-1)}{2} \ . \tag{5.7}$$

The idea of variational 2RDM is to minimize the energy functional (5.2). The 2RDM is a much more compact object than the wave function as its matrix

dimension scales as K^2. However, a direct approach produces unrealistic energies[114]. The variation has to be limited to the class of N-representable 2RDM's[115, 116]: for every 2RDM, there must exist a wave function $|\psi\rangle$ such that (5.3) is satisfied. Unfortunately there is no straightforward way of establishing whether a 2RDM is N-representable. The necessary and sufficient conditions are formally known[145, 146]: a 2RDM is N-representable if and only if, for every two-particle Hamiltonian $\hat{H}_\phi$, the following inequality is true:

$$\mathrm{Tr}\,(K_\phi \Gamma) \geq E_0(\hat{H}_\phi)\ , \tag{5.8}$$

with K_ϕ the reduced Hamiltonian and $E_0(\hat{H}_\phi)$ the exact ground-state energy of the Hamiltonian $\hat{H}_\phi$. This theorem cannot be used as a sufficient condition for N-representability as that would require the ground-state energy of every possible two-particle Hamiltonian $\hat{H}_\phi$, but it can be used as a necessary condition: the theorem (5.8) can be relaxed to Hamiltonians for which a lower bound to its ground-state energy is known. A straightforward choice is

$$\hat{H} = \hat{B}^\dagger \hat{B}, \tag{5.9}$$

a class of manifestly positive semidefinite Hamiltonians. If we restrict $\hat{B}$ to the two-particle space, we find the well-known $\mathcal{P}$, $\mathcal{Q}$ and $\mathcal{G}$ two-index conditions:

1. The $\mathcal{P}$ condition: $\hat{B} = \sum_{\alpha\beta} p_{\alpha\beta} \hat{a}_\alpha \hat{a}_\beta$, for arbitrary $p_{\alpha\beta}$. This trivial condition imposes the positive semidefiniteness of the 2RDM itself:

$$\begin{aligned} \mathcal{P}(\Gamma)_{\alpha\beta;\gamma\delta} &= \langle\psi|\hat{a}^\dagger_\alpha \hat{a}^\dagger_\beta \hat{a}_\delta \hat{a}_\gamma|\psi\rangle \\ \mathcal{P}(\Gamma) &= \Gamma \succeq 0 \end{aligned} \tag{5.10}$$

2. The $\mathcal{Q}$ condition[116]: $\hat{B} = \sum_{\alpha\beta} q_{\alpha\beta} \hat{a}^\dagger_\alpha \hat{a}^\dagger_\beta$, for arbitrary $q_{\alpha\beta}$ leading to

$$\mathcal{Q}(\Gamma) \succeq 0\ , \tag{5.11}$$

where

$$\begin{aligned} \mathcal{Q}(\Gamma)_{\alpha\beta;\gamma\delta} &= \langle\psi|\hat{a}_\alpha \hat{a}_\beta \hat{a}^\dagger_\delta \hat{a}^\dagger_\gamma|\psi\rangle \\ &= \Gamma_{\alpha\beta;\gamma\delta} + (\delta_{\alpha\gamma}\delta_{\beta\delta} - \delta_{\beta\gamma}\delta_{\alpha\delta}) \frac{2\mathrm{Tr}\,(\Gamma)}{N(N-1)} \\ &\quad -\delta_{\alpha\gamma}\rho_{\beta\delta} + \delta_{\beta\gamma}\rho_{\alpha\delta} + \delta_{\alpha\delta}\rho_{\beta\gamma} - \delta_{\beta\delta}\rho_{\alpha\gamma}\ . \end{aligned} \tag{5.12}$$

and the single-particle density matrix (1DM) is defined as

$$\rho_{\alpha\beta} = \langle\psi|\hat{a}^\dagger_\alpha \hat{a}_\beta|\psi\rangle = \frac{1}{N-1} \sum_\lambda \Gamma_{\alpha\lambda;\beta\lambda}\ . \tag{5.13}$$

3. The $\mathcal{G}$ condition[118]: $\hat{B} = \sum_{\alpha\beta} g_{\alpha\beta} \hat{a}^\dagger_\alpha \hat{a}_\beta$, for arbitrary $g_{\alpha\beta}$,

$$\mathcal{G}(\Gamma) \succeq 0 \tag{5.14}$$

with

$$\mathcal{G}(\Gamma)_{\alpha\beta;\gamma\delta} = \langle\psi|\hat{a}^\dagger_\alpha \hat{a}_\beta \hat{a}^\dagger_\delta \hat{a}_\gamma|\psi\rangle = \delta_{\beta\delta}\rho_{\alpha\gamma} - \Gamma_{\alpha\delta;\gamma\beta}\ . \tag{5.15}$$

Furthermore, there are the so-called three-index commutator conditions[119, 134, 147–150] which are computationally much more demanding and are not used here. All these conditions are necessary but not sufficient: the true N-representable space is much more restricted. Because of this, v2RDM will always find a lower bound to the FullCI energy.

The variational optimization of the 2RDM can now be expressed as:

$$\begin{aligned} &\min\left[\mathrm{Tr}\left(K\Gamma\right)\right] \quad \text{while} \\ &\mathcal{P}(\Gamma) \oplus \mathcal{Q}(\Gamma) \oplus \mathcal{G}(\Gamma) \succeq 0 \\ &\mathrm{Tr}\left(\Gamma\right) = \frac{N(N-1)}{2} \ . \end{aligned} \tag{5.16}$$

This optimization problem can be formulated as a semidefinite program (SDP)[132, 133], a class of well-known convex optimization problems[122] for which general-purpose solvers exists[125, 151, 152]. Earlier we developed SDP solvers customized for v2RDM that exploit the specific structure of the problem[126, 129, 130, 153]. Such solvers are much more efficient than the general-purpose solvers. In this chapter a boundary point method[127, 154, 155] is used to solve the SDP problem. In this method, the primal-dual gap is zero by definition, and convergence is reached when both primal and dual feasibility is achieved. The computationally most intensive step in this algorithm is the calculation of the eigenvalues and eigenvectors of the constraint matrices. The computational cost of the program scales as K^6 for floating-point operations and K^4 for memory when using the two-index conditions. A detailed explanation of the solvers can be found in Ref 153.

5.2.2 DOCI tailored v2RDM

We now impose the additional condition that $|\psi\rangle$ in (5.3) is a DOCI wave function. In principle any pairing scheme can be used, but the natural choice is the singlet pairing scheme, in which each spatial orbital is occupied by two electrons of opposite spin. This is based on the assumption that the most important static correlations in a closed-shell molecule can be captured in this way[24]. In CI terms, the wave function can be expanded in Slater determinants where all spatial orbitals are doubly occupied. This is also called a seniority-zero wave function. Formally, the DOCI wave function can be written as

$$|\Psi_{\mathrm{DOCI}}\rangle = \sum_{j=1}^{\binom{K}{\frac{N}{2}}} c_j \prod_{i=1}^{\frac{N}{2}} S^\dagger_{\mathbf{j}(i)} |\theta\rangle \tag{5.17}$$

where $|\theta\rangle$ is the pair vacuum, and $S^\dagger_i = a^\dagger_{i\alpha} a^\dagger_{i\beta}$ is the pair creation operator of the i-th orbital. $\mathbf{j}$ is a vector that maps the $\frac{N}{2}$ pairs to a selected set of

occupied orbitals of the K spatial single-particle orbitals.

$$|\psi\rangle = \sum_{a_1 \ldots a_{(N/2)}} c_{a_1 \ldots a_{(N/2)}} \prod_{k=1}^{N/2} \hat{a}_{a_k}^\dagger \hat{a}_{\bar{a}_k}^\dagger \, |\rangle \ , \tag{5.18}$$

A simple approach would be to project the reduced Hamiltonian (5.4) onto DOCI space and use existing v2RDM codes. However, this does not lead to the desired result as internal consistency conditions on the 2RDM are needed (see below). Also, any computational advantages due to the DOCI structure are lost as the scaling of the program remains unaltered.

It is much more efficient to adapt the N-representability conditions to the DOCI case as they are drastically simplified. The adapted DOCI conditions were already derived by Weinhold and Wilson[137, 138] but to the best of our knowledge never exploited in practical calculations.

Since we work in DOCI space, all operators evaluated between two DOCI wave functions need to have seniority-zero, *i.e.* they cannot change the number of broken pairs. This immediately implies that the 1DM is diagonal and that the chosen set of orbitals is also the set of natural orbitals of $|\psi\rangle$:

$$\begin{aligned} \rho_{ab} \quad = \quad & \langle\psi|\hat{a}_a^\dagger \hat{a}_b|\psi\rangle = \langle\psi|\hat{a}_{\bar{a}}^\dagger \hat{a}_{\bar{b}}|\psi\rangle = \delta_{ab}\rho_a \ , \\ & \langle\psi|\hat{a}_a^\dagger \hat{a}_{\bar{b}}|\psi\rangle = \langle\psi|\hat{a}_{\bar{a}}^\dagger \hat{a}_b|\psi\rangle = 0 \ . \end{aligned} \tag{5.19}$$

Furthermore, it is clear that

$$\rho_a \quad \geq \quad 0 \ , \tag{5.20}$$

$$\sum_a \rho_a \quad = \quad \frac{N}{2} \ . \tag{5.21}$$

A similar simplification occurs for the 2RDM and the $\mathcal{PQG}$ conditions:

1. The $\mathcal{P}$ condition. The operator $\hat{B}$ in eq. (5.9) acting on a DOCI wave functions can create both a seniority-0 and seniority-2 state. The corresponding $\hat{B}^\dagger$ operator can only connect states of the same seniority and therefore block diagonalization will occur. The seniority-0 block is the pair density matrix,

   $$\forall a, b: \quad \langle\psi|\hat{a}_a^\dagger \hat{a}_{\bar{a}}^\dagger \hat{a}_{\bar{b}} \hat{a}_b|\psi\rangle = \Gamma_{a\bar{a};b\bar{b}} = \Pi_{ab} \ . \tag{5.22}$$

   From the positivity of the Hamiltonian $\hat{B}^\dagger \hat{B}$ with

   $$\hat{B}^\dagger = \sum_a p_a \hat{a}_a^\dagger \hat{a}_{\bar{a}}^\dagger \ , \tag{5.23}$$

   it follows that the $K \times K$ pair density matrix has to be positive semidefinite,

   $$\Pi \succeq 0 \ . \tag{5.24}$$

The seniority-2 block is a part of the diagonal of the 2RDM:

$$\begin{aligned} \forall a \neq b: \quad \langle\psi|\hat{a}_a^\dagger \hat{a}_b^\dagger \hat{a}_b \hat{a}_a|\psi\rangle &= \langle\psi|\hat{a}_{\bar{a}}^\dagger \hat{a}_b^\dagger \hat{a}_b \hat{a}_{\bar{a}}|\psi\rangle = \\ \langle\psi|\hat{a}_a^\dagger \hat{a}_{\bar{b}}^\dagger \hat{a}_{\bar{b}} \hat{a}_a|\psi\rangle &= \langle\psi|\hat{a}_{\bar{a}}^\dagger \hat{a}_{\bar{b}}^\dagger \hat{a}_{\bar{b}} \hat{a}_{\bar{a}}|\psi\rangle = \\ \Gamma_{ab;ab} &= D_{ab} \geq 0 \end{aligned} \tag{5.25}$$

For convenience we put $D_{aa} = 0$. Equation (5.25) provides $\frac{K(K-1)}{2}$ linear inequalities that have to be imposed. There are now two independent ways of obtaining the 1DM out of the 2RDM: via the trace relation (5.13) and via the diagonal part of the pairing matrix:

$$\rho_a = \frac{2}{N-2} \sum_b D_{ab} \ , \tag{5.26}$$

$$\rho_a = \Pi_{aa} \ , \tag{5.27}$$

as the operators $\hat{a}_a^\dagger \hat{a}_a = \hat{a}_{\bar{a}}^\dagger \hat{a}_{\bar{a}} = \hat{a}_a^\dagger \hat{a}_{\bar{a}}^\dagger \hat{a}_{\bar{a}} \hat{a}_a$ have the same expectation value for a DOCI wave function. These consistency conditions have to be separately enforced. Note that the trace condition (5.7) can be written in two alternative ways:

$$\sum_a \Pi_{aa} = \frac{N}{2}, \quad \text{and} \quad \sum_{ab} D_{ab} = \frac{N}{4}(N-2) \ . \tag{5.28}$$

2. The $\mathcal{Q}$ condition has exactly the same structure as the $\mathcal{P}$ condition. The constraint for the seniority-0 block is derived from

$$\sum_{ab} q_a \, \langle\psi|\hat{a}_a \hat{a}_{\bar{a}} \hat{a}_{\bar{b}}^\dagger \hat{a}_b^\dagger|\psi\rangle \, q_b \geq 0 \ , \tag{5.29}$$

which leads to the positivity condition $\mathcal{Q}^\Pi \succeq 0$ on a $K \times K$ matrix $\mathcal{Q}^\Pi$, with elements

$$\mathcal{Q}^\Pi_{ab} = \delta_{ab}(1 - \rho_a - \rho_b) + \Pi_{ab} \ . \tag{5.30}$$

The seniority-2 part gives rise to a set of linear inequalities,

$$\forall a \neq b: \quad \langle\psi|\hat{a}_a \hat{a}_b \hat{a}_b^\dagger \hat{a}_a^\dagger|\psi\rangle = 1 - \rho_a - \rho_b + D_{ab} \geq 0 \ . \tag{5.31}$$

3. The $\mathcal{G}$ condition is somewhat more complex as more combinations are non-zero. We work systematically according to seniority and spin.

   Spin projections $M_S = \pm 1$ are equivalent, so we only consider the $M_S = +1$ case and always assume $a \neq b$, since in DOCI space $\hat{a}_a^\dagger \hat{a}_{\bar{a}} \, |\psi\rangle = 0$. The particle-hole operators generating this constraint are of the form $\hat{B}^\dagger = \sum_{ab} g_{ab} \hat{a}_a^\dagger \hat{a}_{\bar{b}}$ which leads to the following seniority-2 positivity condition:

$$\begin{aligned} &\sum_{abcd} g_{ab} \left[\delta_{bd}\delta_{ac}(\rho_a - D_{ab}) - \delta_{ad}\delta_{bc}\Pi_{ab}\right] g_{cd} = \\ &\qquad \sum_{ab} g_{ab} \left[(\rho_a - D_{ab}) g_{ab} - \Pi_{ab} g_{ba}\right] \geq 0 \end{aligned} \tag{5.32}$$

This condition is almost diagonal, as g_{ab} is only connected with itself and g_{ba}, leading to the following 2×2 positivity condition:

$$\forall a < b \qquad \begin{bmatrix} \rho_a - D_{ab} & -\Pi_{ab} \\ -\Pi_{ab} & \rho_b - D_{ab} \end{bmatrix} \succeq 0 \ . \tag{5.33}$$

For the $M_S = 0$ and seniority-2 case, the particle-hole operators are of the form $\hat{B}_1^\dagger = \sum_{ab} g_{ab} \hat{a}_a^\dagger \hat{a}_b$ and $\hat{B}_2^\dagger = \sum_{ab} g_{ab} \hat{a}_{\bar{a}}^\dagger \hat{a}_{\bar{b}}$, with $a \neq b$. These terms are coupled to each other. The diagonal terms ($\hat{B}_1^\dagger \hat{B}_1$ and $\hat{B}_2^\dagger \hat{B}_2$) are

$$\langle \psi | \hat{a}_a^\dagger \hat{a}_b \hat{a}_d^\dagger \hat{a}_c | \psi \rangle = \delta_{ac} \delta_{bd} (\rho_a - D_{ab}) \ . \tag{5.34}$$

The off-diagonal terms ($\hat{B}_1^\dagger \hat{B}_2$ and $\hat{B}_2^\dagger \hat{B}_1$) are

$$\langle \psi | \hat{a}_a^\dagger \hat{a}_b \hat{a}_{\bar{d}}^\dagger \hat{a}_{\bar{c}} | \psi \rangle = \delta_{ad} \delta_{bc} \Pi_{ab} \ , \tag{5.35}$$

which leads to the 2×2 constraint matrix

$$\forall a < b \qquad \begin{bmatrix} \rho_a - D_{ab} & \Pi_{ab} \\ \Pi_{ab} & \rho_b - D_{ab} \end{bmatrix} \succeq 0 \ , \tag{5.36}$$

which is equivalent to (5.33).

The $M_S = 0$ and seniority-0 part is built by two particle-hole operators $\hat{B}_1^\dagger = \sum_a g_a \hat{a}_a^\dagger \hat{a}_a$ and $\hat{B}_2^\dagger = \sum_b g_b \hat{a}_{\bar{b}}^\dagger \hat{a}_{\bar{b}}$. This leads to a $2K \times 2K$ matrix with diagonal elements ($\hat{B}_1^\dagger \hat{B}_1$ and $\hat{B}_2^\dagger \hat{B}_2$)

$$\langle \psi | \hat{a}_a^\dagger \hat{a}_a \hat{a}_b^\dagger \hat{a}_b | \psi \rangle = \delta_{ab} \rho_a + D_{ab} \ , \tag{5.37}$$

and off-diagonal elements ($\hat{B}_1^\dagger \hat{B}_2$ and $\hat{B}_2^\dagger \hat{B}_1$)

$$\begin{aligned} \langle \psi | \hat{a}_a^\dagger \hat{a}_a \hat{a}_{\bar{b}}^\dagger \hat{a}_{\bar{b}} | \psi \rangle &= D_{ab} + \delta_{ab} \Pi_{ab} \\ &= \delta_{ab} \rho_a + D_{ab} \ . \end{aligned} \tag{5.38}$$

Both blocks are identical, which means that K eigenvalues will be zero and we only have to impose the positivity $\mathcal{G}^\Pi \succeq 0$ of a $K \times K$ matrix:

$$\mathcal{G}_{ab}^\Pi = \delta_{ab} \rho_a + D_{ab} \ . \tag{5.39}$$

The $\mathcal{P}$ conditions correspond to eq. (24a) and (30) in Weinhold and Wilson[138], the $\mathcal{Q}$ conditions to eq. (24b) and (34) and the $\mathcal{G}$ conditions to eq. (24c), (44) and (18).

We now look at the reduced Hamiltonian (5.4) which simplifies to the same structure as the $\mathcal{P}$ condition. The DOCI reduced Hamiltonian is

$$\begin{aligned} K_{ab}^\Pi &= \frac{2}{N-1} T_{aa} \delta_{ab} + V_{aabb} \ , \\ K_{ab}^D &= \frac{1}{N-1} (T_{aa} + T_{bb}) + V_{abab} - \frac{1}{2} V_{abba} \ . \end{aligned} \tag{5.40}$$

The energy functional (5.2) for DOCI becomes

$$E = \sum_{ab} \left(K^{\Pi}_{ab} \Pi_{ab} + 2 K^{D}_{ab} D_{ab} \right) \ . \tag{5.41}$$

An advantage of v2RDM-DOCI is that the resulting 2RDM belongs to a singlet state, while the general v2RDM needs additional constraints to ensure the singlet:

$$\langle \psi | \hat{a}^{\dagger}_{\alpha} \hat{a}_{\beta} \hat{S}_z | \psi \rangle = 0 \ , \tag{5.42}$$

with the $\hat{S}_z$ operator defined as,

$$\hat{S}_z = \frac{1}{2} \sum_{a} \left(\hat{a}^{\dagger}_{a} \hat{a}_{a} - \hat{a}^{\dagger}_{\bar{a}} \hat{a}_{\bar{a}} \right) \ . \tag{5.43}$$

In full v2RDM, this constraint needs to be enforced by a zero eigenvalue in the $\mathcal{G}$ matrix[135, 153]. In v2RDM-DOCI however,

$$\begin{aligned}
&\langle \psi | \hat{a}^{\dagger}_{c} \hat{a}_{d} \hat{S}_z | \psi \rangle = \\
&= \frac{1}{2} \delta_{cd} \sum_{a}^{K} \left(\langle \psi | \hat{a}^{\dagger}_{c} \hat{a}_{d} \hat{a}^{\dagger}_{a} \hat{a}_{a} | \psi \rangle - \langle \psi | \hat{a}^{\dagger}_{c} \hat{a}_{d} \hat{a}^{\dagger}_{\bar{a}} \hat{a}_{\bar{a}} | \psi \rangle \right) \\
&= \frac{1}{2} \sum_{a}^{K} \left(\langle \psi | \hat{a}^{\dagger}_{a} \hat{a}_{a} | \psi \rangle - \langle \psi | \hat{a}^{\dagger}_{c} \hat{a}^{\dagger}_{a} \hat{a}_{c} \hat{a}_{a} | \psi \rangle - \langle \psi | \hat{a}^{\dagger}_{c} \hat{a}^{\dagger}_{\bar{a}} \hat{a}_{c} \hat{a}_{\bar{a}} | \psi \rangle \right) \\
&= \frac{1}{2} \sum_{a}^{K} \left(\rho_a + (1 - \delta_{ac}) D_{ac} - \Pi_{ac} \delta_{ac} - (1 - \delta_{ac}) D_{ca} \right) \\
&= 0 \ ,
\end{aligned}$$

which means that the singlet condition is automatically fulfilled. It must be noted that (5.42) is a necessary but not sufficient condition for the 2RDM to be derivable from a $S = 0$ wave function.

In these DOCI N-representability conditions, the largest matrix dimension encountered is K as compared to $(2K)^2$ in the general case. The remainder of the conditions are linear inequalities and the positive semidefiniteness of 2×2 matrices which are trivial to impose. The scaling of our code has been reduced from K^6 to K^3 for the floating point operations and from K^4 to K^2 for the memory. In Figure 5.2 the scaling of the v2RDM and v2RDM-DOCI (with and without orbital optimization) is shown for a growing chain of equidistant hydrogen atoms (interatomic distance = 2 bohr) in the STO-3G basis. Note that for 30 H-atoms the v2RDM-DOCI is already three orders of magnitude faster than the general v2RDM code. We used a v2RDM code that exploits spin symmetry and the singlet conditions are enforced, so we can make a fair comparison with v2RDM-DOCI. The v2RDM-DOCI starts to exhibit a smooth scaling with the number of hydrogen atoms when the runtime was at least 10^4 seconds whereas the general v2RDM reaches this point sooner (10^3 seconds).

	α	β
v2RDM	2.602 10^{-5}	6.485
v2RDM-DOCI	5.268 10^{-5}	3.954
v2RDM-DOCI OPT	2.726 10^{-4}	4.200

Table 5.1: The resulting coefficients of the linear fit in Figure 5.2

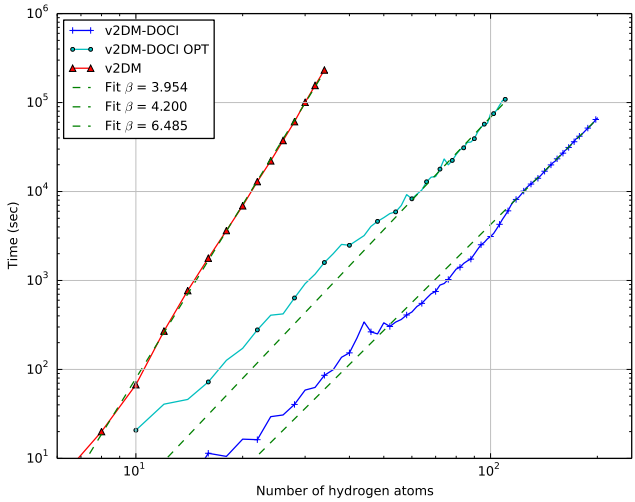

Figure 5.2: Scaling of v2RDM vs v2RDM-DOCI (with and without orbital optimization) on a hydrogen chain (interatomic distance = 2 bohr) in the STO-3G basis on a log-log plot. We fitted a linear curve ($\beta x + \alpha$) to the data.

We performed a linear fit on a log-log plot to find the power of the leading term in the scaling (αx^{β}) resulting in the coefficients found in table 5.1. The scaling is two orders better while the prefactor changes little. If we include the orbital optimization introduced in the next section, the scaling deteriorates with 0.25. We cannot draw any general conclusion from this about the scaling of the entire method (including the orbital optimization) as a hydrogen chain in STO-3G is a fairly special case. Note that the actual scaling parameters $\beta = 6.4$ (v2RDM) and $\beta = 3.9$ (v2RDM-DOCI) deviate from the theoretical scaling parameters $\beta = 6$ (v2RDM) and $\beta = 3$ (v2RDM-DOCI) involved in the v2RDM floating point operations as any v2RDM algorithm contains an iterative scheme with a number of loops that slowly increases with K.

5.3 Orbital Optimization

The DOCI energy is orbital dependent, therefore the choice of the orbitals is crucial. Like in many MCSCF methods, we use an iterative two-step algorithm [4, 140, 143, 156–158] in which we first optimize the 2RDM and then the

orbitals. Orbital optimization is a hard problem as it requires finding the global minimum in a rough and uncharted landscape[110]. There are no known computationally feasible techniques for achieving this in a general way. The most often used approach is to pick a good starting point and use a Newton-Raphson based algorithm to find a local minimum[142, 143]. This involves calculating the computationally expensive Jacobian and Hessian. Furthermore, the four-index transformation of the two-electron integrals is not cheap.

We use a different approach: a Jacobi rotation is performed in every step. A Jacobi rotation[144, 159] is a unitary transformation that rotates in a two-dimensional subspace of the orbital space. While in a Newton-Raphson method all orbitals are updated at every step, in a Jacobi rotation only two orbitals are updated in each step. Jacobi rotations have the advantage of simplicity: only 2 rows and columns need to be updated, which makes the transformation of the two-electron integrals much faster. The Jacobi rotation of orbitals k and l over an angle θ is determined by the rotation matrix

$$Q^{kl} = \begin{array}{c} \\ k \\ \\ l \\ \\ \end{array} \begin{array}{c} \begin{array}{ccccccc} & & & k & & l & \end{array} \\ \begin{pmatrix} 1 & & & & & & \\ & \ddots & & & & & \\ & & \cos\theta & \cdots & -\sin\theta & & \\ & & \vdots & \ddots & \vdots & & \\ & & \sin\theta & \cdots & \cos\theta & & \\ & & & & & \ddots & \\ & & & & & & 1 \end{pmatrix} \end{array}, \tag{5.44}$$

or more formally,

$$\begin{aligned} Q^{kl}_{ij} = \delta_{ij} &+ (\delta_{ik}\delta_{jk} + \delta_{il}\delta_{jl})(\cos\theta - 1) \\ &+ (\delta_{ik}\delta_{jl} - \delta_{il}\delta_{jk}) \sin\theta \end{aligned} \tag{5.45}$$

If we apply a unitary transformation to the matrix elements (5.40) and insert them in the energy functional (5.41), we find

$$\begin{aligned} E' = &\frac{2}{N-1} \sum_{ab} \sum_{a'b'} [\delta_{ab} Q_{aa'} Q_{ab'} \Pi_{ab} + \\ &(Q_{aa'} Q_{ab'} + Q_{ba'} Q_{bb'})\, D_{ab}]\, T_{a'b'} + \\ &\sum_{ab} \sum_{a'b'c'd'} Q_{aa'} Q_{ab'} Q_{bc'} Q_{bd'} V_{a'b'c'd'} \Pi_{ab} + \\ &\sum_{ab} \sum_{a'b'c'd'} Q_{aa'} Q_{bb'} \left(2 Q_{ac'} Q_{bd'} - Q_{bc'} Q_{ad'}\right) \\ &V_{a'b'c'd'} D_{ab} \ . \end{aligned} \tag{5.46}$$

Substituting eq. (5.54) into eq. (5.40) yields, after some work, the following expression for the energy,

$$\begin{aligned} E'(\theta)^{kl} = A\cos 4\theta + B\cos 2\theta + C\sin 4\theta \\ + D\sin 2\theta + F \end{aligned} \tag{5.47}$$

for the rotation over of an angle θ between orbitals k and l. The constants A, B, C, D, F, of which the complete expression is given in the next section (that section contains mathematical details that are not important for the remainder of this chapter), depend on the elements of the 2RDM, T_{ab} and V_{abcd}. As eq. (5.47) has a period of π, we only consider the interval $[-\frac{\pi}{2}, \frac{\pi}{2}]$. The N-representability conditions of section 5.2 are unitarily invariant, so we are guaranteed that a Jacobi rotation does not affect the N-representability, but the energy is not necessarily minimal. This means that the calculated energy (5.47) will always be greater than or equal to the optimized v2RDM minimum.

It is easy and cheap to calculate the gradient and Hessian of this equation. Using a Newton-Raphson algorithm, we can thus easily find the angle for which eq. (5.47) is minimal. The constant term (F) in eq. (5.47) is the only one involving a double sum over the orbitals: it is the original double sum appearing in eq. (5.41) over all orbitals except orbitals k and l. This implies that an evaluation of the energy scales as K^2, but the energy difference, gradient and the Hessian only scale computationally as K. If we iterate over all pairs of orbitals (scaling as K^2) and find the optimal angle for minimization, we have an K^3 algorithm to find the new Jacobi rotation optimizing the energy decrease. If symmetry-adapted orbitals are used, only rotations between orbitals in the same irreducible representation are allowed, which simplifies the two-electron integral transformation even more. A schematic overview is given in Algorithm 1. In the previous section we measured the scaling of the v2RDM-DOCI algorithm combined with the Jacobi orbital optimizer and found a scaling of 4.200. The starting point were the molecular orbitals coming from a previous restricted Hartree-Fock calculation. One should be careful to draw general conclusions from this. It merely shows that, given a suitable starting point, the algorithm has an interesting scaling.

Algorithm 1 The algorithm used to find the optimal Jacobi rotation in pseudocode

```
procedure FindOptimalRotation(Γ, T, V)
    for i ← 1, n_irrep do                ▷ Loop over all irreducible representations
        for all (a, b) ∈ irrep_i do      ▷ Loop over all pairs of orbitals belonging to irrep i
            (E_ab, θ_ab) = FindMinimum(Γ, T, V, a, b)      ▷ Minimum of (5.47)
        end for
    end for
    (k, l, θ) = min (E, θ)               ▷ Find the lowest energy over all pairs
    return (k, l, θ_kl)                  ▷ Return the pair of orbitals and the angle
end procedure
```

As an example, we consider the BH molecule at equilibrium distance (2.32 bohr) in the STO-3G basis. Figure 5.3 contains the energy as a function of the rotation angle between several pairs of orbitals starting from the Hartree-

Fock molecular orbitals. The full (red) curve is the energy as calculated with eq. (5.47) keeping the 2RDM fixed, whereas the dashed (blue) curve involves a 2RDM optimization at each point. We used C_{2v} symmetry for BH (the largest Abelian point group of BH) and we only consider the 4 orbitals that transform according to irreducible representation A_1 (the other 2 orbitals transform according to B_1 and B_2). The orbital energies (in Hartree) of the restricted Hartree-Fock solution are given in Table 5.2.

Doubly occupied orbitals	
$1A_1$	-7.339428
$2A_1$	-0.573370
$3A_1$	-0.246546
Virtual orbitals	
$1B_1$	0.269938
$1B_2$	0.269938
$4A_1$	0.701123

Table 5.2: The restricted Hartree-Fock solution for BH. The orbital energies are in Hartree. We use $C_{2\mathrm{v}}$ symmetry, the orbitals are labelled according to irreducible representations A_1, B_1 or B_2.

The pictures shown for the BH molecule are characteristic for most calculations that we have done. For most pairs of orbitals, the lowest energy is obtained for very small rotation angles except for a few where a larger decrease in energy can be achieved. In Figure 5.3(b) there is a clear new minimum and the angle found using (5.47) is very close to the v2RDM optimized minimum. The $1A_1$ orbital is the localized $1s$ orbital on the Boron atom. The $2A_1$ and $3A_1$ orbitals are a mixture of the $1s$ on the hydrogen atom and the $2s$ and $2p_z$ on the Boron atom. The largest energy gain can be achieved by mixing these orbitals and this already brings us very close to the FullCI energy (-24.810 $\mathrm{E_h}$).

5.3.1 Derivation of the formulas for the local DOCI optimization

All summations in this document run over all spatial orbitals (except when explicitly noted otherwise). The 2RDM energy functional for the DOCI case is,

$$E = \sum_{ab} \left(K_{a\bar{a};b\bar{b}} \Gamma_{a\bar{a};b\bar{b}} + 2 K_{ab;ab} \Gamma_{ab;ab} \right) \ . \tag{5.48}$$

The reduced Hamiltonian K has the form,

$$K_{a\bar{a};b\bar{b}} = \frac{2}{N-1} T_{aa} \delta_{ab} + V_{aabb} \ , \tag{5.49}$$

$$K_{ab;ab} = \frac{1}{N-1} \left(T_{aa} + T_{bb} \right) + V_{abab} - \frac{1}{2} V_{abba} \ , \tag{5.50}$$

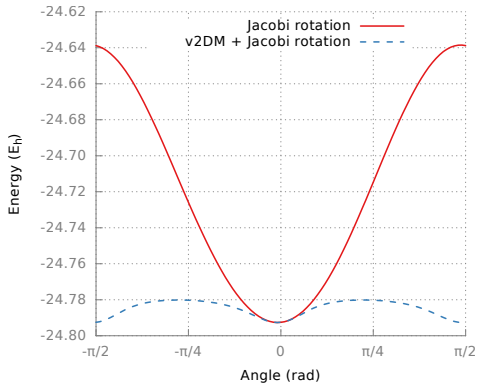

(a) Orbitals $1A_1$ and $2A_1$, min ≈ -0.027 rad

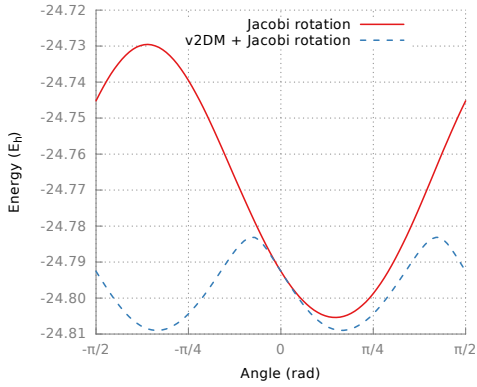

(b) Orbitals $2A_1$ and $3A_1$, min ≈ 0.463 rad

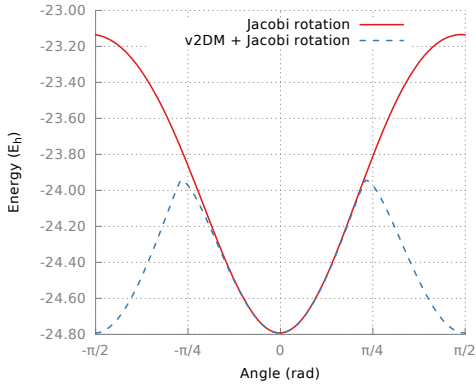

(c) Orbitals $2A_1$ and $4A_1$, min ≈ -0.005 rad

Figure 5.3: The red curve has been calculated using (5.47) while the blue curve uses the same transformed reduced Hamiltonian but an optimized 2RDM-DOCI. These results are for BH in STO-3G. We used an interatomic distance of 2.32 bohr. The min refers to the minimum of the eq. (5.47) (red curve). The FullCI energy is -24.810 E_h.

with T_{ab} and V_{abcd} the one- and two-electron integrals. Under a general unitary transformation U, the reduced Hamiltonian transforms as,

$$K'_{a\bar{a};b\bar{b}} = \frac{2}{N-1}\delta_{ab}\sum_{a'b'} U_{aa'}U_{ab'}T_{a'b'} + \sum_{a'b'c'd'} U_{aa'}U_{ab'}U_{bc'}U_{bd'}V_{a'b'c'd'} \ , \quad (5.51)$$

$$K'_{ab;ab} = \frac{1}{N-1}\sum_{a'b'} \left(U_{aa'}U_{ab'} + U_{ba'}U_{bb'}\right) T_{a'b'} + \sum_{a'b'c'd'} U_{aa'}U_{bb'}\left(U_{ac'}U_{bd'} - \frac{1}{2}U_{bc'}U_{ad'}\right) V_{a'b'c'd'} \ . \quad (5.52)$$

Substituting eq. (5.51),(5.52) in the energy functional (5.48), we find,

$$E' = \frac{2}{N-1}\sum_{ab}\sum_{a'b'} \left(\delta_{ab}U_{aa'}U_{ab'}\Gamma_{a\bar{a};a\bar{a}} + \left(U_{aa'}U_{ab'} + U_{ba'}U_{bb'}\right)\Gamma_{ab;ab}\right) T_{a'b'} + \sum_{ab}\sum_{a'b'c'd'} U_{aa'}U_{ab'}U_{bc'}U_{bd'}V_{a'b'c'd'}\Gamma_{a\bar{a};b\bar{b}} + \sum_{ab}\sum_{a'b'c'd'} U_{aa'}U_{bb'}\left(2U_{ac'}U_{bd'} - U_{bc'}U_{ad'}\right) V_{a'b'c'd'}\Gamma_{ab;ab} \ . \quad (5.53)$$

Let now the unitary transform be a Jacobi rotation between orbitals k and l over an angle θ,

$$U_{ij}^{kl} = \delta_{ij} + (\delta_{ik}\delta_{jk} + \delta_{il}\delta_{jl})(\cos\theta - 1) + (\delta_{ik}\delta_{jl} - \delta_{il}\delta_{jk})\sin\theta \quad (5.54)$$

After some work, we can find the expression for the energy functional under a Jacobi rotation:

$$
\begin{aligned}
&E(\theta) = \\
&\sum_{\substack{ab \\ a,b\notin\{k,l\}}} \left\{ \left(\frac{2}{N-1} T_{aa}\delta_{ab} + V_{aabb} \right) \Gamma_{a\bar{a};b\bar{b}} + \left(2V_{abab} - V_{abba} + \frac{2}{N-1}\left(T_{aa}+T_{bb}\right) \right) \Gamma_{ab;ab} \right\} + \\
&\sum_{\substack{a \\ a\notin\{k,l\}}} \Big\{ 2\left(\cos^2\theta V_{kkaa} - 2\cos\theta\sin\theta V_{klaa} + \sin^2\theta V_{llaa} \right) \Gamma_{k\bar{k};a\bar{a}} + \\
&2\Big[\cos^2\theta V_{llaa} + 2\cos\theta\sin\theta V_{klaa} + \sin^2\theta V_{kkaa} \Big] \Gamma_{l\bar{l};a\bar{a}} + \\
&2\Big[\cos^2\theta \left(2V_{kaka} - V_{kaak}\right) - 2\cos\theta\sin\theta\left(2V_{kala} - V_{kaal}\right) + \sin^2\theta\left(2V_{lala} - V_{laal}\right) \Big] \Gamma_{ka;ka} + \\
&2\Big[\cos^2\theta \left(2V_{lala} - V_{laal}\right) + 2\cos\theta\sin\theta\left(2V_{kala} - V_{kaal}\right) + \sin^2\theta\left(2V_{kaka} - V_{kaak}\right) \Big] \Gamma_{la;la} + \\
&\frac{4}{N-1}\left(T_{aa} + \cos^2\theta T_{kk} - 2\cos\theta\sin\theta T_{kl} + \sin^2\theta T_{ll} \right) \Gamma_{ka;ka} + \\
&\frac{4}{N-1}\left(T_{aa} + \cos^2\theta T_{ll} + 2\cos\theta\sin\theta T_{kl} + \sin^2\theta T_{kk} \right) \Gamma_{la;la} \Big\} + \\
&\frac{2}{N-1}\left(\cos^2\theta T_{kk} - 2\cos\theta\sin\theta T_{kl} + \sin^2\theta T_{ll} \right) \Gamma_{k\bar{k};k\bar{k}} + \\
&\frac{2}{N-1}\left(\cos^2\theta T_{ll} + 2\cos\theta\sin\theta T_{kl} + \sin^2\theta T_{kk} \right) \Gamma_{l\bar{l};l\bar{l}} + \frac{4}{N-1}\left(T_{kk}+T_{ll}\right)\Gamma_{kl;kl} \\
&+ \Big[\cos^4\theta V_{kkkk} + \sin^4\theta V_{llll} + 2\cos^2\theta\sin^2\theta\left(2V_{kkll} + V_{klkl}\right) - 4\sin^3\theta\cos\theta V_{klll} \\
&- 4\cos^3\theta\sin\theta V_{klkk} \Big] \Gamma_{k\bar{k};k\bar{k}} \\
&+ \Big[\cos^4\theta V_{llll} + \sin^4\theta V_{kkkk} + 2\cos^2\theta\sin^2\theta\left(2V_{kkll} + V_{klkl}\right) + 4\sin^3\theta\cos\theta V_{klkk} + \\
&4\cos^3\theta\sin\theta V_{klll} \Big] \Gamma_{l\bar{l};l\bar{l}} \\
&+ 2\Big[\cos^2\theta\sin^2\theta\left(V_{kkkk} + V_{llll} - 2\left(V_{kkll} + V_{klkl}\right)\right) + \left(\sin^4\theta + \cos^4\theta\right) V_{kkll} + \\
&2\left(\sin\theta\cos^3\theta - \cos\theta\sin^3\theta\right)\left(V_{klkk} - V_{klll}\right) \Big] \Gamma_{k\bar{k};l\bar{l}} \\
&+ 2\Big[\cos^2\theta\sin^2\theta\left(V_{kkkk} + V_{llll} - 6V_{kkll} + 2V_{klkl}\right) + \left(\sin^4\theta + \cos^4\theta\right)\left(2V_{klkl} - V_{kkll}\right) \\
&- 2\left(\sin\theta\cos^3\theta - \cos\theta\sin^3\theta\right)\left(V_{klkk} - V_{klll}\right) \Big] \Gamma_{kl;kl} \qquad (5.55)
\end{aligned}
$$

If we reorder to the powers of $\sin\theta$ and $\cos\theta$, we find,

$$
\begin{aligned}
E(\theta) = & \\
& \sum_{\substack{ab \\ a,b\notin\{k,l\}}} \left\{ V_{aabb}\Gamma_{a\bar{a};b\bar{b}} + \left(2V_{abab} - V_{abba} + \frac{2}{N-1}\left(T_{aa}+T_{bb}\right)\right)\Gamma_{ab;ab}\right\} + \\
& \sum_{\substack{a \\ a\notin\{k,l\}}} \left\{ \frac{2}{N-1}T_{aa}\Gamma_{a\bar{a};a\bar{a}} + \frac{4}{N-1}T_{aa}\left(\Gamma_{ak;ak}+\Gamma_{al;al}\right)\right\} + \frac{4}{N-1}\left(T_{kk}+T_{ll}\right)\Gamma_{kl;kl} + \\
& \cos^4\theta\left[V_{kkkk}\Gamma_{k\bar{k};k\bar{k}} + V_{llll}\Gamma_{l\bar{l};l\bar{l}} + 2V_{kkll}\Gamma_{k\bar{k};l\bar{l}} + 2\left(2V_{klkl}-V_{kkll}\right)\Gamma_{kl;kl}\right] + \\
& \sin^4\theta\left[V_{kkkk}\Gamma_{l\bar{l};l\bar{l}} + V_{llll}\Gamma_{k\bar{k};k\bar{k}} + 2V_{kkll}\Gamma_{k\bar{k};l\bar{l}} + 2\left(2V_{klkl}-V_{kkll}\right)\Gamma_{kl;kl}\right] + \\
& \cos^2\theta\Bigg[\sum_{\substack{a \\ a\notin\{k,l\}}} \Bigg\{ 2V_{kkaa}\Gamma_{k\bar{k};a\bar{a}} + 2V_{llaa}\Gamma_{l\bar{l};a\bar{a}} + 2\left(2V_{kaka}-V_{kaak}+\frac{2}{N-1}T_{kk}\right)\Gamma_{ka;ka} \\
& \quad + 2\left(2V_{lala}-V_{laal}+\frac{2}{N-1}T_{ll}\right)\Gamma_{la;la}\Bigg\} + \frac{2}{N-1}\left(T_{kk}\Gamma_{k\bar{k};k\bar{k}} + T_{ll}\Gamma_{l\bar{l};l\bar{l}}\right)\Bigg] + \\
& \sin^2\theta\Bigg[\sum_{\substack{a \\ a\notin\{k,l\}}} \Bigg\{ 2V_{kkaa}\Gamma_{l\bar{l};a\bar{a}} + 2V_{llaa}\Gamma_{k\bar{k};a\bar{a}} + \\
& \quad 2\left(2V_{kaka}-V_{kaak}+\frac{2}{N-1}T_{kk}\right)\Gamma_{la;la} + 2\left(2V_{lala}-V_{laal}\right)\Gamma_{ka;ka} \\
& \quad + \frac{4}{N-1}T_{ll}\Gamma_{ka;ka}\Bigg\} + \frac{2}{N-1}\left(T_{ll}\Gamma_{k\bar{k};k\bar{k}} + T_{kk}\Gamma_{l\bar{l};l\bar{l}}\right)\Bigg] + \\
& 2\cos\theta\sin\theta\Bigg[\sum_{\substack{a \\ a\notin\{k,l\}}} \Bigg\{ 2V_{klaa}\left(\Gamma_{l\bar{l};a\bar{a}} - \Gamma_{k\bar{k};a\bar{a}}\right) \\
& \quad + 2\left(2V_{kala}-V_{kaal}+\frac{2}{N-1}T_{kl}\right)\left(\Gamma_{la;la}-\Gamma_{ka;ka}\right)\Bigg\} \\
& \quad + \frac{2}{N-1}T_{kl}\left(\Gamma_{l\bar{l};l\bar{l}} - \Gamma_{k\bar{k};k\bar{k}}\right)\Bigg] + \\
& 2\cos^2\theta\sin^2\theta\Bigg[\left(2V_{kkll}+V_{klkl}\right)\left(\Gamma_{k\bar{k};k\bar{k}} + \Gamma_{l\bar{l};l\bar{l}}\right) + \left(V_{kkkk}+V_{llll}-2\left(V_{kkll}+V_{klkl}\right)\right)\Gamma_{k\bar{k};l\bar{l}} + \\
& \quad \left(V_{kkkk}+V_{llll}-6V_{kkll}+2V_{klkl}\right)\Gamma_{kl;kl}\Bigg] + \\
& 4\sin^3\theta\cos\theta\left[V_{klkk}\Gamma_{l\bar{l};l\bar{l}} - V_{klll}\Gamma_{k\bar{k};k\bar{k}} - \left(V_{klkk}-V_{klll}\right)\left(\Gamma_{k\bar{k};l\bar{l}} + \Gamma_{kl;kl}\right)\right] + \\
& 4\cos^3\theta\sin\theta\left[V_{klll}\Gamma_{l\bar{l};l\bar{l}} - V_{klkk}\Gamma_{k\bar{k};k\bar{k}} + \left(V_{klkk}-V_{klll}\right)\left(\Gamma_{k\bar{k};l\bar{l}} + \Gamma_{kl;kl}\right)\right]
\end{aligned}
\tag{5.56}
$$

In a compact form, this boils down to,

$$E(\theta) = \tilde{A}\cos^4\theta + \tilde{B}\sin^4\theta + \tilde{C}\cos^2\theta + \tilde{D}\sin^2\theta + 2\tilde{E}\cos\theta\sin\theta + 2\tilde{F}\cos^2\theta\sin^2\theta + 4\tilde{G}\sin\theta\cos^3\theta + 4\tilde{H}\sin^3\theta\cos\theta + I \tag{5.57}$$

where,

$$\tilde{A} = V_{kkkk}\Gamma_{k\bar{k};k\bar{k}} + V_{llll}\Gamma_{l\bar{l};l\bar{l}} + 2V_{kkll}\Gamma_{k\bar{k};l\bar{l}} + 2\left(2V_{klkl} - V_{kkll}\right)\Gamma_{kl;kl} \tag{5.58}$$

$$\tilde{B} = V_{kkkk}\Gamma_{l\bar{l};l\bar{l}} + V_{llll}\Gamma_{k\bar{k};k\bar{k}} + 2V_{kkll}\Gamma_{k\bar{k};l\bar{l}} + 2\left(2V_{klkl} - V_{kkll}\right)\Gamma_{kl;kl} \tag{5.59}$$

$$\tilde{C} = \sum_{\substack{a \\ a\notin\{k,l\}}} \left\{ 2V_{kkaa}\Gamma_{k\bar{k};a\bar{a}} + 2V_{llaa}\Gamma_{l\bar{l};a\bar{a}} + 2\left(2V_{kaka} - V_{kaak} + \frac{2}{N-1}T_{kk}\right)\Gamma_{ka;ka} + 2\left(2V_{lala} - V_{laal} + \frac{2}{N-1}T_{ll}\right)\Gamma_{la;la} \right\} + \frac{2}{N-1}\left(T_{kk}\Gamma_{k\bar{k};k\bar{k}} + T_{ll}\Gamma_{l\bar{l};l\bar{l}}\right) \tag{5.60}$$

$$\tilde{D} = \sum_{\substack{a \\ a\notin\{k,l\}}} \left\{ 2V_{kkaa}\Gamma_{l\bar{l};a\bar{a}} + 2V_{llaa}\Gamma_{k\bar{k};a\bar{a}} + 2\left(2V_{kaka} - V_{kaak} + \frac{2}{N-1}T_{kk}\right)\Gamma_{la;la} + 2\left(2V_{lala} - V_{laal} + \frac{2}{N-1}T_{ll}\right)\Gamma_{ka;ka} \right\} + \frac{2}{N-1}\left(T_{ll}\Gamma_{k\bar{k};k\bar{k}} + T_{kk}\Gamma_{l\bar{l};l\bar{l}}\right) \Bigg] + \tag{5.61}$$

$$\tilde{E} = \sum_{\substack{a \\ a\notin\{k,l\}}} \left\{ 2V_{klaa}\left(\Gamma_{l\bar{l};a\bar{a}} - \Gamma_{k\bar{k};a\bar{a}}\right) + 2\left(2V_{kala} - V_{kaal} + \frac{2}{N-1}T_{kl}\right)\left(\Gamma_{la;la} - \Gamma_{ka;ka}\right) \right\} + \frac{2}{N-1}T_{kl}\left(\Gamma_{l\bar{l};l\bar{l}} - \Gamma_{k\bar{k};k\bar{k}}\right) \tag{5.62}$$

$$\tilde{F} = \left(2V_{kkll} + V_{klkl}\right)\left(\Gamma_{k\bar{k};k\bar{k}} + \Gamma_{l\bar{l};l\bar{l}}\right) + \left(V_{kkkk} + V_{llll} - 2\left(V_{kkll} + V_{klkl}\right)\right)\Gamma_{k\bar{k};l\bar{l}} + \left(V_{kkkk} + V_{llll} - 6V_{kkll} + 2V_{klkl}\right)\Gamma_{kl;kl} \tag{5.63}$$

$$\tilde{G} = V_{klll}\Gamma_{l\bar{l};l\bar{l}} - V_{klkk}\Gamma_{k\bar{k};k\bar{k}} + \left(V_{klkk} - V_{klll}\right)\left(\Gamma_{k\bar{k};l\bar{l}} + \Gamma_{kl;kl}\right) \tag{5.64}$$

$$\tilde{H} = V_{klkk}\Gamma_{l\bar{l};l\bar{l}} - V_{klll}\Gamma_{k\bar{k};k\bar{k}} - \left(V_{klkk} - V_{klll}\right)\left(\Gamma_{k\bar{k};l\bar{l}} + \Gamma_{kl;kl}\right) \tag{5.65}$$

$$\tilde{I} = \sum_{\substack{ab \\ a,b\notin\{k,l\}}} \left\{ V_{aabb}\Gamma_{a\bar{a};b\bar{b}} + \left(2V_{abab} - V_{abba} + \frac{2}{N-1}\left(T_{aa} + T_{bb}\right)\right)\Gamma_{ab;ab} \right\} \tag{5.66}$$

Eq. (5.57) can be made more compact:

$$E(\theta) = A\cos 4\theta + B\cos 2\theta + C\sin 4\theta + D\sin 2\theta + F \tag{5.67}$$

with,

$$A = \frac{\tilde{A} + \tilde{B}}{8} - \frac{\tilde{F}}{4} \tag{5.68}$$

$$B = \frac{\tilde{G} - \tilde{H}}{2} \tag{5.69}$$

$$C = \frac{\tilde{A} - \tilde{B} + \tilde{C}}{2} - \frac{\tilde{D}}{2} \tag{5.70}$$

$$D = \tilde{E} + \tilde{G} + \tilde{H} \tag{5.71}$$

$$F = \frac{3}{8}\left(\tilde{A} + \tilde{B}\right) + \frac{\tilde{C} + \tilde{D}}{2} + \frac{\tilde{F}}{4} + \tilde{I} \tag{5.72}$$

On this form, we can easily calculate the gradient and the Hessian of (5.56),

$$\frac{\mathrm{d}E(\theta)}{\mathrm{d}\theta} = -4A\sin 4\theta - 2B\sin 2\theta + 4C\cos 4\theta + 2D\cos 2\theta \tag{5.73}$$

$$\frac{\mathrm{d}^2E(\theta)}{\mathrm{d}\theta^2} = -16A\cos 4\theta - 4B\cos 2\theta - 16C\sin 4\theta - 4D\sin 2\theta \tag{5.74}$$

It is interesting to note that the calculation of the gradient and the Hessian scales as K while the constant part of the energy (5.66) scales as K^2. This means that it is computationally cheaper to calculate the gradient and Hessian than the actual energy.

5.4 Results

A code is developed to perform variational 2RDM optimizations using the DOCI constraints derived in section 5.2.2 in conjunction with orbital optimization according to eq. (5.47). The one- and two-particle integrals are transformed with the optimized Jacobi rotation (see Algorithm 1) and a new v2RDM optimization is started. This loop continues until the ground-state energy is converged to within 10^{-6} $\mathrm{E_h}$ during at least 25 steps. For the v2RDM calculations, we used a boundary point method with a primal and dual convergence criterion of 10^{-7} [153]. The flow of our program is shown in Algorithm 2.

The code used to generate the data presented can be found online[160] under the GPLv3 license. All simulations were run single-threaded on a Intel Xeon E5-2680 v3 with 64GB of RAM. Psi4[38] is used to generate the one- and two-electron integrals in the Gaussian basis set and the Hartree-Fock molecular orbitals. Unless specified otherwise, the Hartree-Fock molecular orbitals are the starting point for the orbital optimization. In all calculations, the cc-pVDZ basis was used. Benchmark results are provided by CheMPS2[39, 40, 161, 162], an open-source spin-adapted implementation of Density Matrix Renormalization Group (DMRG) for ab initio quantum chemistry, that generates results with FullCI accuracy. To monitor the convergence in CheMPS2, we increased

Algorithm 2 Schematic overview of the complete v2RDM-DOCI algorithm

converged $\leftarrow 0$
while converged < 25 **do** ▷ Do 25 steps within convergence criteria
$E_{\text{new}}, \Gamma = \text{v2RDM}(T, V)$ ▷ Do a v2RDM-DOCI optimization with electron integrals T and V
$(k, l, \theta) = \text{FindOptimalRotation}(\Gamma, T, V)$ ▷ Find the optimal rotation
$T, V = \text{TransformIntegrals}(k, l, \theta, T, V)$ ▷ Rotate the integrals
if $|E_{\text{new}} - E_{\text{old}}| < 10^{-6}$ **then** ▷ Check convergence
converged $\leftarrow$ converged $+ 1$
end if
$E_{\text{old}} \leftarrow E_{\text{new}}$
end while

the bond dimension in steps from 500 to 2500 for all calculations. FullDOCI is the result of a CI solver restricted to the doubly-occupied Slater determinants, combined with the same orbital optimization scheme as v2RDM-DOCI (unless specified otherwise).

5.4.1 Two- and four-electron systems

The DOCI wavefunction for a two-electron system is exact provided that the orbitals are optimized[24]. General v2RDM using only the $\mathcal{P}$ condition is also exact for a two-electron system[116, 135]. It is easy to prove that v2RDM-DOCI combined with orbital optimization also generates exact results for any two-electron system. This is illustrated by the numerical results in Table 5.3 for H_2 and He. Note that in Table 5.3 the FullDOCI results were obtained with the optimal orbitals produced by v2RDM-DOCI.

In the dissociated He_2 dimer, the effect of symmetry breaking can be seen in the third and fourth row of Table 5.3. When we allow the point-group symmetry to lower from D_{2h} to C_1, the orbital optimization algorithm is no longer restricted to orbitals transforming according to the same irreducible representation. When the symmetry is not broken (D_{2h}), the s orbitals of the two He atoms are coupled, in the sense that only (anti-)symmetric combinations are retained. In this case v2RDM-DOCI cannot recover the FullCI energy. When we decouple the orbitals and use C_1 symmetry, the full correlation energy is found. It is important to note the difference with the general v2RDM optimization: general v2RDM always gives a lower bound to the exact ground-state energy, but in the v2RDM-DOCI case, the energy is orbital dependent. The v2RDM-DOCI energy can be higher or lower than the FullCI result. We almost always find a higher energy. It is still true, however, that the v2RDM-DOCI must be lower than or equal to FullDOCI with the same set of orbitals. In principle we combine a lower-bound method (v2RDM) with an upper-bound method (Jacobi rotations). A cancelation of errors can occur and that is why we always compare to FullDOCI as it uses an exact energy solver.

System	Sym.	d	HF	FullCI	Δv2RDM-DOCI	ΔFullDOCI
H_2	D_{2h}	1.438	-1128.629	-1163.673	0.000	0.000
He	D_{2h}		-2855.160	-2887.595	0.000	0.000
He_2	D_{2h}	10.000	-5710.321	-5775.190	40.013	40.022
He_2	C_1	10.000	-5710.321	-5775.190	0.000	0.000

Table 5.3: Ground-state energy for some small systems in the cc-pVDZ basis. Energies are in milliHartree, interatomic distance (d) in bohr. The columns labeled v2RDM-DOCI and FullDOCI contain the deviation from FullCI. The orbital optimization is done with the specified Abelian symmetry in the column labeled 'Sym.'

5.4.2 Hydrogen chain

The symmetric stretching of an equidistant chain of hydrogen atoms is a standard test case for a new method aimed at strong static electron correlation. It is simple yet challenging, because of the strong correlation effects in the transition from metallic hydrogen to dissociated hydrogen. We use a H_8 chain[24, 25] in the cc-pVDZ basis with D_{2h} (symmetry-adapted) or C_1 (symmetry-broken) orbitals. The results shown in Figure 5.4 indicate the importance of the choice of the starting point in the orbital optimization scheme as this dictates the valley in which the local minimizer is active. The underlying basis for the one- and two-electron integrals is always taken to be the Löwdin orthogonalized Gaussian basis set (symmetry-adapted if specified). For the HF-D_{2h} curve, we first performed a calculation at equilibrium distance starting from the Hartree-Fock molecular orbitals. The resulting orthogonal transformation matrix, describing the transition from the Löwdin orthogonalized Gaussian basis set to the optimal set of orbitals at equilibrium, was used as a starting point in the orbital optimization for all other points on the curve. It is clear from the figure that this procedure does not lead to a satisfactory description of the metallic to the non-interacting region, as the dissociation limit is much higher in energy than the FullCI curve.

For the curve labeled dis-D_{2h}, we performed a calculation at 10 bohr determining the optimal orbital transformation with a random search and used this orbital transformation as a starting point for all other distances in the curve. This procedure correctly describes the dissociation limit but the energy rises artificially when we go into the metallic regime. So symmetry-adapted D_{2h} orbitals cannot describe the transition from metallic to non-interacting, localized hydrogen atoms. When starting from several random points, we could not find a lower energy curve for the D_{2h} case. The whole picture changes when we break the symmetry (the curve labeled C_1), and v2RDM-DOCI now gives a physically correct description of the transition. This curve was found by starting from the optimal orbital transformation of a v2RDM-DOCI calculation at 10 bohr using localized orbitals as starting point. Similar results were already

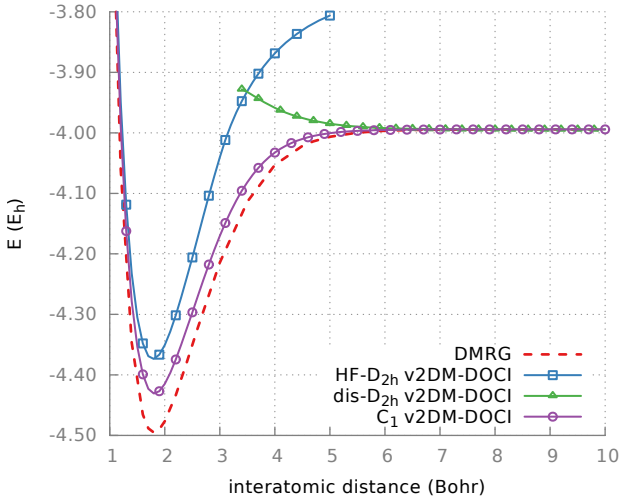

Figure 5.4: The symmetric stretch of H_8 in the cc-pVDZ basis. Not all calculated points are included. For the C_1 curve, the largest deviation from DMRG is 45 milliHartree around the minimum at 1.8 bohr.

reported by Bytautas et al.[24]: they verified that the behaviour is not a two-state crossing or avoided crossing between the ground state and an excited state.

In Figure 5.5, we have plotted the natural orbital occupation numbers from the 1DM extracted from v2RDM-DOCI, for both symmetries. In the C_1 symmetry there is a smooth transition from doubly-occupied hydrogen to singly-occupied hydrogen. In the D_{2h} symmetry the 'localized' orbitals corresponding to dis-D_{2h} curve in Figure 5.4 have a branch of singly-occupied hydrogen that is not present in the C_1 symmetry. The 'molecular orbitals' corresponding to the HF-D_{2h} curve in Figure 5.4 also have branches with no counterpart in the localized orbitals. It is clear that only v2RDM-DOCI results with symmetry-broken optimized orbitals provide a correct description of the transition.

As far as the details of the orbital optimization scheme are concerned, we found that the procedure can be accelerated by not performing a v2RDM-DOCI optimization at each rotation: in practice we see that the energy decreases considerably in the first steps. In subsequent steps, the convergence goes more slowly as the algorithm can only update two orbitals at a time. In this tail of the minimization, we can safely skip the optimization of the 2RDM for a number of updates as all rotation angles are small, only to restart the algorithm with the optimal solution from the previous step at the very end. This technique partially circumvents the downside of the Jacobi rotations, i.e. that only two orbitals are updated at the same time.

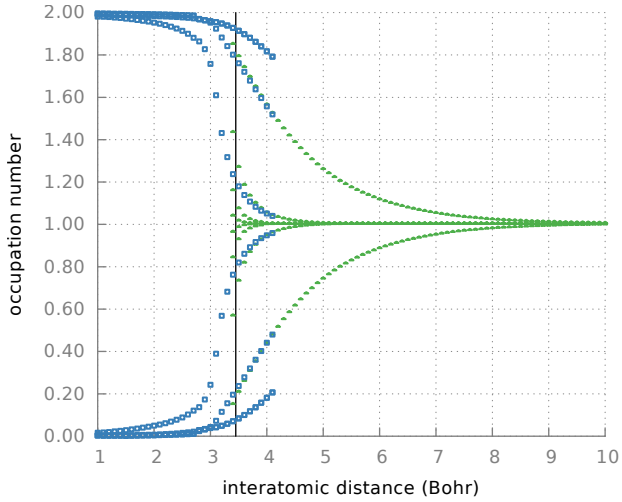

(a) The natural occupation numbers of H_8 for the D_{2h} symmetry

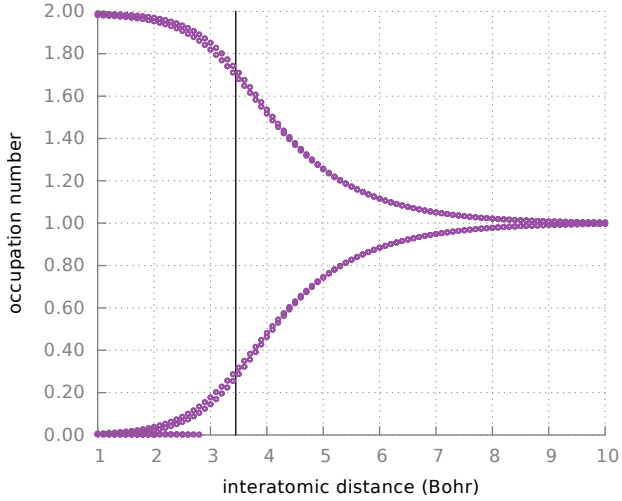

(b) The natural occupation numbers of H_8 for the C_1 symmetry

Figure 5.5: The v2RDM-DOCI natural orbital occupation numbers for both symmetries of the symmetric stretch of H_8. Only points with an occupation number larger than 10^{-3} are shown. The black line marks the energy crossing of the D_{2h} curves in Figure 5.4. The colors also match the curves in Figure 5.4.

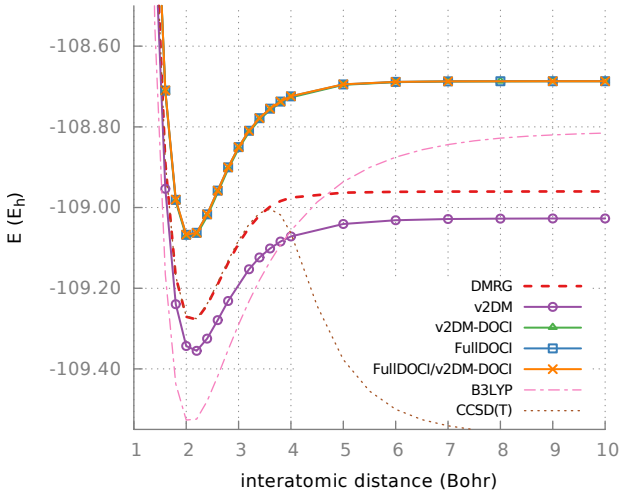

Figure 5.6: The dissociation of N_2 in the cc-pVDZ basis. The DOCI curves shown are for the C_1 symmetry. Note that three curves (v2RDM-DOCI, FullDOCI, FullDOCI/v2RDM-DOCI) coincide visually.

5.4.3 Molecular systems

Another interesting test is the dissociation of a diatomic molecule in which static correlation is of paramount importance at dissociation. The cc-pVDZ basis is used for all molecules. The nomenclature used for the results is as follows: v2RDM-DOCI refers to v2RDM with the DOCI constraints on the 2RDM (see section 5.2.2) and with the Jacobi orbital optimization (see section 5.3). FullDOCI uses the same orbital optimization algorithm. v2RDM-DOCI/FullDOCI is a single-shot v2RDM-DOCI calculation using the optimal set of orbitals from a FullDOCI calculation. FullDOCI/v2RDM-DOCI is exactly the opposite: a single-shot FullDOCI calculation using the optimal set of orbitals from v2RDM-DOCI.

We first present the dissociation of N_2. This is challenging because of the breaking of a triple bond and is often used as a test case[24, 163–166]. In the cc-pVDZ basis, N_2 has 28 orbitals and we perform calculations with both D_{2h} and C_1 symmetry. The results are presented in Figure 5.6 and detailed in Table 5.4. The results are to be compared to DMRG calculations[39, 40, 161, 162] which are to be considered as the FullCI reference. In order to appreciate the performance of v2RDM-DOCI, results of other methods such as Coupled-Cluster with Singles, Doubles and perturbative Triples (CCSD(T))[167] and density functional theory with B3LYP functional[168, 169] are also presented. All DOCI curves give a qualitatively correct description of the dissociation process. In Table 5.4 one can notice that v2RDM-DOCI is a better approximation to FullDOCI than v2RDM is to FullCI. The effect of symmetry breaking

d	Sym.	DMRG	Δv2RDM	Δv2RDM-DOCI	ΔFullDOCI
2.2	D_{2h}	-109.278	-77.375	222.578	224.455
2.2	C_1	-109.278	-77.375	209.891	214.787
4.0	D_{2h}	-108.975	-96.213	257.013	258.842
4.0	C_1	-108.975	-96.213	248.396	250.991
10.0	D_{2h}	-108.960	-66.384	282.966	283.108
10.0	C_1	-108.960	-66.384	273.371	273.464

Table 5.4: Some points on the N_2 curve from Figure 5.6. The interatomic distance (d) is in bohr. The DMRG energy is in Hartree. For v2RDM, v2RDM-DOCI and FullDOCI, the deviation (△) from DMRG is given in milliHartree.

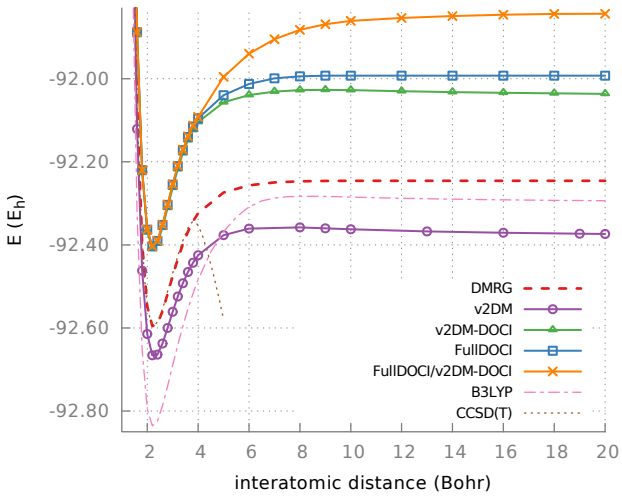

Figure 5.7: The dissociation of CN^- in the cc-PVDZ basis. The DOCI curves shown are for the C_1 symmetry.

is very small for N_2: the energy gains are in the milliHartree region. Note that N_2 dissociates into two N atoms with an odd number of electrons. This forms no problem for FullDOCI as the orbital optimization can handle this[110]. The difference between the DOCI curves and the DMRG reference is due to dynamical correlations and can be added in a subsequent stage, as shown in Ref. 170.

Another interesting case is cyanide, CN^-. This heteronuclear molecule also has a triple bond and dissociates in C^- and N. The effect of breaking the C_{2v} symmetry is again minimal (see results in Table 5.5) so in Figure 5.7 we restrict ourself to the C_1 curve. For this heteronuclear molecule, the dissociation limit for v2RDM and v2RDM-DOCI is incorrect. This is a known failure for v2RDM-based techniques[171]: the energy of the isolated atoms as a function of fractional charge is a convex curve in v2RDM whereas it should

d	Sym.	DMRG	Δv2RDM	Δv2RDM-DOCI	ΔFullDOCI
2.2	C_{2v}	-92.596	-70.208	186.967	192.202
2.2	C_1	-92.596	-70.208	186.967	192.192
4.0	C_{2v}	-92.324	-101.281	219.639	228.307
4.0	C_1	-92.324	-101.281	219.639	228.300
10.0	C_{2v}	-92.246	-116.686	218.333	253.131
10.0	C_1	-92.246	-116.686	218.333	253.130
20.0	C_{2v}	-92.246	-127.996	209.275	253.135
20.0	C_1	-92.246	-127.996	209.275	253.133

Table 5.5: Some points on the CN^- curve from Figure 5.7. The interatomic distance (d) is in bohr. The DMRG energy is in Hartree. For v2RDM, v2RDM-DOCI and FullDOCI, the deviation from DMRG is given in milliHartree.

be a piecewise linear curve[172]. Because of this, v2RDM will favour fractional charges on dissociated atoms and thus give a physically incorrect picture. This can be seen clearly on the FullDOCI/v2RDM-DOCI curve: if we use the optimal basis of v2RDM-DOCI, the FullDOCI energy is much higher than the true FullDOCI energy as the FullDOCI solution cannot use the artificial non-integer atomic charges. A Mulliken population analysis[173] confirms this: at an interatomic distance of 20 bohr, the net charges are $C^{-0.48}N^{-0.52}$. Using so-called subsystem constraints[120, 174] one can force the E vs N curve to be piecewise linear. However, this would require a v2RDM(-DOCI) optimization at each nearby integer value of N. In Figure 5.8, we have used the FullDOCI optimal orbitals for the v2RDM-DOCI calculation. In this case, v2RDM-DOCI gives the correct DOCI dissociation limit. This suggests that it might be possible to find specific DOCI constraints to solve the problem of fractional charges in v2RDM-DOCI.

5.5 Conclusions

In this chapter specific necessary N-representability constraints for a second order density matrix were derived for a seniority-zero CI wavefunction. The standard two-particle conditions $\mathcal{P}$, $\mathcal{Q}$ and $\mathcal{G}$ reduce to a simpler form that allows for a better theoretical scaling: K^3 instead of K^6. As any truncated CI wavefunction is orbital dependent, an orbital optimization scheme has been included. An orbital optimizer based on elementary Jacobi rotations is used. Only two orbitals are optimized at each step, implying that the associated two-electron integral transformation is much more efficient. The theoretical scaling of the orbital optimizer is K^3. In practice, the molecular systems in this manuscript needed less than 50 Jacobi rotations with optimization to convergence. The runtime was on average less than one hour. Both of course are very dependent on the used starting point. We have tested our

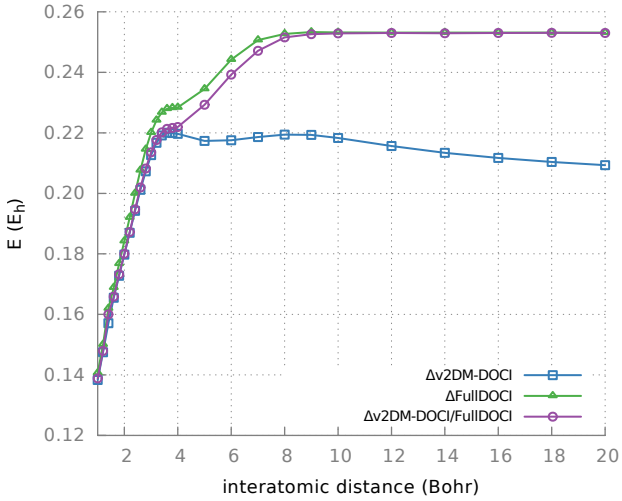

Figure 5.8: The dissociation of CN^- in the cc-PVDZ basis: comparing the v2RDM-DOCI/FullDOCI results with v2RDM-DOCI and FullDOCI. The deviation from DMRG is plotted.

method on several challenging cases. For the H_8 equidistant chain, we find that the symmetry of the system must be broken in order to find the correct DOCI energy curve. The orbital optimizer needs the additional degrees of freedom to find the physically correct set of orbitals. For the dissociation of N_2, v2RDM-DOCI gives good results, and symmetry breaking hardly gives any improvement. It is seen that v2RDM-DOCI provides a good approximation to FullDOCI: the v2RDM-DOCI and FullDOCI energies are consistently closer to each other than the v2RDM and FullCI energies. In the dissociation of CN^-, v2RDM and v2RDM-DOCI fail due to fractional charges although FullDOCI still gives a good description. We note that v2RDM-DOCI with the FullDOCI optimal basis can reproduce the correct FullDOCI energy. This indicates that there could exist specific DOCI constraints to fix the problem of fractional charges in v2RDM-DOCI.

The orbital optimizer works well provided it is given a suitable starting point. Near equilibrium, the Hartree-Fock molecular orbitals are usually a good choice, whereas in the dissociation limit localized orbitals often give a better starting point. Unfortunately this does not always hold: for instance for the H_8 chain the equilibrium energy could only be found by starting from the localized orbitals. However, if a single optimal point is found in the correct DOCI valley, it can usually be used as a starting point for all other calculations on the same system.

The main results of this chapter support the idea that DOCI combined with orbital optimization captures the lion's share of the static correlations. Subse-

quently, the missing dynamic correlations could be added through perturbation theory[170]. We find that v2RDM-DOCI is a good and fast approximation to FullDOCI.

Part II

Exactly solvable pairing Hamiltonians

Chapter 6

The Richardson-Gaudin models

As discussed in the first part of this thesis, the exact solution of the non-relativistic quantum chemical Hamiltonian is only feasible for very small systems due to the exponential scaling of the problem. A way of dealing with this problem is resorting to approximative wave functions that scale better with system size.

However, another approach exists. One could approximate the non-relativistic quantum chemical Hamiltonian with one that grasps the essential physics and chemistry of the problem. In this part some selected pairing Hamiltonians are discussed. These Hamiltonians aim to describe strongly correlated electron effects in nuclei and solid state systems where pairing plays a major role, such as superconductivity and superfluidity.

What makes these Hamiltonians interesting for this thesis is that seniority is an exact quantum number for these systems, as unpaired electrons do not interact with the rest of the system and the pairing Hamiltonian does not allow pair breaking. The Hamiltonian thus becomes block diagonal in sectors labeled by the seniority quantum number. Another remarkable fact of a subset of these models is that they are derivable from an exactly integrable model, the so-called Richardson-Gaudin (RG) models. The reason for this is that they can be constructed as a linear combination of the integrals of motion of the RG models. This makes it, in principle, possible to design a solution method that scales linearly with the system size. In the subsequent chapters two particular pairing models that are derivable from the Richardson-Gaudin models are studied, namely the XXX and the XXZ RG model. The most general pairing Hamiltonian is given by [175]:

$$\hat{H} = \sum_j \epsilon_j \hat{n}_j + \sum_{ij} V_{ij} S_i^\dagger S_j + \sum_{ij} W_{ij} \hat{n}_i \hat{n}_j \tag{6.1}$$

Here, the operator ($\hat{n}_j$) counts the number of particles contained by level j:

$$\hat{n}_j = \sum_{m>0} (a^\dagger_{jm} a_{jm} + a^\dagger_{j-m} a_{j-m}), \tag{6.2}$$

where $a^\dagger_{jm}$ and a_{jm} denote the standard fermion creation and annihilation operators for $D_j = 2j + 1$ fold degenerate single-particle level j and spin-projection m, fulfilling the standard fermion anti-commutation relations. This thesis focusses on electrons and therefore it is assumed that in the following the single-particle levels j are all two-fold degenerate, with maximum spin projection $\frac{1}{2}$. To ease the notation creation and annihilation operators are not denoted with a hat.

$$\{a_{jm}, a^\dagger_{j'm'}\} = \delta_{jj'}\delta_{mm'} \tag{6.3}$$

V_{ij} is the strength of the pairing interaction between single-particle levels i and j, and W_{ij} tunes the probability to find single-particle levels i and j simultaneously occupied. The quasispin operators $S^\dagger_j$ and S_j are given by

$$S^\dagger_j = \sum_{m>0} (-1)^{(j-m)} a^\dagger_{jm} a^\dagger_{j,-m} \tag{6.4}$$

$$S_j = \sum_{m>0} (-1)^{(j-m)} a_{j,-m} a_{jm} \tag{6.5}$$

These operators create or destroy a single pair of electrons or nucleons in the time-reversed states of single-particle level j. To close the quasi-spin $su(2)$ algebra the following operator is defined:

$$S^0_j = \frac{1}{2} \sum_{m>0} (a^\dagger_{jm} a_{jm} + a^\dagger_{j-m} a_{j-m} - 1). \tag{6.6}$$

Together with the operators defined by eq.(6.4) and eq.(6.5) we have a set of orthogonal $su(2)$ algebras:

$$\left[S^0_i, S^\dagger_j\right] = \delta_{ij} S^\dagger_j, \quad \left[S^0_i, S_j\right] = -\delta_{ij} S_j, \quad \left[S^\dagger_i, S_j\right] = 2\delta_{ij} S^0_i \tag{6.7}$$

It is possible to rewrite S^0_j as:

$$S^0_j = \frac{1}{2}\hat{n}_j - \frac{1}{4} D_j, \tag{6.8}$$

with D_j the total degeneracy of level j. It is thus possible to rewrite the Hamiltonian as:

$$\hat{H} = \sum_j \epsilon_j \left(2S^0_j + \frac{1}{2} D_j\right) + \sum_{jj'} V_{jj'} S^\dagger_j S_{j'} \tag{6.9}$$

If we define $d_j = \frac{1}{2}\Omega_j - \frac{1}{4} D_j$ with Ω_j the seniority of the single-particle level j, which can have the values 0 or 1 for systems with twofold degenerate levels. One

can see that the Hamiltonian (eq. 6.1) only couples Slater determinants with equal seniority. The single-particle levels with maximal seniority are blocked in the sense that they do not interact with other single-particle levels for the determination of the energy. The interaction terms never break or create pairs and the Hamiltonian becomes effectively block diagonal in the seniority number.

6.1 The quasi-spin algebra

The pair creation and annihilation operators introduced in the previous section, fulfill the commutation laws of a quasi-spin $su(2)$ algebra. The basis functions are given by:

$$|S_j, M_{S_j}\rangle = |\frac{1}{4}D_j - \frac{1}{2}\Omega_j; \frac{1}{2}n_j - \frac{1}{4}D_j\rangle\,, \tag{6.10}$$

with $S_j = -d_j$. The state with the lowest S_j is the vacuum, which represents a state without pairs.

$$|\theta\rangle := |S_j, -S_j\rangle = |\frac{1}{4}D_j - \frac{1}{2}\Omega_j; \frac{1}{2}\Omega_j - \frac{1}{4}D_j\rangle \tag{6.11}$$

The action of the generators on the basisfunctions is given by:

$$\begin{aligned} S^\dagger\,|S,M\rangle &= \sqrt{(S-M)(S+M+1)}\,|S,M+1\rangle & (6.12)\\ S\,|S,M\rangle &= \sqrt{(S+M)(S-M+1)}\,|S,M-1\rangle & (6.13)\\ S_0\,|S,M\rangle &= M\,|S,M\rangle\,. & (6.14) \end{aligned}$$

6.2 Integrability

The pairing model supports an integrable model. This means that its Hamiltonian can be rewritten as a sum of K commuting operators, where K denotes the total number of degrees of freedom. If the following set of operators is defined as:

$$\hat{R}_i = S_i^0 + g\sum_{k\neq i}^{K}\frac{1}{2}X_{ik}(S_i^\dagger S_k + S_k^\dagger S_i) + Z_{ik}S_i^0 S_k^0 \tag{6.15}$$

The index i runs over the K single-particle levels, g is an arbitrary parameter, and X and Z are matrix parameters that have as dimension the number of degrees of freedom. It is now possible to derive a set of conditions that makes them commute mutually:

$$[\hat{R}_i, \hat{R}_j] = 0 \quad \forall i \in [1,\ldots,K]. \tag{6.16}$$

After a tedious derivation one can see that the above commutation relations are fulfilled if element wise conditions of the matrices X_{ik} and Z_{ik} are fulfilled.

The integrability conditions are given by:

$$X_{ij} = -X_{ji}, \quad Z_{ij} = -Z_{ji} \tag{6.17}$$

$$X_{ij}X_{jk} - X_{ik}(Z_{ij} + Z_{jk}) = 0 \tag{6.18}$$

This gives rise to the integrable XXZ models. All R_i commute when the above conditions are fulfilled, this means that finding the eigenstates of one of them will give us the eigenstates of all.

6.3 Bethe ansatz wave function

In this section the Richardson-Gaudin equations and eigenvalues are derived together with the eigenstates of the integrals of motion R_i. The Gaudin algebra is defined as:

$$S_\alpha^\dagger = \sum_{i=1}^{K} X_{i\alpha} S_i^\dagger \tag{6.19}$$

$$S_\alpha = \sum_{i=1}^{K} X_{i\alpha}^* S_i \tag{6.20}$$

$$S_\alpha^0 = \sum_{i=1}^{K} Z_{i\alpha} S_i^0 \tag{6.21}$$

The index α is not referring to one of the spatial orbitals, but to generalized electron pairs in the context of pairing Hamiltonians. At this moment it is sufficient to know that they stand for a different category of indices. Both categories obey the integrability conditions of eq. (6.17). The commutation relations of the generalized pair operators can be calculated as:

$$[S_\alpha^\dagger, S_\beta] = \sum_i Z_{i\alpha} X_{i\beta} S_i^\dagger \tag{6.22}$$

$$= 2X_{\alpha\beta}(S_\alpha^0 - S_\beta^0) \tag{6.23}$$

$$\left[S_\alpha^0, S_\beta^\dagger\right] = \sum_i X_{i\alpha} X_{i\beta}^* 2S_i^0 \tag{6.24}$$

$$= X_{\alpha\beta} S_\alpha^\dagger - Z_{\alpha\beta} S_\beta^\dagger \tag{6.25}$$

Furthermore it can be shown that the eigenstates of the operators defined by eq. (6.15) are given by product states of the following form:

$$|\psi\rangle = \prod_{\alpha=1}^{N} S_\alpha^\dagger |\theta\rangle \tag{6.26}$$

Acting with the R_i operator on the above product state gives:

$$R_i \prod_{\alpha=1}^{N} S_\alpha^\dagger |\theta\rangle = \sum_{\alpha=1}^{N} \sum_{\beta=\alpha+1}^{N} \left(\prod_{\gamma\neq\alpha,\beta}^{N} S_\gamma^\dagger \right) \left[\left[R_i, S_\alpha^\dagger \right], S_\beta^\dagger \right] |\theta\rangle \quad (6.27)$$

$$+ \sum_{\alpha=1}^{N} \left(\prod_{\beta\neq\alpha}^{N} S_\beta^\dagger \right) \left[R_i, S_\alpha^\dagger \right] |\theta\rangle + \left(\prod_{\alpha=1}^{N} S_\alpha^\dagger \right) R_i |\theta\rangle \quad (6.28)$$

Explicitly calculating the commutators of the above expressions gives:

$$\left[R_i, S_\alpha^\dagger \right] = X_{i\alpha} S_i^\dagger (1 - g S_\alpha^0) - g Z_{\alpha i} S_\alpha^\dagger S_i^0 \quad (6.29)$$

$$\left[\left[R_i, S_\alpha^\dagger \right], S_\beta^\dagger \right] = -g S_i^\dagger Z_{\alpha\beta} (X_{i\beta} S_\alpha^\dagger - X_{i\alpha} S_\beta^\dagger) \quad (6.30)$$

The action on the vacuum is given by:

$$\hat{R}_i |\theta\rangle = d_i \left[-1 + g \sum_{k\neq i} Z_{ik} d_k \right] |\theta\rangle \quad (6.31)$$

$$\left[\hat{R}_i, S_\alpha^\dagger \right] |\theta\rangle = \left[X_{i\alpha} S_i^\dagger (1 + g d_\alpha) + g Z_{\alpha i} S_\alpha^\dagger d_i \right] |\theta\rangle \quad (6.32)$$

$$\left[\left[\hat{R}_i, S_\alpha^\dagger \right], S_\beta^\dagger \right] |\theta\rangle = -g S_i^\dagger Z_{\alpha\beta} (X_{i\beta} S_\alpha^\dagger - X_{i\alpha} S_\beta^\dagger) |\theta\rangle \quad (6.33)$$

To simplify the following expressions the variables $d_\alpha = \sum_{i=1}^{m} Z_{i\alpha} d_i$ are defined, and after combining all of the above, it can be seen that:

$$\hat{R}_i \prod_{\alpha=1}^{N} S_\alpha^\dagger |\theta\rangle = \sum_{\alpha=1}^{N} \left[X_{i\alpha}(1 + g d_\alpha) - g \sum_{\beta\neq\alpha}^{N} Z_{\beta\alpha} X_{i\alpha} \right] S_i^\dagger \prod_{\gamma\neq\alpha}^{N} S_\gamma^\dagger |\theta\rangle \quad (6.34)$$

$$+ d_i \left[-1 + g \sum_{k\neq i} Z_{ik} d_k + g \sum_{\beta=1}^{N} Z_{\beta i} \right] \prod_{\alpha=1}^{N} S_\alpha^\dagger |\theta\rangle . \quad (6.35)$$

It can now be concluded that the Bethe ansatz product state is an eigenstate of $\hat{R}_i$ with eigenvalue given by:

$$r_i = d_i(-1 + g \sum_{k\neq i}^{K} Z_{ik} d_k + g \sum_{\beta=1}^{N} Z_{\beta i}), \quad (6.36)$$

if the following set of equations

$$1 + g d_\alpha - g \sum_{\beta\neq\alpha}^{N} Z_{\beta\alpha} = 0 \ \forall\alpha \quad (6.37)$$

is fulfilled for all N Richardson-Gaudin variables. The set of N equations (6.37) is also known in the literature as the Richardson-Gaudin equations [176].

6.4 Integrability of the reduced BCS Hamiltonian

The rational model is a special variant of the integrable pairing models that can be built from the integrals of motion eq.(6.15). The parametrization of the Gaudin matrices is given by:

$$X_{ij} = Z_{ij} = \frac{1}{2(\epsilon_i - \epsilon_j)} \tag{6.38}$$

It can be checked that the above parametrization fulfills the integrability conditions (see eq. (6.17) and (6.18)). Because the Z Gaudin matrix is equal to the X matrix, for this model, it is also known as the XXX model. The integrals of motion of the XXX model are given by:

$$\hat{R}_i = S_i^0 + g \sum_{k \neq i} \frac{\frac{1}{2}(S_i^\dagger S_k + S_k^\dagger S_i) + S_i^0 S_k^0}{\epsilon_i - \epsilon_k} \tag{6.39}$$

It is now possible to construct the reduced Bardeen-Cooper-Schrieffer (BCS) Hamiltonian, as a linear combination of the above integrals of motion. From this linear combination it follows that the reduced BCS Hamiltonian is exact integrable, and has the same eigenstates as the $\hat{R}_i$ operators of the XXX model. The reduced BCS Hamiltonian is given by the spherical linear contraction:

$$\hat{H}_{red} = \sum_j \epsilon_j (2S_j^0 + \frac{1}{2} D_j) + g \sum_{ij} S_j^\dagger S_i \tag{6.40}$$

The reduced BCS Hamiltonian can be seen as a simplified version of the generalized pairing Hamiltonian, with a level independent coupling constant g. The linear combination of the integrals of motion of the XXX model that generates the reduced BCS Hamiltonian is given by:

$$\hat{H}_{red} = \sum_i 2\epsilon_i \hat{R}_i \tag{6.41}$$

If the above summation is expanded and simplified, one sees the reduced BCS Hamiltonian appearing up to some irrelevant constants. The integrability of the reduced BCS Hamiltonian follows from the above derivation, together with the fact that the eigenstates and eigenvalues of this Hamiltonian can be found by solving eq. (6.37). The reduced BCS Hamiltonian is of great significance as it is used to describe the essential physics of a range of systems ranging from superconductivity, superfluidity, pairing in nuclei, ... The exact integrability of the reduced BCS Hamiltonian is exploited in chapter 7 to study the effects of geometry perturbations on the superconducting state of nano-grains.

6.5 Integrability of the $p_x + ip_y$ Hamiltonian

Another Hamiltonian that can be formed with a linear combination of the integrals of motion of the XXZ Richardson-Gaudin models is the $p_x + ip_y$ pairing Hamiltonian. The $p_x + ip_y$ pairing Hamiltonian is given by:

$$\hat{H}_{fac} = \eta \sum_{i=1}^{K} D_i^2 S_i^0 + \tilde{g} \sum_{ij=1}^{K} D_i D_j^* S_i^\dagger S_j. \tag{6.42}$$

This Hamiltonian describes p-wave pairing which is found in fermionic superfluids (^{3}He), ultra-cold atomic gases and p-wave superconductivity. If one takes the parametrization of the Gaudin matrices [177] as:

$$X_{ij} = \frac{2D_i D_j}{(D_i^2 - D_j^2)} \tag{6.43}$$

$$Z_{ij} = \frac{D_i^2 + D_j^2}{(D_i^2 - D_j^2)}. \tag{6.44}$$

It can be straightforwardly checked that the integrability conditions are fulfilled (see eq. 6.17). The integrals of motion then become:

$$\hat{R}_i = S_i^0 + g \sum_{k \neq i} \frac{D_i D_j}{(D_i^2 - D_j^2)} (S_i^\dagger S_k + S_k^\dagger S_i) + \frac{D_i^2 + D_j^2}{D_i^2 - D_j^2} S_i^0 S_k^0. \tag{6.45}$$

The linear combination of the $\hat{R}_i$ operators that generates the $p_x + ip_y$ Hamiltonian is given by:

$$\hat{H}_{fac} = \lambda \sum_i D_i^2 \hat{R}_i, \tag{6.46}$$

with $\lambda = \frac{\eta}{1+2\gamma(1-N)+\gamma\left(L-\sum_i v_i\right)}$, where γ is a parameter proportional to the interaction constant $g = -2\lambda\gamma$, and N the number of pairs. After some straightforward algebraical calculations and subtraction of the diagonal term $g\sum_i \mathbf{S}_i^2 D_i^2$, the $p_x + ip_y$ pairing Hamiltonian appears (see eq. 6.42). The $\tilde{g}$ parameter that determines the strength of the p-wave pairing interaction (see eq. 6.42) is related to the parameter g of the integrals of motion of eq.(6.45) by: $\tilde{g} = g\lambda$. The exact integrability of the $p_x + ip_y$ pairing Hamiltonian is exploited in chapter 8 to study its interesting phase diagram.

To conclude, it is stated that the generality of eq.(6.37) can be exploited to create a general computer program that is able to solve all kinds of different pairing Hamiltonians with the same underlying machinery. One just needs to provide the specific form of the Gaudin matrices together with the explicit mapping of the parameter g of eq.(6.37) to the parameters of the Hamiltonian one wants to solve. A short summary and link to an implementation can be found in appendix B.

6.6 Exactly integrable models in quantum chemistry?

Imagine that a method could be found that makes it possible to map molecular Hamiltonians on exactly integrable pairing Hamiltonians such that the accuracy of the resulting wave function approximates the one of the seniority zero wave function for the molecular system, then a new powerful method able to describe the correlation of big molecular systems would have been created. Preliminary results have been obtained that indicate that it is possible to obtain DOCI quality energies for small molecular systems such as the hydrogen dimer and BeH_2 with wave functions generated by solving the XXX Richardson-Gaudin model. This can be done by varying the K single-particle energy levels and the pairing constant g of the reduced BCS Hamiltonian such that the solution of this Hamiltonian gives the lowest energy possible for a given quantum chemical Hamiltonian for a respective orthonormal basis in a given atomic basis set. Unfortunately the procedure to obtain those results is very slow at the moment due to the slow convergence of the conjugate gradient method with $K + 1$ degrees of freedom. However, the small amount of memory necessary for this procedure encourages further research. A quicker approach is possible if one weakens the desire to have DOCI quality energies to better than HF quality energies. This can be done by generating the set of single-particle energies of the reduced BCS Hamiltonian with a fast optimal function of the Hartree-Fock single-particle levels and using the restricted orthonormal Hartree-Fock orbitals as single-particle basis. The reduced BCS Hamiltonian with zero pairing constant gives the Hartree-Fock wave function as a solution. Now turning on the pairing constant g will lead to a seniority zero wave function (with the same dimension as the DOCI wave function) and with lower energy than the HF wave function but higher energy than the DOCI wave function. This reduces the problem to finding the minimum of a one dimensional problem for which fast algorithms exist.

Chapter 7

Geometry dependence of superconducting nano-grains

[1]

In a seminal paper, P. W. Anderson [178] addressed the question of how small a metallic grain would have to be such that a superconducting state would cease to exist. He argued that quantum confinement would force the single-particle (sp) spectrum to become discretely resolved. The mean sp energy spacing will increase with decreasing size of the grain, until it becomes comparable to the superconducting gap in the bulk phase. At that point, the bulk gap looses its significance as a clear gap between a single superconducting state and a continuum of excited states, and the superconducting phase would evaporate. The single-electron transistor (SET) experiments of Ralph, Black and Tinkham [179] demonstrated that the energy spectrum of nanometer-scale Al particles is discretely resolved, and moreover, the spectrum was found to be dependent on number parity and externally applied magnetic fields [180, 181], establishing the persistence of pairing correlations at the nanoscale. Bardeen, Cooper and Schrieffer (BCS) [182] had identified an effective electron-electron pairing interaction as the driving force behind the superconducting state in bulk materials. A key feature of BCS theory is that the superconducting ground state of a superconductor is modeled as a coherent condensation of Cooper pairs [183]. While this approximation is essentially valid in the bulk limit, it is no longer sound for finite-size systems because inaccuracies induced by particle-number fluctuations become relatively large. This opened a call for

[1] Has been previously published as: M. Van Raemdonck, S. De Baerdemacker, and D. Van Neck. *Perturbations on the superconducting state of metallic nanoparticles: influence of geometry and impurities.* 2013: The European Physical Journal D 67:14.

theoretical approaches in the canonical regime, such as Lanczos diagonalisation [184], projected-BCS [185], Density Matrix Renormalization Group [186], or the Richardson-Gaudin (RG) formalism [187]. Richardson had shown, within the context of pairing in nuclear structure physics [188], that the reduced, level-independent, BCS Hamiltonian is exactly diagonalizable by means of a Bethe Ansatz product state, provided the RG variables, which occur as rapidities in the Ansatz, form a solution to the set of RG equations [189, 190]. Later, Gaudin decomposed the reduced BCS Hamiltonian into a complete set of commuting conserved charges, adding it to the class of *integrable* models [191]. The main significance of these results is that, as long as a level-independent pair scattering term is considered, the BCS Hamiltonian can be solved exactly for a general sp spectrum, within polynomially scaling computing time. Therefore, in mesoscopic systems it is a practical tool for the investigation of pairing correlations as a function of the sp spectrum. First investigations were performed with a uniform sp energy spacing [184, 185], however, studies with randomly generated spectra showed an enhancement of pairing correlations by randomness [187, 192]. This is related to the observation that pairing correlations are significantly stronger around the Fermi level, such that a random increase of the level density around the Fermi level will have a stronger impact on the mean pair correlations in a uniform sampling. The result of this study triggers the question whether pairing correlations could be enhanced in a controlled fashion. A sensible control parameter for the sp spectrum would be the shape and size of the nanoparticle. In a free-wave "particle in a box" picture, the geometric boundary conditions at the surface of the nanoparticle will fix the spectrum of the particles. The variations in pairing correlations of a rectangularly shaped nanoparticle were investigated in this way as a function of the aspect ratio [193], and more recently, the shell structure in spherically shaped nanostructures has been assessed [194–196] in connection with the scanning tunneling experiments (STM) on deposited Pb [197] and Sn [198] nanoclusters. The reduction from three to two dimensions, relevant for the description of pairing correlations in superconducting spherical coatings or multielectron bubbles in liquid helium, has also been investigated [199, 200]. The theoretical results in rectangular geometries showed a strongly volatile behavior of the pairing condensation as a function of the shape control parameter (see *e.g.* Fig. 1 in [193]), which is understood to be a direct consequence of rapid fluctuations in the density of active sp levels around the Fermi level (also referred to as the Debye window) [198]. This chapter focuses on how the pairing condensation energy varies as a function of an external control parameter. The purpose of this chapter is to investigate whether there exists such a control parameter which is less prone to strong fluctuations and allows for a more controlled manipulation of the condensation energy. Our calculations will be performed within the canonical RG formalism [189, 190], using a recently proposed pseudo-deformed quasispin algorithm [201]. In the next section, the necessary theoretical results of the RG formalism for metallic nanograins are recapitulated. The following section is devoted to a scrutiny of the effect of the fluctuating level densities on the

condensation energy for a small and easily fathomable system. This section is divided into two parts. In close parallel to the work of Gladilin *et. al.* [193], the geometrical effects on the condensation energy are briefly discussed in a first part. In a second part, an impurity in otherwise clean nanograins is introduced.

For a good review on the developments in the field of superconducting metallic nanograins until 2001, the reader is referred to the review paper of von Delft and Ralph [202].

7.1 Richardson-Gaudin

The reduced BCS Hamiltonian is given by

$$\hat{H} = \sum_{i=1}^{M} \varepsilon_i \hat{n}_i + g \sum_{i,j=1}^{M} \hat{S}_i^\dagger \hat{S}_j, \tag{7.1}$$

with the latin indices $\{i, j = 1 \dots M\}$ referring to a set of doubly-degenerate sp energies within the Debye window around the Fermi level. The number operator

$$\hat{n}_i = a_i^\dagger a_i + a_{\bar{i}}^\dagger a_{\bar{i}}, \tag{7.2}$$

counts the number of particles within a level i and the pair scattering term is represented by the pair creation/annihilation operators

$$\hat{S}_i^\dagger = a_i^\dagger a_{\bar{i}}^\dagger, \quad \hat{S}_i = (\hat{S}_i^\dagger)^\dagger = a_{\bar{i}} a_i, \tag{7.3}$$

with $a_i^\dagger$ (a_i) the standard fermion creation (annihilation) operators. The bar notation refers to the time-reversed partner of the corresponding operator. The set of operators (7.2) and (7.3) span an $su(2)$ quasispin algebra

$$[\hat{S}_i^0, \hat{S}_j^\dagger] = \delta_{ij} S_i^\dagger, \quad [\hat{S}_i^0, \hat{S}_j] = -\delta_{ij} S_i, \quad [\hat{S}_i^\dagger, \hat{S}_j] = 2\delta_{ij} S_i^0, \tag{7.4}$$

with $\hat{S}_i^0 = \frac{1}{2}(\hat{n}_i - 1)$. This algebra supports two different $su(2)$ representations, corresponding to unblocked (open) and blocked (pair-broken) levels. This chapter, only open levels will be considered. Richardson's result [189, 190] states that the reduced BCS Hamiltonian can be diagonalised exactly by means of a product state of generalised pairs, acting on the pair vacuum $|\theta\rangle$

$$|\psi(\{x\})\rangle = \prod_{\alpha=1}^{N} \left(\sum_{i=1}^{M} \frac{\hat{S}_i^\dagger}{2\varepsilon_i - x_\alpha} \right) |\theta\rangle, \tag{7.5}$$

provided the set of RG variables $\{x\} = \{x_1, x_2, \dots x_N\}$, with N the total number of pairs, form a solution of the set of non-linear RG equations

$$1 + g \sum_{i=1}^{M} \frac{1}{2\varepsilon_i - x_\alpha} - 2g \sum_{\beta \neq \alpha} \frac{1}{x_\beta - x_\alpha} = 0, \tag{7.6}$$

for $\alpha = 1, 2, \ldots, N$. Since blocked levels are discarded, N is taken as half the total number of particles. Once the RG equations have been solved for $\{x\}$, the eigenstate energy of the Hamiltonian is given by

$$E = \sum_{\alpha=1}^{N} x_\alpha. \tag{7.7}$$

It is convenient to introduce the concept of condensation energy, which is defined as the ground state energy E of the system at a given pairing interaction g, corrected by the ground state energy of the system in the non-interacting limit E_0

$$E_C = \langle\psi(g)|\hat{H}(g)|\psi(g)\rangle - \langle\psi(0)|\hat{H}(0)|\psi(0)\rangle \tag{7.8}$$

Because the ground state of the non-interacting system corresponds to a simple filling of the sp levels until the Fermi energy, the condensation energy of the reduced BCS Hamiltonian reduces to

$$E_C = \sum_{\alpha=1}^{N} x_\alpha - \sum_{i=1}^{N} 2\varepsilon_i. \tag{7.9}$$

The benefit of using the condensation energy over the ground state energy is that the former quantity corrects for global fluctuations in the sp energy, so it is a direct probe for pairing correlations.

7.2 Perturbations

We will employ a simplified "particle in a box" approach to study the effect of perturbations. In this approach, it is assumed that the conductance electrons are completely delocalised from the atoms in the crystal, and move as free particles within a box, only confined by the boundaries. Regarding the qualitative nature of our study, this approach satisfies our needs, however one should consider more sophisticated methods, such as Density Functional Theory [203], if more realistic results are desired.

7.2.1 Geometric perturbations

In a first part, the condensation energy E_C is studied and compared within a rectangular, cylindrical and spherical geometry. The single-particle energies are taken as the solutions to the Schrödinger equation with the infinite-well sp potential $V(\boldsymbol{r})$

$$V(\boldsymbol{r}) = \begin{cases} 0, & \forall \boldsymbol{r} \in \text{ the box} \\ +\infty, & \forall \boldsymbol{r} \notin \text{ the box} \end{cases} \tag{7.10}$$

The wavefunctions and corresponding eigenvalues for rectangular, cylindrical and spherical infinite wells can be found in introductory quantum mechanics

textbooks [1]. For rectangular geometries, the sp energies are given by

$$\varepsilon_{(n_x,n_y,n_z)} = \frac{\hbar^2\pi^2}{2m_e}\left(\frac{n_x^2}{l_x^2} + \frac{n_y^2}{l_y^2} + \frac{n_z^2}{l_z^2}\right), \tag{7.11}$$

with $(n_x, n_y, n_z) \in \mathbb{N}_0^3$ the set of quantum numbers, m_e the effective mass of the electron, and (l_x, l_y, l_z) the dimensions of the rectangular box. We will define a length scale l, such that all lengths will be given relative to l, and energies relative to $\frac{\hbar^2}{2m_e l^2}$. The sp spectrum (7.11) is given in Figure 7.1(a) as a function of l_x, with $l_z = l$ kept as a constant, and l_y defined as such that the volume of the rectangular box also remains a constant $l_x l_y l_z = l^3$. In addition, Figures 7.1(b) and 7.1(c) show the condensation energy for a system of $N = 5$ pairs living in the $m = 10$ lowest sp levels of the rectangular box with respectively a weak- ($g = -1.0[\hbar^2/2m_e l^2]$) and strong ($g = -400.0[\hbar^2/2m_e l^2]$) pairing interaction. Figure 7.1(a) not only depicts the 10 active sp levels, but also the next 10 levels outside of the Debye window (in dotted lines) to illustrate how the sp levels enter and leave the Debye window as a function of l_x. It can be seen that the steep exits and enterings of the sp levels into the Debye window give rise to strong fluctuations in the sp densities, especially higher up in the spectrum. This has an effect on the condensation energies, as can be inferred from Figures 7.1(b) and 7.1(c).

Before discussing the numerical results, it is worthwhile to distill the general features in both regimes of the pairing strength using perturbative techniques. For the weak-coupling regime, standard second order perturbation theory [1] is used to calculate the condensation energy

$$\lim_{g\to 0} E_C = Ng + g^2 \sum_{a=1}^{k_F} \sum_{b=k_F+1}^{M} \frac{1}{2\varepsilon_a - 2\varepsilon_b} + \mathcal{O}(g^3), \tag{7.12}$$

with k_F the Fermi level index, and the dummy indices a and b running over respectively occupied and unoccupied sp levels in the non-interacting limit. For the strong-coupling regime, an approximate expression can be derived for the condensation energy using the RG equations [201, 204]

$$\lim_{g\to\infty} E_C = gN(M - N + 1) + N(\langle 2\varepsilon\rangle - \langle 2\varepsilon\rangle_F) + \mathcal{O}(\tfrac{1}{g}), \tag{7.13}$$

with $\langle 2\varepsilon\rangle = \frac{1}{M}\sum_{i=1}^{M} 2\varepsilon_i$ the mean pair sp energy and $\langle 2\varepsilon\rangle_F = \frac{1}{N}\sum_{i=1}^{k_F} 2\varepsilon_i$ the mean pair sp energy up to the Fermi level. Close inspection of the functional behavior of expressions (7.12) and (7.13) with respect to the sp spectrum gives away the gross features in the corresponding regime. In the strong-coupling regime, the condensation energy is dependent on $\langle 2\varepsilon\rangle$ and $\langle 2\varepsilon\rangle_F$. Therefore, the contributions of the sp levels on the condensation energy only depend on the position of the level with respect to the Fermi level, *i.e.* levels beneath the Fermi level contribute negatively with a weight factor $(\frac{N}{M} - 1)$, and levels above the Fermi level contribute positively with weight factor $(\frac{N}{M})$. There is no

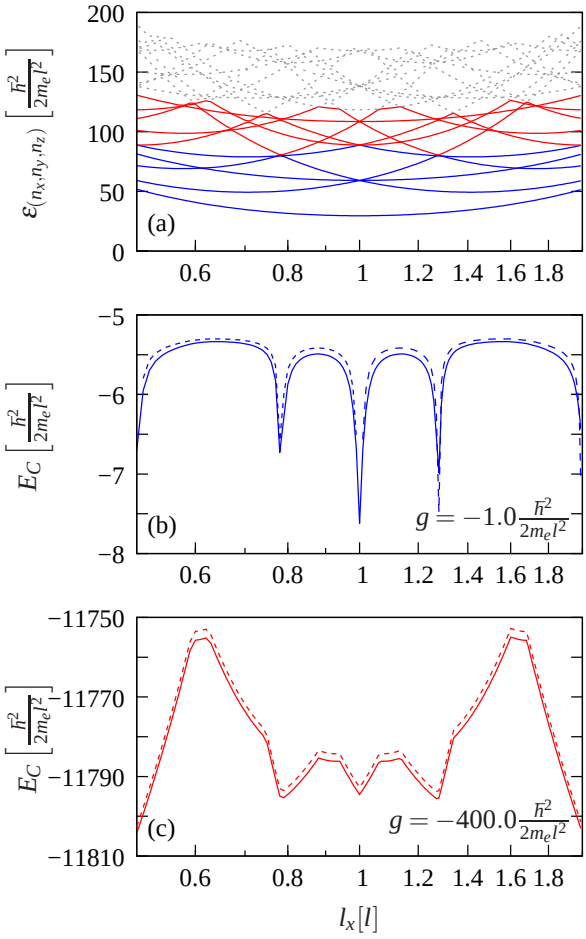

Figure 7.1: The sp spectrum (a) of a rectangular box as a function of one of the dimensions l_x. The lowest 10 levels within the active Debye window are plotted in full lines, whereas the dotted lines depict the next 10 levels outside the Debye window. Figure (b) and (c) depict the condensation energy E_C in full lines for a system of $N = 5$ pairs in the $m = 10$ active levels of Figure (a), for respectively the weak- and strong-coupling regime. The dotted lines are approximations in respective regimes (eqs. (7.12) and (7.13)). Note that the l_x axis is plotted in logarithmic scale to highlight the $l_x \leftrightarrow 1/l_x$ symmetry. Deviations of this symmetry are due to differences in resolution on the logarithmic scale.

direct dependency of local sp-level densities on the condensation energy, rather an indirect dependency entering via the mean sp energy above and below the Fermi level. For instance, it can be seen from Figure 7.1(c) that the local increase in sp-level density around the Fermi level in the vicinity of $l_x \sim 0.8$, 1.0 and 1.25 induces an increase of $\langle 2\varepsilon \rangle_F$, and therefore contributes to the

pairing condensation. Similarly, the local increase in sp-level density at the top of the Debye window around $l_x \sim 0.6$ and 1.6 contributes positively to $\langle 2\varepsilon \rangle$ and therefore decreases the pairing correlations. The situation is different for the weak-coupling regime, where local density fluctuations around the Fermi level contribute more strongly than those away from the Fermi level. This can be verified in Figure 7.1(b), where, in contrast to the strong-coupling regime, the local density increase at $l_x \sim 0.6$ and 1.6 does not influence the condensation energy, whereas the the local density increase at $l_x \sim 0.8$, 1.0 and 1.25 considerably enhances the pairing correlations.

The previous discussion highlights the importance of local sp-level density fluctuations entering directly, or indirectly into the condensation energy. Therefore, it would be desirable to have a more manageable control parameter at hand for the sp-energy levels. As is clear from Ref. [193] and Figure 7.1(a), rectangular geometries are very prone to local density fluctuations and will consequently remain hard to control. For this reason, a similar study is performed of the condensation energy within a cylindrical and spherical configuration. Without going into much detail, the conclusions of these studies agreed well with the results from the previous discussion. The sp spectrum of free particle waves, bounded within a cylinder with radius ρ_0 and height l_z is given by

$$\varepsilon_{(n_\rho, n_\phi, n_z)} = \frac{\hbar^2}{2m_e} \left(\frac{\alpha^2_{|n_\phi| n_\rho}}{\rho_0^2} + \frac{n_z^2 \pi^2}{l_z^2} \right), \tag{7.14}$$

with $(n_\rho, n_\phi, n_z) \in \mathbb{N} \times \mathbb{Z} \times \mathbb{N}$, and $\alpha_{|n_\phi| n_\rho}$ the n_ρ-th root of the Bessel function $J_{|n_\phi|}(\alpha)$. It is clear that the spectrum (7.14) and its density fluctuations has a qualitatively similar dependency on the control parameter l_z as eq. (7.11), when volume conservation is imposed $\pi \rho_0^2 l_z = l^3$. Therefore similar conclusions could be drawn for cylindrical as for rectangular geometries.

Unfortunately, the sphere has no shape control parameter if volume conservation is applied $4\pi\rho_0^3 = l^3$. However, one can notice a gain in condensation energy in comparison with a cube and cylinder with the same dimensions (see Table 7.1).

Table 7.1: The condensation energy E_C (7.9) of a cube, cylinder and sphere with volume l^3 for 3 different values of the pairing interaction strength (g), corresponding to a weak-, intermediate- and strong-coupling regime. The radius ρ_0 of the cylinder is fixed such that the height $l_z = l$. All calculations have been performed with $N = 6$ pairs in the $M = 12$ first sp levels. Energies are given in units $[\hbar^2/2m_e l^2]$

g	cube	cylinder	sphere
-1.000	-8.851	-6.850	-13.067
-10.000	-222.254	-226.183	-246.037
-20.000	-600.819	-608.382	-626.128

This is nicely understood via symmetry considerations; the sphere is more symmetric than the cube, and will therefore exhibit more degeneracies in the sp spectrum, leading to an enhancement of the pair correlations. Analogously, a cylinder is more symmetric than a cube (2D rotational vs dihedral symmetry), which generally translates into an enhancement for the pairing correlations, as illustrated in Table 7.1. The symmetry argument can be tested by breaking the symmetry of the sphere or cylinder to spheroidal shapes. Although such a study is of relevance for the experiments on spherical nanodroplets [197, 198], no significant qualitative differences from our study with rectangular grains are expected and therefore this subject is left for future investigations.

The conclusion of the present subsection is that the condensation energy of a rectangular (and cylindrical) nanograin is highly sensitive to the fluctuations in the sp-level densities, and that these fluctuations are rather strong as a function of the shape control parameter. With this respect, it would be interesting to find a more gentle control parameter such that the pairing correlations can be probed in a more controlable fashion. In the next subsection, impurities are introduced for this particular purpose.

7.2.2 Impurities

From a "particle in a box" perspective, an impurity can be modeled by means of an "obstacle" in the otherwise constant potential of the box. Let this obstacle be a Dirac $\delta(\boldsymbol{r})$ potential. For a 1D system, the potential in the Schrödinger equation becomes

$$V(x) = \begin{cases} v_0 l \delta(x - x_0) & 0 < x < l \\ \infty & x \leq 0 \text{ and } x \geq l \end{cases} \tag{7.15}$$

with $0 < x_0 < l$ and v_0 a weighted strength parameter of the impurity which can be either positive or negative, depending on whether the impurity is considered repulsive or attractive. The solution to the Schrödinger equation can be found by solving the following transcendental equation

$$\tfrac{2m_e l^2}{\hbar^2} v_0 \sin(k[l - x_0]) \sin(kx_0) + kl \sin(kl) = 0, \tag{7.16}$$

for $k \in \mathbb{R}$, leading to the sp spectrum

$$\varepsilon_n = \frac{\hbar^2 k_n^2}{2m_e}. \tag{7.17}$$

If $v_0 < 0$, there may also exist a negative energy state, which is the solution of Eq. (7.16), with the substitution $ik \to \kappa$

$$\tfrac{2m_e l^2}{\hbar^2} v_0 \sinh(\kappa[l - x_0]) \sinh(\kappa x_0) + \kappa l \sinh(\kappa l) = 0. \tag{7.18}$$

The remainder of this chapter only deals with repulsive impurities ($v_0 > 0$). The transcendental equation (7.16) has a few remarkable symmetries. For

instance, it can be verified that for $x_0 = \frac{l}{p}$ with $p \in \mathbb{N}_0$, $k = \frac{q\pi}{l}$ is always a solution of (7.16) independent from v_0, as long as q is a multiple of p. This feature explains the quasi-periodic structure as a function of x_0 in the sp spectrum, which is plotted in Figure 7.2(a) for $v_0 = 100.0[\hbar^2/2m_e l^2]$. It can be seen that each level has its own frequency modulation: the first level undergoes one full quasi-period oscillation, the second level a double quasi-period oscillation, and so on. Therefore, by probing the oscillations in the condensation energy, it can be inferred which sp levels contribute strongly to the final structure. We can recall from the previous discussion that the condensation energy is more sensitive to local sp-level density fluctuations around the Fermi level in the weak-coupling regime, whereas global fluctuations contribute more in the strong-coupling regime. This can be observed in Figures 7.2(b)-(d), where the condensation energy is plotted for a system of $N = 5$ pairs, living in the first $m = 10$ sp levels of Figure 7.2(a), with $g = -1.0$, -200.0, and -100000.0 in units $[\hbar^2/2m_e l^2]$. Taking into account that the mean sp-energy spacing is approximately $100.0(\hbar^2/2m_e l^2)$, these interaction strengths correspond respectively to the weak, intermediate, and strong-coupling regime. In the weak-coupling limit (Figure 7.2(b)), the condensation energy displays 5 peaks of enhanced pairing correlations, corresponding to the 5 quasi periods of the Fermi level. On the other side, the 10 quasi periods at the top of the Debye window are visible in the condensation energy of the strong-coupling limit (Figure 7.2(d)). The intermediate regime (Figure 7.2(c)) displays only 5 quasi periods, but it can be inferred from the shape of the modulations, that the signature of the top level is already present.

The reason why the impurity is a much more gentle control parameter than the shape of a nanograin can be related to the relative impact of the control parameter on the sp spectrum. Whereas altering the size of the nanograin has a large relative effect on the available space of the particles-in-a-box, adding a $\delta(x)$ only perturbs the particles marginally. The question is now whether $\delta(\boldsymbol{r})$ perturbations are not becoming too weak when going to higher dimensions. In order to study this, some exploratory calculations of the condensation energy with one $\delta(\boldsymbol{r} - \boldsymbol{r}_0)$ on a line (1D), in a square (2D), and in a cube (3D) are performed. The number of levels $m = 10$ and pairs $N = 5$ were chosen equal for each dimension, as well as the strength of the impurity $v_0 = 100.0[\hbar^2/2m_e l^2]$, and the pairing strength g. These preliminary calculations pointed out that the condensation energy was enhanced with approximately 20% and 25% for the 2D and 3D systems respectively compared to the 1D case, whereas the relative fluctuations in the condensation energy decreased with 75% and 85%. These numbers hint at a possible survival of impurity induced fluctuations in the condensation energy in higher dimensions, but further investigations are required. More in particular, given the strong influence of the geometry on the condensation energy of the particle, it is unclear whether the gentle impurity-induced perturbations will be observable against the large geometric fluctuations one could encounter by picking different samples in a realistic experimental setting.

The $\delta(x)$ potential has zero-range character, in contrast to the spatial finite-range nature of realistic impurities in 1D systems, which may become relatively large for nano-sized systems [205]. Therefore, the following potential is selected

$$V(x) = \begin{cases} v_0 \frac{kl}{2} \exp(-k|x - x_0|) & 0 < x < l \\ \infty & x \leq 0 \text{ and } x \geq l \end{cases} , \tag{7.19}$$

to investigate the effect of the spatial extent of the impurity on the condensation energy of the 1D system. Besides being a solution of the Helmholtz equation for screened Coulomb potentials of a point-like charged particle in 1D, the potential (7.19) acts as a distribution, including the $\delta(x - x_0)$ potential (7.15) and unperturbed system in the $k \to \infty$ and $k \to 0$ limit respectively. Therefore, the parameter $1/k$ is a control parameter for the spatial extent of the impurity. We have carried out the same calculation as in Figure 7.2 with the same values for v_0 and g, but for different values of k ranging from very large ($\delta(x)$-like) to very small (unperturbed-like) values. The results for $k = 20/l$ are depicted in Figure 7.3. The potential (7.19) will deviate from the $\delta(x - x_0)$ potential as k decreases, so the typical modulations in the sp spectrum and condensation energy of the $\delta(x-x_0)$ case are expected to gradually evaporate as the potential (7.19) broadens. For the sp spectrum, it was observed that the modulations were more suppressed for the high-lying states, compared to the low-lying states. Because the normalization of the potentials (7.19) and (7.15) has been chosen equal, the potential (7.19) has a finite height $V_{\max} = v_0 lk/2$, in contrast with the infinite height of the $\delta(x)$ potential. As a result, the higher-lying excitation sp levels will be less affected by the impurity than the lower-lying sp levels (see Figure 7.3(a) with $V_{\max} = 1000[\hbar^2/2m_e l^2]$). This has an effect on the modulations of the condensation energy in the strong-interaction limit. Because the modulations of the condensation energy in the strong-interaction limit depends approximately on the relative weighting of the sp levels above and beneath the Fermi level ε_F, the fingerprints of the higher sp levels will gradually disappear as k decreases. The value $k = 20/l$ has been chosen for Figure 7.3 because this is the point where the higher sp level modulations start to (visually) disappear from the condensation energy in the strong-interaction limit (see Figure 7.3(d)). The condensation energy in the weak-interacting limit is only dependent on the modulations around the Fermi level (see eq. (7.12)). So, modulations in the condensation energy are observed as long as the levels around the Fermi level are affected by the impurity. Again, this is strongly dependent on the relative position of the Fermi level with respect to the height and strength of the impurity potential. In the limit of $k \to 0$, all impurity induced structure will be lost.

Finally, a calculation of the condensation energy for $N = 128$ pairs living in $m = 256$ levels of the 1D system with a $\delta(x - x_0)$ impurity is performed. From a physics point of view, this particular size of system corresponds to a realistic number of active electron pairs within the Debye window of a nanograin. The Richardson-Gaudin proves particularly useful in this particular situation because the size of the Hilbert space ($\dim \sim 5.7 \times 10^{75}$) is far beyond the capa-

bilities of standard diagonalisation approaches. The result of the calculation is presented in Figure 7.4. The effect of the larger number of particles and levels on the condensation energy is immediately visible in the modulation, which has increased to 128 quasi periods, corresponding to the number of quasi periods of the Fermi level. Therefore, our analysis for the smaller system appears to be valid in larger systems as well.

7.3 Conclusions

We have studied the effect of two qualitatively different control parameters on the pair condensation energy of a finite-size superconducting particle. The control parameters enter into the system via the single-particle spectrum, which is based on a straightforward particle-in-a-box principle. The first control parameter is the shape of the particle, which induces strong fluctuations in the single-particle level densities, precipitating into the condensation energy. By means of perturbation theory, it was found that the condensation energy in the weak-coupling regime is mainly dependent on local single-particle level density fluctuations, whereas the strong-coupling regime is also affected by global level density fluctuations. Introducing impurities, as a second control parameter, proved to be a more gradual probe for pairing correlations. An impurity gives a unique quasi-periodic structure to each single particle level as a function of the position of the impurity, such that it becomes possible to weigh the contributions of the single-particle levels to the condensation energy by investigating the frequency of oscillations.

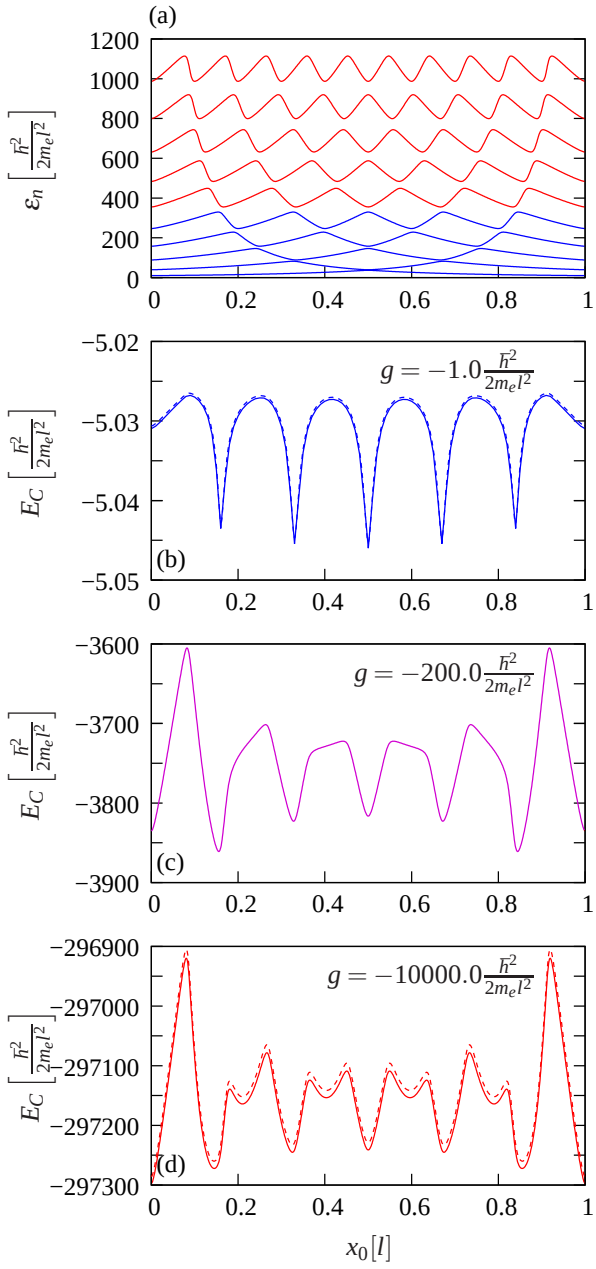

Figure 7.2: In panel (a), the sp spectrum (7.17) of a 1D particle-in-a-box with a $\delta(x - x_0)$ impurity at x_0 is depicted. Panels (b)-(d) show the condensation energy as a function of x_0, for the weak- (b), intermediate- (c), and strong-coupling (d) regime. For the weak-, and strong-coupling regime, the approximative predictions, given in respectively Eqs. (7.12) and (7.13), are plotted in dashed lines.

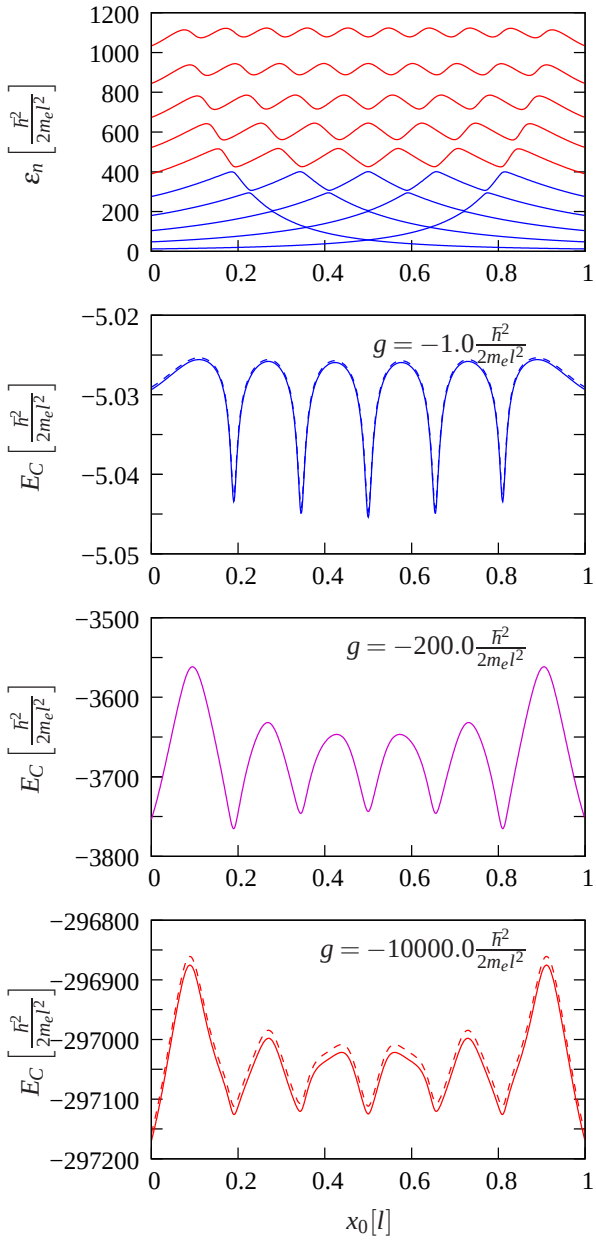

Figure 7.3: In panel (a), the sp spectrum (7.17) of a 1D particle-in-a-box with a $\exp(-k|x - x_0|)$ impurity at x_0 and $k = 20/l$ is depicted. Panels (b)-(d) show the condensation energy as a function of x_0, for the weak- (b), intermediate- (c), and strong-coupling (d) regime. For the weak-, and strong-coupling regime, the approximative predictions, given in respectively Eqs. (7.12) and (7.13), are plotted in dashed lines.

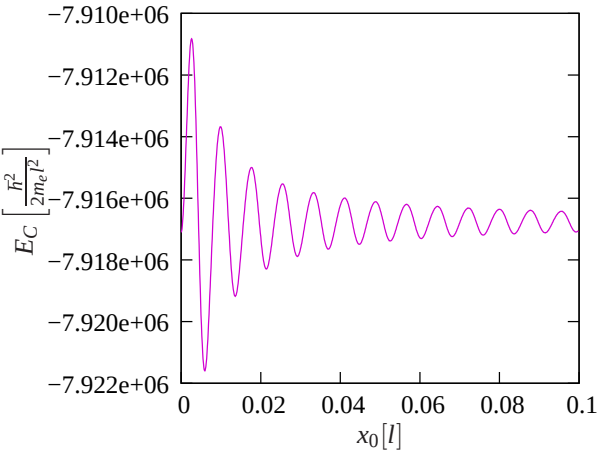

Figure 7.4: The condensation energy of a system consisting of $N = 128$ pair in $m = 256$ levels, with a $\delta(x - x_0)$ impurity, as a function of the position x_0. The strength of the impurity has been chosen as $v_0 = 100.0[\hbar^2/2m_e l^2]$ and the pairing strength is $g = -2000.0[\hbar^2/2m_e l^2]$. For graphical reasons, the condensation energy is only given in the interval $x_0 \in [0, 0.1]$.

Chapter 8

Exploration of the phase-diagram of the $p_x + ip_y$ Hamiltonian

[1]

Recently, interest has increased in the hyperbolic family of integrable Richardson-Gaudin (RG) models. It was pointed out that a particular linear combination of the integrals of motion of the hyperbolic RG model leads to a Hamiltonian that describes p-wave pairing in a two dimensional system [206, 207]. Such an interaction is found to be present in fermionic superfluids (^{3}He), ultra-cold atomic gases and p-wave superconductivity. Furthermore the phase diagram is intriguing, with the presence of the Moore-Read and Read-Green lines. At the Read-Green line a rare third-order quantum phase transition occurs. In this chapter a connection is made between collective bosonic states and the exact solutions of the $p_x + ip_y$ pairing Hamiltonian. This makes it possible to investigate the effects of the Pauli principle on the energy spectrum, by gradually reintroducing the Pauli principle. It also introduces an efficient and stable numerical method to probe all the eigenstates of this class of Hamiltonians. We extend the phase diagram to repulsive interactions, an area that was not previously explored due to the lack of a proper mean-field solution in this region. We found a connection between the point in the phase diagram where the ground state connects to the bosonic state with the highest collectivity, and the Moore-Read line where all the Richardson-Gaudin (RG) variables collapse to zero. In contrast with the reduced BCS case, the overlap between the ground state and the highest collective state at the Moore-Read line is not the largest.

[1] Has been previously published as: M. Van Raemdonck, S. De Baerdemacker, and D. Van Neck. *Exact solution of the $p_x + ip_y$ pairing hamiltonian by deforming the pairing algebra.* 2014: Physical Review B 89:155136.

In fact, it shows a minimum when most other bosonic states show a maximum of the overlap. By investigating the total spectrum, we found remnants of the Read-Green line for finite systems. A symmetry was found between the Hamiltonian with and without single-particle part. When the interaction is repulsive 4 different classes of trajectories of the RG variables are found.

8.1 Introduction

Pairing plays an important role in the description of many phenomena as diverse as superconductivity in condensed matter systems [182], neutron stars [188], and the interaction of nucleons in atomic nuclei [188]. Probably the most notorious Hamiltonian that describes paired fermions is the reduced BCS Hamiltonian [182], which has an exact Bethe ansatz solution obtained by Richardson in 1963 [189]. The Richardson-Gaudin (RG) model belongs to a more general class of integrable Hamiltonians, [177, 208] which can be categorized into three families: the rational (or XXX), hyperbolic (or XXZ) and elliptic (or XYZ) RG models. The reduced BCS Hamiltonian is part of the rational family. The rational model has attracted more interest during the last decade because it describes pairing correlations in finite-size (mesoscopic) metallic nanograins [202]. This has lead to applications in superconductivity[202], quantum optics, cold-atomic physics, quantum dots[177], etc. The other two families remained obscure until recently applications for the hyperbolic model were found in the context of p-wave pairing in ultra-cold Fermi gases [209, 210], exotic superconductors such as Sr_2RuO_4 [211] and in the context of pairing in heavy nuclei. [212]. The long standing importance of p-wave pairing in the ^{3}He superfluid state [213] should also be kept in mind.

Two-dimensional p-wave pairing can be described by means of the $p + ip$ Hamiltonian

$$H = \sum_{\mathbf{k}} \frac{\mathbf{k}^2}{2m} c^\dagger_{\mathbf{k}} c_{\mathbf{k}} - \frac{G}{4m} \sum_{\mathbf{k}\mathbf{k}'} \mathbf{k}\cdot\mathbf{k}' c^\dagger_{\mathbf{k}} c^\dagger_{-\mathbf{k}} c_{-\mathbf{k}'} c_{\mathbf{k}'}, \tag{8.1}$$

with $\mathbf{k}\cdot\mathbf{k}' = k_x k'_x + k_y k'_y$. Its "chiral" variant

$$H = \sum_{\mathbf{k}} \frac{\mathbf{k}^2}{2m} c^\dagger_{\mathbf{k}} c_{\mathbf{k}} - \frac{G}{4m} \sum_{\mathbf{k}\mathbf{k}'} (k_x - ik_y)(k'_x + ik'_y) c^\dagger_{\mathbf{k}} c^\dagger_{-\mathbf{k}} c_{-\mathbf{k}'} c_{\mathbf{k}'}, \tag{8.2}$$

also referred to as the $p_x + ip_y$ Hamiltonian, essentially captures the same physics [214], and is derivable as a linear combination of the integrals of motion of the hyperbolic RG model [215] (see section(8.2)), opposed to the time-reversal symmetric $p + ip$ Hamiltonian. It follows that it is possible to diagonalise the above schematic Hamiltonian by product wave functions of generalized pair creation operators, the so-called Bethe Ansatz states. This solution of the $p_x + ip_y$ Hamiltonian was pioneered by Ibañez et al. [206] and further studied by Rombouts et. al.[207] and Dunning et. al.[216]. The latter serves

as a comprehensive review about the $p_x + ip_y$ pairing Hamiltonian and related integrable models. The free parameters of the Bethe ansatz wave functions (the so called RG variables) are determined through the solution of a system of N RG equations where N is the number of active pairs in the system. This system of equations is highly non linear and solving it for arbitrary excited states and a realistic number of pairs and single-particle levels has been a subject of active research [207, 216–219]. One of the main difficulties of solving the RG equations is circumventing the singular points, also called critical points. These singular points arise when two or more RG variables become equal, and lead to singularities in the RG equations.

The Hamiltonian in Eq. (8.2) has an interesting phase diagram: because of the non-zero rotational order, the ground state exhibits a quantum phase transition between qualitatively different superfluid states [207, 220]. The ground-state energy shows corresponding non-analytical behaviour, as opposed to s-wave pairing of which it is well understood that by increasing the interaction strength there is a crossover (and not a quantum phase transition) between a weak-coupling Bardeen-Cooper-Schrieffer [182] (BCS) and a quasimolecular Bose-Einstein condensate (BEC) phase [221]. In the case of the $p_x + ip_y$ spinless fermion pairing Hamiltonian, this quantum phase transition is only present for sufficiently dilute gases $\rho < \frac{1}{2}$ with ρ the fermion density. The transition itself is continuous, third order and occurs at the so called Read-Green line, defined as the points in the phase-diagram where the chemical potential μ vanishes and BCS mean-field theory predicts a gapless excitation spectrum [206]. The Read-Green line separates the weak pairing regime from the strong pairing regime. The fingerprint of the Read-Green line is clearly visible in the spectrum of finite systems (see section(8.7)). Another interesting line in the phase diagram at weaker interaction constant is the Moore-Read line where the total energy equals zero because all the RG variables collapse to zero, giving rise to a boson-like condensate of equal generalised pairs. The condensation of all distinct generalised pairs into a power of equal generalised pairs is reminiscent of a bosonic state. At stronger interaction constant a second regime occurs, the so-called 'condensate regime'; where a number of RG variables collapse to zero at particular interaction constants. The Moore-Read line is a special case of these dynamics where *all* the RG variables collapse to zero. In contrast with the Read-Green line there is no quantum phase transition at the Moore-Read line [207]. A particular technique that can be used to get more insight into the dynamics of the system and the phase diagram is 'bosonization'. The process of bosonization maps the hard-core bosons present in the system (RG variables) adiabatically onto real bosons. With this method it is also possible to investigate the effects of the Pauli principle on the system, because it allows us to gradually reintroduce the Pauli principle. This technique has already proven its value for the reduced BCS model [201, 222].

The goal of this chapter is to extend the results of Ibañez [206] and Rombouts [207], employing a new view to the phase diagram by linking the eigenstates

to associated bosonic states of the Tamm Dancoff Approximation (TDA), by deforming the quasi-spin algebra. This technique, introduced in a study [201] of the collectivity of the reduced BCS model, can serve as an RG solver, in addition to existing methods [217, 219]. The method is computationally stable and fast. In essence, the singular points are avoided by linking the solution of the N RG equations to the solution of one non-linear secular TDA equation, which is easily solvable. It gives straightforward solutions in the limit of strong and weak interaction constant. In the limit of intermediate interaction constant the situation is more complex, but obtaining all solutions in this regime remains possible, even for large systems.

In the following section (8.2) the basic notions and terminology of the hyperbolic RG model are introduced. To be self-contained, the link with the $p_x + ip_y$ pairing Hamiltonian is shown and the nonlinear RG equations are derived. The concept of the quasi-spin pseudo deformation parameter is introduced in section(8.3), and the connection with collective and bosonic states in the Tamm-Dancoff approximation (TDA) are discussed. In section 8.6 a number of different regimes of the $p_x + ip_y$ Hamiltonian are discussed. It starts with the discussion of the infinite interaction regime for which a symmetry with the finite interaction regime is derived. Some results for the special points of the phase diagram: the Moore-Read and Read-Green line, which define the boundaries of the 'condensation regime' are recalled and derived. Then the associated bosonic states of the ground state of a spinless Fermigas with $p_x + ip_y$ pairing interaction living on a two-dimensional disk is studied[207]. Some interesting shifts of the associated TDA states occur when the interaction constant is varied in particular when the system crosses the Moore-Read line. We calculate the overlaps of the RG ground state with a selection of TDA states to improve our understanding of the three different regimes: the weak pairing regime, the condensation regime, and the strong pairing regime. To finish this section, the properties and peculiarities of a positive interaction constant are discussed. At the end, excited states are discussed. We depict for a small system the RG variables of all the fully paired states in the complex plane. The availability of the entire spectrum of modestly sized systems, makes it possible to investigate the reminiscence of the Read-Green line for finite-size systems. A pattern for the TDA state that connects to the first excited state at the Read-Green line is found.

8.2 The hyperbolic Richardson-Gaudin model

The families of integrable Richardson-Gaudin models have their roots in a generalised Gaudin algebra [191, 208] which is based on the $su(2)$ algebra of the quasi-spin operators [223]. The generators of $su(2)$ with spin representation

s_j such that $\langle S_j^2 \rangle = s_j(s_j+1)$ are given by:

$$S_j^0 = \frac{1}{2}\Big(\sum_{m=-j}^{j} c_{jm}^\dagger c_{jm} - \frac{\Omega_j}{2}\Big), \quad S_j^+ = \sum_{m>0}^{j} c_{jm}^\dagger c_{j\bar{m}}^\dagger, \tag{8.3}$$

$$S_j^- = \left(S_j^+\right)^\dagger, \tag{8.4}$$

with $c_{jm}^\dagger$ an operator creating a fermion in single-particle state jm, with m the projection of the $\Omega_j = 2j+1$ degenerate level j, and $j\bar{m}$ denotes the time reverse of jm. These operators span the standard su(2) algebra which can be straightforwardly deduced from the anticommutation relations of the fermion creation and annihilation operators [223].

$$\left[S_i^0, S_j^\dagger\right] = \delta_{ij} S_j^\dagger, \quad \left[S_i^0, S_j\right] = -\delta_{ij} S_j, \quad \left[S_i^\dagger, S_j\right] = 2\delta_{ij} S_j^0 \tag{8.5}$$

Each su(2) copy is associated with a single-particle level i. The irreducible representations (irreps) are given by

$$|s_i, \mu_i\rangle = |\tfrac{1}{4}\Omega_i - \tfrac{1}{2}v_i, \tfrac{1}{2}n_i - \tfrac{1}{4}\Omega_i\rangle\,, \tag{8.6}$$

where v_i stands for the seniority (the number of unpaired fermions) of the i th level and n_i is the number of fermions present in the ith level. For doubly degenerate levels ($\Omega = 2$), there are only two distinct irreps: $s_i = 0$ or $s_i = \frac{1}{2}$, corresponding respectively with seniority $v_i = 1$ or $v_i = 0$, which are commonly referred to as 'blocked' or 'unblocked' levels. An RG integrable model is defined by L Hermitian, number-conserving, and mutually commuting operators with linear and quadratic terms of L copies of su(2) generators.

$$R_i = S_i^0 - 2\gamma \sum_{j\neq i}^{L} \left[\frac{X_{ij}}{2}\left(S_j^\dagger S_j + S_i S_j^\dagger\right) + Z_{ij} S_i^0 S_j^0\right] \tag{8.7}$$

The number-conservation symmetry is very useful because we only need to search in Hilbert spaces with a fixed particle number to find the eigenstates of the R_i operators, which reduces the complexity of the problem significantly. Following Gaudin [191] it is now possible to find conditions for the X and Z matrices so all the R_i operators commute mutually. There are two families of conditions, the rational and hyperbolic families respectively. The rational model has the conditions,

$$X_{ij} = Z_{ij} = \frac{1}{D_i^2 - D_j^2}, \tag{8.8}$$

whereas the hyperbolic model is represented by

$$X_{ij} = 2\frac{D_i D_j}{D_i^2 - D_j^2}, \quad Z_{ij} = \frac{D_i^2 + D_j^2}{D_i^2 - D_j^2}. \tag{8.9}$$

Any linear combination of the R_i operators with the X and Z matrices fulfilling one of the above conditions gives rise to an integrable model. It is possible to construct a schematic $p_x + ip_y$ pairing Hamiltonian out of the above operators with the X and Z matrices fulfilling the hyperbolic conditions,

$$\hat{H} = \lambda \sum_i D_i^2 R_i \tag{8.10}$$

$$\text{with} \quad \lambda = \frac{\eta}{1 + 2\gamma\,(1 - N) + \gamma\,(L - \sum_i v_i)}, \tag{8.11}$$

where γ is a parameter proportional to the interaction constant $g = -2\lambda\gamma$, η an arbitrary parameter that can be absorbed in λ and N the number of pairs. After some straightforward algebraical calculations and subtraction of the diagonal term $g \sum_i \mathbf{S}_i^2 D_i^2$, the following Hamiltonian appears:

$$\hat{H}_{fac} = \eta \sum_{i=1}^{L} D_i^2 S_i^0 + g \sum_{ij=1}^{L} D_i D_j^* S_i^\dagger S_j. \tag{8.12}$$

The link with the $p_x + ip_y$ Hamiltonian in eq.(8.2) is made by redefining $D_i = \frac{k_x - ik_y}{\sqrt{2m}} e^{i\phi}$ and $g = \frac{-G\eta}{2}$. The phase factor ϕ is chosen such that D_i is real and the residual phase factor is absorbed in the corresponding pair creation and annihilation operators (8.3) without affecting the $su(2)$ quasi-spin algebra. Since 'blocked' levels (seniority $v_i = 1$) do not contribute to the pairing interaction, we focus on a full seniority zero space, or equivalently, the fully paired space. So the number of active levels $L_c = L - \sum_i v_i$ equals L in our examples.

The Hamiltonian (8.12) is built out of L integrals of motion of the hyperbolic RG model. It follows that the Hamiltonian, the L integrals of motion R_i and the z component of the total quasi-spin, $S_z = \sum_{i=1}^{L} S_i^z$ have a common eigenbasis. The eigenstates are parametrised by the ansatz [216]

$$|\psi\rangle = \prod_{\alpha=1}^{N} K_\alpha^\dagger \, |\theta\rangle \tag{8.13}$$

with $K_\alpha^\dagger$ a generalised pair creation operator defined as

$$K_\alpha^\dagger = \sum_{k=1}^{L} \frac{D_k S_k^\dagger}{\eta D_k^2 - E_\alpha}. \tag{8.14}$$

The state (8.13) is an eigenstate of $\hat{H}_{fac}$ if the parameters E_α are solutions of the following system of equations [208]

$$1 + 2g \sum_{i=1}^{L} \frac{D_i^2 s_i}{\eta D_i^2 - E_\alpha} - 2\frac{g}{\eta} \sum_{\beta \neq \alpha}^{N} \frac{E_\beta}{E_\beta - E_\alpha} = 0, \quad \forall \alpha = 1 \ldots N \tag{8.15}$$

The above equations are the RG equations for the p_x+ip_y pairing Hamiltonian. The total energy of the eigenstate is given by:

$$E = \sum_{\alpha=1}^{N} E_\alpha - \eta \sum_{k=1}^{L} D_k^2 s_k \tag{8.16}$$

The system of equations as described in eq.(8.15) is equivalent with the RG equations in [207], with the definition $D_i = \sqrt{\eta_i}$, $g = -G$, and a rearrangement of E_α in the numerator of the third term of eq.(8.15). We have opted for the form in eq.(8.15) for numerical stability, because the constant number 1 in (8.15) acts as a reference point for the solver, as opposed to the form in [207] where the RG variables have an attractor at infinity. Remark that the RG equations are ill-defined for $\eta = 0$, however, it is possible to make a connection with a $\eta \neq 0$ state (see section (8.6.1)). Furthermore the $\eta = 0$ state is already extensively discussed by [224, 225]. The path of the real and imaginary part of the RG variables of a toy model, with 12 doubly degenerate levels, and equidistant $D_i = i$, occupied by 6 pairs, as a function of the interaction constant is depicted in Fig. 8.1.

An aspect of the RG models not much touched upon is the evolution of the integrals of motion see eq.(8.7). If the solution of eq.(8.15) is obtained, and the ground state $|\psi\rangle = \prod_{\alpha=1}^{N} K_\alpha^\dagger |\theta\rangle$ is constructed. It is possible to calculate the integrals of motion corresponding to a particular eigenstate. Acting with R_i on an eigenstate of the factorisable interaction Hamiltonian eq.(8.12), yields the following eigenvalue:

$$r_i = s_i \left(-1 - 2\gamma \sum_{k \neq i}^{L} Z_{ik} d_k - 2\gamma \sum_{\beta=1}^{N} Z_{\beta i} \right) \tag{8.17}$$

with $Z_{\beta i} = \frac{\frac{E_\beta}{\eta} + D_i^2}{\frac{E_\beta}{\eta} - D_i^2}$ and $-2\gamma = \frac{1}{\frac{\eta}{g} + (1-N) + \frac{L_c}{2}}$. The E_β are the RG variables of the eigenstate. A remarkable fact is that the integrals of motion associated to particular eigenstates exhibit singularities at particular g as can be seen in Fig.8.2. The Hamiltonian (8.12) uniquely defines a set of conserved charges R_i (Eq. (8.7)) via the definition of X_{ik}, Z_{ik}, and the parameters (λ, γ). As such, the eigenvalues r_i of R_i exhibit singularities for those values of g where γ becomes singular. For example it is clear that when $\eta = 1$, zero seniority and half filling the integrals of motion exhibit a singularity at $g = -1$, see also Fig. 8.2.

Nevertheless, the eigenvalues of the Hamiltonian contain no traces of these singularities because they cancel exactly by construction via $g = -2\lambda\gamma$.

8.3 Collective and pseudo deformed states

The eigenstate (8.13) is a product state of generalised pair creation operators $K_\alpha^\dagger$ (8.14). Opposed to the constituent fermions, the generalized pair creation

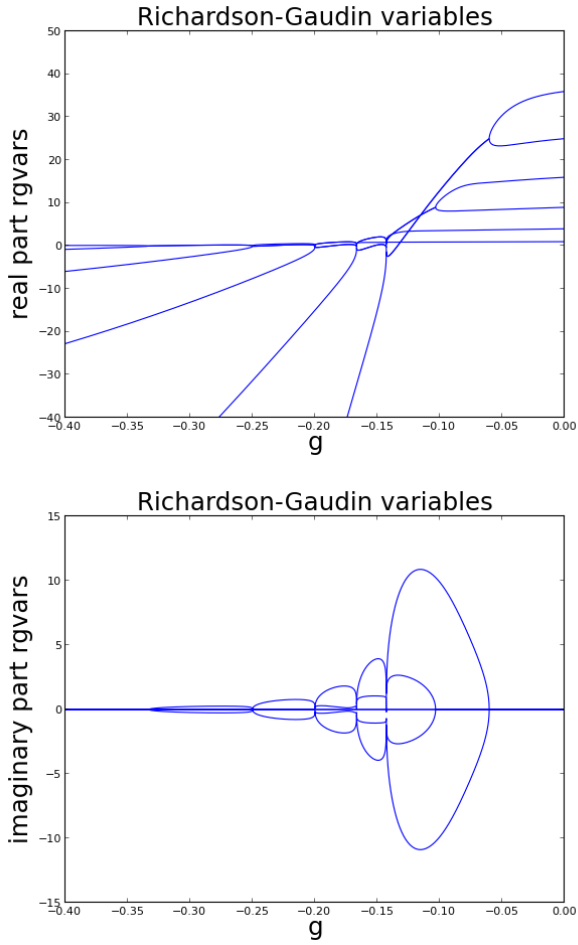

Figure 8.1: For a system with 12 doubly degenerate single-particle levels occupied by 6 pairs, and $D_i = i$, we depict: the real part of the RG variables and the imaginary part of the RG variables as a function of the interaction constant g. Note the qualitative differences between the RG variables of the factorisable Hamiltonian depicted here, and those of the rational picket-fence model (cfr. Fig. 1 in Ref [201]).

generators $K_\alpha^\dagger$ commute, and are therefore commonly referred to as 'hard-core' bosonic states. The product wave structure is reminiscent of bosonic approximations, such as the Random Phase Approximation (RPA) and *pp*-Tamm Dancoff Approximation (TDA) [30, 175]. Recent investigations on the relation between the *pp*-TDA and the rational RG model [201, 222] have shown that a one-to-one correspondence is possible between the bosonic-like TDA states and the Bethe ansatz states of the rational RG model, either by

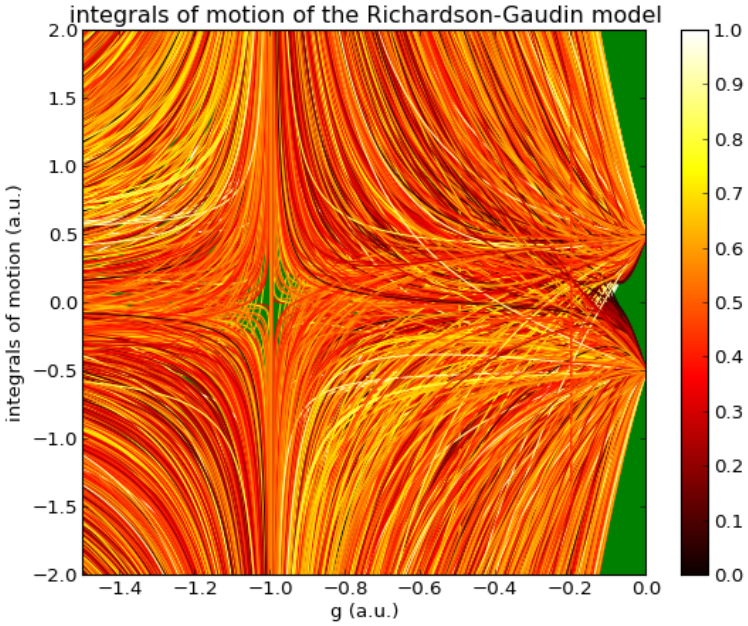

Figure 8.2: The integrals of motion of all the eigenstates of a $p_x + ip_y$ pairing Hamiltonian consisting of 12 doubly degenerate sp levels occupied by 6 pairs as a function of the interaction strength. Colour coded according to the energy of the eigenstate to which they correspond.

calculating overlaps [222], or a pseudo deformation of the algebra [201]. The ground state of the reduced BCS Hamiltonian in the strong interaction regime has a clear-cut connection to a condensate of the collective TDA eigenmode, whereas the weak-interaction regime corresponds to a regular filling of the TDA eigenmodes, as dictated by the Pauli principle. The one-to-one correspondence in the strong interaction limit is particularly remarkable because it is well established that the RG variables in the strong interaction limit are distributed along an arc in the complex plane, which is not a condensate of equal generalised pairs. In contrast to the rational model, the hyperbolic model supports a fully condensed state at the Moore-Read line (and fractionally condensed states). Therefore it is of interest to see whether a similar picture as in the rational model applies for the hyperbolic model. The basic idea behind the TDA is that it approximates the interacting system as a simple product state of single excitation eigenmodes of the pairing Hamiltonian (see eq. (8.18)). In the next subsections we elaborate on the method that is used to link those bosonic states with the 'hard-core' bosonic states which are the N pair eigenstates of the $p_x + ip_y$ pairing Hamiltonian. This is done by adiabatically increasing the

degeneracy of the levels to infinity by means of a deformation parameter in the algebra of the factorisable Hamiltonian, linking the collective TDA states adiabatically with the eigenstates of the $p_x + ip_y$ Hamiltonian. The method turns out to be a very efficient solver of the highly singular system of eq.(8.15). Even for some hundreds of pairs and levels this method stays stable. The only drawback is that in the critical regime corresponding to medium interaction constants the combination of TDA solutions which will lead to a solution of the Hamiltonian is not known a priori.

8.3.1 TDA states

The elementary eigenmodes of the *pp*-TDA are determined by the 1-pair excitation eigenvalue equation.

$$\hat{H}_{fac} \sum_{i=1}^{L} Y_i S_i^\dagger \left|\theta\right\rangle = E \sum_{i=1}^{L} Y_i S_i^\dagger \left|\theta\right\rangle \tag{8.18}$$

This equation is exact for the $N = 1$ pair system, and therefore has the Bethe Ansatz eigenstate eq.(8.13) with E_{TDA} as the solution of the RG equation for $N = 1$.

$$1 + \frac{g}{2} \sum_i \frac{D_i^2 \Omega_i}{\eta D_i^2 - E_{TDA}} = 0. \tag{8.19}$$

which is also commonly referred to as the secular TDA equation. This equation has a geometric interpretation [30]; there are $L-1$ real solutions bound between the successive poles $\eta|D_i|^2$ $(i = 1 \ldots L)$ and one unbound solution below $\eta|D_1|^2$, also called the 'collective' TDA solution. Each solution defines a TDA eigenmode, so a general TDA state can be built by picking N eigenmodes out of the L elementary (repetition is possible). A TDA state can be written as:

$$\left|\psi_{TDA}\right\rangle = \prod_{i=1}^{N} \left(\sum_{k=1}^{L} \frac{D_k S_k^\dagger}{\eta D_k^2 - E_{TDA_i}} \right) \left|\theta\right\rangle, \tag{8.20}$$

which is structurally equivalent to the Bethe Ansatz state (8.13), but instead of using the RG variables as pair energy parameters, the energy of the TDA eigenmodes are used.

The physical interpretation of eq.(8.20) is a state of N 1-pair excitations with no correlations between the pairs. If the pair creation and annihilation operators of eq.(8.12) would have bosonic commutation relations, the above state would be an exact eigenstate of eq.(8.12).

8.3.2 Pseudo-deformation

The pseudo deformation of the quasi-spin algebra provides a convenient means to adiabatically connect the exact RG Bethe Ansatz states with the bosonic

TDA states. The algebra is given by [201, 226]

$$\begin{aligned}\left[S_i^0, S_j^\dagger\right] &= \delta_{ij} S_j^\dagger, \quad \left[S_i^0, S_j\right] = -\delta_{ij} S_j, &(8.21)\\ \left[S_i^\dagger, S_j\right] &= \delta_{ij}\left(\xi \hat{n}_j - \frac{1}{2}\Omega_j\right) \\ &= \delta_{ij}\left(\xi 2 S_i^0 + (\xi - 1)\frac{1}{2}\Omega_j\right), &(8.22)\end{aligned}$$

where ξ is the pseudo deformation parameter, tuning the Pauli principle between the full quasi-spin su(2) algebra for $\xi = 1$ and a bosonic hw(1) Heisenberg-Weyl ($\xi = 0$) algebra. We employ the term pseudo deformation, because the algebra eq.(8.21,8.22) is transformable to a genuine su(2) algebra for $\xi \neq 0$, with irreducible representations labelled by

$$|s_i(\xi), \mu_i(\xi)\rangle = |\tfrac{1}{4\xi}\Omega_i - \tfrac{1}{2}v_i, \tfrac{1}{2}n_i - \tfrac{1}{4\xi}\Omega_i\rangle\,. \tag{8.23}$$

The physical picture associated with the pseudo deformed irreducible representations is an opening of the sp orbitals by a factor of $\frac{1}{\xi}$, giving rise to an increased degeneracy of the orbital, with the possibility to accommodate an arbitrary amount of pairs in the $\xi \to 0$ limit. Because the pseudo deformed algebra is eventually isomorphic to a genuine su(2) quasi-spin algebra, the Hamiltonian eq.(8.12) remains RG integrable with associated pseudo-deformed RG equations:

$$1 + 2g\sum_i \frac{D_i^2 \xi s_i(\xi)}{\eta D_i^2 - E_\alpha} - 2\xi\frac{g}{\eta}\sum_{\beta\neq\alpha}\frac{E_\beta}{E_\beta - E_\alpha} = 0. \quad \forall\alpha = 1\ldots N \tag{8.24}$$

It is easily verified that $\xi = 1$ gives rise to the original RG equations (8.15), whereas the $\xi = 0$ limit decouples the RG equations into N independent 1-pair excitation equations (8.19). To make the connection from the $\xi = 0$ state to the $\xi = 1$ state in which we are interested it is necessary to have the $\xi \ll 1$ limit under control. This is because putting more than one pair in the same TDA eigenstate will blow up the third term of eq.(8.24) at any $\xi \neq 0$. Fortunately, there exists an approximate solution for very small ξ which depends on the collective solutions by making use of the Heine-Stieltjes connection [227, 228]. It resolves the divergences by adding an imaginary part to the collective solutions associated to sp levels that are occupied by more then one pair (see section(8.3.3)).

$$E_\alpha^\nu(\xi) \approx E_\alpha(0) - i\sqrt{\frac{2E_\alpha(0)}{\eta a}}z^\nu \quad \xi \ll 1 \quad \forall\nu = 1\ldots n \tag{8.25}$$

With z_α^ν the ν-th root of the 'physicists' Hermite polynomials $H_n(z)$, a_α given by: $a_\alpha = \frac{1}{2}\sum_i \frac{D_i^2\Omega_i}{\left(\eta D_i^2 - E_\alpha(0)\right)^2}$ and $\nu \in [1,\ldots,n]$ where n is the number of pairs associated with a collective solution $E_\alpha(0)$. Eq.(8.25) contains a lot of information about the underlying structure of the RG variables. By choosing a TDA distribution corresponding to an eigenstate of eq.(8.12), eq.(8.25) answers immediately the question if a RG variable will be complex or real when the system is not in the 'condensate' regime. So the imaginary character of a RG variable depends on the roots of the Hermite polynomials, the number of pairs associated to a TDA level n and the sign of the corresponding TDA solution $E_\alpha(0)$. As an example, in the weak interaction limit, where the structure of the system can be regarded as a simple filling of the Fermi sea with hard-core bosons, with only doubly degenerate levels, all the solutions are real because $n = 1\ \forall\alpha$, and the roots of the Hermite polynomial of first order are zero. In the strong interaction limit all pairs are associated with the lowest TDA eigenmode which is negative for $g \to -\infty$. Therefore we see from eq.(8.25) that all the RG variables are real. So for a set of doubly degenerate levels we can only have complex RG variables at intermediate interaction constant.

8.3.3 The near-contraction limit

Here an approximate solution is derived to the generalised Richardson-Gaudin equations eq.(8.24) for very small ξ. Recall that the RG equations with $\xi = 0$ are given by:

$$1 + \frac{g}{2}\sum_i \frac{D_i^2\Omega_i}{\eta D_i^2 - E_\alpha(0)} = 0. \tag{8.26}$$

The following form of the RG variables for very small ξ is assumed.

$$E_\alpha(\xi) = E_\alpha(0) + \sqrt{\xi}x_\alpha \tag{8.27}$$

ξ is chosen very small so it is possible to perform a series expansion in $\sqrt{\xi}$ in the second term of eq.(8.24)

$$\begin{aligned} 1 + 2g\sum_i \frac{D_i^2\left(\frac{1}{4}\Omega_i - \frac{1}{2}\xi v_i\right)}{\eta D_i^2 - E_\alpha(0)} & \\ \left[1 + \frac{\sqrt{\xi}x_\alpha}{\eta D_i^2 - E_\alpha(0)} + \ldots\right] & \\ - 2\frac{\xi g}{\eta}\sum_{\beta\neq\alpha} \frac{E_\beta(0) + \sqrt{\xi}x_\beta}{E_\beta(0) - E_\alpha(0) + \sqrt{\xi}(x_\beta - x_\alpha)} \approx 0. & \end{aligned} \tag{8.28}$$

Now we split the summation of the third term in the above equation into a part for which $E_\beta(0) = E_\alpha(0)$ and a part for which $E_{\beta'}(0) \neq E_\alpha(0)$.

$$1 + 2g \sum_i \frac{D_i^2 \left(\frac{1}{4}\Omega_i - \frac{1}{2}\xi v_i\right)}{\eta D_i^2 - E_\alpha(0)} \left[1 + \frac{\sqrt{\xi} x_\alpha}{\eta D_i^2 - E_\alpha(0)} + \ldots\right] - 2\frac{\sqrt{\xi} g}{\eta} \sum_{\beta \neq \alpha} \frac{E_\alpha(0) + \sqrt{\xi} x_\beta}{(x_\beta - x_\alpha)} - \frac{2\xi g}{\eta} \sum_{\beta' \neq \alpha} \frac{E_{\beta'}(0) + \sqrt{\xi} x_{\beta'}}{E_{\beta'}(0) - E_\alpha(0) + \sqrt{\xi}(x_{\beta'} - x_\alpha)} \approx 0. \quad (8.29)$$

After gathering the terms of order $O(1)$, we see that they are zero because of eq.(8.26). For the $O\left(\sqrt{\xi}\right)$ terms we obtain:

$$a x_\alpha + \frac{E_\alpha(0)}{\eta} \sum_{\beta \neq \alpha} \frac{2}{x_\alpha - x_\beta} = 0 \quad (8.30)$$

The index β runs only over the n indices such that $E_\beta(0) = E_\alpha(0)$, and $a = \frac{1}{2}\sum_i \frac{D_i^2 \Omega_i}{\left(\eta D_i^2 - E_\alpha(0)\right)^2}$. The equation above is of the Stieltjes type [229], so we can define a Stieltjes polynomial.

$$P(x) = \prod_i^n (x - x_i), \quad (8.31)$$

with x_i the roots of the Stieltjes equations. Remark that $\sum_{j \neq i}^n \frac{2}{x_i - x_j} = \frac{P''(x)}{P'(x)}$, multiply eq.(8.30) with $P'(x)$ and take into account the fact that polynomials of the same order, with the same zeros are equal up to a scale factor which in this case is an. This gives finally the following corresponding differential equation.

$$\frac{E_\alpha(0)}{\eta} P''(x) + a x P'(x) = anP(x) \quad (8.32)$$

If we now apply the transformation $z = i\sqrt{\frac{\eta a}{2E(0)}}x$, we can transform this equation into a 'physicists' Hermite differential equation.

$$H'' - 2zH'(z) + 2nH(z) = 0 \quad (8.33)$$

So finally we get for the $E_\alpha(\xi)$ variables in the $\xi \to 0$ limit:

$$E_\alpha(\xi) \approx E_\alpha(0) + i\sqrt{\frac{2E_\alpha(0)\,\xi}{\eta a}} z_\alpha^\nu \quad \xi \ll 1, \quad \nu = 1 \ldots n \quad (8.34)$$

with z_α^ν the ν-th root of the 'physicists' Hermite polynomial $H_n(z)$.

8.4 Condensation points

The condition is determined for which p pairs with zero energy and q general RG pairs form an eigenstate of the $p_x + ip_y$ pairing Hamiltonian (see eq.(8.12)). For the $E_\alpha = 0$ pairs the generalised pair operators become:

$$K_0^\dagger = \sum_{k=1}^{m} \frac{S_k^\dagger}{\eta D_k^*}, \quad K_0 = \left(K_0^\dagger\right)^\dagger \tag{8.35}$$

$$K_0^0 = \sum_{k=1}^{m} \frac{S_k^0}{\eta} \tag{8.36}$$

So we have to derive under which conditions the state:

$$|\psi\rangle = \left(K_0^\dagger\right)^p \prod_{\alpha=1}^{q} K_\alpha^\dagger |\theta\rangle \tag{8.37}$$

is an eigenstate of the factorisable Hamiltonian (8.12). This will be done by commuting the Hamiltonian through the product state (8.37), and breaking down the resulting state into the eigenstate and the orthogonal part. Pulling the Hamiltonian through the p condensed pairs gives:

$$H\left(K_0^\dagger\right)^p = \frac{1}{2}p\left(p-1\right)\left(K_0^\dagger\right)^{p-2}\left[\left[H, K_0^\dagger\right], K_0^\dagger\right] + p\left(K_0^\dagger\right)^{p-1}\left[H, K_0^\dagger\right] + \left(K_0^\dagger\right)^p H \tag{8.38}$$

The commutators in the above expression are given by:

$$\left[H, K_0^\dagger\right] = -2\frac{g}{\eta}K_D^\dagger K_0^\dagger \tag{8.39}$$

$$\left[\left[H, K_0^\dagger\right], K_0^\dagger\right] = K_D^\dagger\left(1 - 2\frac{g}{\eta}K_0^0\right) \tag{8.40}$$

Where $K_D^\dagger = \sum_k D_k S_k^\dagger$. We already know how the Hamiltonian commutes through the product state $\prod_{\alpha=1}^{q} K_\alpha^\dagger$ yielding the RG equations for q pairs, so we only need to calculate the additional commutator.

$$\left[K_0^0, \prod_{\alpha=1}^{q} K_\alpha^\dagger\right] = q\prod_{\alpha=1}^{q} K_\alpha^\dagger \tag{8.41}$$

At the end we get the following relation;

$$H\left(K_0^\dagger\right)^p\left(\prod_{\alpha=1}^{q} K_\alpha^\dagger\right)|\theta\rangle = \left(K_0^\dagger\right)^p H\left(\prod_{\alpha=1}^{q} K_\alpha^\dagger\right)|\theta\rangle + \left(K_0^\dagger\right)^{p-1} K_D^\dagger \prod_{\alpha=1}^{q} K_\alpha^\dagger \left[-2\frac{g}{\eta}pq - \frac{g}{\eta}p\left(p-1\right) + p\left(1 + 2\frac{g}{\eta}\sum_{k=1}^{m} s_k\right)\right]|\theta\rangle \tag{8.42}$$

The first line corresponds to the standard RG equations for the q remaining pairs, whereas the second line gives an additional constraint if we want the state eq.(8.37) to be an eigenstate:

$$\frac{\eta}{g} = 2q + p - 1 - 2\sum_{k=1}^{m} s_k. \tag{8.43}$$

RG variables are only allowed to 'condense' at N discrete ratios of the interaction constant g and η if one of the two is held constant, where N is the total number of pairs present in the system under investigation, because the number p of condensed pairs can be any number between zero and N and $q = N - p$.

8.5 Around the condensation points

At the condensation points (8.43), p of the N RG variables are condensed to zero, leading to singularities in the RG equations (8.15). However, it is possible to extract the qualitative behaviour of the RG variables around the condensation points by expanding the RG equations (8.15) around the condensation points (8.43). For our purpose, it is convenient to rewrite the RG equations (8.15) in the following form

$$\begin{aligned}\frac{1}{E_\alpha}\left[\frac{\eta}{2g} + \sum_i s_i - (N-1)\right] + \sum_i \frac{s_i}{\eta D_i^2 - E_\alpha} \\ - \sum_{\beta\neq\alpha} \frac{1}{E_\beta - E_\alpha} = 0, \qquad \forall\alpha = 1\ldots N.\end{aligned} \tag{8.44}$$

Expanding the interaction constant $g + \delta g$ around the condensation points eq.(8.43)

$$\frac{\eta}{g+\delta g} \approx \frac{\eta}{g} - \frac{\eta\delta g}{g^2} \tag{8.45}$$

the equations become

$$\begin{aligned}\frac{1}{E_\alpha}\left[\frac{-p+1}{2} - \frac{\eta\delta g}{g^2}\right] + \sum_i \frac{s_i}{\eta D_i^2 - E_\alpha} \\ - \sum_{\beta\neq\alpha} \frac{1}{E_\beta - E_\alpha} = 0, \qquad \forall\alpha = 1\ldots N.\end{aligned} \tag{8.46}$$

It is reasonable to assume that the p condensed variables E_α (with $\alpha = 1\ldots p$) in the vicinity of the condensation points can be developed in a series expansion of δg^γ with γ a yet unknown exponent, whereas the other $q = N - p$ variables can be assumed finite.

$$E_\alpha = \begin{cases} x_\alpha \delta g^\gamma & \alpha = 1\ldots p \\ y_\alpha & \alpha = p+1\ldots N \end{cases} \tag{8.47}$$

The equations break down into two coupled sets

$$\frac{1}{x_\alpha \delta g^\gamma}\left[\frac{-p+1}{2}-\frac{\eta\delta g}{g^2}\right]+\sum_i \frac{s_i}{\eta D_i^2 - x_\alpha \delta g^\gamma} - \sum_{\beta\neq\alpha}^{p}\frac{1}{(x_\beta - x_\alpha)\delta g^\gamma} - \sum_{\beta=p+1}^{N}\frac{1}{y_\beta - x_\alpha \delta g^\gamma} = 0, \tag{8.48}$$

$$\frac{1}{y_\alpha}\left[\frac{-p+1}{2}-\frac{\eta\delta g}{g^2}\right]+\sum_i \frac{s_i}{\eta D_i^2 - y_\alpha} - \sum_{\beta=1}^{p}\frac{1}{x_\beta \delta g^\gamma - y_\alpha} - \sum_{\beta=p+1\neq\alpha}^{N}\frac{1}{y_\beta - y_\alpha} = 0, \tag{8.49}$$

with the first set (8.48) related to the condensed variables ($\alpha = 1 \dots p$) and the second set (8.49) referring to the non-condensed variables ($\alpha = p+1 \dots N$). In lowest order in δg^γ, these equations become decoupled

$$\frac{p-1}{2x_\alpha} + \sum_{\beta\neq\alpha}^{p}\frac{1}{x_\beta - x_\alpha} = 0, \quad \forall\alpha = 1\dots p \tag{8.50}$$

$$\frac{p+1}{2y_\alpha} + \sum_i \frac{s_i}{\eta D_i^2 - y_\alpha} - \sum_{\beta=p+1\neq\alpha}^{N}\frac{1}{y_\beta - y_\alpha} = 0, \tag{8.51}$$

The latter set of equations depend on the parameters in the model, whereas the former set is purely geometric. It can be shown that the variables x_α are located at the corners of a regular p-polygon in the complex plain.

$$x_\alpha = x_0 \omega^{\alpha-1}, \qquad \forall\alpha = 1\dots p \tag{8.52}$$

with $\omega^p = 1$. Substituting (8.52) into (8.50) yields the set of equations

$$\frac{p-1}{2} + \sum_{\beta\neq\alpha}^{p}\frac{1}{\omega^{\beta-\alpha}-1} = 0, \quad \forall\alpha = 1\dots p \tag{8.53}$$

Because of the periodicity $\omega^{\alpha+p} = \omega^\alpha$, this set of equations is equivalent to one single equation

$$\frac{p-1}{2} + \sum_{\beta=1}^{p-1}\frac{1}{\omega^\beta - 1} = 0, \tag{8.54}$$

which can be shown to hold identically for periodic solutions $\omega^p = 1$. As a result, the variables x_α around the condensation point approach $x_\alpha = 0$ along the corners of a regular p-polygon (See Figure 8.4). It is worth pointing out that the geometric solution (8.52) is independent of the free variable x_0 or the scaling parameter γ, for which higher orders in the series expansion should be considered. We leave this for further investigations.

8.5.1 RG solver

The solution method described above for eq.(8.24) can be used as an efficient solver for the hyperbolic RG equations. The absence of correlations in the TDA states reduces the computational complexity of the problem significantly, because only one equation (8.19) needs to be solved as opposed to N coupled equations(8.15). This is the key idea behind the RG solver. The uncorrelated system is solved and then the full pairing problem is retained by adiabatically reintroducing the Pauli principle. We label the TDA eigenstates with a partitioning of N out L integers. This means that the state is labelled by vectors of integers $(\nu_1, \nu_2, \ldots, \nu_l)$ with length L and $\nu_i = 0, \ldots, N$, with the additional constraint that $\sum_{i=1}^{L} \nu_i = N$. Two interesting cases are the fully collective case $(N, 0, \ldots, 0)$ corresponding with the ground-state in the strong-interaction regime, and $\left(\underbrace{\frac{\Omega_1}{2}, \ldots, \frac{\Omega_{n-1}}{2}, \nu_n}_{n\left(\nu_n < \frac{\Omega_n}{2}\right)}, \underbrace{0, \ldots, 0}_{L-n} \right)$ corresponding with the ground-state in the weak interaction regime, which has proven to play a pivotal role in the rational case [201]. When the interaction constant approaches zero, the TDA collective states and the actual physical eigenstates become equal to a filling of pairs of the lowest sp levels up to the Fermi surface. This is because the pairing interaction behaves as a very small perturbation on the sp levels in that case. This makes it possible to label a RG eigenstate with the TDA distribution of pairs that connects to that RG state in the weak interacting limit. The maximum number of pairs that can be associated to a TDA-solution in the weak interaction regime, is never more then the total pair degeneracy of the corresponding sp level. In the intermediate interaction regime the RG states connect to TDA states with some eigenmode multiplicities larger than the degeneracy of the corresponding levels, but lower than or equal to the total number of (collective) pairs. When the interaction constant becomes stronger the collectivity of the TDA state associated to the RG groundstate increases gradually. Until the most collective TDA state connects to the RG ground state, in this TDA state all pairs occupy the collective TDA eigenmode. In the very weak and strong pairing regime it is clear which state connects to the RG ground state. For the intermediate regime this is not the case, and an educated guess for the TDA start distribution has to be made. An alternative solution method is to obtain a solution in the very weak or strong interaction limit and then changing g with small steps until the desired interaction constant is reached. Singular points can be circumvented by a continuation of g in the complex plane [230], or reducing the ξ value which enhances the effective degeneracy of the single-particle levels ($s_i(\xi) = \frac{1}{4\xi}\Omega_i - \frac{1}{2}v_i$), and therefore it has a softening effect on the singular points. Using this approach it is possible to solve systems of hundreds of levels occupied by hundreds of pairs [231]. In practice we use our method to obtain a solution in a limit where the TDA distribution for the state of interest is known and then gradually change the

interaction constant to the interaction constant of interest. Critical points are circumvented by giving the interaction constant a small complex phase or deforming the pairing algebra.

All calculations presented in this chapter were performed on a standard desktop computer. Results for a system with 256 levels and 128 pairs were obtained for a full range of the interaction constant in a few hours. If solutions for a full range of the interaction constant need to be calculated, then most of the calculation time is spent in the circumvention of critical points. When critical points are circumvented it is also necessary to check the continuity of the energy regularly, because the possibility exists that the RG variables jump to a different state. The Newton-Raphson method was used to solve the pseudo-deformed and normal RG equations. The proposed method is very fast and stable if the associated TDA distribution is known a priori for the state of interest, for example for the first excited and ground state at the Read-Green point (Section 8.7).

8.6 Different regimes

In this section we first investigate the connection between the $\eta = 0$ and $\eta \neq 0$ systems. Next we use the tools developed in the previous section to learn more about the Moore-Read line and the two regimes of which the Moore-Read line is the line of demarcation.

8.6.1 The $\eta = 0$ Hamiltonian

A connection is made between the $\eta = 0$ state and the state with $\eta = -2g$. This is relevant because eq.(8.15) diverges when $\eta \to 0$. So by having a method to solve the $\eta \neq 0$ case we are able to generate the solutions of the $\eta = 0$ case. The Bethe ansatz solution of the $\eta = 0$ state was first explored by Pan et. al. [224] and later by Balantekin et. al. [225] who explored some symmetry properties of the Bethe-ansatz equations. Two separate sets of Bethe-ansatz equations were found, solutions of the first set were zero and the solutions of the other set were not constricted to zero.

Suppose that we have found the eigenstate of the factorisable Hamiltonian $|\psi\rangle = \prod_\alpha^N K_\alpha^\dagger |\theta\rangle$ with $\eta = -2g$ for N pairs. Then we can write the Hamiltonian as $\hat{H} = -2gK_D^0 + gK_D^\dagger K_D \equiv gK_D K_D^\dagger$, with

$$K_D^\dagger = \sum_k D_k S_k^\dagger \quad K_D = \sum_k D_k^* S_k \quad K_D^0 = \sum_k D_k^2 S_k^0. \tag{8.55}$$

Note that $K_D^\dagger$ can not be written in the conventional $K_\alpha^\dagger$ form (8.14). By multiplying the eigenvalue equation $\hat{H}|\psi\rangle = E|\psi\rangle$ with $K_D^\dagger$, we obtain:

$$K_D^\dagger g K_D K_D^\dagger \prod_\alpha K_\alpha^\dagger |\theta\rangle = E K_D^\dagger \prod_\alpha K_\alpha^\dagger |\theta\rangle \tag{8.56}$$

So it is clear that the state $K_D^\dagger \prod_\alpha^N K_\alpha^\dagger |\theta\rangle$ is an eigenstate of the Hamiltonian (8.12) with $\eta = 0$ and $N + 1$ pairs. At this point the only question that remains to be solved is: "What accounts for the mismatch in Hilbert space dimensions?". If L denotes the number of levels then the Hamiltonian with $\eta = -2g$ has $\binom{L}{N}$ states in the fully paired space and the Hamiltonian with $\eta = 0$ has $\binom{L}{N+1}$ eigenstates. The resolution of this apparant paradox resides in the fact that with ρ lower than half-filling the extra eigenstates of the system with $\eta = 0$ have zero eigenvalue [224, 225] and these extra eigenstates match exactly the number of missing eigenstates in the $\eta = -2g$ case. Above half-filling the opposite situation occurs, which indicates a symmetry between those states. Another interesting feature is that the RG variables of a particular state with the same energy in both systems are not equal but add up to the same energy eq.(8.16). See Fig. 8.3 for a picture that shows the behaviour of the RG variables as η approaches zero for a system with parameters given in Table 8.1 at quarter filling.

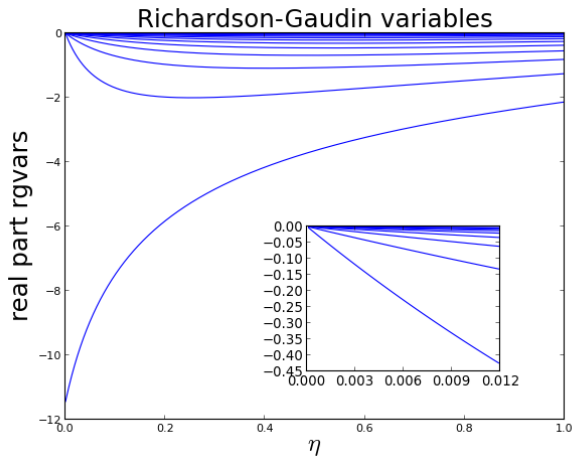

Figure 8.3: Depicted is the evolution of the real part of the RG variables of the ground state when η evolves from zero to one for a system with level parameters as described in Table 8.1 occupied by 10 pairs and $g = -0.075$. Note that the RG variables remain real during the entire trajectory of η because the system remains in the strong pairing regime.

8.6.2 Three regimes at attractive interaction constant

The RG equations become singular when two or more RG variables are equal as can be seen in eq.(8.15). More in particular, at the singular points $2s_i + 1$ RG variables occupy only one single-particle level i and are therefore equal [232]. Those singular points correspond to a reordering of the corresponding bosonic

states in the case of the rational RG model [201]. This is in contrast with the factorisable interaction model, where this is only the case for interaction constants weaker than the Moore-Read point, as we will show in the next subsection. Another difference with the rational RG model is the occurrence of the so called 'condensate regime' where a number of RG variables collapse to zero at particular interaction constants:

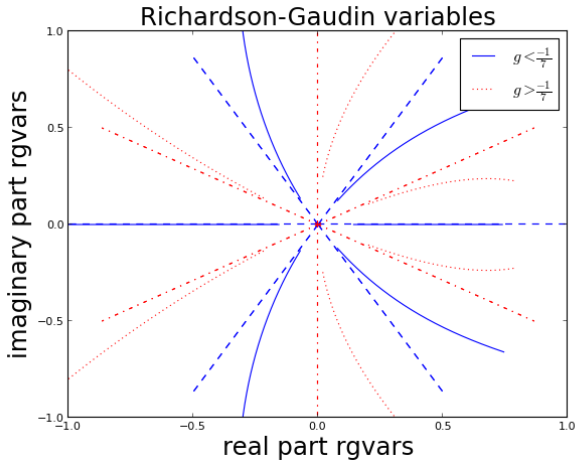

Figure 8.4: The behaviour of the RG variables in the neighbourhood of the Moore-Read point is depicted for a system with 6 pairs in 12 two-fold degenerate levels, and $\eta = 1$ (see Fig. 8.1). The evolution of the corners of the two regular hexagons are depicted respectively by a dashed, and a dot-dashed line. The Moore-Read point occurs at $\frac{\eta}{g} = -7$.

$$\frac{\eta}{g} = 2q + p - 1 - 2\sum_k s_k \tag{8.57}$$

with p the number of RG variables which have condensed to zero and q the number of generic non-zero RG variables[207] (see subsection 8.4 for an alternate derivation of this formula). In the continuum limit, the above formula becomes: $\frac{\eta}{gL} = \rho - 1$ and $\frac{\eta}{gL} = 2\rho - 1$ respectively for N and 1 condensed pairs with $\rho = \frac{N}{L}$ and gL kept constant when $L, N \to \infty$. It follows that the points in phase space with N and 1 condensed pairs correspond to the Moore-Read and Read-Green line for finite systems. The Read-Green and Moore-Read points form the boundaries of the condensation regime. The Read-Green line separates the strong pairing regime and the condensation regime, the Moore-Read line separates the weak pairing regime and the condensation regime. The strong pairing regime only exists below or at half-filling, above half-filling the system never exits the condensate regime. Around those condensation points it is possible to split up the RG equations in two separate sets in lowest order

perturbation theory, a set for the condensed RG variables and one for the non-condensed RG variables. The dynamics of the condensed RG variables in the neighbourhood of their condensation points is described by regular polygons and the requirement that the RG variables need to obey a mirror symmetry with respect to the real axis. To fix ideas, if there are 6 pairs which condense to zero then they approach a condensation point on the corners of a regular hexagon, with all corners in the complex plane. After the condensation point, an extra RG pair stays real, and only an even number of pairs can become complex, so the RG variables leave the condensation point on a regular hexagon with two corners on the real axis (see Fig. 8.4). The system that describes the non-zero RG variables in the neighbourhood of a condensation point is given by:

$$\begin{aligned} &\frac{p+1}{2E_\alpha} + \sum_i \frac{s_i}{\eta|D_i|^2 - E_\alpha} \\ &\quad - \sum_{\beta\neq\alpha,\beta=p+1}^{N} \frac{1}{E_\beta - E_\alpha} = 0. \quad \forall\alpha = p+1,\ldots,N \end{aligned} \tag{8.58}$$

Remark that the labelling of the RG variables is arranged so the first p RG variables correspond to the condensed RG variables and the last $N-p$ RG variables are non-condensed. The position of the collapsed RG variables in the neighbourhood of their condensation point is determined by

$$E_\alpha = z_0 e^{\frac{2\pi i\alpha}{p}}, \quad \alpha = 1\ldots p. \tag{8.59}$$

$z_0 = |z_0|e^{i\phi}$ has a phase that forces mirror symmetry around the x-axis, e.g. for 6 condensed pairs $\phi = 0$ for $g < g_{con}$ and $\phi = -\frac{\pi}{6}$ for $g > g_{con}$, and $|z_0|$ approaches zero. The behaviour of the condensed RG variables around their condensation points is only influenced by the other pairs through their number, and the number of pairs which are real. At the Moore-Read line there are only condensed pairs, and the position of all pairs is determined by eq.(8.59). (For a derivation see subsection 8.5.) In the next two subsections the goal is to gain a better understanding of the three regimes (weak, strong pairing and condensate regime), by investigating, the RG variables and their associated TDA states.

8.6.3 Connecting the TDA state with the RG ground state

We apply the machinery developed above on a spinless Fermi gas with $p_x + ip_y$ pairing interaction symmetry on a disk with a radius of five unit cells in a two-dimensional square lattice of which we found the sp characteristics in [207] (see table(8.1) for the sp characteristics).

From table(8.2), and Fig. 8.5, we notice that the amount of collectivity, as measured by the occupation of the lowest TDA solutions, gradually increases with

$\lvert D_i\rvert^2$	0.04	0.08	0.16	0.20	0.32	0.36	0.40	0. 52	0.64	0.68	0.72	0.80	1.00
Ω_k	4	4	4	8	4	4	8	8	4	8	4	8	12
s_k	1	1	1	2	1	1	2	2	1	2	1	2	3

Table 8.1: Level parameters η_k and Ω_k for a disk with a radius of five unit cells in a two-dimensional square lattice [207]

g	ν_1	ν_2	ν_3	ν_4	...	ν_{12}
0.00000	2	2	2	4	...	0
-0.01518	2	2	6	0	...	0
-0.02329	2	8	0	0	...	0
-0.02525	6	4	0	0	...	0
-0.02550	7	3	0	0	...	0
-0.02564	8	2	0	0	...	0
-0.02690	9	1	0	0	...	0
-0.02750	10	0	0	0	...	0

Table 8.2: The associated collective states of the ground state of a spinless Fermi gas with $p_x + ip_y$ pairing interaction symmetry as a function of the interaction constant g. With single-particle levels given by table(8.1). ν_n corresponds to the occupation of the n^{th} TDA solution. The Moore-Read point is located at $g = -0.03225$.

stronger interaction constant. A particularly interesting result is the fact that the most collective TDA state connects to the RG ground state just before the Moore-Read line where all pairs collapse to zero. However, the connection there is not very stable, and this remains during the entire 'condensation' regime. We have to resort to an imaginary deformation parameter ξ at particular points to make the connection. Outside the 'condensation' regime the connection is stable, and imaginary deformation parameters are not necessary. It is also clear that because of the degeneracy of the sp levels the ground state at low interaction constant corresponds to a TDA distribution of (22240...0) for 10 pairs. Every single-particle level is able to contain an even number of pairs, so if we turn the Pauli principle on by increasing ξ, the RG variables combine into complex conjugate pairs even at very weak interaction constant, as opposed to systems with only two-fold degenerate sp levels where the RG variables are real for small interaction constants. In that case, only one pair is associated to each TDA eigenmode, and the RG variables can only recombine into complex conjugate pairs if two neighbouring pseudo-deformed RG variables approach a singularity, and recombine in a complex conjugate pair. The connection with the (730...) and (910...) state is only present for a very small interval of the interaction constant, and should be seen as a boundary for a transition of the system of one even state to another.

Recapitulating the findings of this section, we find at small interaction constant a regime for which the ground state gradually connects to more collective

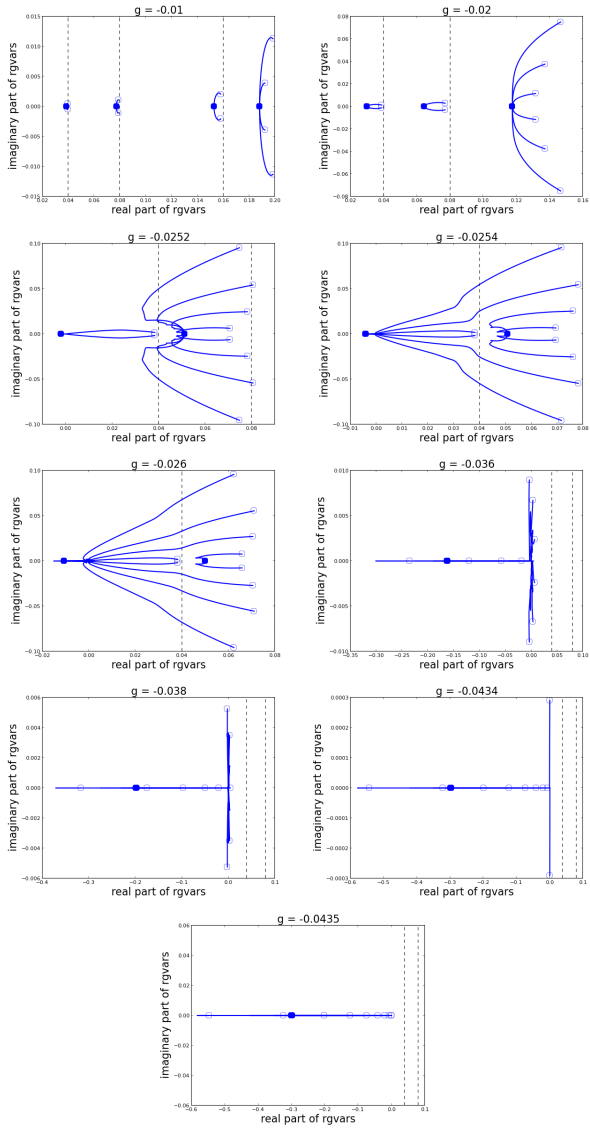

Figure 8.5: The path of the deformed RG variables $E_\alpha(\xi)$ in the complex plane for the two-dimensional Fermigas of which the levels are depicted in Table 8.1, for some well chosen values of g: g = -0.01, g = -0.02, g = -0.0252, g= -0.0254, g = -0.026, g= -0.03600, g=-0.038, g = -0.0434 , g=-0.0435. The path starts from the bosonic eigenmodes $(E_\alpha(0)) = (\hbar\omega)$ depicted with thick dots and ends at the exact RG variables depicted with open dots. The vertical dashed lines indicate the singularities in eq.(8.19).

TDA states with increasing interaction constant. The reordering of pairs of

the associated bosonic state occur at singular points or in between singular points. Whenever a singular point occurs there always is a reordering of the associated TDA state. This happens until the Moore-Read line where the TDA-state is in the most collective form. In the weak pairing regime the connection and the associated TDA states have strong similarities with the reduced BCS Hamiltonian [201]. During the 'condensate' regime when the interaction constant fulfils $2N - 2 - L_c \geq \frac{\eta}{g} \geq N - 1 - L_c$, the connection with the most collective TDA state remains but we have to resort to a complex deformation parameter, until the last condensation point is passed. In the strong pairing regime, the connection with the most collective TDA state is firmly established.

8.6.4 Overlaps with the collective states

In this subsection we investigate the overlap of the ground state of a factorisable interaction Hamiltonian with some selected TDA states over an entire range of the interaction constant. Such overlap has proven to provide valuable information about the RG states and their collective character [201, 222]. Investigations of the overlap shows that at weak interaction constant the behaviour of the RG variables resembles that of the reduced BCS Hamiltonian[201]. Beyond the Moore-Read line this is not the case anymore. Fig. 8.6 depicts the overlap of some well chosen TDA states with the ground state of the system consisting of 6 pairs in 12 doubly degenerate sp levels (cfr. Fig. 8.1). We find that for very small interaction constant the overlap of the RG grounstate with the TDA ground state $(1111110\ldots0)$ is almost equal to one, as expected. Then there is an intermediate regime where some other TDA states with increasing collectivity have the highest overlap with the RG ground state. The interaction constants where this occurs are the same as the interaction constants where the TDA state that connects to the ground state changes. Until this point similar behaviour as in the reduced BCS case is observed. However, the situation alters as the condensation regime is approached. Here, the most collective TDA state $(60\ldots0)$ goes to a local minimum, while most other states exhibit a maximum in that region. The TDA state with 1 pair in the lowest TDA solution and 5 pairs in the first excited TDA state has the largest overlap, although the most collective TDA state connects to the RG ground state. This peculiar behaviour starts around the Moore-Read point, so in the 'condensate regime' it is no longer true that the TDA state with the highest overlap with the RG ground state connects to the RG ground state according to our scheme. The reason for this is that after the Moore-Read point some RG variables that are still complex have very small negative real part. The overlap with the $(150\ldots0)$ state is largest here because 5 RG variables are very close to the 1st excited TDA state and 1 is strongly negative close to the lowest TDA level. The reason why that TDA state does not connect to the RG ground state is probably caused by the singularity in eq.(8.24) when some RG variables approach zero. Therefore, all the deformed RG variables have to depart from the lowest TDA solution

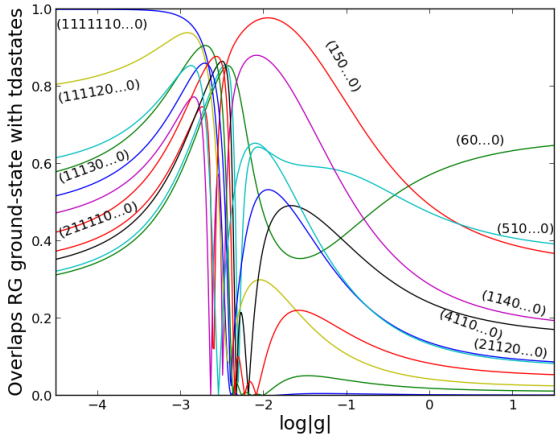

Figure 8.6: Depicted are the overlaps of a selected set of bosonic states with the ground state of a system with 12 doubly degenerate levels, $\eta = 1$, and $|D_i| = 1$ as a function of the interaction constant. The bosonic states are labelled according to their TDA eigenmode occupation. The notation is as follows $(\nu_1\nu_2 0 \ldots 0)$ means that the bosonic state is constituted of ν_1 bosons in the TDA state with the lowest E_{TDA} and ν_2 bosons in the first excited TDA state.

to connect with the RG ground state of eq.(8.12). With increasing interaction constant, the most collective TDA-state gradually becomes the TDA state with the largest overlap with the ground state of the $p_x + ip_y$ pairing Hamiltonian. This happens after the condensate regime when all the RG pairs become real. From then on, the TDA state with the highest overlap with the RG ground state is again the state which connects to the RG ground state, by the pseudo deformation. However, the overlap of the most collective TDA state in the strong interaction regime with the RG ground state is not as prominent as in the reduced BCS case [201]. The natural question that occurs is: "Will the overlap of the most collective TDA state with the RG ground state approach one in the limit of a very strong interaction constant?". If we calculate the overlap of the system depicted in Fig. 8.6 but with $\eta \ll 1$ (which corresponds to the limit of large interaction constant), we see that in this limit all the overlaps of the TDA states with the RG ground state have a value around 0.660 and the $(60 \ldots 0)$ state has the largest overlap with a value of 0.668. This indicates that even at very big interaction constant the overlap of the most collective TDA state with the RG ground state will never approach one. This plateau appears to be density dependent, increasing with decreasing density. We conclude that according to the overlaps there are three different regimes: at low interaction constant a regime that shows similarities with the reduced BCS Hamiltonian and after the Moore-Read point a regime that is significantly

different with a minimum of the overlap of the TDA state which connects to the RG ground state. After the Read-Green line this is restored and the TDA state that connects to the RG ground state has the largest overlap again. Opposed to the rational case, there is no consistent isomorphism between the TDA states connecting to the RG ground state via the pseudo deformation, and the TDA state with a maximal overlap.

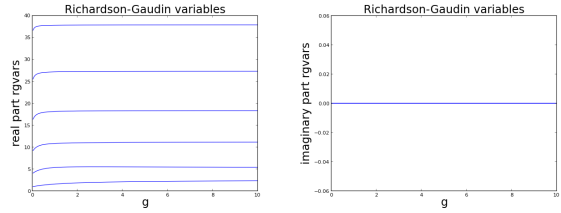

(a) The ground state

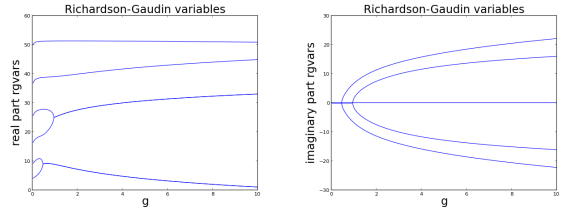

(b) The (0 1 1 1 1 1 1 0 0 0 0 0) state

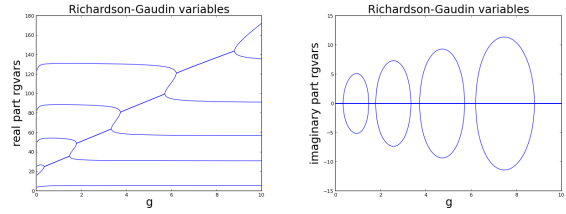

(c) The (0 1 0 1 1 0 1 0 1 0 1 0) state

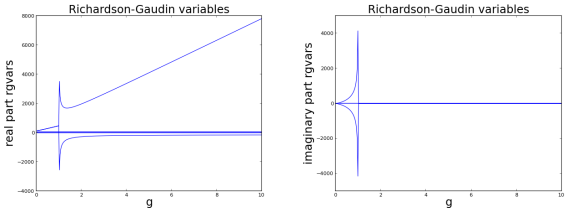

(d) The (1 1 1 0 0 0 0 1 0 0 1 1) state

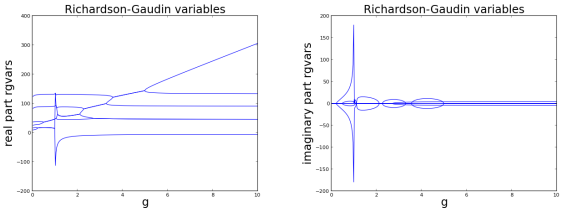

(e) The (0 0 1 1 1 1 0 0 1 0 1 0) state

Figure 8.7: The real and imaginary part of the RG variables of a system with 12 doubly degenerate sp levels and 6 pairs as a function of a positive interaction constant g of some well chosen eigenstates.

8.6.5 Repulsive p-wave interactions

There is no mean-field solution in the yet unexplored repulsive case available. So the exact solution method presented above offers a unique tool to investigate repulsive p-wave interactions. A difference compared to attractive pairing interaction is that the RG variables now recombine to higher TDA states instead of lower, as the interaction strength is increased. Pairs in isolated sp levels can not recombine, so the RG variables corresponding to those sp levels that remain real and close to the TDA solution for the entire range of the interaction strength. There are even start TDA states with neighbouring occupied sp levels that remain real during the entire trajectory, and which do not couple to complex conjugate pairs, as is visible in the trajectories of the RG variables of the ground-state energy in Fig. 8.7a. The RG variables of some excited states follow similar trajectories. In general the trajectories of the RG variables for the hyperbolic RG Hamiltonian with repulsive interaction constant exhibit three different features.

- A RG variable can remain real during the entire trajectory of the interaction constant, see Fig. 8.7(a).
- Two real RG variables can recombine into a pair of complex conjugate variables by creating a singular point in the trajectory space, after which the complex part gradually increases, see Fig. 8.7(b).
- Two complex conjugate RG variables can become real again through a sudden jump in complex space and a similar jump in real space. Remark that the jump of the real parts of the RG variables is in the opposite direction so the energy stays continuous and the path of the other RG variables is not affected.

In general, a trajectory of the RG variables contains all possible combinations of these events. Some trajectories are very similar to the ones of the rational RG model with a positive interaction (see for example the trajectory of the (011111100000) state Fig. 8.7b, in contrast with a negative interaction constant where this similarity is only present before the Moore-Read line. For a nice example of recombinations see Fig. 8.7c for the (010110101010) state. There is no condensate regime at positive interaction constant, and the RG variables do not need to become real for large g. There is a category of trajectories that do not exist in the spectrum of the rational RG model that we shall refer to as 'sudden complex' (sc) trajectories (see Fig. 8.7d). In those trajectories we see that two real RG variables suddenly become a complex conjugate pair with significant complex part, as opposed to the rational RG model, where the formation of complex conjugate pairs of RG variables is a gradual process resulting from a singular point. Finally, we refer to Fig. 8.7e for a combination of the different events described above. Notice also that the energy remains continuous during all those trajectories as is required. We found that the sc

trajectories only occur above half filling, the RG variables under half filling remain real and analytical during the whole trajectory. Furthermore the Read-Green point at positive interaction constant occurs only for filling fractions above half-filling. The system at half-filling seems to have characteristics of a transitional region, because the ground state has the same behaviour as below half-filling but some excited states start to exhibit 'sudden collapses' and singular points as is typical for above half-filling (see Fig. 8.7).

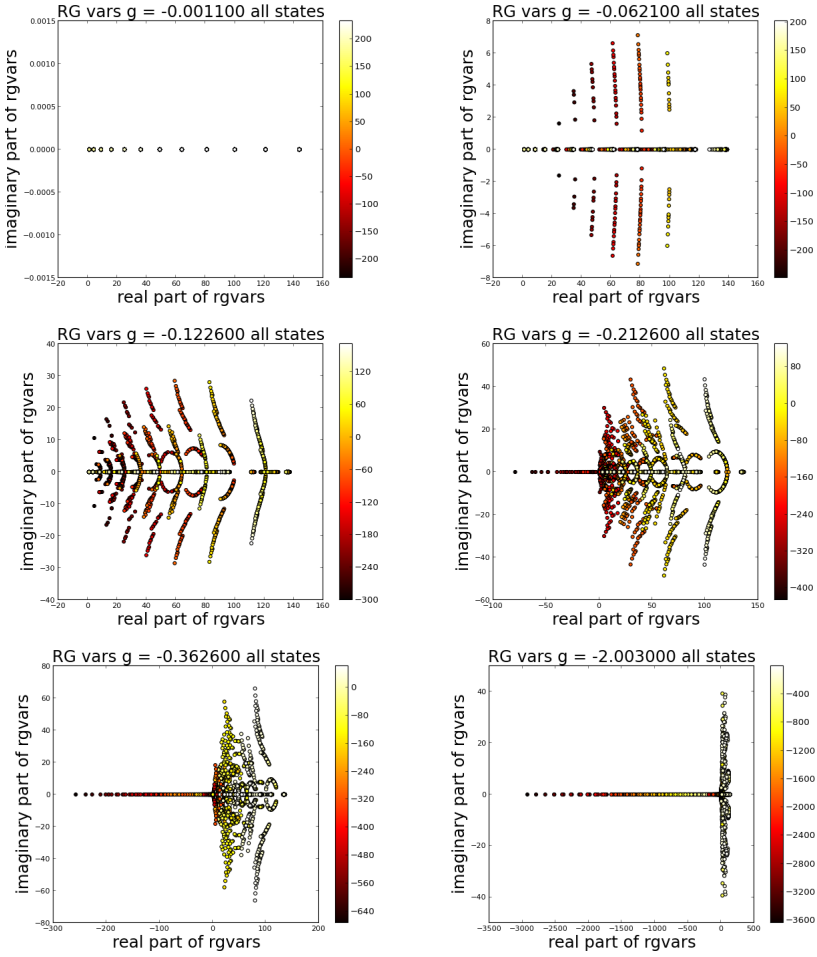

Figure 8.8: This figure shows all the RG variables of the full spectrum with 6 pairs in 12 doubly degenerate equidistant levels and zero seniority as a function of increasing attraction strength. Colour coded according to the energy of the eigenstate to which they correspond.

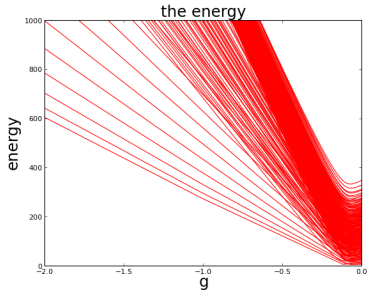

(a) 3 pair

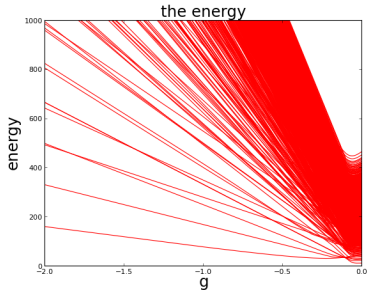

(b) 6 pair

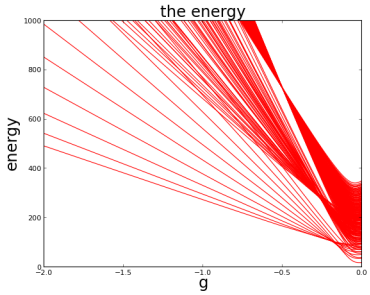

(c) 9 pair

Figure 8.9: All excitation energies of a system with 12 doubly degenerate single particle levels occupied by a) 3, b) 6 and c) 9 pairs and equidistant $D_i = i$ as a function of the interaction constant g.

8.7 Excited states

12 levels	$1p$	$2p$	$3p$	$4p$	$5p$	$6p$
Read-Green point g	-0.0833	-0.1000	-0.1250	-0.1666	-0.2500	-0.5000
TDA label	(010...)	(0110...)	(01110...)	(011110...)	(0111110...)	(01111110...)
TDA Read-Green	(010...)	(110...)	(210...)	(310...)	(410...)	(510...)
Energy	2.108110	4.323544	7.257231	11.627856	20.383734	42.779908

Table 8.3: The interaction constant (g) at the Read-Green point is calculated, for a system with 12 doubly degenerate sp levels and $\eta = 1$. The first excited state reaches a minimum around the Read-Green point, the energy normalized to the ground-state energy at the Read-Green point is given, together with the start TDA distribution (label), and the TDA state that connects to the first excited state at the Read-Green point.

The above proposed algorithm to solve the RG equations is very robust and fast. This makes it possible to study entire spectra of mesoscopic systems. It catches the eye that the RG variables of all states have the same typical

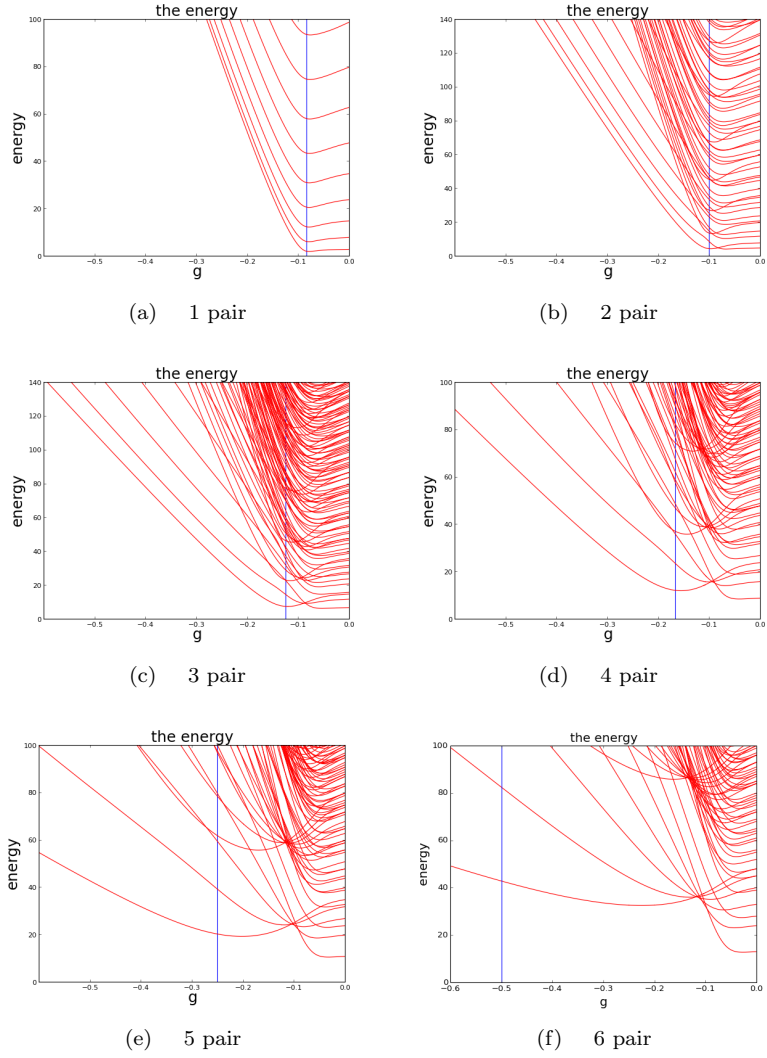

(a) 1 pair (b) 2 pair

(c) 3 pair (d) 4 pair

(e) 5 pair (f) 6 pair

Figure 8.10: The excitation energies of a system with 12 doubly degenerate sp levels occupied by 1 to 6 pairs (a-f) as a function of the interaction constant g. The Read-Green point is depicted by a vertical line that divides the weak from the strong pairing regime.

evolution for changing interaction constant see Fig. 8.8. See reference [233] for a movie that shows the evolution of the RG variables of all seniority zero states as the interaction strength is increased. Another interesting feature of the $p_x + ip_y$ Hamiltonian at half-filling is the fact that the gap between the ground state energy and the energy of the first excited state is of the same order as gaps between higher excited states for an entire range of the interaction constant.

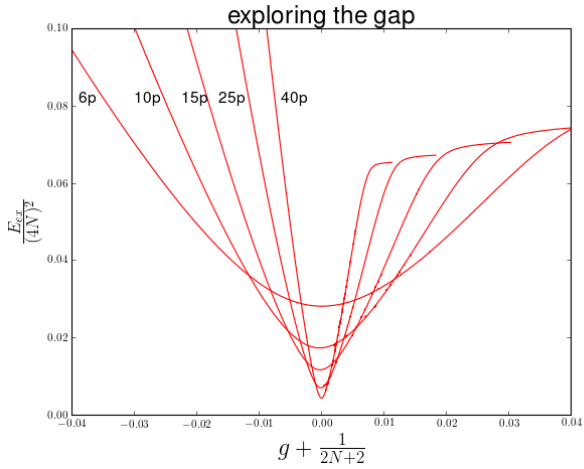

Figure 8.11: The energy differences between the ground state and the first excited state at the Read-Green point are depicted, this for several systems with an increasing number of pairs, all at quarter-filling, $D_i = i$ with $i = 1 \ldots 4N$ and $\eta = 1$. The excitation energies are rescaled with a factor $(4N)^2$ and the interaction constant is shifted so the Read-Green point occurs for all systems at 0 (see eq. (8.57)).

Fig. 8.9 depicts the entire spectrum of a system with 12 doubly degenerate levels occupied by respectively 3,6 and 9 pairs with $\eta = 1$. The Read-Green line for 3 pairs in 12 levels is crossed at $g = -0.125$, which is exactly where the energy difference of the ground state with the excited states reaches a local minimum and starts to increase rapidly. Before the Read-Green line it is also possible for excited states to decrease the energy difference with the ground state, after the Read-Green line this is not allowed any more. This is also the case for 1, 2, 4, and 5 pairs as can be seen in Fig. 8.10. The TDA label associated to the state with the local minimum excitation energy seems to have a pattern namely $(0\underbrace{1 \ldots 1}_{N}0 \ldots)$, and the TDA state that connects to the first excited state at the Read-Green interaction constant has the form $(N{-}1\ 1\ 0 \ldots)$ (see Table 8.3). For 5 and 6 pairs, the minimum of the 1st excited state occurs a bit before the Read-Green point. If the number of levels and pairs is increased while keeping the occupancy constant, the pattern remains and the increase of the excitation energies after the Read-Green point becomes much steeper, and more and more states reach their minimum in excitation energy at the Read-Green point. In the continuum limit BCS theory predicts a strongly degenerate ground-state at the Read-Green point [206]. In order to investigate numerically the gap for growing system sizes approaching the thermodynamic limit, one would need to calculate a combinatorial number of excited states. Because

of the systematic $(0\underbrace{1\ldots1}_{N}0\ldots)$ TDA state labelling, observed in the small system (Fig. 8.10), we conjecture that the same phenomenon holds for larger systems, so we only need to calculate two states to determine the minimum excitation energy at the Read-Green point. Therefore, it is possible to explore the behaviour of the gap for large system sizes. Fig. 8.11 shows the results for a system with an increasing number of pairs at quarter-filling. We take $D_i = i$, with $i = 1 \ldots 4N$ for $N = 6 \ldots 40$. (Note that a full scan of the Hilbert space would require the calculation of $\binom{160}{40} \approx 8.6 \cdot 10^{37}$ states for $N = 40$.) The Read-Green point is predicted to be at $\frac{g}{\eta} = \frac{-1}{2N+2}$. After rescaling the spectrum with $(4N)^2$, in order to guarantee a consistent definition of the thermodynamic limit with the highest sp level at $D_{4N}^2 = 1$, we see that the gap decreases for increasing system size as expected. Another remarkable fact is that for bigger systems the gap, after the Read-Green point, increases much faster than for smaller systems. This effect is stronger for lower filling fractions. Above half filling the system remains weakly paired over the entire range of the interaction constant and there is no hint of the formation of a gap.

8.8 Conclusions

In conclusion, we presented an efficient and stable method to solve a class of integrable pairing Hamiltonians. This makes it possible to probe entire spectra of systems with Hilbert spaces way beyond the realm of exact diagonalisation techniques. The method solves the Bethe ansatz equations by means of a deformation parameter that adiabatically connects the genuine boson limit to the hard-core boson limit. Furthermore, we related the singular points of the RG variables to a change in the associated TDA distribution and corresponding overlaps. The ground state connects with the most collective TDA state slightly before the Moore-Read line. In the low interaction regime, the path of the RG variables of the factorisable interaction has some resemblances with the reduced BCS Hamiltonian which also appeared in the overlaps with the bosonic states. However, after the low interaction regime, an entirely different regime arises that has no resemblance with a regime of the reduced BCS case. Remnants of the Read-Green line for finite size systems are found as a local minimum of the first excited state, before the Read-Green point excited states can lower their energy difference with the ground-state energy after the Read-Green point this is no longer possible. Finite-size effects cause this minimum to shift to weaker interaction strength when half-filling is approached. With an increasing amount of sp levels this shift gets noticeable for higher filling fractions only. A pattern is found for the label of the TDA state that becomes the first excited state at the Read-Green point and the TDA state that connects to the first excited state at the Read-Green point.

Part III

Conclusions

In this thesis the applicability of the seniority number as a new tool to create many body wave functions is investigated. This was done in two parts. The first part dealt with the seniority number as a tool to truncate the Hilbert space and create a hierarchy of methods with rapid convergence towards the FCI limit. In the second part the non-relativistic quantum chemical Hamiltonian was further simplified to grasp the essential physics of electron pairing. These pairing phenomena are important in areas ranging from condensed matter physics and nuclear physics to quantum chemistry. Interestingly, the seniority number is an exact quantum number for pair Hamiltonians and there exist fast linear scaling solution methods for some of those Hamiltonians based on their exact integrability, allowing to obtain solutions for systems with hundreds of electron pairs in hundreds of single-particle levels.

Truncating the full configuration interaction wave functions by the seniority number revealed that the bulk of the static correlation can be attributed to the seniority zero determinants for many molecular systems. It was shown that the optimization of the basis was of upmost importance to obtain good results with this hierarchy. Good bases are the seniority minimized basis of the FCI wave function that turned out to be the best orthonormal basis for wave functions that contain many seniority zero determinants such as the DOCI wave function. Furthermore the natural orbital basis and the seniority minimized basis of the CISD wave function turned out to be good approximations to the seniority minimized basis of the FCI wave function. Another alternative is the orthonormal basis coming from a local optimization using sequences of Jacobi rotations that minimize the energy by rotating to the optimal angle for two randomly chosen orbitals in a self consistent manner. This local basis has the problem that when the starting point was not sufficiently well chosen it got stuck in local minima. A further basis originates from a global optimization procedure such as simulated annealing. This approach yielded the lowest energies, but unfortunately it was the slowest optimization procedure, and to obtain the lowest energies the quality of the wave function is sometimes reduced. Another point is that the DOCI wave function is sensitive with respect to symmetry breaking. Significantly better wave functions and energies are found when the spatial point-group symmetry of the single-particle orbitals is allowed to be broken during the optimization process.

The main advantage of the seniority based procedure is its rapid convergence towards the FCI limit and that to a very low order in this hierarchy the bulk of the static correlation is adequately described. This is probably due to the fact that truncating based on seniority is reference independent, in big contrast with the standard excitation based truncated CI methods. A problem that arises with using the seniority hierarchy is that one needs pair broken terms to describe the dynamic correlation. If dynamic correlation is important, the DOCI wave function alone is not sufficient and one can add CISD determinants or use perturbation theory. Another possible approach is to go towards higher orders of the seniority hierarchy and add the seniority four sector, as we found

that when a well optimized DOCI basis is used the seniority two sector plays very little to no role. Furthermore variationally optimizing the density matrix coming from a seniority zero wave function leads to a more favourable scaling with the system size than the standard variational optimization of the second order reduced density matrix. This method obtains very accurate potential energy curves with a very good scaling. As a last test for the seniority hierarchy constrained CI calculations were performed. Those calculations showed that the DOCI wave function gave the same integer Mulliken populations at infinite distance as the FCI wave function in big contrast with the CISD wave function which obtained fractional mulliken populations. This is probably due to the size consistency of the DOCI wave function.

The main conclusions for the second part are that very fast linear scaling solution methods exist for a class of integrable Richardson-Gaudin models based on a deformation of the quasi spin algebra. This technique was used to obtain solutions for the reduced BCS Hamiltonian and the p_x+ip_y Hamiltonian. For the reduced BCS Hamiltonian the dependency of the superconducting state on the geometry of nano-grains was studied. The dependency on the geometry is introduced by adaptations of the single-particle spectrum based on parameters coming from the geometry as seen by the 'particle in a box' concept. By means of perturbation theory, it was found that the condensation energy in the weak-coupling regime is mainly dependent on local single-particle level density fluctuations, whereas the strong-coupling regime is also affected by global level density fluctuations. Introducing impurities, as a second control parameter, proved to be a more gradual probe for pairing correlations. An impurity gives a unique quasi-periodic structure to each single particle level as a function of the position of the impurity, such that it becomes possible to weigh the contributions of the single-particle levels to the condensation energy by investigating the frequency of oscillations. For the $p_x + ip_y$ Hamiltonian the interesting phase diagram was studied. The singular points of the Richardson-Gaudin (RG) variables were related to a change in the associated Tamm-Dancoff approximation (TDA) distribution and corresponding overlaps. The ground state connects with the most collective TDA state slightly before the Moore-Read line. In the low interaction regime, the path of the RG variables of the factorisable interaction has some resemblances with the reduced BCS Hamiltonian which also appeared in the overlaps with the bosonic states. However, after the low interaction regime, an entirely different regime arises which has no resemblance with a regime of the reduced BCS case. Remnants of the Read-Green line for finite size systems are found as a local minimum of the first excited state, before the Read-Green point excited states can lower their energy difference with the ground-state energy after the Read-Green point this is no longer possible. Finite-size effects cause this minimum to shift to weaker interaction strength when half-filling is approached, with an increasing amount of sp levels this shift gets noticeable for higher filling fractions only. A pattern is found for the label of the TDA state that becomes the first excited state at the Read-Green point and the TDA state that connects to the first excited state at

the Read-Green point. Those applications show the power of the exact solution method based on the integrability of the Richardson-Gaudin models, as many systems were solved during the process that consisted of ten till hundreds of pairs with similar amounts of single-particle levels leading to gigantic Hilbert spaces.

The results of the two parts can be combined in future work. The first part showed that the seniority based hierarchy grasps the bulk of the static correlation if a suitable orthonormal basis is used and the second part showed that there exist fast linear scaling solution methods of approximate pairing Hamiltonians that live in the seniority zero sector of the Hilbert space. This hints on the interesting approach of variationally optimizing the parameters of the Richardson-Gaudin Hamiltonians such that the resulting Richardson-Gaudin wave function approximates as close as possible the DOCI wave function for a given molecular system. Good candidates for the orthonormal basis used for those variational optimized Richardson-Gaudin wave functions are the orthonormal bases that minimize the seniority of the CISD or sen(0,2) wave functions or the LOCAL optimized bases. If this succeeds, a solver for the molecular problem that scales linearly with the system size and that grasps the bulk of the static correlation of many molecules will be available. Promising results were already obtained for the hydrogen dimer and the BeH_2 molecules, but much more work remains to be done, before final conclusions can be made.

Appendices

Appendix A

Second quantization

Let $\phi_i(\mathbf{x})$ be a basis of M orthonormal spin orbitals. $\mathbf{x}$ stands for the spatial and spin coordinates. A Slater determinant is an antisymmetrized product of one or more spin orbitals.

$$\Psi_{det} = \frac{1}{\sqrt{N!}} \begin{vmatrix} \phi_1(\mathbf{x}_1) & \phi_2(\mathbf{x}_1) & \dots & \phi_N(\mathbf{x}_1) \\ \phi_1(\mathbf{x}_2) & \phi_2(\mathbf{x}_2) & \dots & \phi_N(\mathbf{x}_2) \\ \vdots & \vdots & \ddots & \vdots \\ \phi_1(\mathbf{x}_N) & \phi_2(\mathbf{x}_N) & \dots & \phi_N(\mathbf{x}_N) \end{vmatrix} \tag{A.1}$$

In the second quantization approach an abstract vector space is introduced called the Fock space, where each determinant is represented by an occupation-number vector $\mathbf{k}$,

$$|\mathbf{k}\rangle = |k_1, k_2, \dots, k_m\rangle\,, \tag{A.2}$$

with $k_p = 1$ when ϕ_p is occupied and otherwise $k_p = 0$. The occupation number vectors are orthonormal. Creation and annihilation operators are defined by the following relations on the occupation number vectors:

$$a_i^\dagger\,|k_1, k_2, \dots, 0_i \dots, k_m\rangle = \prod_{q=1}^{i-1} -1^{k_q}\,|k_1, k_2, \dots, 1_i \dots, k_m\rangle \tag{A.3}$$

$$a_i^\dagger\,|k_1, k_2, \dots, 1_i \dots, k_m\rangle = 0 \tag{A.4}$$

$$a_i\,|k_1, k_2, \dots, 0_i \dots, k_m\rangle = 0 \tag{A.5}$$

$$a_i\,|k_1, k_2, \dots, 1_i \dots, k_m\rangle = \prod_{q=1}^{i-1} -1^{k_q}\,|k_1, k_2, \dots, 0_i \dots, k_m\rangle\,. \tag{A.6}$$

These creation and annihilation operators fulfill the following anti-commutation relations:

$$a_i^\dagger a_j + a_j a_i^\dagger = \delta_{ij} \tag{A.7}$$

$$a_i^\dagger a_j^\dagger + a_j^\dagger a_i^\dagger = 0 \tag{A.8}$$

$$a_i a_j + a_j a_i = 0. \tag{A.9}$$

Furthermore a vacuum state is defined such that for every annihilation operator:

$$a_i \left|vac\right\rangle = 0 \tag{A.10}$$

$$\left\langle vac|vac\right\rangle = 1. \tag{A.11}$$

This representation has straightforward formulations for the particle-number operator $\hat{N}$ and the excitation operators $\hat{X}_i^p$.

$$\hat{N}\left|\mathbf{k}\right\rangle = \sum_{i=1}^{M} \hat{N}_i \left|\mathbf{k}\right\rangle = \sum_{i=1}^{M} a_i^\dagger a_i \left|\mathbf{k}\right\rangle = \sum_{i=1}^{M} k_i \left|\mathbf{k}\right\rangle \tag{A.12}$$

$$\hat{X}_i^p = a_p^\dagger a_i, \tag{A.13}$$

where M is as before the number of single-particle orbitals.

Appendix B

Computer codes

In this appendix some background information is given about the computer codes developed and used in this work. The two main software packages that were developed are: CIFlow for the configuration interaction theory part, and RG for the Richardson-Gaudin part.

B.1 CIFlow

CIFlow is a very flexible and general configuration interaction program that is available as open source at [46]. It is written in C++ using the BLAS and LAPACK libraries for linear algebra operations and the HDF5 library for storing data. The one- and two-electron integrals are calculated using PSI4 [38] and stored in a HDF5 file using the Hamiltonian class of CheMPS2 [39, 40]. Furthermore, it comes with many python scripts that can be used as examples for preparing input, postprocessing, visualization, ...

The main selling point of CIFlow is its flexibility. In essence all possible Hamiltonians can be solved as long as the one and two body integral matrix elements are known. CIFlow has already been used to generate results for the non-relativistic quantum chemical Hamiltonian (with and without constraints), the Hubbard Hamiltonian, the reduced BCS Hamiltonian, and the $p_x + ip_y$ pairing Hamiltonian. Furthermore it has the flexibility to solve for all possible CI wave functions for all Hamiltonians, this can be done by providing a list of Slater determinants in binary string format. This flexibility makes it possible to test quickly new multi-reference CI methods for interesting Hamiltonians one might encounter. CIFlow makes it also easy to perform basis transformations, keywords for many important orthonormal bases are provided such as the seniority minimized ones, the natural orbitals, the RHF orbitals, ... CIFlow also has the ability to take into account non-orthogonal bases. Furthermore basis sets with up to 512 orbitals are supported. This is in contrast with many

of the big quantum chemistry packages of which the CI solver is mostly limited to 32 or 64 orbitals.

Four main CI routines are available: doci, fci, file, big. The first three are faster than the last because the first three keep the Hamiltonian matrix in a sparse matrix format in memory. If this is no longer possible, only the big option works, which builds the Hamiltonian on the fly while iteratively diagonalizing it. Model Hamiltonians such as the Hubbard model or pairing Hamiltonians can be kept in memory for larger dimensions because the increased sparsity is exploited by the SparseMatrix classes. The DOCI code is quite fast, and most orbital optimization routines are only tailored towards DOCI. The intended use for the FCI code is testing, benchmarking, and generating interesting bases for the other methods. With the file option, one can provide Slater determinants in binary string format contained in a file of which the name should be on the next line in the input file. The combined flexibility of user provided/created integrals and random non-ordered determinants makes it very difficult for speed optimization. Therefore the intended use for the file and big options is to test quickly new fancy multi-reference CI methods and calculate some properties of their wave functions, if they perform well it is always possible to create another program specifically optimized for those methods.

Many orbital optimizations are implemented, however, most are specifically tailored towards low seniority wave functions, as CIFlow was originally intended to be a DOCI solver, and orbital optimization is of utmost importance for DOCI. The following keywords are important:

- local: Very fast optimizer with good results based on a subsequent rotation to the minimum energy of pairs of Jacobi orbitals, but with no guarantee one reaches the global minimum. It is probably the best choice if one is just interested in low DOCI energies for big systems. It needs typically a decent starting base (RHF orbitals are enough around equilibrium geometry).

- sim: Slow optimizer based on a simulated annealing procedure, only suitable for small systems in the STO-3G basis with no point-group symmetry or 6-31g when only orbital rotations are allowed of orbitals corresponding to the same irreducible representation of the point-group. High chance of reaching the global minimum for small systems, and for these systems it generates lower energies than local. Sim can be used for benchmarking.

- fmmin: Generates the seniority minimized FCI bases and uses this basis to calculate the CI energy for the requested wave function. As explained in the thesis, the seniority minimized FCI basis generates the best DOCI wave functions, but is slow because it has to perform many FCI calculations.

- fno: Calculates the CI energy and the wave function in the natural orbital basis.
- hmmin: This keyword seniority minimizes the orthonormal basis for the current CI wave function. It can be used in the following workflow: seniority minimize the basis for a truncated CI wave function such as CISD and use the resulting basis as input for a low seniority method such as DOCI. This also gives very good DOCI wave functions and energies with smaller computational effort than seniority minimizing the full FCI wave function.
- mmind: Is a similar keyword it seniority minimizes the current CI wave function and then uses the resulting basis to generate the DOCI energy and wave function.

When all keywords are provided the general procedure goes as follows. The CI Hamiltonian is built with the Slater-Condon rules for a given orthonormal basis. This Hamiltonian can be kept in memory as a sparse matrix or recalculated on the fly dependent on the method keyword. For the diagonalisation an implicitly restarted Arnoldi algorithm is used[54]. This algorithm finds the ground state energy by using only a sparse matrix-vector product. Every N-particle state is represented by a bit string. Calculating a single element of the Hamiltonian is very quick and as all elements are independent, this is very well suited for parallelization. It is this parallelization that makes it possible to perform CI calculations routinely for Hilbert dimensions of a couple of million determinants. Furthermore, efficient addressing schemes are implemented to find the rank of a particular bitstring (as presented in Helgaker et. al.[4]). To conclude this appendix, some final practical remarks for working with CIFlow are given. The debug flags are default on in the Makefiles: -g -ggdb3 -D_DEBUG. This will slow down the code significantly because many extra checks will be performed during execution, comment this line out and recompile if speed is important. At the moment the code is only tested and stable when the number of up and down electrons is equal. If one wants to use more than 64 orbitals one has to change the type definition in include/Options.h instead of #define TL → #define TLL and recompile everything. This makes it possible to handle determinants with 64-128 orbitals (add an extra L for every extra power of 2). But be warned: this reduces the speed significantly, so if you have a large number of determinants it is best to keep the number of interacting orbitals lower than 64.

B.2 RG

RG is an open source python implementation that solves the general Richardson-Gaudin equations for the XXX, XXZ and Dicke models. It includes routines to variational approximate the general pairing Hamiltonian and the non-

relativistic quantum chemical Hamiltonian by means of RG eigenstates. RG is freely available and can be downloaded at [234].

Appendix C

List of publications

A1 publications

Publications incorporated in this thesis

1. M. Van Raemdonck, S. De Baerdemacker, and D. Van Neck. *Perturbations on the superconducting state of metallic nanoparticles: influence of geometry and impurities.* 2013: The European Physical Journal D 67:14.

MVR generated all results; MVR and SDB wrote the software; SDB wrote the paper and came up with the original idea. All authors edited the manuscript and provided scientific support.

2. M. Van Raemdonck, S. De Baerdemacker, and D. Van Neck. *Exact solution of the $p_x + ip_y$ pairing hamiltonian by deforming the pairing algebra.* 2014: Physical Review B 89:155136.

MVR wrote the software, generated all results and wrote a first version of the paper; SDB performed most of the theoretical derivations and had the initial idea. All authors edited the manuscript and provided scientific support.

3. M. Van Raemdonck, D. R. Alcoba, W. Poelmans, S. De Baerdemacker, A. Torre, L. Lain, G. E. Massaccesi, D. Van Neck, and P. Bultinck. *Polynomial scaling approximations and dynamic correlation corrections to doubly occupied configuration interaction wave functions* 2015: The Journal of Chemical Physics 143:10104106.

MVR wrote the software, generated the results and wrote a first draft of the paper; the simulated annealing procedure was an idea of DRA and PB; the approximations and extensions of DOCI were ideas of DRA and MVR; WP was invaluable for optimizing the software; SDB had the idea of looking to wave function overlaps; PB had a major part in the editing process. All authors edited the manuscript and provided scientific support.

4. W. Poelmans, M. Van Raemdonck, B. Verstichel, S. De Baerdemacker, A. Torre, L. Lain, G. E. Massaccesi, D. R. Alcoba, P. Bultinck, and D. Van Neck. *Variational optimization of the second order density matrix corresponding to a seniority-zero configuration interaction wave function*, 2015: Journal of Chemical Theory and Computation, 11:4064-4076.

WP wrote the software, generated results and wrote a first version of the manuscript; MVR contributed to the orbital optimization and DOCI part of the software; DRA, BV, DVN, SDB, and PB were involved with the 2RDM part of the project. In comparison to the original article the derivation of the optimal Jacobi rotations for the DOCI wave function is incorporated in the body of the text for this thesis. All authors edited the manuscript and provided scientific support.

5. D. R. Alcoba, A. Torre, L. Lain, G. E. Massaccesi, O. B. Oña, P. W. Ayers, M. Van Raemdonck, P. Bultinck, and D. Van Neck. *Performance of Shannon-entropy compacted N-electron wave functions for configuration interaction methods* 2016: Theoretical Chemistry Accounts 135:153.

DRA, TA, LL, MGE, OOB, PA wrote the initial version of the manuscript, generated the first results and had the idea of a Shannon entropy minimized basis; MVR generated the results to test the relationship between Shannon entropy and energy convergence and confirmed the first results; PB had the idea to test the relationship between Shannon entropy and energy convergence. All authors edited the manuscript and provided scientific support.

Other publications

6. D. R. Alcoba, A. Torre, L. Lain, O. B. Oña, P. Capuzzi, M. Van Raemdonck, P. Bultinck, and D. Van Neck. *A hybrid configuration interaction treatment based on seniority number and excitation schemes* 2014: The Journal of Chemical Physics 141:244118.

7. P. Claeys, S. De Baerdemacker, M. Van Raemdonck, and D. Van Neck. *Eigenvalue-based method and form-factor determinant representations for integrable XXZ Richardson-Gaudin models* 2015: Physical Review B 91:155102.

8. P. Claeys, S. De Baerdemacker, M. Van Raemdonck, and D. Van Neck. *Eigenvalue-based determinants for scalar products and form factors in Richardson-Gaudin integrable models coupled to a bosonic mode* 2015: Journal of Physics A-mathematical and Theoretical 48:425201.

9. G. Acke, S. De Baerdemacker, P. Claeys, M. Van Raemdonck, W. Poelmans, D. Van Neck, and P. Bultinck. *Maximum probability domains for Hubbard models* 2016: Molecular Physics 114:1392-1405

P1 publications

1. P. Claeys, S. De Baerdemacker, M. Van Raemdonck, and D. Van Neck. *The Dicke model as the contraction limit of a pseudo-deformed Richardson-Gaudin model* 2015: Journal of Physics : Conference Series 597.

2. S. De Baerdemacker, V. Hellemans, R. van den Berg, J.-S. Caux, K. Heyde, M. Van Raemdonck, D. Van Neck, and P. A. Johnson. *Probing pairing correlations in Sn isotopes using Richardson-Gaudin integrability* 2014: Journal of Physics: Conference series 533:012058.

Oral presentations

1. M. Van Raemdonck, S. De Baerdemacker, F. De Proft, D. Van Neck, and P. Bultinck. *Constrained CI calculations to investigate charge transfer and the effects of the integer nature of the electron* Conceptual Quantum Chemistry: Present Aspects and Challenges for the Future; 4-8 April 2016, Brussels, Belgium.

2. S. De Baerdemacker, P. W. Ayers, P. Bultinck, P. A. Johnson, P. A. Limacher, D. Van Neck, and M. Van Raemdonck. *Richardson-Gaudin Integrable Systems (and Beyond) for Strongly Correlated Quantum Many-Body Systems.* MQM 2013; 2-6 June 2013, Lugano, Switzerland.

Poster presentations

1. M. Van Raemdonck, S. De Baerdemacker, and D. Van Neck. *Exploring the phase diagram of the p_x+ip_y pairing Hamiltonian by linking the eigenstates to associated bosonic states* 14-18 July 2014: XXXth International Colloquium on Group Theoretical Methods in Physics: Ghent, Belgium.

2. M. Van Raemdonck, S. De Baerdemacker, and D. Van Neck. *Interpreting the phase diagram of the $p_x + ip_y$ pairing Hamiltonian by deforming the pairing algebra* 21-23 November 2013: The "March" meeting: Namur, Belgium.

3. M. Van Raemdonck, S. De Baerdemacker, and D. Van Neck. *Perturbations on the superconducting state of metallic nanoparticles* 08-13 July 2012: International symposium on small particles and inorganic clusters XVI: Leuven , Belgium.

Bibliography

[1] B. H. Bransden and C. J. Joachain. *Quantum Mechanics*. Pearson Education, Harlow, 2000.

[2] P. A. M. Dirac. Quantum mechanics of many-electrons systems. *Proc. R. Soc. Lond.*, 123:714–733, 1930.

[3] M. Born and R. Oppenheimer. Zur Quantentheorie der Molekeln. *Ann. Phys.*, 389:457–484, 1927.

[4] T. Helgaker, P. Jørgensen, and J. Olsen. *Molecular Electronic-Structure Theory*. Wiley, Chichester, 2000.

[5] W. Dickhoff and D. Van Neck. *Many-Body Theory Exposed!* Singapore: World Scientific, 2nd edition, 2008.

[6] A. Szabo and N. S. Ostlund. *Modern quantum chemistry: Introduction to Advanced Electronic Structure Theory*. Macmillan, New York, 1982.

[7] I. Shavitt. The method of configuration interaction, in methods of electronic structure theory. *Schaefer HF, ed. Modern Theoretical Chemistry*, pages 189–275, 1977.

[8] H. Weyl. The Theory of Groups and Quantum Mechanics. Hirzel; English translation, 1928.

[9] J. Paldus. Group theoretical approach to the configuration interaction and perturbation theory calculations for atomic and molecular systems. *J. Chem. Phys.*, 61:5321–5330, 1974.

[10] D. C. Sherrill. An Introduction to Configuration Interaction Theory, 1995.

[11] P.-O. Löwdin. Quantum theory of many-particle systems. III. extension of the Hartree-Fock scheme to include degenerate systems and correlation effects. *Phys. Rev.*, 97:1509–1520, 1955.

[12] D. Cremer. From configuration interaction to coupled cluster theory: The quadratic configuration interaction approach. *WIREs Comput. Mol. Sci.*, 3:482–503, 2013.

[13] J. A. Pople. Theoretical models for chemistry. *In: Smith DW, Mc Rae WB, eds. Energy, Structure and Reactivity*, pages 51–61, 1973.

[14] S. Hirata and I. Grabowski. On the mutual exclusion of variationality and size consistency. *Theor. Chem. Acc.*, 133:1440, 2014.

[15] S. R. Langhoff and E. R. Davidson. Configuration interaction calculations on the nitrogen molecule. *Int. J. Quant. Chem.*, 8:61–72, 1974.

[16] W. Duch and G. H. F. Diercksen. Size-extensivity corrections in configuration interaction methods. *J. Chem. Phys.*, 101:3018–3030, 1994.

[17] P.-O. Löwdin. Quantum theory of many-particle systems. I. Physical interpretations by means of density matrices, natural spin-orbitals, and convergence problems in the method of configuration interaction. *Phys. Rev.*, 97:1474–1489, 1955.

[18] C. F. Bender and E. R. Davidson. A natural orbital based energy calculation for helium hydride and lithium hydride. *J. Phys. Chem.*, 70:2675–2685, 1966.

[19] J. Almlöf and P. R. Taylor. General contraction of gaussian basis sets. I. Atomic natural orbitals for first and second row atoms. *J. Phys. Chem.*, 86:4070–4077, 1987.

[20] D. R. Alcoba, A. Torre, L. Lain, G. E. Massaccesi, and O. B. Oña. Seniority number in spin-adapted spaces and compactness of configuration interaction wave functions. *J. Chem. Phys.*, 139:084103, 2013.

[21] D. R. Alcoba, A. Torre, L. Lain, G. E. Massaccesi, and O. B. Oña. Configuration interaction wave functions: A seniority number approach. *J. Chem. Phys.*, 140:234103, 2014.

[22] D. R. Alcoba, A. Torre, L. Lain, O. B. Oña, P. Capuzzi, M. Van Raemdonck, P. Bultinck, and D. Van Neck. A hybrid configuration interaction treatment based on seniority number and excitation schemes. *J. Chem. Phys.*, 141:244118, 2014.

[23] M. Van Raemdonck, D. R. Alcoba, W. Poelmans, S. De Baerdemacker, A. Torre, L. Lain, G. E. Massaccesi, D. Van Neck, and P. Bultinck. Polynomial scaling approximations and dynamic correlation corrections to doubly occupied configuration interaction wave functions. *J. Chem. Phys.*, 143:104106, 2015.

[24] L. Bytautas, T. M. Henderson, C. A. Jiménez-Hoyos, J. K. Ellis, and G. E. Scuseria. Seniority and orbital symmetry as tools for establishing a full configuration interaction hierarchy. *J. Chem. Phys.*, 135:044119, 2011.

[25] P. A. Limacher, P. W. Ayers, P. A. Johnson, S. De Baerdemacker, D. Van Neck, and P. Bultinck. A New Mean-Field Method Suitable for Strongly Correlated Electrons: Computationally Facile Antisymmetric Products of Nonorthogonal Geminals. *J. Chem. Theory and Comput.*, 9:1394, 2013.

[26] K. Boguslawski, P. Tecmer, P. W. Ayers, P. Bultinck, S. De Baerdemacker, and D. Van Neck. Efficient description of strongly correlated electrons with mean-field cost. *Phys. Rev. B*, 89: 201106, 2014.

[27] K. Boguslawski, P. Tecmer, P. A. Limacher, P. A. Johnson, P. W. Ayers, P. Bultinck, S. De Baerdemacker, and D. Van Neck. Projected seniority-two orbital optimization of the antisymmetric product of one-reference orbital geminal. *J. Chem. Phys.*, 140:214114, 2014.

[28] T. Stein, T. M. Henderson, and G. E. Scuseria. Seniority zero pair coupled cluster doubles theory. *J. Chem. Phys.*, 140:214113, 2014.

[29] T. M. Henderson, I. W. Bulik, and G. E. Scuseria. Pair extended coupled cluster doubles. *J. Chem. Phys.*, 142:214116, 2015.

[30] P. Ring and P. Schuck. *The Nuclear Many-Body Problem.* Springer-Verlag, 1980.

[31] P. A. Limacher, D. K. Taewon, P. W. Ayers, P. A. Johnson, S. De Baerdemacker, D. Van Neck, and P. Bultinck. The influence of orbital rotation on the energy of closed-shell wavefunctions. *Mol. Phys.*, 112: 853–862, 2014.

[32] P. R. Surjan. An introduction to the theory of geminals. *CORRELATION AND LOCALIZATION Book series: Topics in Current Chemistry*, 203: 63–88, 1999.

[33] P. A. Limacher. Orbital energies for seniority-zero wave functions. *J. Chem. Theory and Comput.*, 11:3629–3635, 2015.

[34] J. E. Subotnik, Y. Shao, W. Z. Liang, and M. Head-Gordon. An efficient method for calculating maxima of homogeneous functions of orthogonal matrices: Applications to localized occupied orbitals. *J. Chem. Phys.*, 121:9220, 2004.

[35] G. H. Golub and C. F. Van Loan. *Matrix Computations.* The Johns Hopkins University Press, 3 edition, 1996.

[36] P. Pulay. Convergence acceleration of iterative sequences the case of SCF iteration. *Chem. Phys. Lett.*, 73:393, 1980.

[37] P. Pulay. Improved SCF convergence acceleration. *J. Comput. Chem.*, 3: 556, 1982.

[38] J. M. Turney, A. C. Simmonett, R. M. Parrish, E. G. Hohenstein, F. A. Evangelista, J. T. Fermann, B. J. Mintz, L. A. Burns, J. J. Wilke, M. L. Abrams, N. J. Russ, M. L. Leininger, C. L. Janssen, E. T. Seidl, W. D. Allen, H. F. Schaefer, R. A. King, E. F. Valeev, C. D. Sherrill, and T. D. Crawford. Psi4: an open-source ab initio electronic structure program. *WIREs Comput. Mol. Sci.*, 2:556–565, 2012.

[39] S. Wouters, W. Poelmans, P. W. Ayers, and D. Van Neck. CheMPS2: a free open-source spin-adapted implementation of the density matrix renormalization group for ab initio quantum chemistry. *Computer Physics Communications*, 185(6):1501–1514, 2014.

[40] S. Wouters, W. Poelmans, S. De Baerdemacker, P. W. Ayers, and D. Van Neck. CheMPS2: Improved DMRG-SCF routine and correlation functions. *Computer Physics Communications*, 191:235–237, 2015.

[41] Jmol: an open-source java viewer for chemical structures in 3D. URL `www.jmol.org`. (accessed Aug 9, 2016).

[42] W. Poelmans, M. Van Raemdonck, B. Verstichel, S. De Baerdemacker, A. Torre, L. Lain, G. E. Massaccesi, D. R. Alcoba, P. Bultinck, and D. Van Neck. Variational optimization of the second order density matrix corresponding to a seniority-zero configuration interaction wave function. *J. Chem. Theory Comput.*, 11(9):4064, 2015.

[43] S. C. A. H. Pierrefixe and F. M. Bickelhaupt. Aromaticity: Molecular-Orbital Picture of an Intuitive Concept. *Chem. Eur. J.*, 13:6321, 2007.

[44] P. C. Hiberty, S. S. Shaik, J. M. Lefour, and G. Ohanessian. Is the Delocalized p-System of Benzene a Stable Electronic System? *J. Org. Chem.*, 50:4657–4659, 1985.

[45] R. Hoffmann, S. Shaik, and P. C. Hiberty. A Conversation on VB vs MO Theory: A Never-Ending Rivalry? *Acc. Chem. Res.*, 36:750–756, 2003.

[46] M. Van Raemdonck. CIFlow: a flexible and general configuration interaction program., 2016. URL `https://github.com/Mariovr/CIFlow`.

[47] F. A. Evangelista. Adaptive multiconfigurational wave functions. *J. Chem. Phys.*, 140:124114, 2014.

[48] P. J. Knowles. Compressive sampling in configuration interaction wavefunctions. *Mol. Phys.*, 113:1655, 2015.

[49] P. E. Pfeiffer. *Concepts of probability theory.* Dover, New York, 1978.

[50] V. V. Ivanov, D. I. Lyakhy, and L. Adamowicz. Indices for describing the multi-configurational nature of the coupled cluster wave function. *Mol. Phys.*, 103:2131–2139, 2005.

[51] L. Lain, A. Torre, D. R. Alcoba, O.B. Oña, and G. E. Massaccesi. A study of the compactness of wave functions based on Shannon entropy indices: a seniority number approach. *Theor. Chem. Acc.*, 134:85, 2015.

[52] P. A. Johnson, P. W. Ayers, P. A. Limacher, S. De Baerdemacker, D. Van Neck, and P. Bultinck. A size-consistent approach to strongly correlated systems using a generalized antisymmetrized product of nonorthogonal geminals. *Comp. Theor. Chem.*, 1003:101, 2013.

[53] S. Kirkpatrick, C. D. Gelatt, and M. P. Vecchi. Optimization by Simulated Annealing. *Science*, 220:671, 1983.

[54] R. B. Lehoucq, D. C. Sorensen, and C. Yang. ARPACK Users Guide: Solution of Large Scale Eigenvalue Problems by Implicitly Restarted Arnoldi Methods., 1997.

[55] M. D. Andrade, K. C. Mundim, and A. C. Malbouisson. GSA algorithm applied to electronic structure: Hartree–Fock–GSA method. *Int. J. Quant. Chem.*, 103:493–499, 2005.

[56] R. C. Raffenetti, K. Ruedenberg, C. L. Janssen, and H. F. Schaefer. Efficient use of Jacobi rotations for orbital optimization and localization. *Theor. Chim. Acta*, 86:149–165, 1993.

[57] P. E. M. Siegbahn, J. Almlöf, A. Heiberg, and B. O. Roos. The complete active space SCF (CASSCF) method in a Newton-Raphson formulation with application to the HNO molecule. *J. Chem. Phys.*, 74:2384, 1981.

[58] H. J. Werner and P. J. Knowles. A second order multiconfiguration SCF procedure with optimum convergence. *J. Chem. Phys.*, 82:5053, 1985.

[59] B. O. Roos. The complete active space SCF method in a Fock-Matrix-Based Super-CI Formulation. *Int. J. Quant. Chem.*, 18:175, 1980.

[60] C. Edmiston and K. Ruedenberg. Localized Atomic and Molecular Orbitals. *Rev. Mod. Phys.*, 35:457, 1963.

[61] M. Kobayashi, A. Szabados, H. Nakai, and P. R. Surján. Generalized Møller-Plesset Partitioning in Multiconfiguration Perturbation Theory. *J. Chem. Theory Comput.*, 6:2024–2033, 2010.

[62] P. A. Limacher, P. W. Ayers, P. A. Johnson, S. De Baerdemacker, D. Van Neck, and P. Bultinck. Simple and inexpensive perturbative correction schemes for antisymmetric products of nonorthogonal geminals. *Phys. Chem. Chem. Phys.*, 16:5061, 2014.

[63] D. H. Kobe. Maximum-Overlap Orbitals, an Energy Variational Principle, and Perturbation Theory. *Phys. Rev. C*, 3:417, 1971.

[64] W. Brenig. Zweiteilchennäherungen des mehrkörperproblems I. *Nucl. Phys.*, 13:363–374, 1957.

[65] G. D. Purvis and R. J. Bartlett. A full coupled-cluster singles and doubles model: The inclusion of disconnected triples. *J. Chem. Phys.*, 76:1910–1918, 1982.

[66] K. Raghavachari, G. W. Trucks, J. A. Pople, and M. Head-Gordon. A fifth-order perturbation comparison of electron correlation theories. *Chem. Phys. Lett.*, 157:479–483, 1989.

[67] P. Geerlings, F. De Proft, and W. Langenaeker. Conceptual Density Functional Theory. *Chemical Reviews*, 103(5):1793–1874, 2003.

[68] K. Capelle. A Bird's-Eye View of Density-Functional Theory. *Braz. J. Phys.*, 36:1318, 2006.

[69] J. Perdew, R. G. Parr, M. Levy, and J. L. Jr. Balduz. Density-Functional Theory for Fractional Particle Number: Derivative Discontinuities of the Energy. *Phys. Rev. Lett.*, 49:1691, 1982.

[70] W. J. Mortier, K. Van Genechten, and J. Gasteiger. Electronegativity equalization: application and parametrization. *J. Am. Chem. Soc.*, 107: 829, 1985.

[71] W. J. Mortier, S. K. Ghosh, and S. Shankar. Electronegativity equalization method for the calculation of atomic charges in molecules. *J. Am. Chem. Soc.*, 108:4315, 1986.

[72] J. Cioslowski and B. B. Stefanov. Electron flow and electronegativity equalization in the process of bond formation. *J. Chem. Phys.*, 99:5151–5162, 1993.

[73] J. Perdew and M. Levy. Physical Content of the Exact Kohn-Sham Orbital Energies: Band Gaps and Derivative Discontinuities. *Phys. Rev. Lett.*, 51:1884, 1983.

[74] A. J. Cohen, P. Mori-Sánchez, and W. T. Yang. Insights into current limitations of density functional theory. *Science*, 321:792, 2008.

[75] A. J. Cohen, P. Mori-Sánchez, and W. T. Yang. Second-Order Perturbation Theory with Fractional Charges and Fractional Spins. *J. Chem. Theory and Comput.*, 5:786–792, 2009.

[76] A. J. Cohen, P. Mori-Sánchez, and W. T. Yang. Challenges for Density Functional Theory. *Chem. Rev.*, 112:289–320, 2012.

[77] P. Mori-Sánchez, A. J. Cohen, and W. T. Yang. Localization and Delocalization Errors in Density Functional Theory and Implications for Band-Gap Prediction. *Phys. Rev. Lett.*, 100:146401, 2008.

[78] H. Van Aggelen, P. Bultinck, B. Verstichel, D. Van Neck, and P. W. Ayers. Incorrect diatomic dissociation in variational reduced density matrix theory arises from the flawed description of fractionally charged atoms. *Phys. Chem. Chem. Phys.*, 11:5558, 2009.

[79] A. Cedillo, D. Van Neck, and P. Bultinck. Self-consistent methods constrained to a fixed number of particles in a given fragment and its relation to the electronegativity equalization method. *Theoretical Chemistry Accounts*, 131:1, 2012.

[80] J. P. Perdew, A. Ruzsinsky, G. I. Csonka, O. A. Vydrov, G. E. Scuseria, V. N. Staroverov, and J. Tao. Exchange and Correlation in Open Systems of Fluctuating Electron Number. *Phys. Rev. A*, 76:040501, 2007.

[81] T. Verstraelen, P. W. Ayers, V. Van Speybroeck, and M. Waroquier. Acks2: Atom-condensed kohn-sham dft approximated to second order. *J. Chem. Phys.*, 138:074108, 2013.

[82] A. Ruzsinsky, J. P. Perdew, G. I. Csonka, O. A. Vydrov, and G. E. Scuseria. Spurious fractional charge on dissociated atoms: Pervasive and resilient self-interaction error of common density functionals. *J. Chem. Phys.*, 125:194112, 2006.

[83] P. Mori-Sánchez, A. J. Cohen, and W. T. Yang. Discontinuous Nature of the Exchange-Correlation Functional in Strongly Correlated Systems. *Phys. Rev. Lett.*, 102:066403, 2009.

[84] P. Mori-Sánchez and A. J. Cohen. The derivative discontinuity of the exchange-correlation functional. *Phys. Chem. Chem. Phys.*, 16:14378–14387, 2014.

[85] W. T. Yang, P. Mori-Sánchez, and A. J. Cohen. Extension of many-body theory and approximate density functionals to fractional charges and fractional spins. *J. Chem. Phys.*, 139:104114, 2013.

[86] E. R. Davidson and S. Chakravorty. A test of the Hirshfeld definition of atomic charges and moments. *Theor. Chem. Acc.*, 83:319–330, 1992.

[87] M. D. Segall, R. Shah, C. J. Pickard, and M. C. Payne. Population analysis of plane-wave electronic structure calculations of bulk materials. *Phys. Rev. B*, 54:16317, 1996.

[88] P. Mori-Sánchez and A. J. Cohen. Dramatic changes in electronic structure revealed by fractionally charged nuclei. *J. Chem. Phys.*, 140: 044110, 2014.

[89] R. G. Parr and L. J. Bartolotti. On the Geometric Mean Principle for Electronegativity Equalization. *J. Am. Chem. Soc.*, 104:3801–3803, 1982.

[90] R. Carbó-Dorca and P. Bultinck. Quantum mechanical basis for Mulliken population analysis. *J. Math. Chem.*, 36:231, 2004.

[91] M. Soriano and J. J. Palacios. Theory of projections with nonorthogonal basis sets: Partitioning techniques and effective Hamiltonians. *Phys. Rev. B*, 90:075128, 2014.

[92] I. Mayer and A. Hamza. Atomic Decomposition of Identity: General Formalism for Population Analysis and Energy Decomposition. *Int. J. Quantum Chem.*, 103:798–807, 2005.

[93] S. F. Vyboishchikov and P. Salvador. Ab initio energy partitioning at the correlated level. *Chem. Phys. Lett.*, 430:204–209, 2006.

[94] F. Jensen. *Introduction to Computational Chemistry.* Wiley, New York, 1999.

[95] P. W. Ayers and R. G. Parr. Variational Principles for describing chemical reactions: The Fukui Function and Chemical Hardness Revisited. *J. Am. Chem. Soc.*, 122(9):2010–2018, 2000.

[96] T. D. Crawford and H. F. Schaefer. *An Introduction to Coupled Cluster Theory for Computational Chemists*, pages 33–136. Wiley, New York, 2007.

[97] R. J. Bartlett and M. Musiał. Coupled-cluster theory in quantum chemistry. *Rev. Mod. Phys.*, 79:291, 2007.

[98] C. D. Sherrill, A. Dutta, Abrams M. L., and J. S. Sears. *Bond Breaking in Quantum Chemistry: A Comparison of Single- and Multi-Reference Methods*, chapter 6, pages 75–88.

[99] P. G. Szalay, T. Müller, G. Gidofalvi, H. Lischka, and R. Shepard. Multiconfiguration Self-Consistent Field and Multireference Configuration Interaction Methods and Applications. *Chem. Rev.*, 112:108–181, 2012.

[100] S. R. White. Density matrix formulation for quantum renormalization groups. *Phys. Rev. Lett.*, 69:2863, 1992.

[101] S. R. White and R. L. Martin. Ab initio quantum chemistry using the density matrix renormalization group. *J. Chem. Phys.*, 110(9):4127, 1999.

[102] G. K.-L. Chan and M. Head-Gordon. Highly correlated calculations with a polynomial cost algorithm: A study of the density matrix renormalization group. *J. Chem. Phys.*, 116:4462–4476, 2002.

[103] U. Schollwöck. The density-matrix renormalization group in the age of matrix product states. *Ann. Phys.*, 326(1):96, 2011.

[104] H. Fukutome. Unrestricted hartree–fock theory and its applications to molecules and chemical reactions. *Int. J. Quantum Chem.*, 20:955–1065, 1981.

[105] J. L. Stuber and J. Paldus. *Symmetry breaking in the independent particle model*, volume 1 of *Fundamental World of Quantum Chemistry, A Tribute Volume to the Memory of Per-Olov Löwdin*, chapter 4, pages 67–139. Kluwer Academic, 2003.

[106] C. A. Jiménez-Hoyos, T. M. Henderson, and G. E. Scuseria. Generalized hartree–fock description of molecular dissociation. *J. Chem. Theory Comput.*, 7(9):2667–2674, 2011.

[107] C. A. Jiménez-Hoyos, T. M. Henderson, T. Tsuchimochi, and G. E. Scuseria. Projected hartree–fock theory. *J. Chem. Phys.*, 136(16):164109, 2012.

[108] K. Boguslawski, P. Tecmer, P. W. Ayers, P. Bultinck, S. De Baerdemacker, and D. Van Neck. Efficient description of strongly correlated electrons with mean-field cost. *Phys. Rev. B*, 89: 201106, 2014.

[109] P. Ring and P. Schuck. *The Nuclear Many-Body Problem.* Springer-Verlag, 2005.

[110] P. A. Limacher, T. D. Kim, P. W. Ayers, P. A. Johnson, S. De Baerdemacker, D. Van Neck, and P. Bultinck. The influence of orbital rotation on the energy of closed-shell wavefunctions. *Mol. Phys.*, 112:853–862, 2014.

[111] P. A. Johnson, P. W. Ayers, P. A. Limacher, S. De Baerdemacker, D. Van Neck, and P. Bultinck. A size-consistent approach to strongly correlated systems using a generalized antisymmetrized product of nonorthogonal geminals. *Comput. Theor. Chem.*, 1003:101–113, 2013.

[112] K. Husimi. Some formal properties of the density matrix. *Proc. Phys.-Math. Soc. Japan*, 22:264, 1940.

[113] P.-O. Löwdin. Quantum theory of many-particle systems. i. physical interpretations by means of density matrices, natural spin-orbitals, and convergence problems in the method of configurational interaction. *Phys. Rev.*, 97:1474–1489, 1955.

[114] J. E. Mayer. Electron correlation. *Phys. Rev.*, 100:6, 1955.

[115] R. H. Tredgold. Density matrix and the many-body problem. *Phys. Rev.*, 105:5, 1957.

[116] A. J. Coleman. Structure of fermion density matrices. *Rev. Mod. Phys.*, 35:668–686, 1963.

[117] Y.K. Liu, M. Christandl, and F. Verstraete. Quantum computational complexity of the N-representability problem: QMA complete. *Phys. Rev. Lett.*, 98:110503, 2007.

[118] C. Garrod and J. K. Percus. Reduction of the N-particle variational problem. *J. Math. Phys.*, 5:1756–1776, june 1964.

[119] Z. Zhao, B. J. Braams, M. Fukuda, M. L. Overton, and J. K. Percus. The reduced density matrix method for electronic structure calculations and the role of three-index representability conditions. *J. Chem. Phys.*, 120:5, 2004.

[120] B. Verstichel, H. van Aggelen, D. Van Neck, P. W. Ayers, and P. Bultinck. Subsystem constraints in variational second order density matrix optimization: Curing the dissociative behavior. *J. Chem. Phys.*, 132: 114113, 2010.

[121] N. Shenvi and A. F. Izmaylov. Active-space n-representability constraints for variational two-particle reduced density matrix calculations. *Phys. Rev. Lett.*, 105:213003, 2010.

[122] L. Vandenberghe and S. Boyd. Semidefinite programming. *SIAM Rev.*, 38:49, 1996.

[123] Yu. E. Nesterov and M. J. Todd. Self-scaled barriers and interior-point methods for convex programming. *Math. Oper. Res.*, 22(1):1–42, 1997.

[124] Y.E. Nesterov and A. Nemirovski. *Interior Point Polynomial Algorithms in Convex Programming*, volume 13 of *Studies in Applied and Numerical Mathematics*. SIAM, 1994.

[125] M. Yamashita, K. Fujisawa, M. Fukuda, K. Kobayashi, K. Nakata, and M. Nakata. *Latest Developments in the SDPA Family for Solving Large-Scale SDPs*, volume 166. 2012.

[126] B. Verstichel, H. van Aggelen, W. Poelmans, S. Wouters, and D. Van Neck. Extensive v2dm study of the one-dimensional hubbard model for large lattice sizes: Exploiting translational invariance and parity. *Comput. Theor. Chem.*, 1003:12–21, 2013.

[127] D. A. Mazziotti. Large-scale semidefinite programming for many-electron quantum mechanics. *Phys. Rev. Lett.*, 106:083001, 2011.

[128] D. A. Mazziotti. Realization of quantum chemistry without wave functions through first-order semidefinite programming. *Phys. Rev. Lett.*, 93: 213001, 2004.

[129] B. Verstichel, H. van Aggelen, D. Van Neck, P. Bultinck, and S. De Baerdemacker. A primal-dual semidefinite programming algorithm tailored to the variational determination of the two-body density matrix. *Comput. Phys. Commun.*, 182:1235–1244, 2011.

[130] B. Verstichel, H. van Aggelen, D. Van Neck, P. W. Ayers, and P. Bultinck. Variational density matrix optimization using semidefinite programming. *Comput. Phys. Commun.*, 182:2025–2028, 2011.

[131] D. A. Mazziotti. Quantum chemistry without wave functions: Two-electron reduced density matrices. *Acc. Chem. Res.*, 39(3):207–215, 2006.

[132] M. Nakata, H. Nakatsuji, M. Ehara, M. Fukuda, K. Nakata, and K. Fujisawa. Variational calculation of fermion second-order reduced density matrices by semidefinite programming algorithm. *J. Chem. Phys.*, 114: 19, 2001.

[133] D. A. Mazziotti. Variational minimization of atomic and molecular ground-state energies via the two-particle density matrix. *Phys. Rev. A*, 65:062511, 2002.

[134] M. Nakata, B. J. Braams, K. Fujisawa, M. Fukuda, J. K. Percus, M. Yamashita, and Z. Zhao. Variational calculation of second-order reduced density matrices by strong N-representability conditions and an accurate semidefinite programming solver. *J. Chem. Phys.*, 128:164113, 2008.

[135] B. Verstichel, H. van Aggelen, D. Van Neck, P. W. Ayers, and P. Bultinck. Variational determination of the second-order density matrix for the isoelectronic series of beryllium, neon, and silicon. *Phys. Rev. A*, 80: 032508, 2009.

[136] H. van Aggelen, B. Verstichel, P. Bultinck, D. Van Neck, P. W. Ayers, and D. L. Cooper. Chemical verification of variational second-order density matrix based potential energy surfaces for the n2 isoelectronic series. *J. Chem. Phys.*, 132:114112, 2010.

[137] F. Weinhold and B. E. Wilson. Reduced density matrices of atoms and molecules. i. the 2 matrix of double-occupancy, configuration-interaction wavefunctions for singlet states. *J. Chem. Phys.*, 46:2752, 1967.

[138] F. Weinhold and B. E. Wilson. Reduced density matrices of atoms and molecules. ii. on the n-representability problem. *J. Chem. Phys.*, 47(7): 2298, 1967.

[139] P. Siegbahn, A. Heiberg, B. Roos, and B. Levy. A Comparison of the Super-CI and the Newton-Raphson Scheme in the Complete Active Space SCF Method. *Phys. Scr.*, 21:323, 1980.

[140] K. Ruedenberg, L. M. Cheung, and S. T. Elbert. Mcscf optimization through combined use of natural orbitals and the brillouin-levy-berthier theorem. *Int. J. Quantum Chem.*, 16(5):1069, 1979.

[141] Z. Rashid and J. H. van Lenthe. A quadratically convergent VBSCF method. *J. Chem. Phys.*, 138(5):054105, 2013.

[142] B. O. Roos, P. R. Taylor, and P. E. M. Siegbahn. A complete active space scf method (casscf) using a density matrix formulated super-ci approach. *Chem. Phys.*, 48(2):157, 1980.

[143] B. H. Lengsfield. General second order mcscf theory: A density matrix directed algorithm. *J. Chem. Phys.*, 73:382–390, 1980.

[144] R. C. Raffenetti, K. Ruedenberg, C. L. Janssen, and H. F. Schaefer. Efficient use of jacobi rotations for orbital optimization and localization. *Theor. Chim. Acta*, 86:149–165, 1993.

[145] P. W. Ayers. Using classical many-body structure to determine electronic structure: An approach using k-electron distribution functions. *Phys. Rev. A*, 74:042502, 2006.

[146] D. Van Neck and P. W. Ayers. Necessary conditions for the N-representability of the second-order reduced density matrix: Upper bounds on the P and Q matrices. *Phys. Rev. A*, 75:032502, 2007.

[147] J. R. Hammond and D. A. Mazziotti. Variational two-electron reduced-density-matrix theory: Partial 3-positivity conditions for N-representability. *Phys. Rev. A*, 71:062503, 2005.

[148] D. A. Mazziotti. Variational reduced-density-matrix method using three-particle n-representability conditions with application to many-electron molecules. *Phys. Rev. A*, 74:032501, 2006.

[149] D. A. Mazziotti. *Variational Two-Electron Reduced-Density-Matrix Theory*, pages 19–59. 2007.

[150] B. J. Braams, J. K. Percus, and Z. Zhao. *The T1 and T2 Representability Conditions*, page 93. Wiley, 2007.

[151] Y. Makoto, F. Katsuki, and K. Masakazu. Implementation and evaluation of sdpa 6.0 (semidefinite programming algorithm 6.0). *Optim. Method. Softw.*, 18:491–505, 2003.

[152] Sdpa (semidefinite programming algorithm). `http://sdpa.sourceforge.net`. (accessed April 20, 2015).

[153] B. Verstichel. *Variational determination of the two-particle density matrix as a quantum many-body technique*. PhD thesis, Ghent University, 2012.

[154] J. Povh, F. Rendl, and A. Wiegele. A boundary point method to solve semidefinite programs. *Computing*, 78:277–286, 2006.

[155] J. Malick, J. Povh, R. Franz, and A. Wiegele. Regularization methods for semidefinite programming. *SIAM J. Optim.*, 20(1):336–356, 2009.

[156] J. Olsen, D. L. Yeager, and P. Jørgensen. *Optimization and Characterization of a Multiconfigurational Self-Consistent Field (MCSCF) State*, pages 1–176. Wiley, 2007.

[157] M. W. Schmidt and M. S. Gordon. The construction and interpretation of mcscf wavefunctions. *Annu. Rev. Phys. Chem.*, 49:233–266, 1998.

[158] B. H. Lengsfield and B. Liu. A second order mcscf method for large ci expansions. *J. Chem. Phys.*, 75:478–480, 1981.

[159] G. Gidofalvi and D. A. Mazziotti. Active-space two-electron reduced-density-matrix method: Complete active-space calculations without diagonalization of the n-electron hamiltonian. *J. Chem. Phys.*, 129:134108, 2008.

[160] Ward Poelmans. v2DM-DOCI solver. `https://github.com/wpoely86/doci_sdp-atom`. (accessed May 3, 2015).

[161] S. Wouters and D. Van Neck. The density matrix renormalization group for ab initio quantum chemistry. *European Physical Journal D*, 68(9): 272, 2014.

[162] S. Wouters, T. Bogaerts, P. Van Der Voort, V. Van Speybroeck, and D. Van Neck. Communication: Dmrg-scf study of the singlet, triplet, and quintet states of oxo-mn(salen). *J. Chem. Phys.*, 140:241103, 2014.

[163] D. Kats and F. R. Manby. Communication: The distinguishable cluster approximation. *J. Chem. Phys.*, 139:021102, 2013.

[164] X. Li and J. Paldus. Reduced multireference coupled cluster method: Ro-vibrational spectra of n2. *J. Chem. Phys.*, 113:9966–9977, 2000.

[165] M. Couty and M. B. Hall. Generalized molecular orbital theory ii. *J. Phys. Chem. A*, 101(37):6936–6944, 1997.

[166] G. K.-L. Chan, M. Kállay, and J. Gauss. State-of-the-art density matrix renormalization group and coupled cluster theory studies of the nitrogen binding curve. *J. Chem. Phys.*, 121:6110, 2004.

[167] K. Raghavachari, G. W. Trucks, J. A. Pople, and M. Head-Gordon. A fifth-order perturbation comparison of electron correlation theories. *Chem. Phys. Lett.*, 157(6):479 – 483, 1989.

[168] A. D. Becke. A new mixing of hartree-fock and local density-functional theories. *J. Chem. Phys.*, 98:1372–1377, 1993.

[169] C. Lee, W. Yang, and R. G. Parr. Development of the colle-salvetti correlation-energy formula into a functional of the electron density. *Phys. Rev. B*, 37:785–789, 1988.

[170] P. A. Limacher, P. W. Ayers, P. A. Johnson, S. De Baerdemacker, D. Van Neck, and P. Bultinck. Simple and inexpensive perturbative correction schemes for antisymmetric products of nonorthogonal geminals. *Phys. Chem. Chem. Phys.*, 16:5061–5065, 2014.

[171] H. Van Aggelen, P. Bultinck, B. Verstichel, D. Van Neck, and P. W. Ayers. Incorrect diatomic dissociation in variational reduced density matrix theory arises from the flawed description of fractionally charged atoms. *Phys. Chem. Chem. Phys.*, 11:5558, 2009.

[172] W. Yang, Y. Zhang, and P. W. Ayers. Degenerate ground states and a fractional number of electrons in density and reduced density matrix functional theory. *Phys. Rev. Lett.*, 84:5172, 2000.

[173] R. S. Mulliken. Electronic population analysis on lcao–mo molecular wave functions. i. *J. Chem. Phys.*, 23(10):1833–1840, 1955.

[174] H. van Aggelen, B. Verstichel, P. Bultinck, D. Van Neck, P. W. Ayers, and D. L. Cooper. Variational second order density matrix study of F_3^-: Importance of subspace constraints for size-consistency. *J. Chem. Phys.*, 134:054115, 2011.

[175] D. Rowe and J. Wood. *Fundamentals of nuclear models.* World Scientific, 2010.

[176] G. Ortiz, R. Somma, J. Dukelsky, and S. Rombouts. Exactly-solvable models derived from a Gaudin algebra. *Nucl. Phys. B*, 707:421, 2005.

[177] J. Dukelsky, S. Pittel, and G. Sierra. Colloquium: Exactly solvable Richardson-Gaudin models for many-body quantum systems. *Rev. Mod. Phys.*, 76:643, 2004.

[178] P. W. Anderson. Theory of dirty superconductors. *J. Phys. Chem. Solids*, 11:26, 1959.

[179] D. C. Ralph, C. T. Black, and M. Tinkham. Spectroscopic Measurements of Discrete Electronic States in Single Metal Particles. *Phys. Rev. Lett.*, 74:3241, 1995.

[180] C. T. Black, D. C. Ralph, and M. Tinkham. Spectroscopy of the Superconducting Gap in Individual Nanometer-Scale Aluminum Particles. *Phys. Rev. Lett.*, 76:688, 1996.

[181] D. C. Ralph, C. T. Black, and M. Tinkham. Gate-Voltage Studies of Discrete Electronic States in Aluminum Nanoparticles. *Phys. Rev. Lett.*, 78:4087, 1997.

[182] J. Bardeen, L. N. Cooper, and J. Schrieffer. Theory of superconductivity. *Phys. Rev.*, 108:1175, 1957.

[183] L. N. Cooper. Bound Electron Pairs in a Degenerate Fermi Gas. *Phys. Rev.*, 104:1189, 1956.

[184] A. Mastelloni, G. Falci, and R. Fazio. Small Superconducting Grain in the Canonical Ensemble. *Phys. Rev. Lett.*, 80:4542, 1998.

[185] F. Braun and J. von Delft. Fixed-N superconductivity: The Crossover from the Bulk to the Few-Electron Limit. *Phys. Rev. Lett.*, 81:4712, 1998.

[186] J. Dukelsky and G. Sierra. Density Matrix Renormalization Group Study of Ultrasmall Superconducting Grains. *Phys. Rev. Lett.*, 83:172, 1999.

[187] G. Sierra, J. Dukelsky, G. G. Dussel, J. von Delft, and F. Braun. Exact study of the effect of level statistics in ultrasmall superconducting grains. *Phys. Rev. B*, 61:890', 2000.

[188] D. J. Dean and M. Hjorth-Jensen. Pairing in nuclear systems: from neutron stars to finite nuclei. *Rev. Mod. Phys.*, 75:607, 2003.

[189] R. W. Richardson. A restricted class of exact eigenstates of the pairing-force Hamiltonian. *Phys. Lett.*, 3:277, 1963.

[190] R. W. Richardson and N. Sherman. Exact eigenstates of the pairing-force Hamiltonian. *Nucl. Phys.*, 52:221, 1964.

[191] M. Gaudin. Diagonalisation of a class of spin Hamiltonians. *J. Phys. (Paris)*, 37:1087, 1976.

[192] R. A. Smith and V. Ambegaokar. Effect of Level Statistics on Superconductivity in Ultrasmall Metallic Grains. *Phys. Rev. Lett.*, 77:4962, 1996.

[193] V. N. Gladilin, V. M. Fomin, and J. T. Devreese. Shape of nanosize superconducting grains: does it influence pairing characteristics? *Sol. State Comm.*, 121:519, 2002.

[194] V. Z. Kresin and Y. N. Ovchninnikov. Shell structure and strengthening of superconducting pair correlation in nanoclusters. *Phys. Rev. B*, 74: 24514, 2006.

[195] A. M. García-García, J. D. Urbina, E. A. Yuzbashyan, K. Richter, and B. L. Altshuler. BCS superconductivity in metallic nanograins: Finite-size corrections, low-energy excitations, and robustness of shell effects. *Phys. Rev. B*, 83:14510, 2011.

[196] M. D. Croitoru, A. A. Shanenko, C. C. Kaun, and F. M. Peeters. Metallic nanograins: spatially nonuniform pairing induced by quantum confinement. *Phys. Rev. B*, 83:214509, 2011.

[197] I. Brihuega, Antonio M. García-García, P. Ribeiro, M. M. Ugeda, C. H. Michaelis, S. Bose, and K. Kern. Experimental observation of thermal fluctuations in single superconducting Pb nanoparticles through tunneling measurements. *Phys. Rev. B*, 84:104525, 2011.

[198] S. Bose, A. M. García-García, M. M. Ugeda, C. H. Michaelis, I. Brihuega, and K. Kern. Observation of shell effects in superconducting nanoparticles of Sn. *Nature Mat.*, 9:550, 2010.

[199] J. Tempere, V. N. Gladilin, Silvera I. F., and J. T. Devreese. Cooper pairing and superconductivity on a spherical surface: applying the Richardson model to a multielectron bubble in liquid helium. *Phys. Rev. B*, 72:94506, 2005.

[200] V. N. Gladilin, V. M. Fomin, and J. T. Devreese. Critical temperature and specific heat for Cooper pairing on a spherical surface. *Phys. Rev. B*, 74:104512, 2006.

[201] S. De Baerdemacker. Richardson-Gaudin integrability in the contraction limit of the quasispin. *Phys. Rev. C*, 86:044332, 2012.

[202] J. Von Delft and D.C. Ralph. Spectroscopy of discrete energy levels in ultrasmall metallic grains. *Phys. Rep.*, 345:61, 2001.

[203] J. Hafner. Ab-Initio Simulations of Materials Using VASP: Density-Functional Theory and Beyond. *J. Comput. Chem.*, 29:2044, 2008.

[204] E. A. Yuzbashyan, A. A. Baytin, and B. L. Altshuler. Strong-coupling expansion for the pairing Hamiltonian for small superconducting metallic grains. *Phys. Rev. B*, 68:214509, 2003.

[205] J. A. Reyes and M. del Castillo-Mussot. Screened Coulomb potential for a quantum wire in the Thomas-Fermi approximation. *Phys. Rev. B*, 57: 9869, 1998.

[206] M. Ibanez, J. Links, G. Sierra, and S.-Y. Zhao. Exactly solvable pairing model for superconductors with $p_x + ip_y$-wave symmetry. *Phys. Rev. B*, 79:180501, 2009.

[207] S. M. A. Rombouts, J. Dukelsky, and G. Ortiz. Quantum phase diagram of the integrable $p_x + ip_y$ fermionic superfluid. *Phys. Rev. B*, 82:224510, 2010.

[208] G. Ortiz, R. Somma, J. Dukelsky, and S. Rombouts. Exactly-Solvable Models Derived from a Generalized Gaudin Algebra. *Nucl. Phys. B*, 707: 421, 2005.

[209] Y. Nishida. Induced p-wave superfluidity in two dimensions: Brane world in cold atoms and nonrelativistic defect CFTs. *Ann. Phys.*, 324:897, 2009.

[210] C. Zhang, S. Tewari, R. M. Lutchyn, and S. D. Sarma. p_x+ip_y superfluid from s-wave interactions of fermionic cold atoms. *Phys. Rev. Lett.*, 101:160401, 2008.

[211] J. Xia, Y. Maeno, P.T. Beyersdorf, M.M. Fejer, and A. Kapitulnik. High Resolution Polar Kerr Effect Measurements of Sr2RuO4: Evidence for Broken Time Reversal Symmetry in the Superconducting State. *Phys. Rev. Lett.*, 97:167002, 2006.

[212] J. Dukelsky, H. S. Lerma, L. M. Robledo, R. Rodriguez-Guzman, and S. M. A. Rombouts. Exactly solvable pairing Hamiltonian for heavy nuclei. *Phys. Rev. C*, 84:061301, 2011.

[213] V. Gurarie and L. Radzihovsky. Resonantly paired fermionic superfluids. *Ann. Phys.*, 322:2, 2007.

[214] M. S. Foster, M. Dzero, V. Gurarie, and E. A. Yuzbashyan. Quantum quench in a p+ip superfluid: Winding numbers and topological states far from equilibrium. *Phys. Rev. B*, 88:104511, 2013.

[215] J. Dukelsky, C. Esebbag, and P. Schuck. Class of Exactly Solvable Pairing Models. *Phys. Rev. Lett.*, 87:066403, 2001.

[216] C. Dunning, M. Ibanez, J. Links, G. Sierra, and S.-Y. Zhou. Exact solution of the p+ip pairing Hamiltonian and a hierarchy of integrable models. *Journal of Statistical Mechanics: Theory and Experiment*, 2010: 8025, 2010.

[217] J. Links and I. Marquette. Generalised Heine-Stieltjes and Van Vleck polynomials associated with degenerate, integrable BCS models. *J. Stat. Mech.*, 2012:8019, 2012.

[218] O. El Araby, V. Gritsev, and A. Faribault. Bethe ansatz and ordinary differential equation correspondence for degenerate Gaudin models. *Phys. Rev. B*, 85:115130, 2012.

[219] A. Faribault, O. El Araby, C. Sträter, and V. Gritsev. Gaudin models solver based on the correspondence between Bethe ansatz and ordinary differential equations. *Phys. Rev. B*, 83:235124, 2011.

[220] H. S. Lerma, S.M.A. Rombouts, J. Dukelsky, and G. Ortiz. Integrable two-channel p_x+ip_y-wave model of a superfluid. *Phys. Rev. B*, 75:100503, 2011.

[221] Q. Chen, J. Stajic, S. Tan, and K. Levin. BCS–BEC crossover: From high temperature superconductors to ultracold superfluids. *Physics Reports*, 412:1, 2005.

[222] M. Sambataro. Pair condensation in a finite Fermi system. *Phys. Rev. C*, 75:054314, 2007.

[223] I. Talmi. *Simple models of complex nuclei.* Harwood academic publishers, 1993.

[224] F. Pan, J.P. Draayer, and W.E. Ormand. A particle-number-conserving solution to the generalized pairing problem. *Physics Letters B*, 422:422, 1998.

[225] A.B. Balantekin, J.H. de Jesus, and Y. Pehlivan. Spectra and symmetry in nuclear pairing. *Phys. Rev. C*, 75:064304, 2007.

[226] F.T. Arrechi, E. Courtens, R. Gilmore, and T. Harry. Atomic Coherent States in Quantum Optics. *Phys. Rev. A*, 6:2211, 1972.

[227] X. Guan, K. Launey, M. Xie, L. Bao, F. Pan, and J.P. Draayer. The heine-stieltjes correspondence and the polynomial approach to the standard pairing problem. *Phys. Rev. C*, 86:024313, 2012.

[228] T.J. Stieltjes. *Sur quelques Theorèmes d' Algèbre, Oeuvres Completes.* Noordhoff, Groningen, 1914.

[229] B. S. Shastry and A. Dhar. Solution of a generalized Stieltjes problem. *J. Phys. A: Math. Gen.*, 34:6197, 2001.

[230] G. G. Dussel, S. Pittel, J. Dukelsky, and P. Sarriguren. Cooper pairs in atomic nuclei. *Phys. Rev. C*, 76:011302, 2007.

[231] M. Van Raemdonck, S. De Baerdemacker, and D. Van Neck. Perturbations on the superconducting state of metallic nanoparticles: influence of geometry and impurities. *European Physical Journal D*, 67:14, 2013.

[232] F. Dominguez, C. Esebbag, and J. Dukelsky. Solving the Richardson equations close to the critical points. *J. Phys. A*, 39:11349, 2006.

[233] M. Van Raemdonck. Movie of the evolution of the Richardson-Gaudin variables for the XXZ model with increasing interaction strength, 2014. URL `http://arxiv.org/src/1402.0339v1/anc`.

[234] M. Van Raemdonck. A versatile Richardson-Gaudin solver, 2014. URL `https://github.com/Mariovr/RG`.